

Quantum (in)stability of maximally symmetric space-times

Jewel K. Ghosh^{*,§}, Elias Kiritsis^{‡,¶}, Francesco Nitti[‡], Valentin Nourry[‡]

^{*} *Independent University Bangladesh (IUB), Bashundhara RA, Dhaka 1229, Bangladesh*

[§] *Center for Computational and Data Sciences, Independent University, Bangladesh, Bashundhara RA, Dhaka 1229, Bangladesh*

[‡] *Université Paris Cité, CNRS, Astroparticule et Cosmologie, F-75013 Paris, France*

[¶] *Crete Center for Theoretical Physics, Institute for Theoretical and Computational Physics, Department of Physics, Voutes University Campus, GR-70013, Vasilika Vouton, Heraklion, Greece*

ABSTRACT: Classical gravity coupled to a CFT_4 (matter) is considered. The effect of the quantum dynamics of matter on gravity is studied around maximally symmetric spaces (flat, de Sitter and Anti de Sitter). The structure of the graviton propagator is modified and non-trivial poles appear due to matter quantum effects. The position and residues of such poles are mapped as a function of the relevant parameters, the central charge of the CFT_4 , the two R^2 couplings of gravity as well as the curvature of the background space-time. The instabilities induced are determined. Such instabilities can be important in cosmology as they trigger the departure from de Sitter space and in some regions of parameters are more important than the well-known scalar instabilities. It is also determined when the presence of such instabilities is unreliable if the associated scales are larger than the “species” cutoff of the gravitational theory.

**Dedicated to the memory of Stavros Katsanevas,
a universal scientist and a visionary.**

Contents

1. Introduction	2
1.1 Cutoffs in effective gravity theories	8
1.2 Summary and results	11
1.3 Discussion	21
2. The theory	24
2.1 Setup	25
2.2 Constructing the renormalized action	26
2.3 The induced stress tensor	30
2.4 Background solutions	31
3. Bulk metric perturbations	33
4. The boundary scalar perturbation	37
4.1 Gauge fixing	37
4.2 Scalar equation of motion	38
4.3 Scalar tachyonic instabilities	40
5. The spin-two spectral equations	43
5.1 Flat-slicing	43
5.2 dS-slicing	47
5.3 AdS-slicing	50
5.3.1 Dynamical gravity on one side	51
5.3.2 Symmetric boundary conditions	53
5.4 Identifying ghosts from poles in the propagator	54
6. Tensor instabilities in pure gravity	55
6.1 When are tensor ghosts light?	57
7. Poles of the Minkowski spin-two propagator and stability	59
8. Poles of the dS spin-two propagator and stability	64
8.1 Numerical results for two typical sets of parameters	64
8.2 Analytic results for tensor tachyonic modes in dS at large $ \nu $	70
8.3 Tachyonic and ghost-like instabilities for dS in parameter space	73
9. Poles of the AdS spin-two propagator and stability	83
9.1 Results for two typical sets of parameters	84
9.2 Analytic results for tensor tachyonic modes in AdS in the large- $ \nu $ regime	87
9.3 Infinite series of stable solutions	90
9.4 Tachyons and ghosts in parameter space for the AdS case	94

Acknowledgements	98
Appendix	100
A. Ghosts and tachyons in Effective Field Theory	100
A.1 A simple model	100
A.2 EFT	100
A.3 The IR expansion	101
B. Renormalized action	102
C. Comparison with the Starobinsky model	104
D. AdS slicing coordinates	105
E. Schrodinger problem in the bulk	108
F. Flat space tachyonic time scale	110
G. Tachyonic tensor eigenmodes in de Sitter	114
H. Tachyonic tensor eigenmodes in anti de Sitter	119
I. Asymptotic behaviour of Legendre functions	122
J. Quadratic action for tensor modes	126
K. Dynamics of scalar modes	129
K.1 Constrained scalar mode	131
L. Comparison with previous results for a dS boundary	133
M. Snapshots for the spin-2 propagator	134
M.1 Minkowski	134
M.2 de Sitter	135
M.3 Anti-de Sitter	150
References	164

1. Introduction

The interplay between semiclassical gravity and the quantum effects of Quantum Field Theory (QFT) is a topic of research that has been in the spotlight for several decades. The most important area of applicability motivating these issues arises from cosmology.

In cosmology, we treat gravity as semiclassical¹ and we couple it with QFTs. The class of semiclassical metrics relevant in this case is cosmological metrics, with the most prominent example being the maximally symmetric cosmological metric, i.e., de Sitter.

Other contexts also are relevant, like semiclassical effective actions of string theory with asymptotically AdS or flat asymptotics. In this context, quantum effects in gravity and matter seem to go hand in hand as they are controlled by the same underlying parameter, the string coupling constant. However, we understand that there are two types of quantum effects associated with string loops or the α' expansion, although their separation is “duality-frame” dependent. There are however limits, (known as double scaling limits) in which gravitational quantum effects can be made subleading to “matter” quantum effects. In the context of holography, relevant for AdS or asymptotically AdS spaces typically (bulk) gravity and matter are treated semiclassically, but subleading corrections in N involve quantum effects in both sectors.

The case of QFTs on de Sitter space is an especially hot issue, as we believe that our universe has been near de Sitter at least twice during its history. Defining a QFT on de Sitter space and, in particular, answering questions about QFT backreaction on the geometry is a subtle issue. Perturbative field quantization (and renormalization) on fixed classical curved space-times is text-book material [1]. However, answering concrete questions about the observable effects of quantum fields backreacting on classical geometry is not straightforward. This concerns particularly theories which are gapless in the infrared, due to the presence of infrared divergences (and in most cases strong IR dynamics).

It is well known that in classical GR, both de Sitter space and Flat Minkowski space are non-linearly stable², [3]-[7]. However, in the presence of quantum effects from matter, instabilities can appear. For the case of flat space this was established in [8]-[18].

In (quasi) de Sitter space, there are several other issues arising when one considers QFTs. In [19]-[23] a divergence of scalar correlators was observed at large times. This was addressed in [24, 25, 26] using a stochastic approach. The case of interacting massive scalar fields has been treated thoroughly more recently in [27, 28]. A systematic approach to compute corrections in the massless case is lacking and the problem remains still open.

The accumulation of long wavelength fluctuations in an expanding universe is another issue that has been studied, starting with references [29, 30]. Their analysis was extended further in [31]. Another issue concerned the fact that the two-point function of a massless scalar in de Sitter space had to break de Sitter symmetry, due to the presence of a zero mode, [32, 33]. This issue is of a different nature and is more similar to the fact that in two dimensions, a massless scalar is IR singular. The resolution of this issue may be therefore similar: massless scalars are not good acceptable fields on de Sitter space³ as argued in [34].

¹Exceptions exist where gravity is treated in perturbation theory, [36] or where the curvature is very strong and a more fundamental theory (an example is string theory) can take over.

²Famously, AdS is not non-linearly stable, [2], (and citations to it) even at the level of classical gravity. The instability is towards the formation of black holes.

³We shall later conclude in this paper that in all the theories we examine and which are all gapless, there is no breaking of de Sitter invariance, and the de Sitter invariant vacuum is chosen.

The expectation that QFTs in de Sitter space render the manifold unstable at the non-linear level has been entertained for a long time [35]-[43]. In particular, destabilizing effects were most important from massless particles, and a gravity 2-loop computation in [36] suggested such an instability. Similar calculations with massless scalars implied similar effects, [29, 30], see however [44].

The topic of quantum effects has been revived after cosmological (CMB) data became precise, and in [45, 46, 47] it was argued that large time-dependent logs from quantum effects of quantum fields, could give large corrections to inflationary observables. A different approach in [48], provided different results. Therefore, the question of the consequences of the secular terms (growing with time) which arise in perturbation theory of a massless scalar field in the cosmological patch of de Sitter remains controversial. Do these contributions indicate an instability of de Sitter space against quantum perturbations? Or is this conclusion an artefact of finite orders in perturbation theory, which is expected to disappear once an appropriate resummation is performed (as is the case for infra-red effects in thermal perturbation theory)? A review of these developments and additional references can be found in [49]. Furthermore, the persistent difficulty of constructing de Sitter vacua in string theory, see [50] for a review, has led to the conjecture that de Sitter space cannot be attained in a weakly curved/coupled quantum theory of gravity [51].

There is another issue where de Sitter instabilities induced by quantum dynamics can be important: they trigger an exit from the inflationary regime that is an important ingredient of any inflationary model. Indeed, scalar instabilities triggered by coupling gravity to a CFT_4 , provided an exit from inflation, [52, 53, 54] induced by the conformal anomaly, [55]. However, this exit was not good enough and the model was modified to what is now called the Starobinsky model, where inflation is triggered by a (rather large) R^2 term. This is a very successful model when compared to current data [56]. In that model also the exit from inflation is triggered by the unstable scalar mode, which in this context is the scalaron of R^2 gravity.

So far the quantum effects studied and the backreaction on de Sitter and Minkowski spaces used weakly-coupled QFTs. The holographic gauge/gravity duality provides a way to tackle non-perturbative (large- N) four-dimensional quantum field theories by mapping them to higher-dimensional semiclassical General Relativity. Moreover, one controls the dynamics of holographic QFTs even when the manifold they are defined upon is curved. Holography has been applied to cosmological issues already in several works, [57, 58, 54], [59]-[73]. One important arena where this technique can provide important information is when *four-dimensional* gravity (described by Einstein General Relativity or its higher-derivative extensions) is coupled to a strongly coupled QFT. Among the issues that may arise are for example the stability under small (metric and matter) perturbations as well as the non-perturbative stability of cosmological backgrounds.

The holographic approach allows for recasting these questions in terms of a classical higher-dimensional gravity theory, which via holography captures the effects of the QFT, coupled to a classical four-dimensional gravitational theory. To be more specific, the holographic setup consists of two coupled sectors:

1. The holographic sector describes the strongly coupled (holographic) CFT, whose dual is living in a higher-dimensional space-time (*the bulk*) with metric \mathcal{G}_{ab} .
2. The four-dimensional gravity sector is defined in terms of a metric $g_{\omega\sigma}^{(0)}$. This metric plays the role of a boundary condition for \mathcal{G}_{ab} , and it has no bulk dynamics. From the CFT point of view, it corresponds to the source of the field theory stress tensor.

The action describing classical 4d gravity coupled to the holographic QFT has the form:

$$S = S_{\text{grav}}[g_{\omega\sigma}^{(0)}] + S_{\text{bulk}}[\mathcal{G}_{ab}, \dots] \quad (1.1)$$

The first term can be taken to be the usual Einstein-Hilbert action plus eventually higher curvature terms, and it has the effect of making $g_{\omega\sigma}^{(0)}$ dynamical. The second term describes the higher-dimensional holographic dual of the QFT, and the dots represent bulk fields other than the metric. Both terms are treated classically, but the bulk action encodes holographically the full quantum dynamics of the dual field theory. The two sectors are coupled by the requirement that on the conformal boundary $\mathcal{G}_{\omega\sigma}$ asymptotes to $g_{\omega\sigma}^{(0)}$. “Integrating out” the CFT consists in evaluating $S_{\text{bulk}}[\mathcal{G}_{ab}, \dots]$ on shell. This results in an effective gravitational action for $g_{\omega\sigma}^{(0)}$ alone,

$$S_{\text{eff}}[g_{\omega\sigma}^{(0)}] = S_{\text{grav}}[g_{\omega\sigma}^{(0)}] + S_{\text{bulk}}^{\text{on-shell}}[g_{\omega\sigma}^{(0)}, \dots] \quad (1.2)$$

The second term in (1.2) is now a functional of the boundary value $g_{\omega\sigma}^{(0)}$, i.e. the four-dimensional metric. Varying the effective action results in the semi-classical Einstein equation :

$$E_{\omega\sigma} = \langle T_{\omega\sigma} \rangle_{\text{CFT}} \quad (1.3)$$

where $E_{\omega\sigma}$ is the variation of the first term in (1.1) (i.e. the Einstein tensor if S_{grav} is purely GR) and $\langle T_{\omega\sigma} \rangle_{\text{CFT}}$ is obtained by varying $S_{\text{bulk}}^{\text{on-shell}}$ with respect to $g_{\omega\sigma}^{(0)}$.

In a previous work [72], some of the authors have used the setup described above to address the issue of non-perturbative existence of 4d de Sitter space coupled to a (gap-less) holographic field theory. For this, the attention was limited to boundary metrics $g_{\omega\sigma}^{(0)}$ of maximal symmetry. In this case, the effective action (1.2) takes the form of an effective $f(R)$ theory,

$$S_{\text{eff}}[g_{\omega\sigma}^{(0)}] = \int d^4x \sqrt{g^{(0)}} f(R), \quad (1.4)$$

where R is the Ricci scalar of $g_{\omega\sigma}^{(0)}$. It was shown in [72] that such a theory generically still admits de Sitter solutions (albeit with a smaller cosmological constant than that of the “bare” 4d gravity) after the full quantum effects of the field theory are taken into account.

The results of [72] suggest that, at least in the holographic context, IR effects from a QFT do not always destroy de Sitter space-time. However, that analysis could only be applied to *constant curvature* 4d space-times. Therefore, it says nothing about the stability of the solutions under non-homogeneous perturbations. The form (1.4) of the effective action is only good for obtaining maximally symmetric solutions, and it would be misleading to expand it in perturbations around one such background. Rather, to

study small perturbations of a holographic QFT coupled to gravity one has to go back to the original theory (1.1) and study its perturbation spectrum. This has been considered already in [58], albeit in a slightly different context (Randall-Sundrum cosmology), and more recently in [74] for the case of a two derivative gravitational action coupled to a holographic CFT around de Sitter space. In [74], beyond the scalar instabilities that have been known for several decades, [53], a spin-2 instability was found for small enough de Sitter curvatures.

Our goal in this paper is to extend previous results on the stability of maximally symmetric spacetimes due to quantum effects in several ways:

- We consider not only de Sitter but also flat space and Anti-de Sitter space.
- We consider a classical gravitational theory with all couplings necessary for renormalization which are relevant at low energies. This implies that we have a cosmological constant and Einstein terms as well as the two independent R^2 terms with (finite) dimensionless renormalized couplings α, β .
- In our case, the only non-trivial (i.e. in which the CFT degrees of freedom participate) quadratic action for the fluctuations is that in the spin-2 sector. We analyze not only the possible tachyonic poles that are responsible for the instabilities but also the presence of negative residues that signal the presence of ghosts
- Moreover, we investigate when such tachyons or ghosts are below the effective UV cutoff for the classical gravitational theory, which is given by the so-called species cutoff, [75].
- Although we use holographic techniques to solve our problems, *our results apply to all four-dimensional CFTs*. The reason is that *our results depend only on the two-point function of the energy-momentum tensor of the CFT. For a CFT around a maximally symmetric space, and given a coordinate system and an invariant state, such a two-point function is universal up to an overall multiplicative constant that is the central charge c of the CFT.*
- Our results do not apply to non-conformal theories. However, as in the case of reference [72], if we consider a QFT_4 as a flow between CFT_{UV} and CFT_{IR} , then our results relevant to CFT_{UV} , CFT_{IR} , provide bounds on the results relevant to QFT_4 . This is expected to be valid for generic QFT_4 although special cases may need further analysis. The analysis for general QFTs will be done in a future publication.
- Our results on ghost instabilities are independent of the choice of coordinates on the maximally symmetric space in which the CFT lives.
- In the case of de Sitter, the presence of tachyonic instabilities may depend on the choice of coordinates. We have performed the analysis in global, cosmological and static coordinates, and found that the conditions for the absence of tachyonic instabilities are the same in all three cases.

Concretely, we consider general perturbations around maximally symmetric four-dimensional space-times in a holographic setup, given by (1.1), where the matter content is a four-dimensional holographic conformal field theory. The coupling to gravity is entirely described by the exact one-point correlation function of the CFT stress-energy tensor, as in equation (1.3). This stress-tensor is obtained on a boundary of AdS_5 from a holographic calculation and has the correct conformal Weyl anomaly (see [55] for a review of the conformal quantum anomaly, and [82] for the holographic CFT stress-tensor).

The perturbation analysis is obtained by fluctuating the bulk and boundary metrics and then writing the linearized version of the effective Einstein equation (1.3) for the four-dimensional metric $g_{\omega\sigma}^{(0)}$. We perform this analysis around maximally symmetric 4d space-times of positive curvature (dS), negative curvature⁴ (AdS) and vanishing curvature (Minkowski).

In this work, we pursue two main objectives:

1. We first obtain analytic spectral equations (in terms of transcendental functions) for the boundary metric fluctuations of the 4d gravity+ holographic CFT system, around a general maximally symmetric background;
2. We then perform a full numerical analysis of the spectrum in momentum space, (defined by the eigenvalue of the Laplacian on the corresponding maximally symmetric space-time) and determine criteria for the presence of instabilities of both tachyonic and ghostlike type. This way, we obtain a detailed map of the stable and unstable regions of parameter space.

Our approach is similar in spirit to other works in the context of weakly coupled field theory: a similar analysis was performed with a matter content given by quantum corrections of free massless scalar CFT [53], for *homogeneous* time-dependent metric perturbations around de Sitter. A similar perturbation analysis around flat space was carried out for a free scalar coupled to higher-derivative gravity in [15].

Here, we use the holographic setup to perform a full parameter-space analysis of the gravity+CFT system, and we establish stable and unstable regions of parameter space around background solutions with zero, negative and positive constant curvature. Specifically, the parameters of the model are:

- The boundary gravity renormalized couplings $\Lambda, G, \alpha, \beta$, corresponding to local covariant functions of $g_{\omega\sigma}^{(0)}$ of dimension up to four, which we define as follows:

$$\frac{\Lambda}{8\pi G} \sqrt{g^{(0)}}, \quad \frac{1}{16\pi G} \sqrt{g^{(0)}} R, \quad \frac{\alpha}{384\pi} \sqrt{g^{(0)}} R^2, \quad \frac{\beta}{64\pi} \sqrt{g^{(0)}} \left[R_{\omega\sigma} R^{\omega\sigma} - \frac{1}{3} R^2 \right] \quad (1.5)$$

Here Λ is the 4d cosmological constant, G is 4d Newton's constant, $R_{\omega\sigma}$ is the Ricci tensor of $g_{\omega\sigma}^{(0)}$ and R the corresponding Ricci scalar and α, β two dimensionless parameters.

⁴The case of negative curvature is special. It corresponds to foliating AdS_5 by AdS_4 slices, which leads to a geometry with two connected boundaries, which is dual to two copies of the CFTs with an interface between them (see e.g. [83] and the recent discussion in [84]). One has then different options on how to couple dynamical gravity to the system, the most general case being a bi-gravity theory with each metric coupled to one of the CFTs. Here, we discuss the special cases in which only one metric is dynamical.

- The parameter N , counting the degrees of freedom of the CFT. This can be traded for the central charge of the CFT.
- The value R of the curvature of the background solution. This is not an independent parameter, as it is determined by the other parameters via the background solution. However, it is convenient to use this as an independent parameter instead of e.g. the 4d cosmological constant.
- An extra parameter is the *renormalization scale* μ of the CFT, which arises from the conformal anomaly. Since this is universal, its only effect is to shift the parameter β so that it enters only in the combination:

$$\beta_{\text{eff}} = \beta - \frac{N^2}{\pi} \log(4\mu^2 GN^2). \quad (1.6)$$

Although the QFT we couple to gravity is a holographic CFT_4 , it is important to stress that our result holds for *any* generic CFT coupled to gravity: as we shall observe below, the spectral properties of the system are determined by the stress-tensor 2-point function, which for a CFT in any conformally flat space-time is completely fixed by the central charge⁵. Therefore, although the method we use to compute the fluctuation spectra is specific to a large- N holographic CFT, to obtain the result for a generic CFT it is enough to trade the parameter N with the appropriate central charge.

1.1 Cutoffs in effective gravity theories

In order to have semiclassical 4d gravity, we require that the 4d curvature R is small compared to the cutoff of the theory. Typically, this is assumed to be the Planck scale or, in the case of string theory, the string scale, but it may be different from both in other possible realizations.

However, as argued in [75], if the matter theory has many degrees of freedom, the perturbativity condition imposes a lower cutoff (the so-called “species scale”) than the Planck scale. For example if, like in our case, the matter theory has $\mathcal{O}(N^2)$ degrees of freedom⁶, and the original cutoff was the Planck scale, then the species cutoff M_{species} is

$$M_{\text{species}} \equiv \frac{M_{\text{Planck}}}{N} \sim \frac{1}{\sqrt{GN}}. \quad (1.7)$$

One reason for this is that the bare Planck scale receives corrections that are $\mathcal{O}(N^2\Lambda^2)$ where Λ is the overall cutoff of the gravity+QFT. For $N \gg 1$, $M_P \sim N\Lambda$ and then solving for Λ we obtain (1.7). Another reason may be that one would like to keep perturbativity, which implies that the QFT corrections to M_P (which are of order $N\Lambda$) should be small: demanding $N\Lambda \ll M_P$ again implies that $\Lambda \ll \frac{M_P}{N}$.

⁵In general such a two-point function depends on initial conditions or equivalently, the initial state. We assume that we use the maximal symmetry invariant state. In de Sitter, this is the Bunch-Davies vacuum.

⁶For a general CFT_4 , a measure of the number of degrees of freedom is the central charge a . One can always replace everywhere in the paper $N^2 \rightarrow 4a$ as explained later on in section 2.3.

However, both arguments have loopholes.

- The corrections to the Planck mass, being quadratic in the cutoff are very difficult to calculate in a theory, preserving diffeomorphism invariance. The ϵ -expansion is not well suited for this calculation as was extensively argued in [76]. The only reliable calculations of the coefficients of the $\mathcal{O}(N^2\Lambda^2)$ corrections to the Planck mass have been done in many ground-states of string theory at the one-loop level, [77]-[81]. In such cases, the coefficients can be either positive or negative depending on the type of matter fields that are integrated out. Moreover, the duality frame matters, in the sense that on-shell equivalent states give different one-loop corrections to the Planck scale. In short, generic coefficients are of order one, but fine-tuning is possible (like in susy theories where such corrections may vanish depending on the amount of supersymmetry).

- The original argument for the species cutoff has another loophole: the cutoff Λ should be a physical scale, ie. a scale associated with a relevant coupling constant of the theory. If for example, we have gravity and a CFT as in our examples, the CFT has no intrinsic cutoff. We need to introduce one to renormalize the combined CFT+gravity theory, but we can then remove it by keeping the renormalized couplings finite. In that case, the renormalized Planck scale is completely independent of N .

- There is no reason why one should require that matter corrections are perturbative, especially if such corrections can be computed beyond perturbations theory, a fact that may happen in holographic or supersymmetric theories.

The conclusion of the above discussion is that although assuming the validity of the species cutoff is a rather conservative approach, there may be many cases where the cutoff may be different and in particular much higher than the species cutoff. Our results will be presented at all scales, and one can then apply the relevant cutoff before concluding.

Generically, the effective action of gravity may contain higher derivative terms before adding the effects of the CFT. These terms can be schematically written as

$$S_{grav} = \bar{M}_{\text{Planck}}^2 R + \bar{\alpha} R^2 + \sum_{n=1}^{\infty} \bar{a}_n R^{n+2} \quad (1.8)$$

The bar over the coefficients indicates they are bare coefficients that arose from integrating out the high-energy degrees of freedom of the gravitational sector. However, these bare coefficients will be renormalized by the CFT_4 . To do this we must introduce an arbitrary cutoff Λ in the CFT_4 , perform our quantum calculations and write the effective corrections to the bare gravitational couplings. All such corrections will be controlled by the number of degrees of freedom (N^2) of the CFT_4 as well as the cutoff scale.

$$\delta \bar{M}_{\text{Planck}}^2 \sim N^2 \Lambda^2 \quad , \quad \delta \bar{\alpha} \sim N^2 \log \Lambda^2 \quad , \quad \delta \bar{a}_n \sim N^2 \Lambda^{-2n} \quad (1.9)$$

We now add counterterms to remove the divergent contributions as $\Lambda \rightarrow \infty$, and we then take $\Lambda \rightarrow \infty$ obtaining

$$S = M_{\text{Planck}}^2 R + \alpha R^2 + \sum_{n=1}^{\infty} \bar{a}_n R^{n+2} + W_{\text{CFT}}(R) \quad (1.10)$$

where now M_{Planck}^2 , α are renormalized couplings (independent of N), $a_{n \geq 1}$ are unaffected by renormalization, and $W_{CFT}(R)$ are the renormalized CFT_4 contributions to the gravitational action.

Typically the size of a_n is controlled by the original bare $\bar{M}_{\text{Planck}}^2$ as

$$a_n \sim \frac{1}{\bar{M}_{\text{Planck}}^{2n}} \quad (1.11)$$

As long as $M_{\text{Planck}} \ll \bar{M}_{\text{Planck}}$ the higher curvature terms beyond the quadratic ones can be neglected, and this is what we shall assume in this paper.

Moreover, as $W_{CFT} \sim N^2$, it is clear that our results will not depend separately on M_{Planck}^2 and N^2 but only on the combination $\frac{M_{\text{Planck}}^2}{N^2}$ which is the species scale.

The same considerations about the cut-off apply to the analysis of fluctuations and in particular of instabilities. In effective field theory, any mode with a mass of the order or above the cutoff is outside the reach of the theory. In particular, it is only when the ghost or tachyon mass is well below the EFT cut-off that one can unambiguously conclude that the theory truly has stability issues.

Indeed, as it is well known (and as we review in a simple example in Appendix A), an EFT originating from an otherwise healthy UV theory may display some unstable modes as an artefact of the low-energy expansion. In this case, the unstable modes will have masses of the order of the EFT cut-off (the scale of the fields that have been integrated out). Turning this around, we can say that one cannot conclude anything about the actual stability or instability of an EFT based on the occurrence of ghosts or tachyons whose mass scale is at or above the EFT cut-off: one would have to know the UV completion to reach a definite conclusion. For the same reason, within EFT one cannot reach any definite conclusion about the stability of space-times whose curvature scale (H or χ) is at or larger than the cut-off.

Throughout this work, we shall encounter many instabilities (tensor and scalar ghosts and tachyons). Whether they are physical, depends on whether they are above or below the cutoff of the effective theory. We may take the attitude that the cut-off is the one in (1.7) but other cutoffs can be in principle envisaged as we can freely choose our renormalized parameters.

An important point is the following. It seems that our previous argument indicates that the condition on tachyons and ghosts depends on the combination $M_{\text{species}} = \frac{M_{\text{Planck}}}{N}$. This in turn implies that for scales well below this cutoff, the CFT_4 corrections should be negligible. This argument is correct for local contributions to the dynamics of fluctuations. However, as we shall later see, most of the relevant contributions are non-local due to massless modes being integrated out. Such non-local contributions, due to logs can become large, and therefore the question of instabilities is non-trivial.

We devote the rest of this introduction to an extended summary of these techniques as well as a discussion of the results obtained in this work. Although they stem from a holographic calculation, we insist that they are valid for a generic CFT, and describe the results mostly in the language of the field theory side. We leave the details of the holographic approach to the rest of the paper.

1.2 Summary and results

The setup studied here consists of higher curvature gravity coupled to a Conformal Field Theory (CFT). For the gravitational part, we consider the Einstein-Hilbert action with a cosmological constant plus quadratic curvature term:

$$S_{\text{grav}} = S_{EH} + S_2 \quad (1.12)$$

where

$$S_{EH} = -\frac{1}{16\pi G} \int d^4x \sqrt{-g^{(0)}} (R - 2\Lambda) \quad (1.13)$$

and

$$S_2 = \frac{\alpha}{384\pi} \int d^4x \sqrt{-g^{(0)}} R^2 + \frac{\beta}{64\pi} \int d^4x \sqrt{-g^{(0)}} \left(R_{\omega\sigma} R^{\omega\sigma} - \frac{1}{3} R^2 \right) \quad (1.14)$$

Here, $g_{\mu\nu}^{(0)}$ is the 4d space-time metric, $g^{(0)}$ its determinant and R its curvature. The parameters $G, \Lambda, \alpha, \beta$ are the (finite) renormalized parameters which already contain the contributions of the CFT⁷

Coupling to a large- N CFT is implemented via holography: we identify the 4d space-time with the conformal boundary of AdS₅ bulk manifold, and $g_{\mu\nu}^{(0)}$ with the leading term in the Fefferman-Graham expansion of the 5d bulk metric:

$$ds_{\text{bulk}}^2 = L^2 \frac{d\rho^2}{4\rho^2} + \frac{1}{\rho} \left[g_{\mu\nu}^{(0)} + O(\rho) \right] dx^\mu dx^\nu \quad \rho \rightarrow 0 \quad (1.15)$$

where $\rho \rightarrow 0$ corresponds to the AdS boundary and L is the AdS length. This way, one can obtain 4d maximally symmetric metrics g^0 whose Ricci curvature \bar{R} satisfies the relation:

$$\Lambda = \frac{1}{4} \left(\bar{R} - \frac{GN^2 \bar{R}^2}{48\pi} \right). \quad (1.16)$$

The Ricci curvature \bar{R} of the maximally symmetric background space-time can be positive, negative or vanishing. It is convenient to parametrize it in the various cases as follows:

$$\bar{R} = \begin{cases} 12H^2, & \text{de Sitter,} \\ 0, & \text{Minkowski} \\ -12\chi^2, & \text{Anti de Sitter} \end{cases} \quad (1.17)$$

The parameter N , characterizing the number of degrees of freedom of the CFT, is related to the bulk Planck scale M and bulk AdS length L by $N^2 \propto (ML)^3$. The first term in equation (1.16) is the contribution from the vacuum Einstein equation, and the second term is the CFT contribution.

⁷These parameters are defined so that they are finite in an appropriate scaling limit after removing the UV cut-off. The detailed procedure is described in section 2.

To conclude, the *independent* parameters of the theory are the curvature of the background space⁸ \bar{R} , the four-dimensional Newton constant G , the two R^2 couplings α and β_{eff} , where β_{eff} is defined in (1.6) and the number of colors⁹ N of the holographic CFT₄. It will be convenient to express quantities in terms of the following “reduced” parameters:

$$\tilde{\alpha} = \frac{\pi\alpha}{N^2}, \quad \tilde{\beta}_{\text{eff}} = \frac{\pi\beta_{\text{eff}}}{N^2}. \quad (1.18)$$

Our goal is to determine, as a function of the parameters of the model, the spectrum of gravitational fluctuations of the boundary metric around any maximally symmetric 4d boundary metric $\bar{\zeta}_{\mu\nu}$. We use this information to determine the perturbative stability of the system.

The perturbed boundary metric is taken to be:

$$g_{\mu\nu}^{(0)} = \bar{\zeta}_{\mu\nu} + \delta\zeta_{\mu\nu}^b \quad (1.19)$$

In an appropriate gauge, the boundary perturbation can be written as

$$\delta\zeta_{\omega\sigma}^b = \psi\bar{\zeta}_{\omega\sigma} + h_{\omega\sigma}^{(0)} \quad (1.20)$$

where ψ is a scalar degree of freedom, and $h_{\omega\sigma}^{(0)}$ is a tensor perturbation which is transverse and traceless with respect to the boundary metric. The scalar is a pure boundary mode¹⁰, whereas the four-dimensional gravity tensor modes couple to tensor perturbations in the bulk.

The metric perturbations are coupled to the CFT via the bulk dynamics: the boundary field $h_{\omega\sigma}^{(0)}(x)$ is the leading term in a near-boundary expansion of the perturbation of the *bulk* metric.

Spectral functions

The spectral analysis around the holographic background is tightly connected to the holographic two-point function of the boundary stress tensor. When working at linear order in fluctuations both in the bulk and on the boundary, all one needs is the structure of the effective action (1.2) at quadratic order as a function of the boundary metric perturbation $\delta\zeta^b$:

$$S_{\text{eff}}^{(2)} = \int d^4x \frac{1}{2} \delta\zeta_{\mu\nu}^b O_{\text{grav}}^{\mu\nu,\rho\sigma} \delta\zeta_{\rho\sigma}^b - \frac{1}{2} \int d^4x \int d^4y \delta\zeta^b(x)_{\mu\nu} \langle T^{\mu\nu}(x) T^{\rho\sigma}(y) \rangle_{\text{CFT}} \delta\zeta_{\rho\sigma}^b(y) \quad (1.21)$$

These two terms correspond to the quadratic order approximation of each of the two terms in (1.2): O_{grav} is the local kinetic operator of the quadratic term in the 4d gravity action

⁸Even if \bar{R} is not a parameter in the action, we can trade Λ for \bar{R} using (1.16). Although the relation between Λ and \bar{R} is not one-to-one, by scanning over all values of Λ we can obtain any value of \bar{R} .

⁹In fact, one should take the central charge as a parameter for the CFT. We shall use N as a proxy for the central charge

¹⁰The scalar mode couples to the trace of the stress-energy tensor of the CFT₄. Since this theory is conformally invariant, the two-point function of the trace vanishes. Therefore the non-trivial action for the scalar mode is generated by the boundary R^2 terms as well as the conformal anomaly of the CFT₄, [53]. If the theory is instead a QFT, extra contributions are expected for the dynamics of the scalar mode.

S_{grav} in (1.12); $\langle T^{\mu\nu} T^{\rho\sigma} \rangle_{CFT}$ is the holographic two-point function of the stress tensor, which is by definition:

$$\langle T^{\mu\nu}(x) T^{\rho\sigma}(y) \rangle_{CFT} = -\frac{\delta}{\delta \zeta_{\mu\nu}^b(x)} \frac{\delta}{\delta \zeta_{\rho\sigma}^b(y)} S_{bulk}^{on-shell} \quad (1.22)$$

The stress tensor two-point function contains both local and non-local contributions. The local contributions simply renormalize the coefficients of local terms which are already present in O_{grav} . The non-local contributions are genuine new effects of the CFT which one cannot find in a local gravity theory.

Equation (1.21) shows that by computing the holographic two-point function we have access to the full propagator, which we denote by \mathcal{F}^{-1} , of the boundary metric fluctuations: the inverse propagator is

$$\mathcal{F}^{\mu\nu\rho\sigma} \equiv O_{\text{grav}}^{\mu\nu,\rho\sigma} - \langle T^{\mu\nu} T^{\rho\sigma} \rangle_{CFT} \quad (1.23)$$

and the spectrum of the system are the solutions of the integrodifferential equation

$$\mathcal{F}^{\mu\nu\rho\sigma} \delta \zeta_{\rho\sigma}^b = 0. \quad (1.24)$$

The linear equation (1.24) can be recast into two separate *scalar* spectral equations for the scalar and tensor modes defined in (1.20), by going to the appropriate “momentum space” of the boundary coordinate. This is done by decomposing the modes in eigenfunctions of the d’Alembert operator ∇^2 of the background boundary metric $\bar{\zeta}_{\omega\sigma}$: in the positive, zero and negative curvature case we take the fluctuation to satisfy

$$\left(\nabla^2 - r \frac{\bar{R}}{12} \right) \delta\varphi(x) = \begin{cases} -H^2 \left(\nu^2 - \frac{9}{4} \right) \delta\varphi(x) & dS \\ -k^2 \delta\varphi & \text{Minkowski} \\ \chi^2 \left(\nu^2 - \frac{9}{4} \right) \delta\varphi(x) & AdS \end{cases} \quad (1.25)$$

where $\delta\varphi(x)$ stands for either ψ or $h_{\mu\nu}^{(0)}$, r is the spin of the perturbation ($r = 0$ for ψ and $r = 2$ for $h_{\omega\sigma}^{(0)}$), H is the Hubble parameter in the case of positive curvature boundary (de Sitter) and χ is the inverse AdS length in the case of negative curvature boundary, as in (1.17). For flat space, this is the usual Fourier decomposition where $k^2 = k^\mu k_\mu$. In both curved cases, ν is a dimensionless eigenvalue measuring the invariant “momentum” in units of the background curvature.

The values of ν^2 (or k^2 in the flat case) are determined by the spectral equation (1.24), which in momentum space becomes a transcendental equation for ν^2 (or k^2) of the form:

$$\mathcal{F}(\nu) = 0 \quad (1.26)$$

where the precise form of the function \mathcal{F} depends both on the nature of the mode (scalar or tensor) and the background curvature and the parameters in the action.

Before proceeding further with the results, we discuss here two ingredients that affect the results.

(a) The coordinate system used on the maximally symmetric space (AdS, dS, flat) on which the CFT_4 is defined. It is a well-known fact that quantum field theory data, like correlation functions, do depend crucially on the coordinate system. In flat space, we use only Minkowski coordinates. In AdS, we use both Poincaré and global coordinates. In dS, we examine global coordinates, Poincaré coordinates and static patch coordinates.

(b) The state on which the two-point function of the energy-momentum tensor is calculated. In flat space, we choose the (unique) Poincaré invariant vacuum. In global AdS and Poincaré AdS, similarly, we choose the AdS invariant vacuum. In Global coordinates dS as well as Poincaré coordinates dS we choose again the unique dS Invariant state that in the latter case is known as the Bunch-Davis vacuum. In dS with static coordinates, we choose the dS-invariant vacuum corresponding to outgoing boundary conditions at the cosmological horizon.

Overall the correlator we compute is the Lorentzian retarded correlator. This is defined for real eigenvalues of the Laplacian on (AdS, dS, flat) space. In the space-like case, this correlator is similar to the Euclidean correlator. Its analytic continuation to the complex plane is unique. In the time-like case, extra imaginary parts arise from the logarithmic branch cut of the correlator, but these do not affect the analytic continuation.

The expressions obtained can be found below:

Scalar mode In this case, the inverse propagator is a polynomial in ν^2 (or k^2), because it results from a quadratic action which is local on the boundary. The expression of the inverse propagator is given by

- **Minkowski**

$$\mathcal{F}_{scalar}(k) = -\frac{3}{16\pi G} \left(k^2 - \frac{4}{\alpha G} \right) \quad (1.27)$$

- **de Sitter and Anti-de Sitter**

$$\mathcal{F}_{scalar}(\nu) = -\frac{1}{64\pi G} \left[\alpha G \bar{R} - 12 + \frac{GN^2 \bar{R}}{2\pi} \right] \left\{ \frac{4}{G\alpha} - \frac{N^2 \bar{R}}{6\pi\alpha} - \frac{\bar{R}}{12} \left(\nu^2 - \frac{9}{4} \right) \right\}. \quad (1.28)$$

This is the "physical" scalar inverse propagator. For the details, see section 4.

Tensor modes For tensor modes, the non-local contribution from the CFT stress-tensor correlator in (1.23) gives rise to non-polynomial expressions for the inverse propagators:

- **Minkowski**

$$\mathcal{F}_{\text{tensor,Mink}}(k) = \frac{N^2}{64\pi^2} k^2 \left\{ -\frac{2\pi}{GN^2} + \frac{k^2}{2} \left[\frac{1}{2} - 2\gamma_E - \log(GN^2 k^2) - \frac{\pi\beta_{\text{eff}}}{N^2} \right] \right\} \quad (1.29)$$

- **de Sitter**

$$\mathcal{F}_{\text{tensor,dS}}(\nu) = \frac{N^2 H^2}{64\pi^2} \left(\nu^2 - \frac{9}{4} \right) \left\{ 1 - \frac{2\pi}{GN^2 H^2} + \frac{2\pi\alpha}{N^2} - \frac{1}{2} \left(\nu^2 - \frac{1}{4} \right) \left[2 \log(GN^2 H^2) - \frac{1}{2} + 2\mathcal{H} \left(\nu - \frac{1}{2} \right) + \frac{\pi\beta_{\text{eff}}}{N^2} \right] \right\}. \quad (1.30)$$

where \mathcal{H} is the harmonic number function defined in (5.34). The expression (1.30) with $\alpha = 0$ was already obtained in [74]¹¹. In this work, we rederive it in our setup and generalise it to negative and zero curvature and arbitrary values of the α parameter.

- **Anti-de Sitter**

In this case, there are two connected boundaries, corresponding to two - a priori independent - copies of the CFT. Therefore, one has freedom in how to couple 4d gravity to the system. Here, we discuss two concrete cases:

a) Dynamical gravity on one side: In this case only one of the two CFTs is coupled to dynamical gravity, and the metric on the second boundary is frozen.

$$\begin{aligned} \mathcal{F}_{\text{tensor,AdS}}^-(\nu) = & \frac{N^2\chi^2}{64\pi^2} \left(\nu^2 - \frac{9}{4} \right) \left\{ 1 + \frac{2\pi}{N^2} \left(\frac{1}{G\chi^2} + \alpha \right) + \right. \\ & - \frac{1}{2}(\nu^2 - 1/4) \left[\frac{\pi\beta_{\text{eff}}}{N^2} + \log(GN^2\chi^2) - \frac{1}{2} + \right. \\ & \left. \left. + \mathcal{H} \left(-\frac{1}{2} - \nu \right) + \mathcal{H} \left(-\frac{1}{2} + \nu \right) \right] \right\}. \end{aligned} \quad (1.31)$$

b) Symmetric boundary conditions: In this case, there is effectively a single boundary (see [84] for a recent discussion), and there is again a single dynamical gravity theory coupled to a single 4d CFT on AdS. This leads to the following spectral density:

$$\begin{aligned} \mathcal{F}_{\text{tensor,AdS}}^{\text{sym}}(\nu) = & \frac{N^2\chi^2}{64\pi^2} \left(\nu^2 - \frac{9}{4} \right) \left\{ 1 + \frac{2\pi}{N^2} \left(\frac{1}{G\chi^2} + \alpha \right) + \right. \\ & - \frac{1}{2}(\nu^2 - 1/4) \left[\frac{\pi\beta_{\text{eff}}}{N^2} + \log(GN^2\chi^2) - \frac{1}{2} \right. \\ & \left. \left. + \mathcal{H} \left(\nu - \frac{1}{2} \right) + \mathcal{H} \left(-\nu - \frac{1}{2} \right) - \frac{\pi}{\cos \pi\nu} \right] \right\}. \end{aligned} \quad (1.32)$$

Stability

Instabilities of the system are encoded in the properties of the zeros of \mathcal{F} . We perform a full analysis of all parameter space, which we summarize below. As a byproduct, by setting $N = 0$ we obtain the pure gravity spectral functions and study the corresponding zeros, which give indications about the stability of quadratic gravity around any constant curvature background.

When discussing the gravity + CFT system, we always compare the results with those of pure gravity theories with the appropriate renormalized parameters. This allows us to identify the new effects (if any) which arise specifically from the coupling to the CFT. For a CFT with parameter N , the comparison should be made by choosing the pure gravity parameters α and β such that $\alpha = \tilde{\alpha}/\pi$ and $\beta = \tilde{\beta}_{\text{eff}}/\pi$, in terms of the quantities defined in (1.18): these are the quantities which are expected to be of order unity after renormalization of the local terms by the CFT is taken into account.

Depending on the curvature, there are different criteria for instabilities. On any background, instabilities can be of two types:

¹¹In [74] β was fixed but the renormalization scale μ (called E in that paper) was allowed to vary.

- **Tachyonic instabilities** correspond to modes which grow exponentially in time and are related to the *position* of the root ν in the complex plane. Specifically, a root ν of $\mathcal{F}(\nu)$ is *tachyon-stable* in the following cases:

$$\left\{ \begin{array}{ll} |Re(\nu)| \leq \frac{3}{2} & dS \\ k^2 \leq 0 & \text{Minkowski} \\ Re(\nu) \neq 0 & AdS \end{array} \right\} \Rightarrow \text{tachyon-stable} \quad (1.33)$$

In all other cases, the mode is tachyonic.

Since they were derived requiring a bounded late-time behaviour for the modes, one may worry that the bounds (1.33) depend on the coordinates chosen on the slice, and in particular on the choice of the time coordinate. In space-times endowed with a global time-like killing vector, there is a preferred choice of time coordinate and the bounds (1.33) for Minkowski and AdS translate into the usual ones, i.e. respectively positive mass squared and validity of the BF bound (the latter can be obtained equivalently both in global AdS coordinates or in Poincaré coordinates, although global time and Poincaré time do not coincide).

In dS, however, things may be more subtle. We have derived the tachyon-stability criterion for the three more widely used local coordinate systems in de Sitter, namely global coordinates, Poincaré coordinates and static patch coordinates. In all three cases the condition one obtains is the same bound (1.33). This analysis relies on tracking the time-dependence of eigenfunctions of the D'Alembertian in different coordinate systems and can be found -in the case of scalar modes- in section 4.3. In the case of tensor modes, after decomposing them further into irreducible tensors of the fixed time-slice symmetry group, one finds the same conditions as for scalars, as can be seen from the analysis in Appendix G.

- **Ghost instabilities** correspond to a mode with eigenvalue ν_0^2 (or k_0^2) developing a “wrong sign” kinetic term, and are related to the value of the residue of \mathcal{F} at the pole:

$$\left\{ \begin{array}{ll} Res\mathcal{F}^{-1}(\nu_0^2) < 0 & dS \\ Res\mathcal{F}^{-1}(k_0^2) < 0 & \text{Minkowski} \\ Res\mathcal{F}^{-1}(\nu_0^2) > 0 & AdS \end{array} \right\} \Rightarrow \text{ghost-stable} \quad (1.34)$$

The sign conventions are discussed in section 6. In the case of ghosts, the stability criterion only depends on the sign of the residue and not on the choice of coordinates.

A heavy ghost can be tolerated if its mass is above the cut-off of the theory because in this case it cannot be described in the context of effective theory (and it may become healthy in the UV-completion).

In this work, we compare ghost masses with two cut-offs: the 4d Planck scale $G^{-1/2}$ (the ultimate cut-off in the semiclassical approach) and the species cutoff scale, M_{species}

$$M_{\text{species}} \equiv (GN^2)^{-1/2}, \quad (1.35)$$

which can be argued to be the true cut-off of a gravity theory coupled to N^2 degrees of freedom [75]. Moreover, it seems that the latter is the natural scale in which to measure boundary curvature R in the present set-up: it always appears in the combination

$$GN^2 R \sim \frac{R}{M_{\text{P}}^2 N^2} \sim \frac{R}{M_{\text{species}}^2}.$$

An unstable mode can be a ghost, a tachyon, or both. In what follows we summarize our results in the scalar and tensor sector and for zero, positive and negative background curvature. One important point to which we have to pay attention is whether the unstable mode is within the limits of effective field theory, i.e. whether it is light in Planck units (in the case of pure gravity) or light in units of the species scale (1.7) (in the case of gravity coupled to the CFT).

Stability in the scalar sector

For the scalar mode, it is straightforward to read off the conditions (1.33-1.34) from equations (1.27-1.28): this leads to the following conclusions:

- In Minkowski space, the scalar spectral function (1.27) is the same in pure gravity and in the presence of the CFT and does not depend on N as the conformal anomaly of the CFT is not relevant. The scalar mode is never a ghost, and it is tachyonic if $\alpha > 0$. This agrees with previous analysis (e.g. [15]). The tachyonic mode is within the bounds of the theory if its mass is below the cut-off, which in terms of the “reduced” $\tilde{\alpha}$ parameter defined in (1.18) requires $\tilde{\alpha} \gg 1$ (the same condition as in pure gravity, since $\alpha = \tilde{\alpha}$).
- In de Sitter space, scalar tachyon-stability requires:

$$\frac{1}{\alpha} \left(1 - \frac{GN^2 H^2}{2\pi} \right) \leq 0. \quad (1.36)$$

For consistency, $GN^2 H^2 \ll 1$ and therefore the second factor is always positive in effective field theory. Therefore, tachyon stability implies $\alpha < 0$.

Moreover, the scalar mode is a ghost if:

$$\left(\frac{\pi\alpha}{N^2} + \frac{1}{2} \right) \frac{GN^2 H^2}{12\pi} > 1. \quad (1.37)$$

ie. when $\alpha \gg 1$. For pure gravity, (1.36) with $N = 0$ is the same condition ($\alpha < 0$) as for Minkowski space. In pure de Sitter gravity, the scalar can also be a ghost, if α is very large (at least of order $1/(GH^2) \gg 1$). This mode is light in Planck units if $|\alpha| \gg 1$.

In the presence of the CFT, the tachyon stability condition is modified by the second term proportional to N^2 in (1.36). However, note that this term is small if we insist the curvature is below the species cutoff, which requires $GN^2H^2 \ll 1$. If this is the case, the tachyon-stability condition is not affected much by the CFT in the context of low-energy EFT¹². The scalar mode is below the species cut-off if $|\tilde{\alpha}| \gg 1$ (the same condition as for pure gravity). Finally, both with and without the CFT the time-scale τ of the tachyonic instability is roughly the inverse tachyon mass, $\tau \sim \sqrt{G|\alpha|}$. In effective field theory ($GH^2 \ll 1$) this is much faster than the de Sitter Hubble rate H^{-1} (i.e. the tachyon instability is very strong) unless $|\alpha| \gg (GH^2)^{-1}$. Therefore, for $\tilde{\alpha}$ in the interval

$$1 \ll \tilde{\alpha} \ll \frac{1}{GH^2N^2} \quad (1.38)$$

we have a strong instability (faster than one Hubble time) within effective field theory. This condition also applies to pure gravity, if we set $N = 1$ and $\tilde{\alpha} = \alpha$.

- The discussion is similar for Anti-de Sitter. Scalar tachyon-stability requires:

$$\frac{9}{4} - \frac{4}{\alpha G \chi^2} \left(1 + \frac{GN^2 \chi^2}{2\pi} \right) \geq 0. \quad (1.39)$$

and the scalar mode is a ghost if

$$- \left(\frac{\pi\alpha}{N^2} + \frac{1}{2} \right) \frac{GN^2 \chi^2}{12\pi} > 1. \quad (1.40)$$

Like before, to be in the effective field theory we must require that $GN^2\chi^2 \ll 1$. The condition for the scalar modes (whether a tachyon or a ghost) to be within the bounds of effective field theory is $|\tilde{\alpha}| \gg 1$.

Stability in the tensor sector

Unlike the case of the scalar, exploring the roots of the tensor spectral function can only be done numerically, except in some corners where analytic approximations for the transcendental functions can be used (in particular the large eigenvalue limit $\nu \rightarrow \infty$). Below we give the broad features of the stability results in the three cases (zero, positive and negative curvature). More details can be found in the main body of the paper.

In each case, we emphasize what happens for two special parameter values:

- (a) $N = 0$ which corresponds to pure gravity with higher curvature terms;
- (b) $\alpha = \beta_{\text{eff}} = 0$, which corresponds to setting the (renormalized) local quadratic curvature terms to zero. This gives a measure of the truly non-local contributions from the CFT.

- **Minkowski**

¹²A notable case in which this condition is violated is the Starobinsky realization of de Sitter (or more generally, inflation), in which the cosmological constant term is absent and the de Sitter curvature is fixed to $GN^2H^2 = 4\pi$ [52, 53]. In this case, the tachyon stability condition is reversed to $\alpha > 0$. We comment on this case in Appendix C.

- In the special case of pure gravity ($N = 0$), for $\beta \neq 0$ (and independently of α) the quadratic Ricci tensor term always generates a ghost, whose mass is, [85],

$$m_{ghost}^2 = \frac{4}{\beta G}. \quad (1.41)$$

For $\beta < 0$ this is also a tachyon. This mode is light compared to the cut-off $G^{-1/2}$ when $|\beta| \gg 1$. Therefore, the gravity theory is a good and stable effective theory only if β is positive and $\beta \lesssim 1$.

- In the presence of the CFT, the spectral function is (1.29) and its non-trivial roots are the solutions of a transcendental equation of the type $X \log X = a$, where X is proportional to k^2 and a is a real constant. The analysis can be done semi-analytically and it leads to the conclusion that for any value of $\tilde{\alpha}$ and $\tilde{\beta}_{\text{eff}}$ Minkowski space always contains two tachyonic tensor modes. The theory becomes eventually tachyon-stable only in the extreme limit $\tilde{\beta}_{\text{eff}} \rightarrow +\infty$. In this limit, one always finds a light ghost (light compared to the “species” scale $(GN^2)^{-1/2}$), as in the pure gravity case. All in all, the masses of the unstable tensor modes are above the species cut-off for $O(1)$ values of β_{eff} (this includes the special case $\alpha = \beta_{\text{eff}} = 0$), while Minkowski space is unstable within EFT iff $|\tilde{\beta}_{\text{eff}}| \gg 1$ and independently of $\tilde{\alpha}$.

• de Sitter

- In the special case of pure higher curvature gravity ($N = 0$), there are always two tensor modes, one of which is the massless graviton, and the other is massive. The massive mode is tachyonic if the following condition is violated:

$$\frac{2}{\beta} \left(\alpha - \frac{1}{GH^2} \right) < 1. \quad (1.42)$$

Because $GH^2 \ll 1$, the condition (1.42) is violated if $\beta < 0$ for α and β of order unity (this matches the Minkowski result).

Whether or not (1.42) holds, either mode is necessarily a ghost. If $\beta - 2\alpha < 2(GH^2)^{-1}$, the ghost is the massless spin-2 mode, otherwise it is the massive mode. For $O(1)$ values of α and β , the ghost is the massive mode, and its mass is of order $\mathcal{O}(M_p)$. One can have a light ghost only if $\alpha \gg (GH^2)^{-1} \gg 1$ (in which case the ghost is the massless graviton) or if $|\beta| \gg 1$ (in this case which one is the ghost depends on the sign of β). All in all, in pure gravity the theory is stable and ghost-free within EFT (i.e. below the cut-off M_p) if α and β are both $O(1)$.

- We now turn to the case of gravity coupled to the CFT. In de Sitter, the presence of tachyonic tensor modes depends on the curvature, on N and the parameters $\tilde{\alpha}$ and $\tilde{\beta}_{\text{eff}}$. The dS curvature H always enters in the combination GN^2H^2 , i.e. the natural scale to which the curvature is compared is the “species” scale (1.7).

For a de Sitter background, the presence or absence of tachyonic instabilities is illustrated in figure 7. For a fixed value of GN^2H^2 , tachyon-stability corresponds to values of $\tilde{\beta}_{\text{eff}}$ larger than a certain critical value, which is typically of order unity. For fixed $\tilde{\beta}_{\text{eff}}$, there are two regimes, depending on the value of $\tilde{\alpha}$: for small $\tilde{\alpha}$, and into negative values, the theory is tachyon-stable for GN^2H^2 larger than a certain critical value (generically of order unity); for large and positive $\tilde{\alpha}$ there are also intermediate regions of stability: the theory goes from unstable at small GN^2H^2 , to stable as GN^2H^2 increases, to again unstable, and finally to stable at large GN^2H^2 . In the specific case $\tilde{\alpha} = \tilde{\beta}_{\text{eff}} = 0$ there is a critical value for GN^2H^2 below which de Sitter space is tachyon-unstable, as it was also shown in [74]. The critical value corresponds to $GN^2H^2 \approx 0.32$. For small curvatures, and for $\tilde{\alpha}$ of order unity, the tachyon pole is generically located around the cut-off scale, unless one takes $|\tilde{\beta}_{\text{eff}}| \gg 1$.

For any values of the parameters, there are tensor ghosts (tachyonic or not). However, generically, these ghosts are heavy (in units of the “species” cut-off $(GN^2)^{-1/2}$) or they occur for curvatures of the order of the cut-off.

- In the special case $\tilde{\alpha} = \tilde{\beta}_{\text{eff}} = 0$, like in the generic case above, for any curvature (including zero-curvature flat space-time), the mass of the ghost is always larger but comparable to the species scale.

- **Anti-de Sitter.**

- In the special case of pure gravity ($N = 0$), the situation is similar to the one in de Sitter. There are two tensor modes, one of them massless and the other massive. For generic $O(1)$ parameters α and β , the massive mode is a tachyon for $\beta < 0$ (up to small corrections). One of the two tensor modes is always a ghost, and it is light only when α and/or β are very large. Therefore, as in de Sitter, for $O(1)$ values of the parameters, the theory does not have instabilities within EFT. This is what happens in top-down string theory [86]. On the other hand, this analysis means that one has to be careful in taking α and β too large. This is standard practice to obtain a qualitatively different behaviour from Einstein AdS gravity. This is common in phenomenological holographic models and some examples with commentary are [87, 88].
- In the presence of the CFT, as in de Sitter, tensor modes can be tachyonic or not depending on the parameters $\tilde{\alpha}$, $\tilde{\beta}_{\text{eff}}$. The situation is represented in figure 19. For fixed AdS curvature, there are tachyonic modes for large and negative values of $\tilde{\beta}_{\text{eff}}$ up to a certain critical value (which depends on $\tilde{\alpha}$ for large curvatures but is independent of $\tilde{\alpha}$ for small curvatures) above which the theory is tachyon-stable. The critical value is generically $\mathcal{O}(1)$. For a fixed $\tilde{\beta}_{\text{eff}}$ there are different possibilities: the theory may be tachyon-stable ($\tilde{\beta}_{\text{eff}}$ large and positive, $\alpha \gtrsim 0$), or be tachyon-stable only above a certain curvature ($\tilde{\beta}_{\text{eff}}$ large and negative) or cross from tachyon-stability to instability to stability again for $\tilde{\beta}_{\text{eff}} \sim O(1)$ and $\alpha < 0$. Unless $|\tilde{\beta}_{\text{eff}}| \gg 1$, the tachyonic modes are above the species cut-off.

- The special case $\tilde{a} = \tilde{\beta}_{\text{eff}} = 0$. Here, AdS space-time is tachyon-stable for any curvature below the species cut-off.

Finally, we note that until now it was the scalar instability in de Sitter (or near de Sitter) that was employed as a mechanism for exiting inflation. However, our results show that, depending on the parameters, the “fastest” instability may be in the scalar or the tensor sector. It should be stressed though that if the fastest instability is the spin-2 one, this is a disaster for cosmology. The reason is that this instability generates large transverse variations of the background metric destroying fast its homogeneity and therefore the main principle of cosmology. Consequently, for cosmology, spin-2 instabilities must be avoided.

Up to specific details which may vary depending on the parameters, the general features of the spectra discussed above can be summarised as follows:

Pure gravity:

• **Minkowski:**

- scalar tachyon if $\alpha > 0$
- if $\beta \neq 0$, two tensor modes: one massless graviton and one massive ghost (tachyonic or not).

• **dS and AdS**

- scalar tachyon if $\alpha > 0$ if $GN^2H^2 \ll 1$.
- scalar (light) ghost if $\alpha \gg 1/(GH^2)$.
- If $\beta \neq 0$, two tensor modes, one massless and one massive. One of them is necessarily a ghost.

In all these cases, these ghosts/tachyons are below the cutoff M_p *only* if $|\alpha| \gg 1$ and/or $|\beta| \gg 1$.

Gravity coupled to the CFT:

- The bounds on the ghost/tachyon regions vary, and there may be more massive tensor modes in the spectrum (in particular in AdS).
- The cut-off is now lowered to the species scale, M_p/\sqrt{N}
- The presence of *light* ghosts/tachyons still requires the effective coefficients of the R^2 and $R_{\mu\nu}R^{\mu\nu}$ to be large $|\tilde{\alpha}| \gg 1$ and/or $|\tilde{\beta}_{\text{eff}}| \gg 1$.

1.3 Discussion

Our findings show that there are whole regions of parameter space where the holographic matter + gravity theory suffers from both scalar and tensor instabilities, for all signs of the curvature. In particular, the unstable region contains the whole of flat space except eventually in the limit where we decouple the CFT.

Even though ghosts and tachyons seem ubiquitous, as we argued earlier, only when the unstable modes are lighter than our EFT cut-off (1.7) do they signal an unequivocal instability. From our analysis, it emerges that, at small curvatures (compared to the cut-off), if the renormalized coefficients of the local quadratic curvature terms, (1.18), are $O(1)$, unstable modes generically have masses above the UV cut-off M_p/N . On the other hand, the presence of light ghosts or tachyons requires very large values of the parameters (1.18).

It turns out that, for large values of the higher curvature parameters (1.18), one *also* finds light ghosts in pure quadratic-curvature gravity (in dS, AdS or Minkowski) without the CFT. Based on our analysis of parameter space, we can make the following statement:

Within the validity of EFT, for parameter values for which pure gravity shows no pathologies, neither does the gravity+CFT system.

In other words, for background curvatures below the cut-off, light unstable modes in the gravity + CFT system are due essentially to (effective) large *local* higher curvature terms which would result in the same instabilities in the pure gravity with the same parameters. It should be remembered though, that in pure gravity the cutoff is taken to be the Planck scale while in the gravity+CFT system, the cutoff is taken to be the (renormalized) species cutoff in (1.35).

Note that if we insist instead on taking the EFT cut-off to be the Planck scale (rather than the species scale) even in the presence of the CFT, this conclusion changes, and we are led to the fact that coupling a healthy CFT to gravity *does* introduce instabilities within EFT. This is another indication that the correct cut-off is indeed M_p/\sqrt{N} .

From the holographic standpoint, in the case of a CFT coupled to gravity, the scalar modes are the simplest since they do not propagate in the bulk, the only dynamical scalars are boundary degrees of freedom whose dynamics are determined by the R^2 terms and the conformal anomaly [58]. Therefore, any scalar instabilities can be simply traced purely to a local boundary gravity action.

The unstable scalar is a pure-gauge mode in Einstein gravity, but it becomes dynamical thanks to the higher curvature terms and the conformal anomaly, and depending on the coefficients, it may become tachyonic and/or ghost-like. In this context, scalar instabilities were studied in 4-dimensional higher-curvature gravity around flat space in [8]. Around de Sitter, scalar instabilities were investigated in [53] in the (original) Starobinsky model [52], and here we recover the results obtained in the linearized version of Vilenkin's analysis. It is worth mentioning that this model falls outside of the EFT description: indeed, in [52, 53] the 4d cosmological constant is set to zero, which fixes the dS curvature to satisfy $GN^2H^2 = 4\pi$. The value of H is above the species cut-off $1/(\sqrt{GN})$ (although for large N it may still be sub-Planckian). In this case, the no-tachyon condition in the scalar sector is $\alpha > 0$, (see equation (1.36)). However for phenomenological reasons, it is rather desirable to have a scalar tachyon in order to leave the de Sitter solution in the early universe, and one should choose $\alpha < 0$.

Similar considerations can be made if we want to make a comparison with what goes

nowadays under the name of the Starobinsky model for inflation¹³,

$$S = - \int \sqrt{-g} \left(\frac{1}{16\pi G} R - \hat{\alpha} R^2 \right). \quad (1.43)$$

This may be thought of as a simplified version of the anomaly-driven realization of de Sitter in [52, 53] in which one neglects the non-local contribution from the conformal anomaly $\sim R^2 \log R$. For this model, one does not need a CFT, but pure higher curvature gravity is enough. The model (1.43) does not admit de Sitter solutions since the absence of the logarithmic term pushes this solution to infinite curvature. However, it admits quasi-de Sitter slowly-rolling FRW solutions (in an appropriately defined Einstein frame) for $\hat{\alpha} < 0$, i.e. precisely where one expects a scalar tachyonic instability (see equation (1.36) for large curvature): it is this tachyon that eventually pushes the solution away from the near-de Sitter geometry, thus ending inflation. This is the choice made in phenomenological models of inflation, where the parameter

$$\alpha = 384\pi\hat{\alpha} \sim -5.95 \times 10^{11}$$

to reproduce the amplitude of the primordial perturbation spectrum. For $\hat{\alpha} < 0$, the scalar mode is not a ghost in pure $R + R^2$ gravity, as can be seen by setting $N = 0$ in (1.37). More details about how our results compare to these models can be found in Appendix C.

A general discussion of higher-derivative gravity including the tensor modes can be found in [85], where it was pointed out that the $R_{\mu\nu}R^{\mu\nu}$ term gives rise to a tensor ghost around flat space. Here, we also extend this discussion to de Sitter and AdS.

In the holographic context of gravity coupled to a large- N CFT, instabilities were already found in certain corners of parameter space by [74], and we agree with their results. A general analysis of the gravitational spectrum around de Sitter space was also performed in [58] for a specific value of the dS Hubble parameter (namely $GN^2H^2 = 4\pi$) for which the (renormalized) cosmological term is zero (this case however, is outside of the range of EFT since $R \sim H^2 > M_{species}$). As we mentioned above, here we find that these tensor instabilities are either outside of the EFT validity, or they require large effective values of the higher curvature coefficients which would make the pure gravity theory pathological as well. A more detailed comparison with [74] and [58] appears in appendix L.

When there are light tensor tachyons or ghosts, it is interesting to ask which direction in solution space the instability leads to. The scalar instability contains a homogeneous mode which can be understood as an instability of the de Sitter solution towards a more general FRW. These are the instabilities of the type considered in [53]. However, non-homogeneous scalar instabilities and tensor instabilities break FRW.

A related question is whether this analysis around maximally symmetric space-times persists in more realistic cosmological solutions such as FRW. The same holographic setup used here can in principle be applied to FRW boundary metrics, by generalizing the bulk solution along the lines of [60, 61, 63, 89].

¹³ $\hat{\alpha}$ in equation (1.43) is related to our α as $\hat{\alpha} = \frac{\alpha}{384\pi}$.

This paper is organized as follows. The setup of our work is presented in section 2, where we start from a theory of gravity in AdS_5 and obtain the boundary action with higher curvature terms induced on a regularized boundary.

Metric perturbations are set up in section 3 for the bulk perspective, and in section 4 for the boundary theory. Section 4 also studies the dynamics of the pure boundary scalar perturbation. The five remaining degrees of freedom for metric perturbations are contained in a transverse-traceless tensor studied in section 5, where its equation of motion is obtained. In section 6 we discuss tensor instabilities in pure gravity with quadratic curvature terms. Tensor instability in the general case of the CFT coupled to gravity is studied in section 7 for flat space-time, in section 8 for positive curvatures and in section 9 for negative curvatures.

The appendix contains some of the technical details of this paper. We briefly review here the different sections. In appendix A, we provide an explicit example of effective field theory which develops instabilities (ghosts and tachyons) due to the IR expansion. We also find that the mass of these unstable modes is always above the EFT cut-off. Appendix B reviews the computation of the counterterms for the bulk renormalization procedure [82]. In appendix C, we relate our setup to Starobinsky’s inflation [52]. The geometry of AdS-slicing coordinates is reviewed in appendix D where we map them to the more usual *global coordinates* of AdS. We also remark that AdS-slicing coordinates are *global* in the sense that they cover the whole AdS manifold. Appendix E relates the bulk radial equation of spin-2 perturbation to a Schrodinger problem, which allows us to study the normalizability of its solutions. In appendix F, we compute the decay rate of Minkowski space-time in terms of the mass of a tachyonic pole. Appendices G and H derive the criteria (1.33) for the spin-2 modes in dS and AdS respectively. appendix I studies the asymptotic behaviour of associated Legendre functions which enter into the solution for spin-2 perturbations in AdS-slicing coordinates of AdS. Appendix J computes the quadratic terms of the boundary action, which enter into the definition of the two-point functions for metric perturbations. Appendix K proves that one can discard an unphysical scalar mode appearing in the quadratic action, by showing that this mode is constrained. Appendix L compares our results to previous papers which have used a similar setup. We find the values of our parameters which reduce our setup to their case. Finally, appendix M provides supplementary material concerning the poles of the spin-2 propagators in curved space.

The arXiv webpage of this paper contains supplementary material, including 5 animated gifs showing the poles of the spin-2 propagator for different choices of parameters ($GN^2\bar{R}$, $\tilde{\alpha}$ and $\tilde{\beta}_{\text{eff}}$). These gifs and their associated parameters are presented in the “animated_gifs.pdf” ancillary file.

2. The theory

We use the following notation for the various metrics:

symbol	name	relation/definition
\mathcal{G}_{ab}	5d bulk metric	Fefferman-Graham coordinates (2.19)
$g_{\omega\sigma}$	Fefferman-Graham slice metric	defined in (2.19)
$g_{\omega\sigma}^{(0)}$	4d space-time metric	leading term of (2.21)
$\gamma_{\omega\sigma}$	induced metric on the regulated boundary	related to $g_{\omega\sigma}^{(0)}$ as (2.20)
$\bar{\zeta}_{\omega\sigma}$	background 4d space-time metric	maximally symmetric background of $g_{\omega\sigma}^{(0)}$ (4.1)
$\delta\zeta_{\omega\sigma}$	slice metric perturbation	defined in (3.2)
$\delta\zeta_{\omega\sigma}^b$	$\delta\zeta_{\omega\sigma}$ evaluated on the boundary	defined in (4.1), gauge fixed in (4.3)

2.1 Setup

We consider a semi-classical theory of gravity in four dimensions, described by a 4d metric $g_{\omega\sigma}^{(0)}$, including quadratic curvature terms and coupled to a 4d Conformal Field Theory (CFT). The total action is

$$S = S_{\text{grav}} + S_{\text{CFT}}. \quad (2.1)$$

The first term, S_{grav} , is the gravity action:

$$S_{\text{grav}} = S_{\text{EH}} + S_{\alpha} + S_{\beta}, \quad (2.2)$$

which includes the Einstein-Hilbert plus the cosmological constant term¹⁴,

$$S_{\text{EH}} = -\frac{1}{16\pi G} \int d^4x \sqrt{g^{(0)}} (R - 2\Lambda), \quad (2.3)$$

as well as two quadratic curvature terms:

$$S_{\alpha} = \frac{\alpha}{384\pi} \int d^4x \sqrt{g^{(0)}} R^2, \quad (2.4)$$

$$S_{\beta} = \frac{\beta}{64\pi} \int d^4x \sqrt{g^{(0)}} \left(R^{\omega\sigma} R_{\omega\sigma} - \frac{1}{3} R^2 \right). \quad (2.5)$$

Here, G is the Newton constant, Λ the cosmological constant, α and β are the dimensionless R -squared couplings.

The second term S_{CFT} in (2.1) is the quantum effective action of a CFT in a background metric $g_{\omega\sigma}^{(0)}$, and it is a functional of the background metric $g_{\omega\sigma}^{(0)}$.

The action (2.1) is meant to be the renormalized action, in which all the divergences have been renormalized. The parameters $G, \Lambda, \alpha, \beta$ are therefore to be interpreted as finite, physical parameters left after the renormalization procedure (which will be described in detail in subsection 2.2 and reference [72]).

¹⁴In our notation, the curvature tensors are understood to be those built from the metric $g_{\omega\sigma}^{(0)}$, unless otherwise specified explicitly.

Variation of the action with respect to the boundary metric yields the following Einstein equation:

$$R_{\omega\sigma} - \frac{1}{2}Rg_{\omega\sigma}^{(0)} + \Lambda g_{\omega\sigma}^{(0)} + 8\pi G \left({}^{(\alpha)}H_{\omega\sigma} + {}^{(\beta)}H_{\omega\sigma} \right) = 8\pi G \langle T_{\omega\sigma} \rangle. \quad (2.6)$$

where

$${}^{(\alpha)}H_{\omega\sigma} = \frac{\alpha}{96\pi} \left\{ \nabla_{\omega} \nabla_{\sigma} R - R R_{\omega\sigma} - \left(\square R - \frac{1}{4} R^2 \right) g_{\omega\sigma}^{(0)} \right\}, \quad (2.7)$$

$$\begin{aligned} {}^{(\beta)}H_{\omega\sigma} = \frac{\beta}{32\pi} \left\{ \frac{1}{2} \left(R_{\kappa\lambda} R^{\kappa\lambda} - \frac{1}{3} R^2 + \frac{1}{3} \square R \right) g_{\omega\sigma}^{(0)} - 2R_{\omega\kappa\sigma\lambda} R^{\kappa\lambda} - \square R_{\omega\sigma} \right. \\ \left. + \frac{1}{3} (2R R_{\omega\sigma} + \nabla_{\omega} \nabla_{\sigma} R) \right\}. \end{aligned} \quad (2.8)$$

In Eq. (2.6), the right-hand side is the renormalized CFT stress-energy tensor expectation value,

$$\langle T_{\omega\sigma} \rangle = \frac{2}{\sqrt{g^{(0)}}} \frac{\delta S_{CFT}}{\delta g^{(0)\omega\sigma}}. \quad (2.9)$$

Before we present the computation of the CFT stress tensor, we comment on the terms which are explicit on the left-hand side of (2.6). It is important to remark that ${}^{(\beta)}H_{\omega\sigma}$ is traceless. Furthermore, ${}^{(\alpha)}H_{\omega\sigma}$ is also traceless if the boundary has a constant curvature.

For convenience, in the following, we define the tensor

$$E_{\omega\sigma} \equiv -\frac{16\pi G}{\sqrt{g^{(0)}}} \frac{\delta S}{\delta g^{(0)\omega\sigma}}. \quad (2.10)$$

We then write Einstein's equations as:

$$E_{\omega\sigma} = 0. \quad (2.11)$$

From now on, we shall assume the CFT is a large- N theory which has a holographic description in terms of a (semiclassical) five-dimensional gravity dual. We shall review how the renormalized stress tensor (2.9) is computed in this context [82], and how the renormalized parameters of the effective gravity theory arise. However, as we shall argue, our results do not depend on this assumption. Below we present the main results and give more details in appendix B.

2.2 Constructing the renormalized action

To arrive at (2.1) we replace the CFT contribution with its dual description, namely an Einstein-Hilbert theory on a 5-dimensional manifold \mathcal{M} (the bulk, on which the metric will be denoted by \mathcal{G}) together with covariant boundary terms on the boundary, $\partial\mathcal{M}$. However, this is divergent and to regulate the divergences we move the boundary $\partial\mathcal{M}$ to the regulated boundary $\partial\mathcal{M}_{\epsilon}$ which is inside \mathcal{M} and this also defines the regulated bulk space \mathcal{M}_{ϵ} . γ is the induced metric on the regulated boundary.

The bare regularized gravity dual action is:

$$S_{\text{reg}} = S_{\text{bulk}} + S_{\text{grav}}^0. \quad (2.12)$$

The first term is the usual Einstein-Hilbert action with a boundary $\partial\mathcal{M}_\epsilon$,

$$S_{\text{bulk}} = -M^3 \left[\int_{\mathcal{M}_\epsilon} d^5x \sqrt{\mathcal{G}} (R[\mathcal{G}] - 2\Lambda_5) - 2 \int_{\partial\mathcal{M}_\epsilon} d^4x \sqrt{\gamma} K \right]. \quad (2.13)$$

where M is the 5-dimensional Planck mass, γ is the determinant of the induced metric on $\partial\mathcal{M}_\epsilon$ and K is the corresponding extrinsic curvature¹⁵. The second term in (2.12) is a boundary term which depends only on intrinsic tensors on $\partial\mathcal{M}_\epsilon$,

$$S_{\text{grav}}^0 = S_{\text{EH}}^0 + S_\alpha^0 + S_\beta^0, \quad (2.14)$$

where

$$S_{\text{EH}}^0 = -\frac{1}{16\pi G^0} \int d^4x \sqrt{\gamma} (R[\gamma] - 2\Lambda^0), \quad (2.15)$$

a R^2 term

$$S_\alpha^0 = \frac{\alpha^0}{384\pi} \int d^4x \sqrt{\gamma} (R[\gamma])^2, \quad (2.16)$$

and an additional term proportional to the 4-dimensional Weyl anomaly¹⁶ [55]

$$S_\beta^0 = \frac{\beta^0}{64\pi} \int d^4x \sqrt{\gamma} \left(R[\gamma]^{\kappa\lambda} R[\gamma]_{\kappa\lambda} - \frac{1}{3} (R[\gamma])^2 \right). \quad (2.17)$$

This action looks similar to (2.5), and depends on a set of bare parameters α^0 , β^0 , Λ^0 and G^0 . Below we shall relate these bare parameters to the physical ones (α , β , Λ and G) in the renormalized action (2.1).

We also define a length L associated with the bulk cosmological constant,

$$\Lambda_5 = -\frac{6}{L^2}. \quad (2.18)$$

We consider asymptotically AdS solutions, for which the ansatz for the full metric is written using Fefferman-Graham coordinates [90], given by

$$ds^2 = \mathcal{G}_{ab} dX^a dX^b = L^2 \frac{d\rho^2}{4\rho^2} + \frac{1}{\rho} g_{\omega\sigma}(x, \rho) dx^\omega dx^\sigma, \quad (2.19)$$

where L and x^σ have the dimension of a length and ρ is dimensionless. This coordinate system is the one of an asymptotically AdS space with a conformal boundary located at $\rho \rightarrow 0$. We define the regulated boundary $\partial\mathcal{M}_\epsilon$ as the hypersurface $\rho = \epsilon$, on which the induced metric is:

$$\gamma_{\omega\sigma}(\epsilon, x) = \frac{1}{\epsilon} g_{\omega\sigma}(\epsilon, x). \quad (2.20)$$

The metric $g_{\omega\sigma}$ is determined by solving the bulk Einstein equation order by order in ρ as $\rho \rightarrow 0$, starting with an arbitrary metric $g_{\omega\sigma}^{(0)}$ to lowest order [82]:

$$g_{\omega\sigma}(x, \rho) = g_{\omega\sigma}^{(0)} + \rho g_{\omega\sigma}^{(2)} + \rho^2 g_{\omega\sigma}^{(4)} + \hat{g}_{\omega\sigma} \rho^2 \log \rho + \mathcal{O}(\rho^3). \quad (2.21)$$

¹⁵Geometrical tensors follow the same conventions as Wald's book *General Relativity*

¹⁶In our notation, the Latin letters will denote the bulk coordinates, and the Greek indices such as ω, σ denote 4-dimensional slice coordinates.

The leading term in this expansion, $g_{\omega\sigma}^{(0)}$, is identified with the metric of the dual field theory side. The terms $g_{\omega\sigma}^{(2)}$ and $\hat{g}_{\omega\sigma}$ are given by¹⁷:

$$g_{\omega\sigma}^{(2)} = -\frac{L^2}{2} \left(R_{\omega\sigma} - \frac{R}{6} g_{\omega\sigma}^{(0)} \right), \quad (2.22)$$

$$\hat{g}_{\omega\sigma} = \frac{L^4}{16} \left\{ 2R_{\omega\kappa\sigma\lambda} R^{\kappa\lambda} - \frac{1}{3} \nabla_\omega \nabla_\sigma R + \nabla^2 R_{\omega\sigma} - \frac{2}{3} R R_{\omega\sigma} + \left(\frac{1}{6} R^2 - \frac{1}{6} \nabla^2 R - \frac{1}{2} R_{\kappa\lambda} R^{\kappa\lambda} \right) g_{\omega\sigma}^{(0)} \right\} \quad (2.23)$$

These expressions are found by solving the bulk Einstein equation in a near-boundary expansion [82]. Note that, comparing Eqs. (2.8) and (2.23), we can write:

$${}^{(\beta)}H_{\omega\sigma} = -\frac{\beta}{2\pi} \hat{g}_{\omega\sigma}. \quad (2.24)$$

Unlike $g_{\omega\sigma}^{(2)}$ and $\hat{g}_{\omega\sigma}$, $g_{\omega\sigma}^{(4)}$ is not fully determined from $g_{\omega\sigma}^{(0)}$, except for its trace, which is given by¹⁸ [82]:

$$\text{Tr} \left[g^{(4)} \right] = \frac{1}{4} \text{Tr} \left[\left(g^{(2)} \right)^2 \right]. \quad (2.25)$$

Divergences of S_{bulk} , which arise when we remove the regulator and take $\epsilon \rightarrow 0$, are made explicit when S_{bulk} is written in terms of $g_{\omega\sigma}^{(0)}$. The method to obtain these divergences is briefly reviewed in appendix B, resulting in:

$$S_{\text{bulk}} = \frac{M^3}{L} \int d^4x \sqrt{g^{(0)}} \left\{ -\frac{6}{\epsilon^2} + \frac{1}{8} \log \epsilon \left(R^{\kappa\lambda} R_{\kappa\lambda} - \frac{1}{3} R^2 \right) \right\} + \mathcal{O}(\epsilon^0), \quad (2.26)$$

The first term in curly brackets contains all the divergent terms of S_{bulk} . These can also be written covariantly in a series expansion involving curvature tensors of the induced metric on the boundary.

$$S_{\text{bulk}} = \frac{M^3}{L} \int d^4x \sqrt{\gamma} \left\{ -6 - \frac{L^2}{2} R[\gamma] + \frac{L^4}{8} \left(\frac{1}{2} + \log \epsilon \right) \left(R^{\kappa\lambda}[\gamma] R_{\kappa\lambda}[\gamma] - \frac{1}{3} (R[\gamma])^2 \right) \right\} + \dots \quad (2.27)$$

where ... indicates higher curvature invariants. The explicit ϵ dependence in (2.27) reflects the conformal anomaly.

The quadratic curvature term in (2.26) can be shifted by a finite amount by redefining the cut-off. This scheme dependence is made explicit by introducing as an extra parameter, a scale μ , and defining the divergent part of the action S_{div} as follows:

$$S_{\text{div}} \equiv \frac{M^3}{L} \int d^4x \sqrt{g^{(0)}} \left\{ -\frac{6}{\epsilon^2} + \frac{1}{4} \log(\sqrt{\epsilon} \mu L) \left(R^{\omega\sigma} R_{\omega\sigma} - \frac{1}{3} R^2 \right) \right\}. \quad (2.28)$$

¹⁷Recall that all the geometrical tensors are built from the metric $g_{\omega\sigma}^{(0)}$ unless otherwise stated

¹⁸As in [82], when matrix components are not written, it means that both matrix multiplication and trace operations are done using the metric $g^{(0)}$.

We now turn to the bare “boundary” gravitational action (2.14). It is also divergent in the limit $\epsilon \rightarrow 0$. This can be made manifest by expressing it in terms of curvature tensors of $g_{\omega\sigma}^{(0)}$ using the expansion (2.21) and the expressions (2.22-2.23). The result for the Einstein-Hilbert part is

$$\begin{aligned} S_{\text{EH}}^0 &= -\frac{1}{16\pi G^0} \int d^4x \sqrt{\gamma} (R[\gamma] - 2\Lambda^0), \\ &= -\frac{1}{16\pi G^0} \int d^4x \sqrt{g^{(0)}} \left\{ -\frac{2\Lambda_0}{\epsilon^2} + \frac{1}{\epsilon} \left(1 + \frac{\Lambda_0 L^2}{6} \right) R + \right. \\ &\quad \left. + \frac{L^2}{4} \left(2 + \frac{\Lambda_0 L^2}{4} \right) \left(R^{\omega\sigma} R_{\omega\sigma} - \frac{1}{3} R^2 \right) + \mathcal{O}(\epsilon) \right\}, \end{aligned} \quad (2.29)$$

while S_α^0 and S_β^0 are finite. Note that additional finite quadratic terms appear when we expand S_{EH}^0 in powers of ϵ .

Therefore, the full boundary action S_{grav}^0 written in terms of $g_{\omega\sigma}^{(0)}$, including all divergent and finite terms, has the form:

$$\begin{aligned} S_{\text{grav}}^0 &= -\frac{1}{16\pi G^0} \int d^4x \sqrt{g^{(0)}} \left\{ -\frac{2\Lambda_0}{\epsilon^2} + \frac{1}{\epsilon} \left(1 + \frac{\Lambda_0 L^2}{6} \right) R \right\} + \\ &+ \left[\beta^0 - \frac{1}{16\pi G^0} \frac{L^2}{4} \left(2 + \frac{\Lambda_0 L^2}{4} \right) \right] \int d^4x \sqrt{g^{(0)}} \left(R^{\omega\sigma} R_{\omega\sigma} - \frac{1}{3} R^2 \right) \\ &+ \alpha^0 \int d^4x \sqrt{g^{(0)}} R^2 + \mathcal{O}(\epsilon). \end{aligned} \quad (2.30)$$

The renormalisation procedure we adopt consists in taking the limit $\epsilon \rightarrow 0$ by choosing appropriately the bare parameters (Λ^0 , G^0 , α^0 and β^0) as a function of the cut-off, such that the quantity

$$S_{\text{grav}} \equiv S_{\text{grav}}^0 + S_{\text{div}} \quad (2.31)$$

remains finite¹⁹ in the limit $\epsilon \rightarrow 0$.

We write the resulting finite action in terms of new *physical* parameters (Λ , G , α and β), each corresponding to the one boundary term:

$$\Lambda = \frac{1}{\epsilon} \left(1 + \frac{\Lambda^0 L^2}{6} \right)^{-1} \left[\Lambda^0 - \frac{48\pi G^0 M^3}{L} \right], \quad (2.32)$$

$$G = \frac{\epsilon G^0}{1 + \frac{\Lambda^0 L^2}{6}}, \quad (2.33)$$

$$\alpha = \alpha^0, \quad (2.34)$$

$$\beta = \beta^0 + 16\pi M^3 L^3 \log(\sqrt{\epsilon} L \mu) - \frac{2L^2}{G^0} \left(1 + \frac{\Lambda^0 L^2}{8} \right). \quad (2.35)$$

¹⁹This is different from the standard holographic renormalization procedure [82], in which the bare parameters (Λ^0 , G^0 , α^0 and β^0) are independent on the cut-off and a counterterm action (whose coefficients are completely fixed) is introduced to cancel all divergences coming from S_{bulk} (2.27). This leaves only finite quadratic curvature terms in the renormalized action and no Einstein-Hilbert term.

and we take $\epsilon \rightarrow 0$ together with appropriate limits of $(\Lambda_0, G_0, \alpha_0$ and $\beta_0)$ so that the left hand sides are finite.

Finally, combining (2.12) and (2.32) we write the renormalized action as

$$S = \lim_{\epsilon \rightarrow 0} [S_{\text{bulk}} - S_{\text{div}}] + S_{\text{grav}}, \quad (2.37)$$

$$\equiv S_{\text{CFT}} + S_{\text{grav}}, \quad (2.38)$$

i.e. equation (2.1). The bulk contribution inside the square brackets is interpreted as the renormalized effective action of the CFT.

2.3 The induced stress tensor

The renormalized stress tensor is defined by

$$\langle T_{\omega\sigma} \rangle = \lim_{\epsilon \rightarrow 0} \left[\frac{1}{\epsilon} \frac{2}{\sqrt{\gamma}} \frac{\delta S_{\text{CFT}}}{\delta \gamma^{\omega\sigma}} \right] = \frac{2}{\sqrt{g^{(0)}}} \frac{\delta S_{\text{CFT}}}{\delta g^{(0)\omega\sigma}}. \quad (2.39)$$

It can be shown that this definition leads to

$$\frac{2}{\sqrt{\gamma}} \frac{\delta S_{\text{bulk}}}{\delta \gamma^{\omega\sigma}} = 2M^3 (K_{\omega\sigma} - K \gamma_{\omega\sigma}). \quad (2.40)$$

As shown in [82] the divergent pieces of (2.40) cancel the ones of the S_{div} . We are then left with the renormalized stress tensor given by ²⁰

$$\begin{aligned} \langle T_{\omega\sigma} \rangle = & -\frac{2M^3}{L} \left\{ 2 [2 \log(\mu L) - 1] \hat{g} - 2g^{(4)} + \left(g^{(2)}\right)^2 - \frac{1}{4} g^{(0)} \text{Tr} \left[\left(g^{(2)}\right)^2 \right] + \right. \\ & \left. + \frac{1}{4} g^{(0)} \left(\text{Tr} \left[g^{(2)} \right] \right)^2 - \frac{1}{2} g^{(2)} \text{Tr} \left[g^{(2)} \right] \right\}_{\omega\sigma}, \end{aligned} \quad (2.41)$$

where $g_{\omega\sigma}^{(2)}$, $g_{\omega\sigma}^{(4)}$ and $\hat{g}_{\omega\sigma}$ are the terms of the Fefferman-Graham expansion (2.21), the expressions for $g_{\omega\sigma}^{(2)}$ and $\hat{g}_{\omega\sigma}$ in terms of $g_{\omega\sigma}^{(0)}$ are given in Eqs. (2.22,2.23). $g_{\omega\sigma}^{(4)}$ must be obtained from solving the bulk dynamics. The stress-tensor expectation value in (2.41) is to be inserted into the right-hand side of the Einstein equation (2.6).

Even if the stress-tensor is not fully constrained by the boundary data, its trace is known using (2.25). It gives

$$g^{(0)\omega\sigma} \langle T_{\omega\sigma} \rangle = \frac{(ML)^3}{4} \left(R^{\omega\sigma} R_{\omega\sigma} - \frac{1}{3} R^2 \right). \quad (2.42)$$

In a generic CFT with a 5d gravity dual, the parameter $M^3 L^3$ is large, and proportional to the central charge²¹ a :

$$(ML)^3 = \frac{a}{2\pi^2}. \quad (2.43)$$

²⁰For a notational simplification, there is no difference in subscript and superscript in Fefferman-Graham metric expansion.

²¹Recall that in holographic CFTs, the two central charges a and c are equal, up to $1/N^2$ corrections

When the CFT is a large- N gauge theory in 4d, then $a \propto N^2$. For example, in $\mathcal{N} = 4$ SYM we have, in the large- N limit:

$$a = \frac{N^2}{4}. \quad (2.44)$$

In what follows we assume, for definiteness, the $\mathcal{N} = 4$ relation (2.44), and set:

$$M^3 L^3 = \frac{N^2}{8\pi^2}. \quad (2.45)$$

This will allow us to replace $M^3 L^3$ with N^2 and write all equations which pertain to the field theory side purely in terms of 4d parameters. Readers can keep in mind that, for any other CFT (even for those that are not large- N) they can substitute

$$N^2 \rightarrow 4a.$$

2.4 Background solutions

In this section, we discuss the background (i.e. homogeneous) solutions of the equations of motion for the 5d theory (2.12). We take these solutions to be the AdS_5 metric with three different maximally symmetric slicings,

$$ds_5^2 = L^2 du^2 + a^2(u) \bar{\zeta}_{\omega\sigma} dx^\omega dx^\sigma, \quad (2.46)$$

where $a(u)$ is a dimensionless scale factor and the slice metric $\bar{\zeta}_{\omega\sigma}$ is a u -independent maximally symmetric 4d metric. This results in three possible coordinate systems for AdS_5 , that correspond to the dual CFT on three distinct four-dimensional maximally symmetric metrics: AdS_4 , dS_4 and M_4 .

- $\bar{\zeta}$ being the Minkowski metric. In this case

$$a(u) = e^u, \quad (2.47)$$

where $u > 0$ and the AdS boundary is located at $u \rightarrow +\infty$.

- $\bar{\zeta}$ being the de Sitter metric with Hubble curvature H , in which case

$$a(u) = LH \sinh u, \quad (2.48)$$

where $u \in \mathbb{R}$. $u = 0$ is a horizon. From now on, we take u positive. Therefore, $u \rightarrow +\infty$ is the AdS_5 boundary. The curvature of dS is given by

$$\bar{R} = 12H^2. \quad (2.49)$$

- $\bar{\zeta}$ being the Anti-de Sitter metric with radius χ^{-1} , in which case

$$a(u) = L\chi \cosh u. \quad (2.50)$$

In this case, there are two asymptotic boundaries, located at $u = \pm\infty$. These two boundaries are connected. More details for the geometry of AdS-slicing coordinates

are given in appendix D. In the field theory interpretation, these correspond to two independent copies of the CFT on AdS₄ that interact via their common AdS₄ boundary²². It is a matter of choice whether only one or both are coupled to dynamical metric perturbations, as we shall discuss in section 5.3. Since there is no horizon at $u = 0$, we shall observe that both sides are reachable by the bulk metric perturbations. The boundary curvature is related to χ by:

$$\bar{R} = -12\chi^2. \quad (2.51)$$

The bulk metric (2.46) can also be written in Fefferman-Graham coordinates as

$$ds_5^2 = L^2 \frac{d\rho^2}{4\rho^2} + \frac{1}{\rho} f(\rho) ds_4^2. \quad (2.52)$$

where $ds_4^2 = \bar{\zeta}_{\omega\sigma} dx^\omega dx^\sigma$ and the function f for each different slicing is then given by

space-time	ds_4^2	ρ	$f(\rho)$
M ₄	ds_{flat}^2	$\rho = e^{-2u}$	1
dS ₄	ds_{dS}^2	$\rho = \left(\frac{2}{LH}\right)^2 e^{-2u}$	$f_{dS}(\rho) = 1 - \frac{(LH)^2}{2}\rho + \left(\frac{LH}{2}\right)^4 \rho^2$
AdS ₄	ds_{AdS}^2	$\rho = \left(\frac{2}{L\chi}\right)^2 e^{-2\text{sign}(u)u}$	$f_{AdS}(\rho) = 1 + \frac{(L\chi)^2}{2}\rho + \left(\frac{L\chi}{2}\right)^4 \rho^2$

(2.53)

In these coordinates, $\rho > 0$ and the AdS₅ boundary is located at $\rho = 0$. In de Sitter slicing, we are free to choose a sign of u (here we took positive u) because of the horizon $u = 0$ which separates the two sides of the bulk. However, in AdS slicing where there is no such horizon, the bulk AdS₅ needs two different Fefferman-Graham patches such that $\rho \rightarrow 0$ is the AdS₅ boundary $u \rightarrow \pm\infty$. Hence the $\text{sign}(u)$ in the expression for ρ in AdS-slicing.²³

The background solutions (2.52) are then related to the general Fefferman-Graham expansion (2.19) by

$$g_{\omega\sigma}(x, \rho)|_{\text{background}} = f(\rho) \bar{\zeta}_{\omega\sigma}, \quad (2.54)$$

from which every term of the expansion (2.21) are fixed. In particular, we can read off the corresponding boundary theory metric $g_{\omega\sigma}^{(0)}$ as the leading term as $\rho \rightarrow 0$:

$$g_{\omega\sigma}^{(0)} = \bar{\zeta}_{\omega\sigma} \quad (2.55)$$

and it is either the Minkowski metric or the de Sitter metric with Hubble scale H , or the anti-de Sitter metric with AdS length χ^{-1} . We denote the background curvature $R[\bar{\zeta}] \equiv \bar{R}$,

$$\bar{R} = \begin{cases} 12H^2, & \text{de Sitter,} \\ 0, & \text{Minkowski} \\ -12\chi^2, & \text{Anti de Sitter} \end{cases} \quad (2.56)$$

²²A conformal rescaling of such a setup corresponds to an interface between two copies of the same CFT in flat space, see the extended discussion in [70].

²³The global embedding of dS and AdS slices in AdS₅ is discussed in detail in [91] for dS, and in [84] for AdS.

For a maximally symmetric background, the trace of the Einstein equation (2.6) gives

$$\Lambda = \frac{1}{4} \left(\bar{R} - \frac{GN^2 \bar{R}^2}{48\pi} \right), \quad (2.57)$$

where N was defined in (2.42). Note that, for each value of the boundary parameters Λ and G , there are either two values of the curvature \bar{R} satisfying equation (2.57), or there are none. On the other hand, by scanning all values of Λ , we can obtain any value of \bar{R} . Therefore, it is convenient to trade Λ for \bar{R} : in what follows we shall replace Λ in terms of \bar{R} using (2.57) in all equations. This leaves $GN^2 \bar{R}$ as the only dimensionless background curvature parameter.

Equation (2.57) does not depend on α or β since they multiply tensors that are traceless when evaluated on the background metric $\bar{\zeta}_{\omega\sigma}$ with constant curvature.

The maximally symmetric backgrounds were discussed in detail (for holographic CFTs and holographic RG flows on de Sitter) in [72]. We now move to the perturbations around these background solutions. These are described by turning on perturbations in both the bulk and the boundary metric and solving the corresponding Einstein's equation and boundary conditions. This will be the subject of the next section.

3. Bulk metric perturbations

Equation (2.54) holds for the unperturbed, background metric. In this section, we study perturbations of the bulk metric, by adopting the same gauge invariant decomposition of metric perturbations as in [58].

In a perturbed geometry, the bulk metric reads

$$ds_{\mathfrak{S}}^2 = (\mathcal{G}_{ab} + \delta\mathcal{G}_{ab}) dX^a dX^b. \quad (3.1)$$

Using (2.46), one can relate the slice component perturbations to actual perturbations of the slice metric $\delta\zeta_{\omega\sigma}$ defined as

$$\delta\mathcal{G}_{\omega\sigma} = a^2(u) \delta\zeta_{\omega\sigma}, \quad (3.2)$$

such that the full metric can now be written as

$$ds_{\mathfrak{S}}^2 = (\mathcal{G}_{uu} + \delta\mathcal{G}_{uu}) du^2 + 2(\mathcal{G}_{u\sigma} + \delta\mathcal{G}_{u\sigma}) du dX^\sigma + a^2(u) (\bar{\zeta}_{\omega\sigma} + \delta\zeta_{\omega\sigma}) dx^\omega dx^\sigma. \quad (3.3)$$

Even if a 5×5 symmetric matrix contains 15 independent elements, only 10 degrees of freedom are invariant under the gauge transformation

$$\delta\mathcal{G}_{ab} \rightarrow \delta\mathcal{G}_{ab} + 2\nabla_{(a}^{(\mathcal{G})} \xi_{b)}. \quad (3.4)$$

One can construct these 10 invariant quantities by decomposing the perturbation \mathcal{G}_{ab} into transverse and traceless elements for the slice covariant derivative $\hat{\nabla}$ built with $\zeta_{\omega\sigma}$ as follows [58]:

$$\delta\mathcal{G}_{uu} = A, \quad (3.5)$$

$$\delta\mathcal{G}_{u\sigma} = B_\sigma + \hat{\nabla}_\sigma B, \quad (3.6)$$

$$\delta\zeta_{\omega\sigma} = h_{\omega\sigma} + 2\hat{\nabla}_{(\omega}\chi_{\sigma)} + \bar{\zeta}_{\omega\sigma}\psi + \hat{\nabla}_{(\omega}\partial_{\sigma)}\phi, \quad (3.7)$$

where B_{σ} , χ_{σ} are transverse and $h_{\omega\sigma}$ is transverse-traceless:

$$\hat{\nabla}^{\sigma}\chi_{\sigma} = 0 = \bar{\zeta}^{\omega\sigma}h_{\omega\sigma}, \quad (3.8)$$

$$\hat{\nabla}^{\omega}h_{\omega\sigma} = 0. \quad (3.9)$$

As it is well known (and rederived in [58] in the present context), the only propagating degree of freedom in the bulk of *AdS* with pure gravity is the *tensor* (transverse-traceless) perturbation $h_{\omega\sigma}$ which contains 5 degrees of freedom. On top of this, there exists a scalar mode which has purely boundary dynamics, and that will be discussed in the next section. Therefore, here we set to zero all components of the perturbation except for the tensor mode.

The next step is to obtain the equation of motion for this tensor mode. The bulk Einstein equation is:

$$R_{ab}[\mathcal{G}] = -\frac{4}{L^2}\mathcal{G}_{ab}. \quad (3.10)$$

When linearized with respect to $h_{\omega\sigma}$, the above equation yields:

$$(L^2\nabla^{(\mathcal{G})2} + 2)a^2(u)h_{\omega\sigma} = 0, \quad (3.11)$$

where the differential operator into parenthesis is known as the Lichnerowicz operator for AdS. This operator can be decomposed into the (u, x^{ω}) slicing coordinates (2.46). Equation (3.11) then takes the following form

$$\left\{ \partial_u^2 + 4\frac{a'}{a}\partial_u + 2\left[1 - \left(\frac{a'}{a}\right)^2\right] + L^2a^{-2}\hat{\nabla}^2 \right\} h_{\omega\sigma} = 0. \quad (3.12)$$

This equation will be specialized to different slicings and solved in section 5.

Tensor perturbations $h_{\omega\sigma}$ can be expanded in a similar way as in (2.19):

$$h_{\omega\sigma} = h_{\omega\sigma}^{(0)} + \rho h_{\omega\sigma}^{(2)} + \rho^2 h_{\omega\sigma}^{(4)} + \rho^2 \log \rho \hat{h}_{\omega\sigma} + \mathcal{O}(\rho^3). \quad (3.13)$$

We shall now linearize the boundary Einstein field equation (2.6) and obtain an equation which involves the various terms in the near-boundary expansion (3.13). To this end, we need to relate perturbations of the metric $g_{\omega\sigma}$ defined in (2.19) to the slice perturbations $h_{\omega\sigma}$ defined in (3.7). We introduce the following notation, for any tensor A of the slice metric:

$$(\delta_h A)[\bar{\zeta}] \equiv \lim_{\varepsilon \rightarrow 0} \frac{A[\bar{\zeta} + \varepsilon h^{(0)}] - A[\bar{\zeta}]}{\varepsilon}. \quad (3.14)$$

We identify term by term the expansion (2.21) with the expansion of the bulk metric (2.46) close to the boundary $\rho \rightarrow 0$ where $\rho(u)$ is given in table 2.53. The result for both AdS and dS is given by

$$\delta_h g_{\omega\sigma}^{(0)} = h_{\omega\sigma}^{(0)}, \quad (3.15a)$$

$$\delta_h g_{\omega\sigma}^{(2)} = h_{\omega\sigma}^{(2)} - \frac{L^2 R}{24} h_{\omega\sigma}^{(0)}, \quad (3.15b)$$

$$\delta_h g_{\omega\sigma}^{(4)} = h_{\omega\sigma}^{(4)} - \frac{L^2 R}{24} h_{\omega\sigma}^{(2)} + \left(\frac{L^2 R}{48} \right)^2 h_{\omega\sigma}^{(0)}, \quad (3.15c)$$

$$\delta_h \hat{g}_{\omega\sigma} = \hat{h}_{\omega\sigma}. \quad (3.15d)$$

The quantities $h^{(2)}$ and \hat{h} can be written in terms of $h^{(0)}$ and of boundary curvature tensors: as is summarized in appendix B, $g_{\omega\sigma}^{(2)}$ and $\hat{g}_{\omega\sigma}$ are obtained in terms of $g^{(0)}$ by solving perturbatively the bulk Einstein equation for small ρ [82]. By varying the solution for $g^{(2)}$ and \hat{g} given in (B.6, B.7) with respect to $h_{\omega\sigma}^{(0)}$, we obtain using (3.15):

$$h_{\omega\sigma}^{(2)} = \frac{L^2}{4} \left(\nabla^2 - \frac{R}{6} \right) h_{\omega\sigma}^{(0)}, \quad (3.16)$$

$$\hat{h}_{\omega\sigma} = -\frac{2\pi L^4}{\beta} \delta_h^{(\beta)} H_{\omega\sigma} = -\frac{L^4}{32} \left(\nabla^2 - \frac{R}{6} \right) \left(\nabla^2 - \frac{R}{3} \right) h_{\omega\sigma}^{(0)}, \quad (3.17)$$

where the laplacian operator ∇^2 is constructed with the Fefferman-Graham metric $g_{\omega\sigma}^{(0)}$. On the contrary, we need to solve (3.11) in the whole bulk (with appropriate conditions in the interior) to find $h_{\omega\sigma}^{(4)}$. We postpone this to section 5.

Using the equations above, all linearized quantities can be expressed purely in terms of $h_{\omega\sigma}^{(0)}$ and $h_{\omega\sigma}^{(4)}$, which for now are independent.

The variation of the holographic stress-tensor (2.41) in the presence of a perturbation $\delta h_{\mu\nu}$ is given by:

$$\delta_h \langle T_{\omega\sigma} \rangle = \frac{N^2}{2\pi^2 L^4} \left[\delta_h g_{\omega\sigma}^{(4)} - \left(\frac{L^2 R}{24} \right)^2 \delta_h g_{\omega\sigma}^{(0)} + (1 - 2 \log(\mu L)) \delta_h \hat{g}_{\omega\sigma} \right], \quad (3.18)$$

where $\delta_h g_{\omega\sigma}^{(4)}$, $\delta_h g_{\omega\sigma}^{(0)}$ and $\delta_h \hat{g}_{\omega\sigma}$ have to be written using equations (3.15a-3.15d) and (3.16-3.17).

We now turn to the linearization of the left-hand side of Einstein's equation (2.6), in which the cosmological constant can be replaced by a function of the background curvature \bar{R} using (2.57). Note that the CFT stress-tensor also contributes to the value of Λ through the trace of the background Einstein equation (2.57). By moving all the CFT contributions (i.e. those proportional to N) to the right-hand-side of the linearized Einstein equation, we find

$$\left(-\nabla^2 + \frac{R}{6} \right) h_{\omega\sigma}^{(0)} + 8\pi G \delta_h^{(\alpha)} H_{\omega\sigma} + {}^{(\beta)} H_{\omega\sigma} = 8\pi G \delta_h \langle T_{\omega\sigma} \rangle^T, \quad (3.19)$$

where

$$\langle T_{\omega\sigma} \rangle^T \equiv \langle T_{\omega\sigma} \rangle - \frac{1}{4} g_{\omega\sigma}^{(0)} \langle T_{\mu}^{\mu} \rangle. \quad (3.20)$$

The curvature squared terms ${}^{(\alpha)} H_{\omega\sigma}$ and ${}^{(\beta)} H_{\omega\sigma}$ are then linearized with respect to the tensor perturbation. Then, equation (3.19) is written as a sum of contributions from the Fefferman-Graham terms $h_{\omega\sigma}^{(0)}$, $h_{\omega\sigma}^{(4)}$ and $\hat{h}_{\omega\sigma}$:

$$h_{\omega\sigma}^{(4)} + \frac{L^4 R}{24} \left\{ \frac{3\pi}{GN^2 R} - \frac{1}{4} - \frac{\pi\alpha}{4N^2} \right\} \left(\nabla^2 - \frac{R}{6} \right) h_{\omega\sigma}^{(0)} + \left(1 - 2 \log(\mu L) + \beta \frac{\pi}{N^2} \right) \hat{h}_{\omega\sigma} = 0, \quad (3.21)$$

where $\hat{h}_{\omega\sigma}$ is to be expressed in terms of $h_{\omega\sigma}^{(0)}$ using (3.17).

Equation (3.21) is a linear equation relating $h_{\omega\sigma}^{(4)}$ to $h_{\omega\sigma}^{(0)}$. As usual in holography however, $h_{\omega\sigma}^{(4)}$ is determined by $h_{\omega\sigma}^{(0)}$ by solving the bulk equation and imposing a regularity condition in the interior. This makes $h_{\omega\sigma}^{(4)}$ into a (non-local) linear functional of $h_{\omega\sigma}^{(0)}$. Therefore, all in all, equation (3.21) takes the form of a dynamical equation for $h_{\omega\sigma}^{(0)}$, of the form:

$$\mathcal{F}^{\mu\nu\omega\sigma}(\nabla^2, \bar{R})h_{\omega\sigma}^{(0)} = 0. \quad (3.22)$$

Determining the explicit form of the functional \mathcal{F} will be the goal of section 5. Here we conclude by the remark that equation (3.22) can also be obtained by varying the quadratic part of the action (2.1) evaluated on-shell: indeed, as shown in appendix J, once it is evaluated on the solution of the linear bulk equation, the quadratic part of the action (2.1) is equal to the boundary expression:

$$S^{(2)}[h^{(0)}] = \frac{N^2}{2\pi^2} \int d^4x \sqrt{\bar{\zeta}} h^{(0)\omega\sigma} \left\{ h_{\omega\sigma}^{(4)} + \left(\frac{\pi\beta}{N^2} + 1 - 2 \log(\mu L) \right) \hat{h}_{\omega\sigma} + \frac{RL^4}{24} \left(\nabla^2 - \frac{R}{6} \right) \left(\frac{3\pi}{GN^2R} - \frac{1}{4} - \frac{\pi\alpha}{4N^2} \right) h_{\omega\sigma}^{(0)} \right\}. \quad (3.23)$$

Using (3.17) for \hat{h} and the determination of $h^{(4)}$ in terms of $h^{(0)}$ from the bulk solution, this expression can be written again as a quadratic functional of $h^{(0)}$:

$$S^{(2)}[h^{(0)}] = \int d^4x \sqrt{g^{(0)}} \int d^4y \sqrt{g^{(0)}} h^{(0)\mu\nu}(x) \mathcal{F}_{\mu\nu\omega\sigma}(\nabla^2, \bar{R})[x, y] h^{(0)\omega\sigma}(y) \quad (3.24)$$

where \mathcal{F} is the same functional which gives the equation of motion (3.22), as it is clear by varying (3.24) with respect to $h^{(0)\mu\nu}$. The quantity $\mathcal{F}_{\mu\nu\omega\sigma}$ is the inverse propagator of the induced boundary gravity tensor fluctuations $h_{\omega\sigma}^{(0)}$:

$$\mathcal{F}_{\mu\nu\omega\sigma} \equiv \frac{1}{\sqrt{g^{(0)}(x)}} \frac{1}{\sqrt{g^{(0)}(y)}} \frac{\delta^2 S^{(2)}}{\delta h^{(0)\mu\nu}(x) \delta h^{(0)\omega\sigma}(y)} \quad (3.25)$$

Using the definition (2.38) in the quadratic action,

$$S^{(2)} = S_{\text{grav}}^{(2)} + S_{CFT}^{(2)}, \quad (3.26)$$

the right-hand side of equation (3.25) can be seen as the sum of two contributions, one from S_{grav} and one from S_{CFT} .

As S_{grav} is local (it is quadratic in the boundary curvature), the first contribution is a *local* 4-derivative differential operator,

$$\frac{1}{\sqrt{g^{(0)}(x)}} \frac{1}{\sqrt{g^{(0)}(y)}} \frac{\delta^2 S_{\text{grav}}^{(2)}}{\delta h^{(0)\mu\nu} \delta h^{(0)\omega\sigma}} = \delta(x, y) O_{\mu\nu\rho\sigma}(\nabla^2, \bar{R}). \quad (3.27)$$

The part coming from the CFT is by definition the renormalized stress tensor correlator of the CFT:

$$\frac{1}{\sqrt{g^{(0)}(x)}} \frac{1}{\sqrt{g^{(0)}(y)}} \frac{\delta^2 S_{CFT}^{(2)}}{\delta h^{(0)\mu\nu} \delta h^{(0)\omega\sigma}} = -\langle T_{\mu\nu}(x) T_{\omega\sigma}(y) \rangle_{CFT}. \quad (3.28)$$

Therefore, the full inverse graviton propagator (3.25) has the form :

$$\mathcal{F}_{\mu\nu\omega\sigma} = \delta(x, y) O_{\mu\nu\rho\sigma}(\nabla^2, \bar{R}) - \langle T_{\mu\nu}(x) T_{\omega\sigma}(y) \rangle_{CFT}. \quad (3.29)$$

The non-local part is fully contained in the term $h^{(4)}$ in equation (3.23), and to determine it one has to solve the bulk radial equations.

We make a final comment on the appearance of the bulk AdS radius L in equation (3.23). As L is *not* a parameter of the 4d theory (only ML is, see equation (2.43), this quantity should not enter the full spectral operator $\mathcal{F}_{\mu\nu\rho\sigma}$. This is indeed the case: as will become obvious with the explicit computations in section 5, there is a similar logarithmic contribution to (3.23) coming from $h^{(4)}$, which will effectively replace $\log \mu L \rightarrow -2 \log(2\mu\sqrt{GN})$. These terms come from the variation of Weyl anomaly in the CFT, which has the form of the term with coefficient β in the gravitational action (see equation (2.5)). This implies that effectively β and μ will always appear in the combination:

$$\beta_{\text{eff}} = \beta - \frac{N^2}{\pi} \log(4\mu^2 GN^2). \quad (3.30)$$

4. The boundary scalar perturbation

In this section, we focus on scalar perturbations²⁴. In the special case of pure Einstein-Hilbert gravity, the scalar mode is not dynamical because it is constrained by the non-diagonal components of Einstein's equations. But this perturbation is rendered dynamical by the higher curvature terms in the 4d gravitational action.²⁵

In the present setup, where gravity lives on the boundary of AdS_5 , the scalar mode exists only on the boundary because only tensor perturbations are dynamical in the bulk (see e.g. [58]) as the trace of the energy-momentum tensor has trivial dynamics in a CFT.

4.1 Gauge fixing

To study the dynamics of this boundary scalar mode, we define boundary metric perturbations:

$$ds_4^2 = g_{\omega\sigma}^{(0)} dx^\omega dx^\sigma = (\bar{\zeta}_{\omega\sigma} + \delta\zeta_{\omega\sigma}^b) dx^\omega dx^\sigma, \quad (4.1)$$

where $\bar{\zeta}_{\omega\sigma}$ is the background metric (flat, dS or AdS) defined in 2.4 and $\delta\zeta_{\omega\sigma}^b$ is a perturbation which, unlike the general perturbation in equation (3.3), depends only on the slice coordinates x^μ .

The decomposition (3.7) still applies, and the boundary gauge transformations are:

$$\delta\zeta_{\omega\sigma}^b \rightarrow \delta\zeta_{\omega\sigma}^b + 2\hat{\nabla}_{(\omega}\xi_{\sigma)}. \quad (4.2)$$

One can do a gauge transformation to eliminate the transverse and longitudinal vector components, by choosing ξ_b in (3.4) to be:

$$\xi_\sigma = -\chi_\sigma - \frac{1}{2}\partial_\sigma\phi. \quad (4.3)$$

²⁴Here by scalar we mean with respect to the slice isometry group.

²⁵If the QFT is not conformal, then the coupling of the QFT to gravity will also contribute to the scalar dynamics via the two-point function of the trace of the energy-momentum tensor.

Keeping only the scalar mode, one is left with:

$$\delta\zeta_{\omega\sigma}^b = \psi \bar{\zeta}_{\omega\sigma}. \quad (4.4)$$

Equation (4.4) is the definition of the scalar perturbation, and we study its dynamics in the following subsections.

4.2 Scalar equation of motion

The classical equations of motion for ψ are obtained by linearizing the Einstein equation (2.6), which we rewrite here for convenience:

$$0 = E_{\omega\sigma}[g^{(0)}] \equiv -\frac{16\pi G}{\sqrt{g^{(0)}}} \frac{\delta S[g^{(0)}]}{\delta g^{(0)\omega\sigma}} \quad (4.5)$$

$$= R_{\omega\sigma} - \frac{1}{2}Rg_{\omega\sigma}^{(0)} + \Lambda g_{\omega\sigma}^{(0)} + 8\pi G({}^{(\alpha)}H_{\omega\sigma} + {}^{(\beta)}H_{\omega\sigma}) - 8\pi G \langle T_{\omega\sigma} \rangle, \quad (4.6)$$

where quadratic curvature terms ${}^{(\alpha)}H_{\omega\sigma}$, ${}^{(\beta)}H_{\omega\sigma}$ are defined in (2.7) (2.8) and the CFT stress tensor is given in (2.41). The equation of motion for ψ is obtained by linearizing $E_{\omega\sigma}[g^{(0)}]$ around $E_{\omega\sigma}[\bar{\zeta}]$. Linear and quadratic curvature terms are linearized using the definitions (4.1-4.4). However, to obtain the CFT stress tensor, one needs to solve the bulk equations. Nevertheless, its trace (2.42) and its divergence (which is zero) are fully constrained by the boundary geometrical tensors. Hence, one can take a shortcut and perturb the trace of Einstein's equation. It will then be convenient to define the trace of the generalized Einstein tensor (4.5) as

$$E[g^{(0)}] \equiv g^{(0)\omega\sigma} E_{\omega\sigma}[g^{(0)}]. \quad (4.7)$$

Then, the full, non-linear, traced Einstein equation is given by

$$0 = E[g^{(0)}] = -R + 4\Lambda - \frac{\alpha G}{4}\square R - \frac{GN^2}{4\pi} \left(R^{\omega\sigma} R_{\omega\sigma} - \frac{1}{3}R^2 \right), \quad (4.8)$$

where \square is the Laplacian operator ∇^2 applied to a scalar quantity. Equation (4.8) only contains scalar geometric quantities of the boundary. When evaluated on the background metric $\bar{\zeta}$, equation (4.8) reduces to (2.57).

The linearization of geometrical quantities which appear in (4.8) for an arbitrary perturbation (4.1) around $\bar{\zeta}$ are given by

$$\delta R = -(3\square + \bar{R})\psi, \quad \delta(R^{\omega\sigma}R_{\omega\sigma}) = \frac{\bar{R}}{2}\delta R. \quad (4.9)$$

We observe that these linearized scalar quantities depend on ψ only, due to $h^{(0)}$ being traceless. This leads to the linearized version of equation (4.8):

$$\left[1 + \frac{\alpha G}{4}\square - \frac{GN^2\bar{R}}{24\pi} \right] (3\square + \bar{R})\psi = 0. \quad (4.10)$$

Equation (4.10) is a linear *local* equation for $\psi(x)$. However, this equation is misleading, as only one of the two modes appearing in this equation is propagating. The correct computation of the scalar propagator comes from varying the action as in (4.5). In appendix K, we carefully derive the propagator of the single scalar propagating mode.

$$\mathcal{F}^{-1} = -64\pi G \left[\alpha G \bar{R} - 12 + \frac{GN^2 \bar{R}}{2\pi} \right]^{-1} \left\{ \frac{1}{\square + \frac{4}{G\alpha} - \frac{N^2 \bar{R}}{6\pi\alpha}} \right\}. \quad (4.11)$$

Both the position of the pole and the sign of the residue depend on the parameters of the model: there are regions in parameter space where the scalar can be a ghost or a tachyon, [52, 53]. In our scheme, there is no (scheme-dependent) $\square R$ contribution to the conformal anomaly, and therefore the kinetic term for this mode originates in the R^2 term of the gravity action.

There is also a second mode that is not propagating²⁶, as we show in Appendix K. It should be however stressed that the mode, although non-propagating, can affect the dynamics as a non-propagating mode, if boundary conditions are non-trivial, [20, 21]. In more general situations such a mode may become propagating. We expect this to happen if the quantum theory we couple gravity to is a QFT rather than a CFT. In such a case, the two-point function of the trace of the energy-momentum tensor contributes non-trivially to scalar modes, and a novel analysis needs to be done in the scalar sector. Another such example can be found in [99].

We now focus on the propagating scalar mode. We first discuss under which condition the scalar is ghostlike.

In any background, the scalar mode is a ghost if the residue of the pole has the “wrong” sign, the “right” sign being that of the pole of the massless spin-2 pole in pure gravity, which in our conventions is:

$$\mathcal{F}_{massless\,spin2}^{-1} = 32\pi G \frac{1}{\nabla^2 - \frac{\bar{R}}{6}}. \quad (4.12)$$

Therefore, the scalar mode is a ghost if the residue of (4.11) is positive, i.e:

$$\left(\frac{\pi\alpha}{N^2} + \frac{1}{2} \right) \frac{GN^2 \bar{R}}{12\pi} > 1 \quad \Rightarrow \quad \text{scalar mode is a ghost.} \quad (4.13)$$

This condition is valid both for positive and negative \bar{R} . In sections 8 and 9, we shall see that this inequality also appears in the context of the tensor sector, but not exactly for the same reasons.

It is useful to compare the equation of motion (4.10) to other discussions in the literature. If either $\bar{R} = 0$ or $N = 0$, the equation of motion (4.10) agrees with the $R + R^2$ modified gravity analysis of [85]. The first case, $N = 0$, corresponds to pure gravity with no CFT; the second case, $\bar{R} = 0$, corresponds to flat space, in which the boundary scalar mode decouples even in the presence of the CFT.

²⁶This was discussed in [8] for flat space with quadratic curvature terms only.

Neglecting the unphysical solution in (4.10), we are left with a single scalar mode satisfying a massive Klein-Gordon equation:

$$\square\psi = \frac{4}{G\alpha} \left[\frac{GN^2\bar{R}}{24\pi} - 1 \right] \psi. \quad (4.14)$$

4.3 Scalar tachyonic instabilities

We define a mode to be *tachyonic* if the associated wavefunction in coordinate space grows exponentially at late times. To carry out the analysis we have to specify the background, upon which the form of the mode solutions of equation (4.14) depends.

Minkowski

We label modes by the eigenvalue of the D'Alembertian operator,

$$\square\psi = -k^2\psi. \quad (4.15)$$

Then, equation (4.14) translates, for $\bar{R} = 0$, to:

$$k^2 = \frac{4}{G\alpha}. \quad (4.16)$$

The theory is tachyon-stable if the invariant four-momentum k^2 is timelike or null, $k^2 \leq 0$. In any other case, the solution to (4.15) will contain solutions which are real exponentials in time, and will generically diverge as $t \rightarrow +\infty$.

From equation (4.16) we conclude that:

$$\alpha > 0 \quad \Rightarrow \quad \text{scalar mode is tachyonic.} \quad (4.17)$$

Note that for $\alpha = 0$, the scalar mode is decoupled (at quadratic order).

anti-de Sitter

It is useful to parametrize the eigenvalues in terms of a complex “total momentum eigenvalue” ν^2 as follows:

$$\square\psi = -\frac{\bar{R}}{12} \left(\nu^2 - \frac{9}{4} \right) \psi, \quad (4.18)$$

Equation (4.14) then translates into

$$\nu^2 - \frac{9}{4} = \frac{48}{G\alpha\bar{R}} \left(1 - \frac{GN^2\bar{R}}{24\pi} \right), \quad (4.19)$$

In AdS, a free massive scalar ϕ satisfying $\square\phi = m^2\phi$ is tachyonic if it violates the BF bound, [93], which in 4 space-time dimensions means

$$m^2\chi^2 < -\frac{9}{4}, \quad (4.20)$$

where χ is the AdS length. Comparing with equation (4.18) with $\bar{R} = -12\chi^2$, violation of the BF bound is equivalent to:

$$\nu^2 < 0. \quad (4.21)$$

Using (4.19) we then conclude:

$$\frac{9}{4} - \frac{4}{\alpha G \chi^2} \left(1 + \frac{GN^2 \chi^2}{2\pi} \right) < 0 \quad \Rightarrow \quad \text{scalar mode is tachyonic.} \quad (4.22)$$

- For $\alpha = 0$ the scalar mode decouples as in the other cases.
- For pure gravity, in the absence of the CFT ($N^2 = 0$), the tachyonic condition (4.22) becomes

$$\frac{16}{\alpha G \chi^2} > 9. \quad (4.23)$$

In particular, this cannot be satisfied for $\alpha < 0$ (this is the opposite compared to the de Sitter case, as we shall see below).

de Sitter.

Since de Sitter has no global time-like killing vector, there may not be a universal (coordinate-independent) definition of what a tachyon is. We use the practical criterion that, *in a given coordinate system*, a tachyon is a mode whose amplitude diverges exponentially at late times. We establish this criterion in the three most widely used cases, i.e. Poincaré coordinates (covering the expanding (or cosmological) patch), global coordinates, and static coordinates (covering the static patch).

We use the same parametrization (4.18) of the D'Alembertian eigenvalues, where now $\bar{R} = 12H^2$.

Cosmological patch (Poincaré) coordinates.

In cosmological (Poincaré) coordinates, the de Sitter metric is given by

$$ds_{dS}^2 = \frac{1}{(H\tau)^2} \eta_{\omega\sigma} dx^\omega dx^\sigma = -dt^2 + e^{2Ht} \eta_{\omega\sigma} dx^\omega dx^\sigma, \quad \bar{R} = 12H^2, \quad (4.24)$$

where $\tau = \frac{e^{-Ht}}{H}$ is the conformal time. $\tau \rightarrow 0$ or $t \rightarrow +\infty$ is the future boundary of dS, \mathcal{I}^+ . $\tau \rightarrow +\infty$ or $t \rightarrow -\infty$ is a past horizon that touches the past boundary of dS, \mathcal{I}^- at one point.

The solutions of Eq. (4.18) are given in terms of Bessel functions (see for example [74]):

$$\psi = (H\tau)^{\frac{3}{2}} J_{\pm\nu}(\tau p) \sim e^{Ht(\pm\nu-3/2)}, \quad , t \rightarrow +\infty (\tau \rightarrow 0) \quad (4.25)$$

where $p \equiv \sqrt{\delta_{ij} p^i p^j}$ is the norm of the 3-dimensional Fourier momentum in the spatial directions. At the far past horizon ($\tau \rightarrow +\infty$) one should impose infalling boundary conditions for the bulk wave-function, i.e. a Hankel function. This correspond both to the retarded correlator in the holographic calculation, and to picking the Bunch-Davis vacuum.

Both solutions (4.25) are bounded as $\tau \rightarrow 0$ if :

$$|\text{Re}(\nu)| \leq 3/2. \quad (4.26)$$

Defining a tachyon as a mode which grows exponentially in time, equation (4.19) then translates into the statement²⁷:

$$\frac{1}{\alpha} \left(1 - \frac{GN^2 H^2}{2\pi} \right) > 0 \quad \Rightarrow \quad \text{scalar mode is tachyonic.} \quad (4.27)$$

By inserting equation (4.19) into the exponent of (4.25), we obtain the “decay rate” Γ of de Sitter due to the tachyon instability:

$$\Gamma = H \left[\sqrt{\frac{9}{4} + \frac{4\pi}{GN^2 H^2 \tilde{\alpha}} \left(1 - \frac{GN^2 H^2}{2\pi} \right)} - \frac{3}{2} \right], \quad (4.28)$$

which is real and positive if we are in the tachyonic regime (4.27).

We now discuss a few special cases.

- As in flat space, if $\alpha = 0$, the scalar mode is non-propagating.
- The special case $GN^2 H^2 = 4\pi$ corresponds to a vanishing 4d cosmological constant $\Lambda = 0$ (by equation (2.57)). This is the case studied in [58]. We find, in agreement with that work, that scalar tachyonic instabilities occur for $\alpha < 0$. This also includes the homogeneous scalar mode from the original Starobinsky model [52, 53].
- In the absence of the CFT, i.e. for $N^2 = 0$, de Sitter is tachyon-unstable in the scalar sector for $\alpha > 0$. This is the opposite sign compared to the previous paragraph case. There is no contradiction here, since (2.57) shows that de Sitter is not a solution when both Λ and N^2 vanish.

Global de Sitter coordinates

In global coordinates, the de Sitter metric reads:

$$ds_{dS}^2 = H^2 (-dT^2 + \cosh^2 T d\Omega^2) \quad (4.29)$$

where $-\infty < T < +\infty$ and $d\Omega^2$ is the metric on the unit 3-sphere. As their name suggests, these coordinates cover the entirety of dS space. $T \rightarrow -\infty$ is the past dS boundary, \mathcal{I}^- and $T \rightarrow +\infty$ is the future dS boundary, \mathcal{I}^+ .

At late times $T \rightarrow \infty$, this metric looks like the metric (4.24) with $t \rightarrow HT$, except for the fact that Euclidean 3-space is replaced by a sphere. Therefore, the solutions of the D’Alembert equation at late times will again take the form (4.25), with p^2 now appropriately quantized. Consequently, the condition that the solution diverges at late time is the same in global coordinates as in cosmological coordinates, namely (4.26), leading again to (4.27).

The difference with respect to the cosmological patch is that now one is free to chose any solution at the past boundary, and this defines different quantum states in de Sitter. Our calculation translates into selecting a dS-invariant state.

²⁷In an expanding background such a mode is still ok to have around as long as the growth rate is much smaller than the Hubble time, i.e. $|Re(\nu)| - 3/2 \ll 1$. In this case one can say that de Sitter space is unstable but long-lived.

Static Patch coordinates

The static patch of de Sitter is described by the metric:

$$ds^2 = -(1 - H^2 r^2) dt^2 + \frac{dr^2}{1 - Hr^2} + r^2 d\Omega_2^2 \quad (4.30)$$

where $0 < r < H^{-1}$ and $d\Omega^2$ is the metric on the unit 2-sphere. This metric contains only a single point from each of the $\mathcal{I}^+, \mathcal{I}^-$.

This metric has a (cosmological) horizon at $r_h = H^{-1}$, where one should impose infalling²⁸ or normalizable boundary conditions for the wave-function, in addition to regularity at the origin $r = 0$.

The calculation of the spectrum of the de Sitter D'Alembertian with these boundary condition results in obtaining the static patch quasi-normal modes, with time dependence $e^{-i\omega t}$. The spectrum of quasi-normal frequencies for a scalar field of mass $m^2 = -H^2(\nu^2 - 3/2)$ can be found for example in [100], and reads:

$$\omega_{n,l} = -iH \left(l + 2n + \frac{3}{2} \pm \nu \right), \quad (4.31)$$

where l and n are non-negative integers. Stability requires all the quasi-normal frequencies to lie in the lower complex plane (so that the time dependence $e^{-i\omega t}$ is exponentially damped at late times). The most stringent requirement occurs for $l = 0, n = 0$, and it translates into $|Re(\nu)| < 3/2$, i.e. the same condition (4.26) we found in cosmological and global coordinates.

This establishes the validity of the the condition (4.27) about the tachyonic (in)stability of scalar modes in the static patch of de Sitter as well.

5. The spin-two spectral equations

We now move to tensor perturbations $h_{\omega\sigma}^{(0)}$ defined in (3.25). The linearized Einstein equation (3.21) contains $h^{(4)}$, which can only be specified by solving the perturbation equations in the bulk. This section is devoted to expressing $h^{(4)}$ in terms of the boundary perturbation $h^{(0)}$ by solving the bulk tensor equation (3.11). This has to be done separately for each slice geometry (flat, positive and negative curvature). We treat each case in a separate subsection.

5.1 Flat-slicing

The bulk equation of motion for the tensor mode (3.11) simplifies significantly in flat slicing coordinates. First, one can write the bulk metric as a conformally flat space by defining the usual Poincaré coordinate Z as

$$Z \equiv e^{-u} = \sqrt{\rho}. \quad (5.1)$$

²⁸This way, the holographic correlator is fixed to be the retarded one

The perturbed bulk metric (3.3) in which we only keep the propagating tensor $h_{\omega\sigma}$ is then written as

$$ds_5^2 = \frac{1}{Z^2} [L^2 dZ^2 + (\eta_{\omega\sigma} + h_{\omega\sigma}) dx^\omega dx^\sigma]. \quad (5.2)$$

The bulk equation of motion (3.11) describes the dynamics of a massless graviton in AdS. In flat slicing coordinates (5.2), we can insert $a = e^u$ into (3.12), which boils down to the massless scalar equation

$$\square_5 h_{\omega\sigma} = 0, \quad (5.3)$$

where \square_5 is the *AdS* scalar Laplacian in Poincaré coordinates (2.47), given by

$$L^2 \square_5 = Z^2 (\partial_Z^2 + L^2 \eta^{\kappa\lambda} \partial_\kappa \partial_\lambda) - 3Z \partial_Z. \quad (5.4)$$

Now the strategy is to search for separable solutions, which we write as

$$h_{\omega\sigma}(Z, x) = F(Z, k) \tilde{h}_{\omega\sigma}^{(0)}(x, k), \quad (5.5)$$

where $\tilde{h}^{(0)}$ solves the eigenvalue equation parametrized by k^2 as

$$\partial^\sigma \partial_\sigma \tilde{h}_{\omega\kappa}^{(0)} = -k^2 \tilde{h}_{\omega\kappa}^{(0)} \equiv (m_2)^2 \tilde{h}_{\omega\kappa}^{(0)}, \quad (5.6)$$

and $(m_2)^2$ can be a complex number in general.

The second equation is an ordinary differential equation for $F(Z, k)$,

$$(Z^2 \partial_Z^2 - 3Z \partial_Z - k^2 L^2 Z^2) F(Z, k) = 0. \quad (5.7)$$

Note that, ultimately, we want to write an equation for the boundary tensor perturbation of the form (3.22) in Fourier space, with ∇^2 replaced by $-k^2$. The solution will be the physical mass² of a propagating 4d mode. As the solutions of this equation may be complex, we must allow for complex values of k^2 beyond the usual choices of timelike ($k^2 < 0$) and spacelike ($k^2 > 0$) momentum one obtains for real wavenumbers. With this caveat, it is now convenient to write (5.7) as:

$$\left[y^2 \frac{d^2}{dy^2} - y^2 - 3y \frac{d}{dy} \right] F(y) = 0, \quad y \equiv LkZ. \quad (5.8)$$

where we define k , for any complex k^2 outside of the negative real axis, as the complex root of k^2 with *positive* real part²⁹ and with a slight abuse of notation, we have replaced $F(Z, k)$ by $F(y)$.

We now solve the equations for $\tilde{h}^{(0)}$ (5.6) and for F (5.8). First, the solution of (5.6) are the Fourier modes :

$$\tilde{h}_{\omega\kappa}^{(0)}(k^\sigma) = e^{\pm i k^\sigma x_\sigma} = e^{\pm i(-\omega t + \mathbf{k} \cdot \mathbf{x})}, \quad \mathbf{k} \in \mathbb{R}^3, \quad \omega \equiv \sqrt{-k^2 + \mathbf{k}^2}. \quad (5.9)$$

²⁹This prescription is enough to identify tachyonic modes, for which $Re(k) \neq 0$. Instead, real negative k^2 corresponds to non-tachyonic propagating particles, and as usual, their propagator needs a further prescription. We use the analytic continuation of the results to purely imaginary values of k , which corresponds to taking the retarded stress tensor 2-point function .

For a non-negative eigenvalue k^2 , modes with $|\mathbf{k}| < |k|$ will necessarily feature an imaginary part in ω and one of the two solutions in (5.9) will diverge with time. This is the usual tachyon instability for flat space, which occurs for massive Klein-Gordon equations with negative mass square, and more generally it persists also for a complex mass. Therefore, the condition that a mode characterised by k^2 is non-tachyonic is:

$$\text{Re}(k) = 0. \quad (5.10)$$

where, as above, we have defined k as the complex root of k^2 with positive real part³⁰.

Equation (5.8) is solved by modified Bessel functions,

$$F(y) = y^2(\lambda_1 K_2(y) + \lambda_2 I_2(y)). \quad (5.11)$$

We must impose that the solution (5.11) is regular at the horizon $Z \rightarrow +\infty$. This requires $\lambda_2 = 0$ because in this limit $I_2(y) \sim \exp[kLZ]$ and by definition $\text{Re}(k) > 0$. The remaining solution $K_2(y)$ is a vanishing exponential at $Z \rightarrow +\infty$.

We fix the remaining parameter λ_1 by choosing the normalization at the AdS₅ boundary $Z = 0$ so that:

$$F(Z = 0) = 1. \quad (5.12)$$

This way, the solution (5.5) for the bulk tensor perturbation $h_{\omega\sigma}(x, Z)$ coincides at $Z = 0$ with the boundary tensor mode $h_{\omega\sigma}^{(0)}$ defined in the FG expansion (3.13). For this reason, the leading term $\tilde{h}_{\omega\sigma}^{(0)}$ of $h_{\omega\sigma}$ in (5.5) is identified as the Fourier mode of the leading term in the Fefferman-Graham expansion (3.13) which was defined as $h_{\omega\sigma}^{(0)}$. We drop the tilde from now on.

For small y , the Bessel function K_2 behaves as:

$$K_2(2y) \underset{y \rightarrow 0}{=} \frac{1}{2} \left\{ y^{-2} - 1 + \frac{3}{4}y^2 - y^2 [\gamma_E + \log(y)] \right\} + \mathcal{O}(y^4), \quad (5.13)$$

where γ_E is the Euler-Mascheroni constant. Then, equation (5.12) fixes $\lambda_1 = 1/2$ in (5.11).

Having completely fixed $F(Z, k)$, we can read-off $h_{\omega\sigma}^{(4)}$ and $\hat{h}_{\omega\sigma}$ from its near-boundary expansion, (5.13) and (5.5) and compare with the corresponding terms in equation (3.13), recalling that $Z = \sqrt{\rho}$. We find:

$$h_{\omega\kappa}^{(2)} = - \left(\frac{kL}{2} \right)^2 h_{\omega\kappa}^{(0)}, \quad (5.14a)$$

$$h_{\omega\kappa}^{(4)} = \left(\frac{kL}{2} \right)^4 \left[\frac{3}{4} - \gamma_E - \log \left(\frac{kL}{2} \right) \right] h_{\omega\kappa}^{(0)}, \quad (5.14b)$$

$$\hat{h}_{\omega\kappa} = - \frac{1}{2} \left(\frac{kL}{2} \right)^4 h_{\omega\kappa}^{(0)}. \quad (5.14c)$$

The terms $h_{\omega\kappa}^{(2)}$ and $\hat{h}_{\omega\kappa}$ agree with the perturbative solutions of the bulk Einstein equation (B.5) that are given in appendix B by (B.6) and (B.7). To perform this comparison and

³⁰This is simply a convention since the equation has a symmetry in $k \rightarrow -k$.

check that they agree, it is enough to linearize $g_{\omega\kappa}^{(2)}$ (B.6) and $\hat{g}_{\omega\kappa}$ (B.7) with respect to the transverse traceless perturbation $h_{\omega\sigma}^{(0)}$.

The linearization of the stress tensor (2.41) around a flat background for the tensor perturbation is given by³¹:

$$\delta_h \langle T_{\omega\kappa} \rangle = \frac{N^2}{2\pi^2 L^4} \left[h_{\omega\kappa}^{(4)} + (1 - 2 \log \mu L) \hat{h}_{\omega\kappa} \right]. \quad (5.15)$$

We can use the bulk solutions (5.14) into (5.15), to obtain the perturbed stress-tensor in terms of h^0 alone:

$$\delta_h \langle T_{\omega\kappa} \rangle = \frac{N^2}{2\pi^2} \left(\frac{k}{2} \right)^4 \left[\frac{1}{4} - \gamma_E - \log \left(\frac{k}{2\mu} \right) \right] h_{\omega\kappa}^{(0)}. \quad (5.16)$$

As a final step, inserting the expressions (5.14) in (3.21) we obtain the linearized Einstein equation specialized to a flat background, in the form of an equation for $h^{(0)}$ alone:

$$\frac{N^2}{64\pi^2} k^2 Q_{\text{flat}}(k) h_{\omega\sigma}^{(0)} = 0, \quad (5.17)$$

where

$$Q_{\text{flat}}(k) \equiv \left\{ -\frac{2\pi}{GN^2} + k^2 \left[\frac{1}{4} - \gamma_E - \log \left(\frac{k}{2\mu} \right) - \frac{1}{2} \frac{\pi\beta}{N^2} \right] \right\}. \quad (5.18)$$

From (5.18), as anticipated in Section 3, we can observe that the contributions from the renormalization scale μ coming from the CFT and the quadratic curvature term proportional to β combine into the parameter β_{eff} given in equation (3.30). For convenience, we also define

$$\tilde{\beta}_{\text{eff}} \equiv \frac{\pi\beta_{\text{eff}}}{N^2}. \quad (5.19)$$

The spectral equation (5.17) is then written as

$$Q_{\text{flat}}(k) \equiv \left\{ -\frac{2\pi}{GN^2} + \frac{k^2}{2} \left[\frac{1}{2} - 2\gamma_E - \log(GN^2 k^2) - \tilde{\beta}_{\text{eff}} \right] \right\}. \quad (5.20)$$

The quantity multiplying $h^{(0)}$ in (5.17) is the inverse propagator (3.25) for a flat space-time. Its expression is given by³²:

$$\mathcal{F}_{\text{flat}}(k) = \frac{N^2}{64\pi^2} k^2 Q_{\text{flat}}(k). \quad (5.21)$$

Non-trivial solutions ($h_{\omega\sigma}^{(0)} \neq 0$) to the equation of motion (5.17) correspond to the propagating momentum modes k of the boundary perturbation $h^{(0)}$ and are found by solving the spectral equation

$$k^2 Q_{\text{flat}}(k) = 0. \quad (5.22)$$

³¹The term $h^{(2)}$ does not contribute in (5.15) because it always appears in the CFT stress tensor (2.41) multiplied by $g^{(2)}[\bar{c}]$, which vanishes on a flat background.

³²For the overall coefficient in this expression, see Appendix J.

Solutions of this equation are the poles of the propagator $\mathcal{F}_{\text{flat}}^{-1}$. An obvious solution to that equation is the massless mode $k^2 = 0$ which is present in pure Einstein-Hilbert gravity. “Exotic” Modes with $k^2 \neq 0$ satisfy:

$$1 = \frac{GN^2 k^2}{4\pi} \left(\frac{1}{2} - 2\gamma_E - \log(GN^2 k^2) - \tilde{\beta}_{\text{eff}} \right). \quad (5.23)$$

The only solutions which are non-tachyonic are those for which $k^2 < 0$. The absence of tachyon-instabilities of flat space is then equivalent to the absence of solutions k to (5.23) with a non-zero real part. We study the existence of such unstable solutions in section 7.

5.2 dS-slicing

We now consider the CFT on de Sitter and we turn to equation (3.12) applied to dS slicing coordinates (2.48). As a result, we obtain

$$\left\{ \partial_u^2 + 4 \coth u \partial_u + \frac{H^{-2} \hat{\nabla}^2 - 2}{\sinh^2 u} \right\} h_{\omega\sigma} = 0. \quad (5.24)$$

The operator inside curly brackets is similar to the expression of the Laplace operator of AdS_5 acting on scalars, in which case the numerator of the last term would be replaced by the 4-dimensional slice scalar Laplacian.

Similarly to the flat slicing case (5.5), we search for separable solutions of the form:

$$h_{\omega\sigma}(x, u) = F(u, \nu) \tilde{h}_{\omega\sigma}^{(0)}(x, \nu). \quad (5.25)$$

This results in two equations: the first one is an eigenvalue problem on the slice, which we write as:

$$(\hat{\nabla}^2 - 2H^2) \tilde{h}_{\omega\sigma}^{(0)} = -H^2 \left(\nu^2 - \frac{9}{4} \right) \tilde{h}_{\omega\sigma}^{(0)} \equiv (m_2)^2 \tilde{h}_{\omega\sigma}^{(0)}. \quad (5.26)$$

The second equation is an ODE in the radial direction:

$$\left\{ \frac{d^2}{du^2} + 4 \coth u \frac{d}{du} - \frac{\nu^2 - \frac{9}{4}}{\sinh^2 u} \right\} F(u, \nu) = 0. \quad (5.27)$$

The information about tachyonic instabilities is contained in the value of ν . As shown in Appendix G, and as it is pointed out in [58, 74], modes with

$$|\text{Re}(\nu)| > 3/2 \quad (5.28)$$

are tachyonic because (5.26) contains a solution which diverges with time (see appendix G for the details).

In pure 4d gravity, the only propagating mode would be the transverse-traceless graviton, which is a zero eigenvalue for the Lichnerowicz operator of de Sitter (the left-hand side of equation (5.26) and corresponds to $\nu = \pm 3/2$).

Turning on the CFT matter content and the quadratic curvature terms will allow for modes with different values of ν . These will be determined by solving the boundary spectral equation, which we derive below.

As in the flat case, to obtain the boundary spectral equation we have to solve the radial equation (5.27). The most general solution of (5.27) is a linear combination of two hypergeometric functions given by

$$F(u, \nu) = C_+ \tanh u^{\nu - \frac{3}{2}} {}_2F_1 \left[\frac{1}{2} \left(\nu - \frac{3}{2} \right), \frac{1}{2} \left(\nu - \frac{1}{2} \right); 1 + \nu; \tanh^2 u \right] + \\ + C_- \tanh u^{-\nu - \frac{3}{2}} {}_2F_1 \left[\frac{1}{2} \left(-\nu - \frac{3}{2} \right), \frac{1}{2} \left(-\nu - \frac{1}{2} \right); 1 - \nu; \tanh^2 u \right], \quad (5.29)$$

where C_{\pm} are integration constants. This solution may have a singularity at the horizon $u = 0$, depending on the real part of ν . As we show in appendix E, requiring the solution (5.29) to be normalizable at $u = 0$ gives the following constraints :

- If $\text{Re}(\nu) > 0$, we need to set $C_- = 0$ for normalizability at $u = 0$.
- If $\text{Re}(\nu) < 0$, we need to set $C_+ = 0$ for normalizability at $u = 0$.
- If $\text{Re}(\nu) = 0$, both solutions oscillate at the horizon $u = 0$.

Since the problem (5.27) is symmetric in $\nu \leftrightarrow -\nu$, we can choose $\text{Re}(\nu) \geq 0$ without loss of generality. In this case, the most general regular solution at $u = 0$ is the one with $C_- = 0$. The case where ν is imaginary lies in the stable region (5.28) and needs a further prescription (e.g. infalling boundary conditions). We shall define the spectral function by analytic continuation to purely imaginary ν .

We fix the normalization of F by imposing that in the UV, at $u \rightarrow +\infty$:

$$F(u, \nu) \xrightarrow{u \rightarrow +\infty} 1. \quad (5.30)$$

This condition ensures that $\tilde{h}_{\omega\sigma}^{(0)}$ defined in (5.25) identifies with the leading term $h_{\omega\sigma}^{(0)}$ of the Fefferman-Graham expansion (3.13). From now on, we drop the tilde on $h^{(0)}$ although it only represents a single mode ν (5.26).

Using Gauss' hypergeometric theorem

$${}_2F_1 [a, b; c; 1] = \frac{\Gamma(c)\Gamma(c-a-b)}{\Gamma(c-a)\Gamma(c-b)}, \quad (5.31)$$

valid for $\text{Re}(c) > \text{Re}(a+b)$, the boundary condition (5.30) fixes the value of the integration constant to

$$C_+ = \frac{\Gamma\left(\frac{5}{2} + \nu\right) \sqrt{\pi} 2^{-\nu - \frac{3}{2}}}{\Gamma(1 + \nu)}. \quad (5.32)$$

The near-boundary expansion of $F(u, \nu)$ can be obtained using a hypergeometric transformation (page 49 of [94]). It allows us to transform $F(u, \nu)$ into a power series of e^{-u} instead of $\tanh^2 u$ (hypergeometric functions are defined as a power series of their last argument). The first few terms of the result are given by

$$F(u, \nu) = 1 - e^{-2u} \left(\nu^2 - \frac{9}{4} \right) - e^{-4u} \left(\nu^2 - \frac{9}{4} \right) \left\{ 1 + \right.$$

$$+ \left(\nu^2 - \frac{1}{4} \right) \left[-u - \frac{3}{4} + \mathcal{H} \left(\nu - \frac{1}{2} \right) \right] \Big\} + \mathcal{O}(e^{-6u}), \quad (5.33)$$

where \mathcal{H} is the harmonic number function defined in terms of the Euler Gamma function, Γ as

$$\mathcal{H}(z) = \frac{\Gamma'(z+1)}{\Gamma(z+1)} + \gamma_E. \quad (5.34)$$

The terms in (5.33) are enough to read all of the Fefferman-Graham expansion (3.13) using the relation between positive u and ρ in tabular 2.53:

$$h_{\omega\sigma}^{(2)} = -h_{\omega\sigma}^{(0)} \left(\frac{LH}{2} \right)^2 \left(\nu^2 - \frac{9}{4} \right) \quad (5.35a)$$

$$h_{\omega\sigma}^{(4)} = -h_{\omega\sigma}^{(0)} \left(\frac{LH}{2} \right)^4 \left(\nu^2 - \frac{9}{4} \right) \left\{ 1 + \left(\nu^2 - \frac{1}{4} \right) \left[\log \left(\frac{LH}{2} \right) - \frac{3}{4} + \mathcal{H} \left(\nu - \frac{1}{2} \right) \right] \right\} \quad (5.35b)$$

$$\hat{h}_{\omega\sigma} = -\frac{h_{\omega\sigma}^{(0)}}{2} \left(\frac{LH}{2} \right)^4 \left(\nu^2 - \frac{9}{4} \right) \left(\nu^2 - \frac{1}{4} \right). \quad (5.35c)$$

As we already discussed for the flat slicing, $h^{(2)}$ and \hat{h} can be found using an independent method discussed in appendix B. This method consists in solving perturbatively the bulk Einstein equation at small values of the Fefferman-Graham coordinate ρ for an arbitrary boundary metric $g^{(0)}$. The solution for $g^{(2)}$ and \hat{g} , given in (B.6) and (B.7), can be linearized with respect to $h^{(0)}$ to obtain the same result as (5.35a) and (5.35c) using the formulae (3.15). However, this alternative method does not determine $h^{(4)}$ in terms of $h^{(0)}$, but only its trace and divergence.

Inserting (5.35b)-(5.35c) into the linearized Einstein equation for the tensor mode (3.21), we find the equation of motion of the boundary spin-2 perturbation in momentum space given by

$$\frac{N^2 H^4}{64\pi^2} \left(\nu^2 - \frac{9}{4} \right) Q_{dS}(\nu) h_{\omega\sigma}^{(0)} = 0, \quad (5.36)$$

where

$$Q_{dS}(\nu) \equiv 1 - \frac{2\pi}{GN^2 H^2} + 2\tilde{\alpha} - \frac{1}{2} \left(\nu^2 - \frac{1}{4} \right) \left[\log(GN^2 H^2) - \frac{1}{2} + 2\mathcal{H}(\nu - 1/2) + \tilde{\beta}_{\text{eff}} \right], \quad (5.37)$$

$$\text{Re}(\nu) > 0,$$

where, as in flat space, we have combined the contributions from μ and β into a single parameter $\tilde{\beta}_{\text{eff}}$ defined via equations (3.30) and (5.19). We have also defined the parameter $\tilde{\alpha}$ as

$$\tilde{\alpha} \equiv \frac{\pi\alpha}{N^2}. \quad (5.38)$$

From now on, we shall always refer to the new quadratic curvature coefficients $\tilde{\alpha}$ and $\tilde{\beta}_{\text{eff}}$, except in subsection 6 where we set $N = 0$ in which case these new quantities become ill-defined.

The inverse spin-2 propagator defined in (3.25) is then given by

$$\mathcal{F}_{\text{dS}}(\nu) = \frac{N^2 H^4}{64\pi^2} \left(\nu^2 - \frac{9}{4} \right) Q_{\text{dS}}(\nu), \quad \text{Re}(\nu) > 0. \quad (5.39)$$

The overall coefficient of (5.39) is obtained in appendix J. The expression for Q_{dS} given in (5.37) is only valid for positive real parts of ν because we chose $C_- = 0$ for normalizability of the bulk solution (5.29) at $u = 0$. By symmetry of the bulk equation (5.27) in $\nu \leftrightarrow -\nu$, and in $\nu \leftrightarrow \nu^*$, the propagator $\mathcal{F}_{\text{dS}}(\nu)$ must also obey the same symmetries. The combination of these two symmetries implies that both the real and imaginary axes of ν are axes of symmetry for \mathcal{F}_{dS} . As a consequence, the inverse propagator for $\text{Re}(\nu) < 0$ is obtained by replacing $\nu \rightarrow -\nu$ in (5.37).

Each value of $\nu \in \mathbb{C}$ solving equation (5.36) is a pole of the 2-point function \mathcal{F}_{dS} and corresponds to a propagating mode. The positions and residues of these poles depend on the Hubble rate H of the boundary metric $\bar{\zeta}_{\omega\sigma}$ (2.46), the quadratic curvature coefficient $\tilde{\alpha}$ (5.38, 2.4), the scheme-dependent quadratic curvature coefficient $\tilde{\beta}_{\text{eff}}$ (5.19, 2.5) and the colour number N^2 .

The existence of tachyonic modes $|\text{Re}(\nu)| > 3/2$ will be studied in section 8.

5.3 AdS-slicing

Deriving the analogous spin-2 spectral equation (5.36) for AdS slicing follows the same steps as in the previous subsection, with the difference that now there are two UV boundaries, located at $u \rightarrow \pm\infty$, corresponding to two CFTs, [84].

The equation of motion for bulk metric perturbations (3.11) in AdS slicing (2.50) is

$$\left\{ \partial_u^2 + 4 \tanh u \partial_u + \frac{\chi^{-2} \hat{\nabla}^2 + 2}{\cosh^2 u} \right\} h_{\omega\sigma} = 0, \quad (5.40)$$

which is the analogue of equation (5.24). As it was done for dS slicing, we search for separable solutions of the form:

$$h_{\omega\sigma} = F(u, \nu) \tilde{h}_{\omega\sigma}^{(0)}(x, \nu). \quad (5.41)$$

We then separate equation (5.40) into an eigenvalue problem on the slice,

$$(\hat{\nabla}^2 + 2\chi^2) \tilde{h}_{\omega\sigma}^{(0)} = \chi^2 \left(\nu^2 - \frac{9}{4} \right) \tilde{h}_{\omega\sigma}^{(0)} \equiv (m_2)^2 \tilde{h}_{\omega\sigma}^{(0)}, \quad (5.42)$$

and a radial equation,

$$\left\{ \frac{d^2}{du^2} + 4 \tanh u \frac{d}{du} + \frac{\nu^2 - \frac{9}{4}}{\cosh^2 u} \right\} F(u, \nu) = 0. \quad (5.43)$$

Before solving the radial equation, we first comment on the role the eigenvalues ν play in the tachyonic instability. Note that the massless graviton is associated with the eigenvalue $\nu = \pm 3/2$. Unlike de Sitter, where the eigenvalue for a massless spin-2 graviton

separates between tachyonic and non-tachyonic modes, in AdS, some negative masses are non-tachyonic because they are allowed by the BF bound [93]. Thus, in AdS, the massless graviton does not saturate the stability bound.

For general complex ν , we study the stability of metric perturbations in the Poincaré patch of AdS in appendix H. To obtain a condition on the value of ν in the complex plane, we study the existence of normalizable tachyonic modes of AdS_4 for an arbitrary ν . As a result, such normalizable tachyonic modes exist if and only if

$$\nu^2 < 0. \tag{5.44}$$

When ν^2 is real, this statement reduces to the usual BF bound. Furthermore, we find that any complex ν with a non-zero real part is not tachyonic.

The most general solution of equation (5.43) is given by associated Legendre functions

$$F(u, \nu) = (\cosh u)^{-2} \left(\lambda_1 P_{\nu-1/2}^2(\tanh u) + \lambda_2 Q_{\nu-1/2}^2(\tanh u) \right). \tag{5.45}$$

Since AdS-slicing coordinates (2.50) do not contain a horizon at $u = 0$, tensor perturbations $h(u, \nu)$ can propagate in the whole bulk, between the two UV boundaries at $u \rightarrow \pm\infty$. As a consequence, we are left with a choice of boundary conditions that we did not have for dS-slicing (in which case we imposed normalizability at the horizon). In AdS-slicing coordinates, different linear combinations of the two independent bulk solutions (5.45) correspond to different combinations of sources coupled to the CFT on each boundary. In our case, the boundary source is $h_{\omega\sigma}^{(0)}$, the boundary metric perturbation. Therefore, generically, this setup corresponds to a bimetric theory.

One possible choice is that only the boundary metric at $u \rightarrow -\infty$ is chosen to be dynamical. Then, one should impose that on the other boundary, at $u \rightarrow +\infty$, the source term of boundary metric perturbation vanishes. Another possibility to have a single dynamical metric is to identify the two boundaries, which corresponds to imposing a \mathbb{Z}_2 symmetry $u \rightarrow -u$ on the solution. We consider each of these cases in the following two subsections.

The discussion above is relevant for a holographic CFT. For a generic CFT on AdS_4 , the two-point function of the energy-momentum tensor depends on boundary conditions. For the simplest boundary conditions, Neumann or Dirichlet, the two-point function of the energy-momentum tensor can be calculated by mapping it to flat space by a conformal transformation and then using the method of images. We shall not pursue this further in the present paper.

5.3.1 Dynamical gravity on one side

We choose to turn off leading (i.e. source-like) metric perturbations on the boundary at $u \rightarrow +\infty$. This corresponds to the boundary conditions:

$$F(u, \nu) \xrightarrow{u \rightarrow \pm\infty} \begin{cases} 2\lambda_2 & = 0, \\ \frac{4}{\pi}\lambda_1 \cos(\pi\nu) - 2\lambda_2 \sin(\pi\nu) & = 1, \end{cases} \tag{5.46}$$

such that $\tilde{h}^{(0)}$ (5.41) coincides with the leading term $h^{(0)}$ of the Fefferman-Graham expansion (3.13) at the $u \rightarrow -\infty$ side of the AdS_5 boundary. These conditions fix the coefficients in (5.45) as

$$\lambda_2 = 0, \quad (5.47)$$

$$\lambda_1 = \frac{\pi}{4 \cos(\pi\nu)}, \quad (5.48)$$

valid for $\nu \neq n + \frac{1}{2}$, $n \in \mathbb{Z}$. In the case where $\nu = n + \frac{1}{2}$, we still have the requirement that $\lambda_2 = 0$ but λ_1 is unconstrained.

The case of $\nu = n + 1/2$ is special because it corresponds to the spectrum of normalizable modes in AdS_5 , which can be seen from the asymptotic behaviour of Legendre functions in (I.21). Since λ_1 diverges in the limit $\nu \rightarrow n + 1/2$, this discrete series of modes correspond to poles of the stress-tensor propagator or zeros of the propagator for tensor metric perturbations. Therefore, they cannot be the solution of the spin-2 spectral equation. As a consequence, we can ignore them for the rest of the paper.

The unique solution (5.45) which satisfies the boundary conditions (5.46) can then be expanded near the dynamical boundary $u \rightarrow -\infty$. This expansion is given by

$$F(u, \nu) = 1 + \left(\nu^2 - \frac{9}{4}\right) \left\{ e^{2u} - e^{4u} \left[1 + \left(\nu^2 - \frac{1}{4}\right) \left(u - \frac{3}{4}\right) + \frac{1}{2} \mathcal{H}\left(\nu - \frac{1}{2}\right) + \frac{1}{2} \mathcal{H}\left(-\nu - \frac{1}{2}\right) \right] \right\} + \mathcal{O}(e^{6u}), \quad (5.49)$$

where \mathcal{H} is again the harmonic-number function defined in (5.34). To read-off the Fefferman-Graham terms of the spin-2 perturbation from (5.49), we need to replace u by the Fefferman-Graham coordinate given in 2.53 by

$$e^{2u} = \left(\frac{L\chi}{2}\right)^2 \rho. \quad (5.50)$$

Then, each term of the Fefferman-Graham expansion (3.13) can be identified from (5.49) as

$$h_{\omega\sigma}^{(2)} = h_{\omega\sigma}^{(0)} \left(\frac{L\chi}{2}\right)^2 \left(\nu^2 - \frac{9}{4}\right) \quad (5.51a)$$

$$h_{\omega\sigma}^{(4)} = -h_{\omega\sigma}^{(0)} \left(\frac{L\chi}{2}\right)^4 \left(\nu^2 - \frac{9}{4}\right) \left\{ 1 + \left(\nu^2 - \frac{1}{4}\right) \left[\log\left(\frac{L\chi}{2}\right) - \frac{3}{4} + \frac{1}{2} \mathcal{H}\left(-\frac{1}{2} - \nu\right) + \frac{1}{2} \mathcal{H}\left(-\frac{1}{2} - \nu\right) \right] \right\} \quad (5.51b)$$

$$\hat{h}_{\omega\sigma} = -\frac{h_{\omega\sigma}^{(0)}}{2} \left(\frac{L\chi}{2}\right)^4 \left(\nu^2 - \frac{9}{4}\right) \left(\nu^2 - \frac{1}{4}\right). \quad (5.51c)$$

The relation between the expansion of $h_{\omega\sigma}(\rho, x^\alpha)$ and $\delta_h g_{\omega\sigma}(\rho, x^\alpha)$ is given by (3.15). If we compare with the de Sitter slicing case (5.35), the analytic continuation $H^2 \rightarrow -\chi^2$ does not hold for $h_{\omega\sigma}^{(4)}$ given in AdS by (5.51b) and in dS by (5.35b). The only difference between the two resides in the combination of harmonic functions \mathcal{H} . For AdS (5.51b),

the combination is symmetric in $\nu \leftrightarrow -\nu$, which is not the case in de Sitter because the singularity at the horizon forced us to pick a sign for $\text{Re}(\nu)$ and break the \mathbb{Z}_2 symmetry in ν for the bulk solution (5.29).

Inserting the relations (5.51) into the linearized Einstein equation for the tensor perturbation (3.21), we obtain the spectral equation $h^{(0)}$:

$$\frac{N^2 \chi^4}{64\pi^2} \left(\nu^2 - \frac{9}{4} \right) Q_{(-)}(\nu) h_{\omega\sigma}^{(0)} = 0, \quad (5.52)$$

where

$$Q_{(-)}(\nu) = 1 + 2 \left(\frac{\pi}{GN^2 \chi^2} + \tilde{\alpha} \right) - \frac{1}{2}(\nu^2 - 1/4) \left[\tilde{\beta}_{\text{eff}} + \log(GN^2 \chi^2) - \frac{1}{2} + \mathcal{H} \left(-\frac{1}{2} - \nu \right) + \mathcal{H} \left(-\frac{1}{2} + \nu \right) \right]. \quad (5.53)$$

We have used $\tilde{\alpha}$ defined in (5.38) and $\tilde{\beta}_{\text{eff}}$ defined in (5.19). The inverse propagator for tensor perturbations is then given by³³:

$$\mathcal{F}_{(-)} = \frac{N^2 \chi^4}{64\pi^2} \left(\nu^2 - \frac{9}{4} \right) Q_{(-)}(\nu). \quad (5.54)$$

5.3.2 Symmetric boundary conditions

As an alternative way to couple AdS boundary gravity to the holographic sector, here we impose that the bulk tensor perturbation $h_{\alpha\beta}$ has equal sources $h^{(0)}$ on both boundaries $u \rightarrow \pm\infty$. This is implemented by the boundary condition:

$$F(u, \nu) \xrightarrow{u \rightarrow \pm\infty} \begin{cases} 2\lambda_2 & = 1, \\ \frac{4}{\pi}\lambda_1 \cos(\pi\nu) - 2\lambda_2 \sin(\pi\nu) & = 1. \end{cases} \quad (5.55)$$

As for the previous boundary conditions, the case where $\nu = n + 1/2$ where n is an integer leaves λ_1 unconstrained. However, we need to distinguish between the two following cases :

- If n is odd, $\lambda_2 = 1/2$ solves (5.55) and λ_1 is unconstrained. This constant can therefore be set to an arbitrary value while (5.55) still holds.
- If n is even, there is no solution for (5.55). Such modes are then forbidden in the symmetric case.

If ν is not a half-integer then the integration constants are given by

$$\lambda_2 = \frac{1}{2}, \quad (5.56)$$

$$\lambda_1 = \frac{\pi}{4} \left(\tan(\pi\nu) + \frac{1}{\cos(\pi\nu)} \right). \quad (5.57)$$

One can observe from (5.57) that the limit $\nu \rightarrow n + 1/2$ can possibly make $\lambda_1(\nu)$ diverge. As already discussed in the asymmetric case 5.3.1, these modes are the discrete spectrum of normalizable modes in AdS_5 . We again discuss the two cases :

³³The overall coefficient is determined in Appendix J

- If $\nu \rightarrow n+1/2$ with n even, then $\lambda_1(\nu)$ diverges. This limit corresponds to a pole of the stress-tensor correlator. Therefore, half-integer ν with even n , which are forbidden as discussed below (5.55), cannot be a solution to the spectral equation.
- If $\nu \rightarrow n+1/2$ with n odd, then $\lambda_1(\nu) \rightarrow 0$. As a reminder, $\lambda_1(\nu = n+1/2)$ can be set to an arbitrary value when n is odd. We can therefore extend λ_1 by continuity to half integers with odd n . Then, the solution (5.57) for $\lambda_1(\nu)$ is continuous at $\nu = n+1/2$, n odd, and we can include these half integers into our analysis while working with (5.57).

The solution for $F(u, \nu)$ given by (5.56) and (5.57) is then symmetric under $u \leftrightarrow -u$. Its behaviour near both sides of the boundary $u \rightarrow \pm\infty$ is obtained in appendix I, and the result is given by equation (I.26). We observe that the terms of the Fefferman-Graham expansion are all identical to (5.51) except $h_{\omega\sigma}^{(4)}$ which now reads:

$$h_{\omega\sigma}^{(4)} = -h_{\omega\sigma}^{(0)} \left(\nu^2 - \frac{9}{4} \right) \left[1 + \frac{1}{2} \left(\nu^2 - \frac{1}{4} \right) \left(2 \log \left(\frac{L\chi}{2} \right) + \frac{3}{2} + \mathcal{H}(\nu - 1/2) + \mathcal{H}(-\nu - 1/2) - \frac{\pi}{\cos \pi\nu} \right) \right]. \quad (5.58)$$

Inserting the bulk data (5.58) into the equation of motion (3.21) we obtain our final result for the spectral equation in AdS with symmetric boundary conditions:

$$\frac{N^2 \chi^4}{64\pi^2} \left(\nu^2 - \frac{9}{4} \right) Q_{\text{sym}}(\nu) h_{\omega\sigma}^{(0)} = 0, \quad (5.59)$$

where

$$Q_{\text{sym}}(\nu) = 1 + 2 \left(\frac{\pi}{GN^2 \chi^2} + \tilde{\alpha} \right) - \frac{1}{2} (\nu^2 - 1/4) \left[\tilde{\beta}_{\text{eff}+} + \log(GN^2 \chi^2) - \frac{1}{2} + \mathcal{H}(\nu - 1/2) + \mathcal{H}(-\nu - 1/2) - \frac{\pi}{\cos \pi\nu} \right]. \quad (5.60)$$

This expression is similar to the one obtained in the asymmetric case (5.53), except for the last term $\pi/\cos(\pi\nu)$. This term becomes negligible if ν is far from the real axis, as it decreases exponentially with the imaginary part of ν .

The inverse propagator for an AdS space-time with symmetric sources is then:

$$\mathcal{F}_{\text{sym}} = \frac{N^2 \chi^4}{64\pi^2} \left(\nu^2 - \frac{9}{4} \right) Q_{\text{sym}}(\nu). \quad (5.61)$$

5.4 Identifying ghosts from poles in the propagator

Ghost instabilities are determined from the residue of the poles of the propagator. Whether a mode is a ghost is determined by the sign of the residue of the pole in ν^2 : if it has the same sign as for the massless graviton in Einstein GR theory (on the same background), then the mode is healthy, otherwise, it is a ghost.

It is convenient to identify the residue from the derivative of $\mathcal{F}(\nu)$ with respect to the real part of ν : indeed using the holomorphic property of \mathcal{F} on the complex half-plane with positive real part, we have:

$$\mathcal{F}'(a + ib) = \left. \frac{\partial \mathcal{F}}{\partial a} \right|_{a+ib}. \quad (5.62)$$

By symmetry of $\mathcal{F}(\nu)$ under $\nu \leftrightarrow -\nu$, and by subtracting the Taylor expansion of \mathcal{F} close to a pole ν_0 with the expansion close to $-\nu_0$, one finds:

$$\frac{1}{\mathcal{F}(\nu)} \underset{\nu \rightarrow \nu_0}{=} \frac{\nu_0}{\mathcal{F}'(\nu_0)} \frac{1}{\nu^2 - \nu_0^2} + \mathcal{O}(1). \quad (5.63)$$

Therefore, the residue of the pole in ν^2 can be obtained as:

$$\text{Res}[\mathcal{F}^{-1}](\nu_0^2) \equiv \frac{\nu_0}{\mathcal{F}'(\nu_0)}. \quad (5.64)$$

In pure gravity, the sign of the residue of the massless spin-2 pole in de Sitter is negative in our conventions. Therefore, ghosts are defined to be poles with a residue which is not real and negative. It can be real and positive, or even complex. If $\mathcal{F}'(\nu_0) = 0$, then ν_0 is a higher order pole. In AdS, however, the massless spin-2 pole of Einstein-Hilbert gravity has a positive residue.

In flat space, ν has to be replaced by k in equation (5.64). The residue of a pole k_0 in the k^2 plane is related to $\mathcal{F}'_{\text{flat}}(k_0)$ as

$$\text{Res}[\mathcal{F}_{\text{flat}}^{-1}](k_0^2) \equiv \frac{k_0}{\mathcal{F}'(k_0)}. \quad (5.65)$$

In Einstein-Hilbert gravity, our conventions lead to a negative residue of the massless spin-2 pole. Positive and complex residues (5.65) will then be associated with ghost-like poles.

6. Tensor instabilities in pure gravity

Before we discuss the instabilities arising from tensor modes in the gravity coupled to the holographic CFT, we pause here to give a brief overview of the tensor instabilities in pure gravity with higher curvature terms, described by the action (2.2).

The spectral functions in pure gravity can be obtained simply by taking $N = 0$ in the expressions obtained in the previous section³⁴, namely equations (5.20-5.21) for flat space, (5.37-5.39) for de Sitter and (5.53-5.54) or (5.60-5.61) for Anti-de Sitter.

Minkowski

In the flat case, setting the $N = 0$ in $\mathcal{F}_{\text{flat}}$ (5.21) leads to:

$$\mathcal{F}_{\text{flat}} \underset{N=0}{=} -\frac{k^2}{64\pi} \left\{ \frac{2}{G} + \frac{\beta}{2} k^2 \right\}. \quad (6.1)$$

³⁴Even if the $N \rightarrow 0$ limit cannot be treated in holography, taking $N = 0$ in our setup is a quick way to decouple the bulk gravity theory from the boundary, and retrieve the results one would have obtained in a 4d modified gravity theory with Einstein-Hilbert plus quadratic curvature terms α and β given by the action (2.2).

The propagator is then a sum of two simple poles given by

$$\mathcal{F}_{\text{flat}}^{-1} = -32\pi G \left\{ \frac{1}{k^2} - \frac{1}{k^2 + \frac{4}{\beta G}} \right\}. \quad (6.2)$$

Therefore, the poles of the 2-point functions are the massless solutions $k^2 = 0$ and an additional massive solution,

$$k^2 = -\frac{4}{\beta G}. \quad (6.3)$$

If β is negative, the 4-momentum corresponding to this solution is space-like, which implies a tachyonic instability. Thus, when the CFT is removed, flat space is then tachyon-unstable for strictly negative β and tachyon-stable for positive β . As $\beta \rightarrow 0$ the massive mode decouples and one recovers Einstein gravity. These results agree with [15] concerning the stability of flat space with a quadratic curvature action. Such perturbations around Minkowski space were first derived in [85].

Note that, in our conventions, the residue of the massless mode is negative. As we have seen above, the massive pole could be tachyonic or not depending on the sign of β . However, it always corresponds to a ghost because its residue is positive for any β . This pole is the usual ghost of quadratic gravity theories [85, 8].

Note that, when the mass of the ghost is above the cut-off (which for pure gravity is the 4d Planck scale $G^{-1/2}$) our results are not trustworthy in the context of a low-energy effective field theory of gravity. This is the case for $|\beta| \lesssim 1$.

In conclusion, in pure gravity, flat space-time is tachyon-stable when $\beta > 0$ and ghost-unstable for any β , with the caveat that for $|\beta|$ small or of order unity the mass of the ghost is above the cutoff for the analysis to be trusted.

(anti-)de Sitter

First, we remark that (as shown in Appendix G), the criterion for tachyonic stability in de Sitter in the tensor sector can be reduced to the one in the scalar sector (it applies to the spatially transverse traceless tensors). Therefore, one can repeat the analysis we performed for the scalar mode in section 4.3, where we found that the condition for tachyonic stability is the same in global, cosmological and static dS coordinates, namely $|Re(\nu)| < 3/2$.

For de Sitter, the pure gravity spectral function is obtained by setting $N = 0$ in (5.39), which gives:

$$\mathcal{F}_{dS}(\nu) \stackrel{N=0}{=} -\frac{H^4}{64\pi} \left(\nu^2 - \frac{9}{4} \right) \left\{ \frac{2}{GH^2} - 2\alpha + \frac{\beta}{2} \left(\nu^2 - \frac{1}{4} \right) \right\}. \quad (6.4)$$

One simply needs to replace $H^2 \rightarrow -\chi^2$ to obtain the result for AdS, so we treat positive and negative curvature together.

The propagator can then be written as a sum of two poles,

$$\mathcal{F}_{dS}^{-1}(\nu) \stackrel{N=0}{=} -\frac{64\pi}{H^4} \left[\frac{2}{GH^2} - 2\alpha + \beta \right]^{-1} \left\{ \frac{1}{\nu^2 - \frac{9}{4}} - \frac{1}{\nu^2 - \frac{1}{4} + \frac{4}{\beta} \left(\frac{1}{GH^2} - \alpha \right)} \right\}. \quad (6.5)$$

The first pole is the massless graviton, which is the only propagating mode that remains for $\beta = 0$. If $\beta \neq 0$, the second pole is located at

$$\nu^2 = \frac{1}{4} + \frac{4}{\beta} \left(\alpha - \frac{1}{GH^2} \right). \quad (6.6)$$

This equation shows that the $\beta \rightarrow +\infty$ limit (while keeping α and GH^2 fixed) always makes a solution converge to $\nu = \pm \frac{1}{2}$. In the opposite limit $\beta \rightarrow 0$ this massive mode disappears and only the massless graviton remains.

Note that if $\beta = 0$, the factor in curly braces in (6.4) vanishes for:

$$\alpha = \frac{1}{GH^2}. \quad (6.7)$$

Therefore, in the $\beta = 0$ case, and for any value of α , there exists a special value of the curvature scale H such that the tensor mode has a vanishing quadratic kinetic term and therefore it is strongly coupled³⁵. In other words, the theory is strongly coupled for $\beta = 0$ and α and H related by (6.7).

From (6.4) we observe that zeros of \mathcal{F} correspond to real ν^2 . The de Sitter tachyon-stability condition (5.28) becomes $\nu^2 \leq 9/4$, while the anti-de Sitter condition (5.44) becomes $\nu^2 > 0$. In pure gravity, these conditions translate to

$$\frac{2}{\beta} \left(\alpha - \frac{1}{GH^2} \right) < 1 \quad \Rightarrow \quad \text{dS tachyon stable}, \quad (6.8)$$

and anti-de Sitter is tachyon-stable if

$$\frac{4}{\beta} \left(\alpha + \frac{1}{G\chi^2} \right) > -\frac{1}{4} \quad \Rightarrow \quad \text{AdS tachyon stable}. \quad (6.9)$$

We now turn to ghost instabilities, starting with de Sitter. When the prefactor in the square brackets of (6.5) is positive, then the massless pole located at $\nu^2 = 9/4$ has the same sign as the massless pole in pure gravity ($\alpha = \beta = 0$) and therefore it is not a ghost, whereas the massive pole represents a ghost. On the contrary, if the prefactor in square brackets is negative, then the massless pole is ghost-like and the massive pole becomes ghost-free. All in all, the higher derivative pure gravity theory always has a ghost, be it the massless graviton or the massive mode.

For AdS the conclusions are opposite: in our conventions, the massless graviton in pure Einstein gravity has positive residue in AdS, as can be seen by setting $\alpha = \beta = 0$ and replacing $H^2 \rightarrow -\chi^2$ in (6.5).

6.1 When are tensor ghosts light?

The discussion above holds if we take the spectral functions at face value. However, these conclusions can be trusted only when the poles lie within the validity of effective field

³⁵In such cases, there is a possibility of a Vainshtein-like mechanism operating. We do not know whether this has been investigated in this context.

theory, i.e. when the masses of the unstable modes are below the cut-off, which in pure gravity can be taken to be the Planck scale $M_p = (8\pi G)^{-1/2}$. For the same reasons, all the expressions above make sense in effective field theory if the curvature is sub-Planckian, i.e. if $GH^2 \ll 1$.

We shall verify when the unstable mode mass is sub-Planckian in the various cases.

- **Flat space.** By equation (6.3), the modulus of the massive pole in Planck units is roughly $G|m^2| = 4/|\beta|$. Therefore, we conclude that:

$$|\beta| \gg 1 \quad \Rightarrow \quad \text{flat space gravity has a light tensor ghost.} \quad (6.10)$$

If in addition $\beta < 0$, this is also a light tachyon.

- **de Sitter.** In this case, we have to distinguish two situations, depending on the sign of the prefactor in (6.5):

1. If $\beta - 2\alpha < -2/(GH^2)$, then the massless mode is a ghost, and it is by definition below the cut-off. Since $GH^2 \ll 1$, this requires either β very large and negative, or α very large and positive.
2. $\beta - 2\alpha > -2/(GH^2)$ then the massive mode is a ghost. This is the most “natural” situation, as it does not require extreme values of α and β . By equation (6.6) the modulus of its mass squared in Planck units is³⁶:

$$G|m_{ghost}^2| = \left| -2GH^2 + \frac{4}{\beta} (\alpha GH^2 - 1) \right|. \quad (6.11)$$

The ghost is sub-Planckian when the second term on the left-hand side is smaller than unity (since the first term GH^2 is always small in effective theory). For α not too large, this is the case if $|\beta| \gg 1$:

$$\alpha \sim O(1), |\beta| \gg 1 \Rightarrow \quad \text{de Sitter gravity has a light tensor ghost.} \quad (6.12)$$

All in all, we observe that for large $|\beta|$, there is *always* a light ghost in de Sitter (it may be massive, massless, or tachyonic).

- **anti-de Sitter.** For AdS, the situation is the same as for de Sitter (with $H^2 \rightarrow -\chi^2$), except that the role of points 1 and 2 above are exchanged:

1. If $\beta - 2\alpha > 2/(G\chi^2)$ then the massless pole is a ghost. Note that this is the generic situation for $O(1)$ values of α and β , since the right-hand side of that inequality is a small number.
2. If instead $\beta - 2\alpha < 2/(G\chi^2)$, then the ghost is the massive mode. Its mass in Planck units is, in modulus:

$$G|m_{ghost}^2| = \left| 2G\chi^2 - \frac{4}{\beta} (\alpha G\chi^2 + 1) \right|. \quad (6.13)$$

³⁶Recall that the mass is $H^2(\nu^2 - 9/4)$.

For the ghost to be sub-Planckian this again requires $\beta \gg 1$, but now this must be accompanied by a fine-tuning $\alpha \simeq \beta/2 \gg 1$ to ensure the ghost is the massive mode.

We conclude that *generically*, AdS higher-curvature gravity has a light tensor ghost, unless $\beta - 2\alpha < 2/(G\chi^2) \ll 1$.

7. Poles of the Minkowski spin-two propagator and stability

In this section, we analyse the flat-space spectral function found in section 5.1 and determine for which values of the parameters flat space-time are unstable under tensor perturbations.

All the information about the tachyonic instability is contained in the location of the poles of the propagator, i.e. the zeros of the spectral function (5.21). As we have explained in section 5.1, in our conventions, a zero of (5.21) at a value k with a non-zero real part corresponds to a tachyonic mode³⁷.

Ghost instabilities are determined by computing the residue of these poles. In particular, a pole is not a ghost if its residue is negative, as is the case for the massless pole of the propagator in pure gravity (6.2).

The spectral equation for non-trivial modes on Minkowski is given in equation (5.23), which we rewrite here for convenience:

$$1 = \frac{GN^2k^2}{4\pi} \left[\frac{1}{2} - 2\gamma_E - \log(GN^2k^2) - \tilde{\beta}_{\text{eff}} \right]. \quad (7.1)$$

As in our conventions we are taking $\text{Re}(k) > 0$, we can use the identity

$$\log(k^2) = 2 \log k. \quad (7.2)$$

Equation (5.23) can then be written in the simpler form:

$$X \log X = -a, \quad (7.3)$$

where X and a are defined as:

$$X \equiv GN^2k^2 \exp \left\{ -\frac{1}{2} + 2\gamma_E + \tilde{\beta}_{\text{eff}} \right\}, \quad a \equiv 4\pi e^{-\frac{1}{2} + 2\gamma_E + \tilde{\beta}_{\text{eff}}}. \quad (7.4)$$

The new variable X contains all information about tachyonic instabilities, the same way that k did. The stability condition (5.10) translates into

$$X < 0. \quad (7.5)$$

Our problem is now simply to solve (7.3) for X , which is a $W(-a)$ Lambert's function, containing two branches. As a result, one or at most two solutions exist for a complex X . To determine this, we write

$$X = xe^{i\theta} \quad (7.6)$$

³⁷Recall that, in terms of momenta of Fourier modes, k represents the square root of $k^2 = -(k^0)^2 + \mathbf{k}^2$ with positive real part.

and inject this expression into (7.3). Then (7.3) is equivalent to the two real equations

$$x\theta = a \sin \theta \quad , \quad \theta \cot \theta = -\log x \quad (7.7)$$

The stability condition (7.5) translates into $\theta = \pm\pi$. If a solution for any other value for θ exists, it corresponds to a tachyonic mode.

- First, we study the existence of purely real tachyonic solutions $k^2 > 0$, for which $\theta = 0$. This is the case which was considered in [58]. If $0 \leq a < e^{-1}$, equation (7.3) has two solutions (one with a larger mass than the other), which merge at $a = e^{-1}$. If on the other hand $a > e^{-1}$, there is no solution with $\theta = 0$. Using this property, we can write a condition on $\tilde{\beta}_{\text{eff}}$ such that flat space has two tachyonic modes with $k^2 > 0$:

$$\tilde{\beta}_{\text{eff}} \leq \tilde{\beta}_{\text{eff}}^{\text{merge}} \equiv -\log\left(4\pi e^{\frac{1}{2}+2\gamma_E}\right) \quad \Rightarrow \quad \text{Two tachyonic modes.} \quad (7.8)$$

When (7.8) is an equality, we observe a double pole located at $X = e^{-1}$. In k^2 space, this double pole is located at

$$GN^2k^2 = 4\pi. \quad (7.9)$$

- We now consider the general case $\theta \neq 0$. The imaginary and real parts of equation (7.3) give (7.7), that can be rewritten as

$$\log x = -\theta \cot \theta, \quad (7.10a)$$

$$e^{-\theta \cot \theta} = a \frac{\sin \theta}{\theta}, \quad (7.10b)$$

The number of solutions of (7.10b) depends on the values of a . Since $\theta \cot \theta < 1$ and $\frac{\sin \theta}{\theta} < 1$ for $\theta \neq 0$, we can conclude that solutions of (7.10b) with $\theta \neq 0$ exist only in the range:

$$a > e^{-1}. \quad (7.11)$$

These solutions are tachyonic as long as they do not move to the negative real axis $\theta = \pm\pi$. This occurs as $\tilde{\beta}_{\text{eff}} \rightarrow +\infty$: in this limit, the instability approaches the imaginary axis, corresponding to $k^2 < 0$. This was already noted in [58], and can be shown as follows: The two extremal values $\theta = \pm\pi$ can be reached only if we take $a \rightarrow +\infty$. Indeed, using the fact that the left-hand side of (7.10b) is bounded:

$$\left|e^{-\theta \cot \theta}\right| \leq 1, \quad (7.12)$$

then $a \sin \theta / \theta$ must also be bounded as $a \rightarrow +\infty$. Therefore,

$$\theta \xrightarrow{a \rightarrow \infty} \pm\pi. \quad (7.13)$$

The limit $a \rightarrow +\infty$ is reached by taking $\tilde{\beta}_{\text{eff}} \rightarrow +\infty$. From the definitions (3.30-5.19), one way of obtaining this limit is by setting $N = 0$ which corresponds to decoupling the CFT as we have discussed in subsection 6. The pure gravity case for flat space was also

studied in [15], and the analysis we have presented here agrees with the conclusion of that work: in pure gravity, flat space is tachyon-stable for positive β and tachyon-unstable for negative β .

To summarize, there are 2 real tachyonic poles when $0 \leq a < e^{-1}$. They merge at $a = e^{-1}$ and they become complex at $a > e^{-1}$.

The complex poles of the spin-2 propagator can be found numerically, and are shown in figure 25 for some illustrative values of $\tilde{\beta}_{\text{eff}}$. Each snapshot corresponds to a different $\tilde{\beta}_{\text{eff}}$. Poles correspond to the intersections of the blue lines (zeros of the real part of the inverse propagator) and of the orange lines (zeros of the imaginary part). The massless pole is not shown in this Figure, it is always located at $k = 0$ for any value of the parameters $\tilde{\alpha}$ and $\tilde{\beta}_{\text{eff}}$.

In figure 25, we start at large and negative values of $\tilde{\beta}_{\text{eff}}$ in the upper-left panel³⁸. Of the two tachyonic solutions, only the lighter one close to the origin is visible in the upper-left panel, while the heavier one is far away along the real axis. As $\tilde{\beta}_{\text{eff}}$ is increased, the heavier solution comes closer to the lighter solution as shown in snapshot (b). Then, they merge in snapshot (c) where $a = e^{-1}$, i.e. where $\tilde{\beta}_{\text{eff}}$ is chosen such that (7.8) is an equality. The complex instability continues to travel along the fixed orange curve and then becomes closer to the imaginary axis as $\tilde{\beta}_{\text{eff}}$ is increased.

We now turn to the analysis of ghosts. In the $a < e^{-1}$ regime, there are two tachyonic modes, the heavier one is a ghost and the lighter is not. The mass of the ghost is always comparable to GN^2 in this regime.

When $\tilde{\beta}_{\text{eff}}$ is increased, after the merging at $a = e^{-1}$ has occurred in snapshot (c) of Figure 25, the tachyonic complex ghost pole moves on the complex plane and approaches towards the imaginary axis as $\tilde{\beta}_{\text{eff}}$ becomes large and positive. The ghost becomes lighter and lighter in units of GN^2 .

In the large- $\tilde{\beta}_{\text{eff}}$ regime, the ghost sticks to the imaginary axis where its residue becomes real and positive. More precisely, the imaginary part of the residue becomes smaller and smaller compared to the real part.

In the limit $\tilde{\beta}_{\text{eff}} \rightarrow +\infty$, the mass squared of the spin-2 mode $(m_2)^2$ defined in (5.6) becomes negative. This limit can be taken in (5.23) to obtain the value

$$GN^2(m_2)^2 \underset{|\tilde{\beta}_{\text{eff}}| \rightarrow +\infty}{\sim} \frac{4\pi}{\tilde{\beta}_{\text{eff}}}. \quad (7.14)$$

This equation agrees with what is seen in Figure 25.

In Figures 1 and 2 we show the behaviour, respectively, of the real part and the complex modulus of the spin-2 poles. As it is shown in appendix F, the real part of k corresponds to the typical inverse time scale of the tachyonic instability. From these figures, one can follow the trajectory of the poles as a function of $\tilde{\beta}_{\text{eff}}$. As one can observe, for $O(1)$ values of $\tilde{\beta}_{\text{eff}}$, the poles are above the (species) cut-off, therefore they are outside of the regime of our EFT analysis. It is only for $\tilde{\beta}_{\text{eff}}$ very large and positive or very large and negative

³⁸Solutions of (7.3) are always a pair of complex conjugates due to the symmetry under $\theta \rightarrow -\theta$, which is explicit in equations (7.10a,7.10b). This, and the fact that we chose the square root with $\text{Re}(k) > 0$, are the reasons why we only display the top-right quarter of the complex plane in Figure 25.

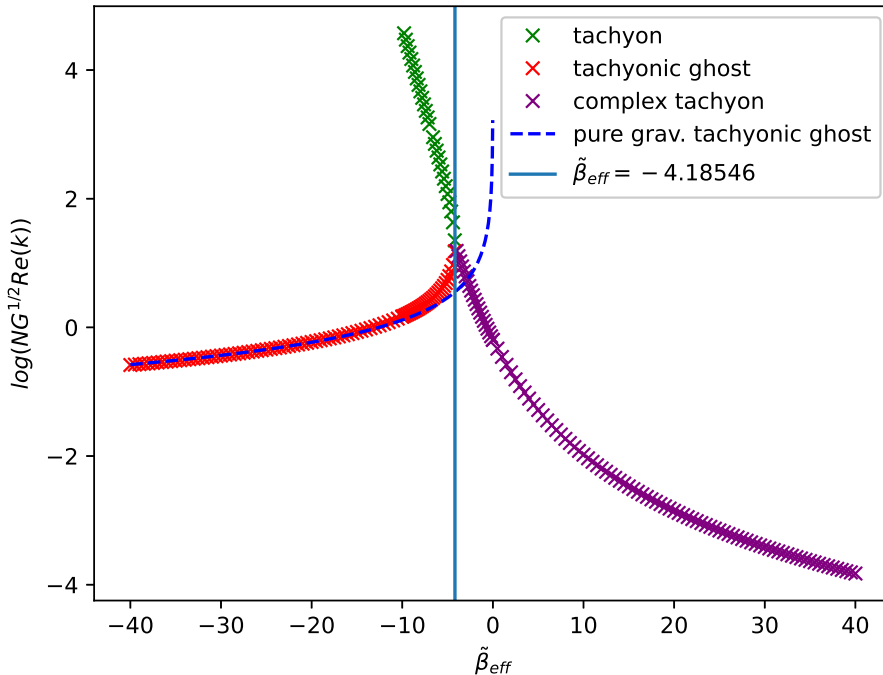


Figure 1: In this plot, we show the real part of the two tachyonic spin-2 poles in flat space (which also gives the inverse time scale of the Minkowski space spin-2 tachyonic instability, see app. F) in units of the species cutoff, as a function of $\tilde{\beta}_{\text{eff}}$. Red and green markers correspond respectively to the ghost-like (lighter) tachyon and a non-ghostly (heavier) tachyon. Purple markers correspond to two complex conjugate ghost-like tachyonic poles. The blue vertical line is the value of $\tilde{\beta}_{\text{eff}}$ which saturates (7.8), where these two poles merge and move to the complex plane as two complex conjugate poles as $\tilde{\beta}_{\text{eff}}$ is further increased. Large (positive and negative) values of $\tilde{\beta}_{\text{eff}}$ correspond to a long-lived tachyon. For comparison, the black curve corresponds to the case of pure gravity with $\beta = \tilde{\beta}_{\text{eff}}/\pi$, where the tachyonic pole is given by equation (6.3). For this curve, the vertical axis is $\log(G^{\frac{1}{2}} \text{Re}(k))$ while the horizontal axis is $\pi\beta$.

that at least one pole becomes lighter than the cut-off scale. However, this is the same regime in which even pure gravity (black curves in figures 1 and 2) has a light instability (although in the case of pure gravity, large positive β corresponds to a ghost which is not also a tachyon, unlike in the presence of the CFT). In any regime where pure gravity does not have light unstable modes, adding the CFT does not make the effective field theory unstable.

The behaviour of the complex solutions for X right after the merging can be described analytically by performing an expansion for small θ in (7.10):

$$\log x = -1 + \frac{\theta^2}{3} + \mathcal{O}(\theta^3), \quad (7.15a)$$

$$x \left[\log x \left(1 - \frac{\theta^2}{2} \right) - \theta^2 + \mathcal{O}(\theta^3) \right] = -a. \quad (7.15b)$$

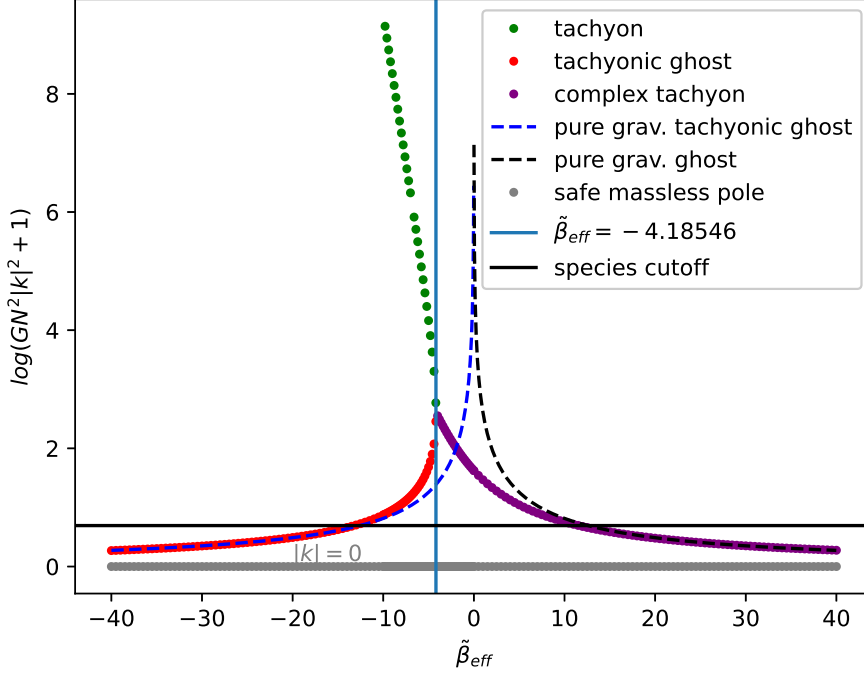


Figure 2: In this plot, we show the modulus of the mass of the spin-2 tachyonic poles in flat space, defined in (5.6), in units of the species scale (1.7), as a function of $\tilde{\beta}_{\text{eff}}$. Red and green markers correspond respectively to the light ghost-like tachyon and the heavy non-ghostly tachyon. The tachyon exists for large and negative $\tilde{\beta}_{\text{eff}}$ but its mass is too large to appear in the window. Purple markers correspond to two complex conjugate ghost-like tachyonic poles. The black curves correspond to the massive ghost in pure gravity with $\beta = \tilde{\beta}_{\text{eff}}/\pi$: the solid line is the ghost-like tachyon ($\beta < 0$), and the dashed line is the non-tachyonic ghost ($\beta > 0$). The blue vertical line is the value of $\tilde{\beta}_{\text{eff}}$ which saturates (7.8), where these two poles merge and move to the complex plane as two complex conjugate poles as $\tilde{\beta}_{\text{eff}}$ is further increased. The black horizontal line marks the species cut-off (or the Planck scale cut-off for pure gravity). For this curve, the vertical axis is $\log(G^{\frac{1}{2}} \text{Re}(k))$ while the horizontal axis is $\pi\beta$. There are unstable modes lighter than the species cutoff only for large values of $|\tilde{\beta}_{\text{eff}}|$.

We can therefore eliminate x to find a solution for θ given by

$$\theta^2 \approx 2(ae - 1). \quad (7.16)$$

The two complex branches of X then start at $a = e^{-1}$. The solution for $X = xe^{i\theta}$ is then

$$x = e^{-1 + \frac{\theta^2}{3} + \mathcal{O}(\theta^3)}, \quad (7.17)$$

and

$$\theta \approx \pm \sqrt{2(ae - 1)}. \quad (7.18)$$

8. Poles of the dS spin-two propagator and stability

We now consider the positive curvature case and study the stability under tensor perturbations of 4d gravity plus a holographic CFT on de Sitter space-time. Both tachyonic and ghost instabilities will be determined numerically, but we also provide analytical insight into these results.

Tachyonic instability is identified by studying the location of zeros of the de Sitter tensor inverse propagator (5.39) in the complex ν domain: such instability is characterized by the condition $\text{Re}(\nu) > 3/2$ (5.28).

Whether or not the mode is a ghost is determined by the sign of the residue of the pole, as explained in subsection 5.4

8.1 Numerical results for two typical sets of parameters

Before performing a full analysis in the parameter space spanned by $(GN^2H^2, \tilde{\alpha}, \tilde{\beta}_{\text{eff}})$, in this subsection we present, as an illustrative example, the results for two distinct sets of parameters which give different results but are typical cases of the more general behaviour of the system. For each of these two sets of parameters, we fix $(GN^2H^2, \tilde{\alpha})$ and solve numerically the equation (5.36) for several values of $\tilde{\beta}_{\text{eff}}$.

The first example, shown in Figure 26 is an example of the small curvature regime. For instance, we observe that in this figure, the theory is tachyon-unstable from the snapshot (a) to snapshot (e) because one (or two) solutions are tachyonic ($\text{Re}(\nu) > 3/2$). The two tachyons merge in snapshot (c) to form a double pole, where $\mathcal{F}'_{\text{dS}}(\nu)$ vanishes³⁹.

After the merging, the double pole separates into two complex conjugate solutions. We only display positive imaginary parts in this Figure. In snapshot (f) the tachyon with complex ν enters the stability region $|\text{Re}(\nu)| < 3/2$ because its real part decreases as $\tilde{\beta}_{\text{eff}}$ is increased. Therefore, the theory is tachyon-stable from snapshot (f) to snapshot (i) and will continue to be stable for even larger values of $\tilde{\beta}_{\text{eff}}$. As $\tilde{\beta}_{\text{eff}}$ is increased, the pole which became tachyon-stable in (f) goes to the imaginary axis and then forms a double pole at the intersection of the real and imaginary axes.

When a tachyon is present, it is important to determine the time scale of the instability, which is fixed by the value of ν in the same way for both scalars and tensors (see appendix G for details). For a tachyonic mode with $\text{Re}(\nu) > 3/2$, the solution of (4.25) which dominates at large t behaves as⁴⁰:

$$\tilde{\theta}_{ij} \underset{Ht \rightarrow +\infty}{\propto} e^{-Ht(3/2-\nu)}. \quad (8.1)$$

The characteristic rate Γ of the exponential divergence in (8.1) is therefore given by

$$\Gamma = H(|\text{Re}(\nu)| - 3/2). \quad (8.2)$$

We now turn to the analysis of ghost instabilities. The sign of the residue of each pole is obtained by computing numerically $\mathcal{F}'(\nu)$ and applying the formula (5.64). The

³⁹Theories with a double pole have been recently discussed in [95].

⁴⁰For $\text{Re}(\nu) < -3/2$, there would be a sign flip $\nu \rightarrow -\nu$ in (8.1).

resulting sign is encoded in the colour of each dot in Figure 26. Green dots correspond to negative residues, indicating a ghost-free pole. Red dots correspond to ghosts with positive residue, and purple dots correspond to complex residues. One can observe that from Figure 26, a ghost (either positive or complex residue) is always present, for any value of $\tilde{\beta}_{\text{eff}}$. For generic values of $\tilde{\beta}_{\text{eff}}$, the mass of the ghost defined by (5.26) is large compared to the Hubble rate H . For large values of $\tilde{\beta}_{\text{eff}}$ (both positive and negative), the ghost pole approaches $\nu = 1/2$, matching the $N = 0$ case (6.5) in the limit $\beta \rightarrow \infty$.

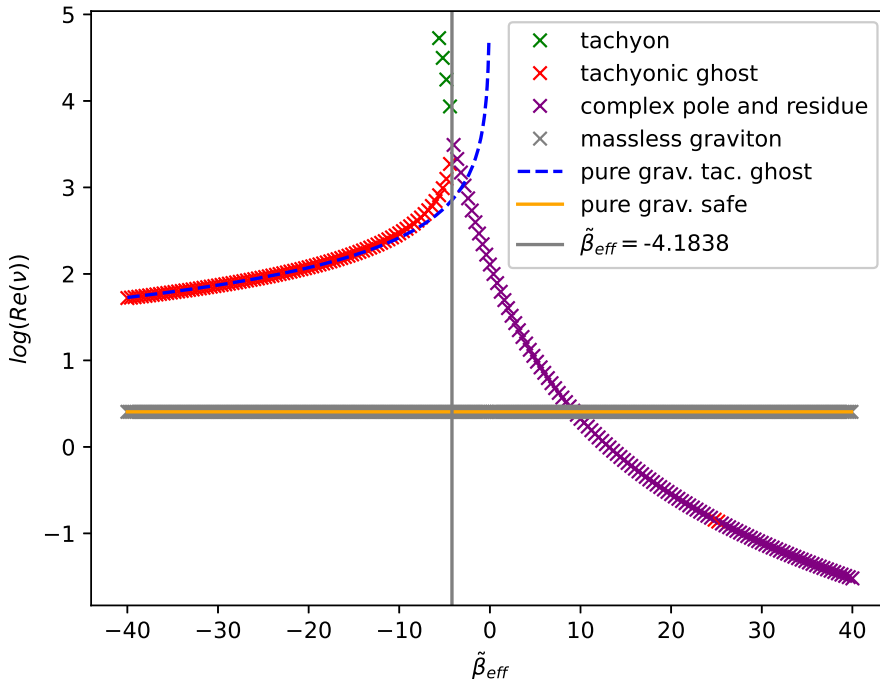


Figure 3: In this plot, we show the real part of the spin-2 poles in de Sitter with the same parameters as in Figure 26. The real part also gives the inverse time scale, or strength, (8.2) of the dS tachyonic instability, in units of the species cutoff, as a function of $\tilde{\beta}_{\text{eff}}$. Red and green markers correspond respectively to the ghost-like (lighter) tachyon and a non-ghostly (heavier) tachyon. Purple markers correspond to two complex conjugate ghost-like poles. For comparison, the blue dashed line and the yellow line correspond to the case of pure gravity with $\beta = \tilde{\beta}_{\text{eff}}/\pi$ (6.4). For pure gravity curves, the horizontal axis is $\pi\beta$. The grey vertical line is the value of $\tilde{\beta}_{\text{eff}}$ which saturates (8.11), (corresponding to snapshot (c) of Figure 26), where two poles merge and move to the complex plane as two complex conjugate poles as $\tilde{\beta}_{\text{eff}}$ is further increased. Each pole above the green line at $\text{Re}(\nu) = 3/2$, is tachyonic. The complex pole crosses this green line around $\tilde{\beta}_{\text{eff}} \approx 9.3$, it then becomes non-tachyonic for larger values of $\tilde{\beta}_{\text{eff}}$.

The divergence rate Γ is computed numerically as a function of $\tilde{\beta}_{\text{eff}}$, and the results are shown in Figure 3 for the set of parameters we have used in Figure 26. Figure 3 shows in green the tachyonic pole, in red the tachyonic ghost, in purple the complex pole and in grey the massless pole which is neither a ghost nor a tachyon. The two poles of pure gravity, are also shown for comparison. The massive pole (6.6) is a blue dashed curve, while the

massless pole is an orange line. As $\tilde{\beta}_{\text{eff}}$ is increased, the tachyonic rate Γ (8.2) decreases, down to the point where the spin-2 mode becomes tachyon-stable around $\tilde{\beta}_{\text{eff}} \sim 9.3$. The pure gravity massive pole for large and negative β coincides with the ghost pole for large and negative $\tilde{\beta}_{\text{eff}}$ if we set $\tilde{\beta}_{\text{eff}} = \pi\beta$, i.e $N = 1$ in the definition of $\tilde{\beta}_{\text{eff}}$ (5.19). Large and positive $\tilde{\beta}_{\text{eff}}$ also agree with the pure gravity result, even if this is not visible from this figure. One would need to look at much higher values of $\tilde{\beta}_{\text{eff}}$ (a few thousand) to see that the complex pole goes to the real axis, as it is shown in snapshots (g,h,i) of Figure 26. In this case, both the massive pole of pure gravity and the ghost asymptote at $\nu = 1/2$, as expected by a naive $\tilde{\beta}_{\text{eff}} \rightarrow +\infty$ limit of (5.39). For very large and negative $\tilde{\beta}_{\text{eff}}$ the massless pole becomes a ghost. According to (6.5), one would need to have $\tilde{\beta}_{\text{eff}} \leq -\frac{2\pi}{GN^2H^2} \approx -628.3$. In the presence of the CFT, however, we find numerically that the massless pole is a ghost for $\tilde{\beta}_{\text{eff}} \lesssim -624.2$. This critical value of $\tilde{\beta}_{\text{eff}}$ corresponds to the merging of the ghost with the massless pole which were both present in snapshot (a) of Figure 26.

The results of Figure 3 are compatible with the paper [74] because they have $\alpha = 0$ and study the $GN^2H^2 \ll 1$ regime where they also find a complex pole, which is also present in flat space (see Figure 2). In this paper, the authors have found an approximate value of $\tilde{\beta}_{\text{eff}}$ at which the complex pole crosses the massless line displayed in orange. Larger values of $\tilde{\beta}_{\text{eff}}$ then correspond to an absence of tachyonic instabilities. However, the pole is still complex up to $\tilde{\beta}_{\text{eff}} \approx 5026.43$ where it becomes a *real* ghost.

Figure 4 shows the modulus of the mass squared of the tensor modes in de Sitter, plotted in units of the species scale (1.7). This figure is a numerical evaluation for the same parameters as the ones chosen in Figures 26 and 3. As in Figure 3, the green, red and blue curves are respectively the tachyonic, the ghost and the massive mode of pure gravity. The modulus of the ghost mass agrees with the pure gravity massive mode for large values of $|\tilde{\beta}_{\text{eff}}|$. For generic values, both the ghost and the tachyon lie above the species cutoff. The complex pole, which appears for $\tilde{\beta}_{\text{eff}} \gtrsim -4.1838$, goes beyond the species scale for large and positive values of $\tilde{\beta}_{\text{eff}}$.

Our second example corresponds to GN^2H^2 of order unity (rather than $GN^2H^2 \ll 1$ as was the case in figure 26). Specifically, we take $GN^2H^2 = \pi/4$ and $\tilde{\alpha} = 10$. The spin-2 poles of de Sitter in this case are shown in Figure 27. For large and negative values of $\tilde{\beta}_{\text{eff}}$ we find a different behaviour than in Figure 26: in the present case there is only one tachyon, and it is not a ghost. However, the massless pole at $\nu = 3/2$ is now a ghost. As $\tilde{\beta}_{\text{eff}}$ is increased, the tachyon becomes lighter and lighter from snapshot (a) to (c). It stays on the positive real axis (another difference from Figure 26).

Snapshots (a-f) correspond to a tachyon-unstable theory because the heaviest solution has a real part larger than $3/2$. The tachyon merges with the massless graviton in snapshot (g) and becomes a ghost when $\tilde{\beta}_{\text{eff}}$ is increased. This ghost then moves towards $\nu = 1/2$ for large and positive values of $\tilde{\beta}_{\text{eff}}$ in snapshot (i). This matches the decoupling limit $N = 0$, as can be seen from (6.5). For large and negative $\tilde{\beta}_{\text{eff}}$, the massless pole $\nu^2 = 9/4$ is a ghost whereas the $\nu^2 = 1/4$ is not. For large and positive $\tilde{\beta}_{\text{eff}}$, the respective signs of their residues are switched. This is what is observed by comparing snapshots (a) and (i), where the red and green poles are interchanged.

The characteristic rate of the tachyonic instability is plotted in Figure 5 as a function

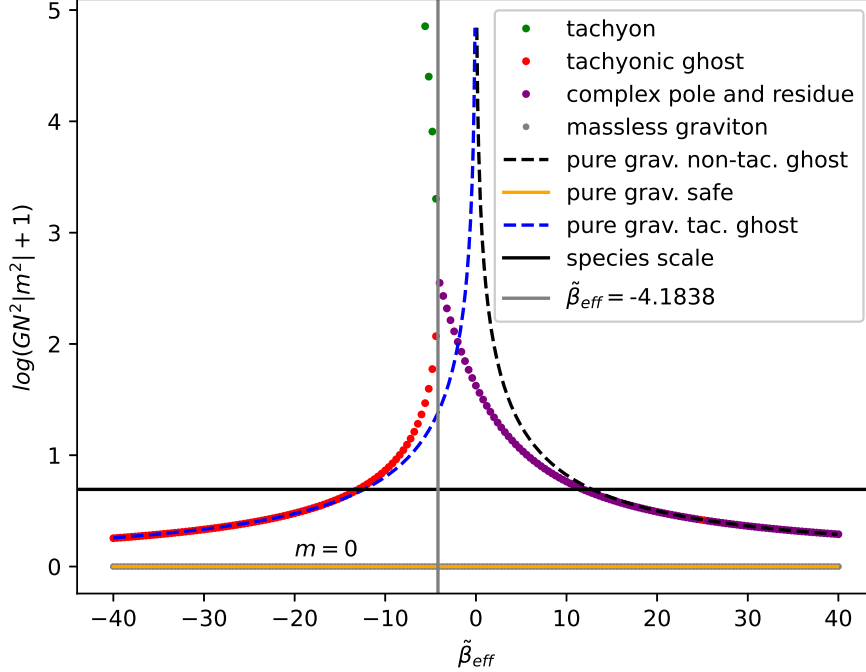


Figure 4: In this plot, we show, for the same parameters as in Figure 26, the complex modulus of the mass of the spin-2 tachyonic poles in de Sitter, defined in (5.26), in units of the species scale (1.7), as a function of $\tilde{\beta}_{\text{eff}}$. Red and green markers correspond respectively to the light ghost-like tachyon and the heavy non-ghostly tachyon. Purple markers correspond to two complex conjugate ghost-like poles. The species scale is shown by a horizontal solid black line. For comparison, different curves show the poles in pure gravity with $\beta = \tilde{\beta}_{\text{eff}}/\pi$: the dashed blue and black curves are respectively tachyonic and non-tachyonic ghosts. The orange curve is safe. For pure gravity curves, the vertical axis is $\log(G^{\frac{1}{2}}|m|^2 + 1)$ while the horizontal axis is $\pi\beta$. The grey vertical line is the value of $\tilde{\beta}_{\text{eff}}$ which saturates (8.11), (corresponding to snapshot (c) of Figure 26), where these two poles merge and move to the complex plane as two complex conjugate poles as $\tilde{\beta}_{\text{eff}}$ is further increased. The black horizontal line marks the species cut-off (or the Planck scale cut-off for pure gravity). There are unstable modes lighter than the species cutoff only for large values of $|\tilde{\beta}_{\text{eff}}|$.

of $\tilde{\beta}_{\text{eff}}$. This figure is obtained with the same parameters as Figure 27. Compared with 3, in Figure 5 there is no merging between two unstable massive poles (which is denoted by a grey vertical line in Figure 3). Here instead, we have a single tachyon moving along the real axis as $\tilde{\beta}_{\text{eff}}$ is increased, it merges with the massless pole at $\nu = 3/2$ to form a safe massless pole and a ghost. The grey vertical line in Figure 5 marks the value of $\tilde{\beta}_{\text{eff}}$ for above which the theory becomes tachyon-stable. This corresponds to the value in snapshot (g) of Figure 27.

Figure 6 shows the modulus of the mass squared of the tensor modes in de Sitter, plotted in units of the species scale (1.7). This figure is a numerical evaluation for the same parameters as the one chosen in Figures 27 and 5. As in Figure 5, the green, red and blue curves are respectively the tachyonic, the ghost and the massive mode of pure gravity.

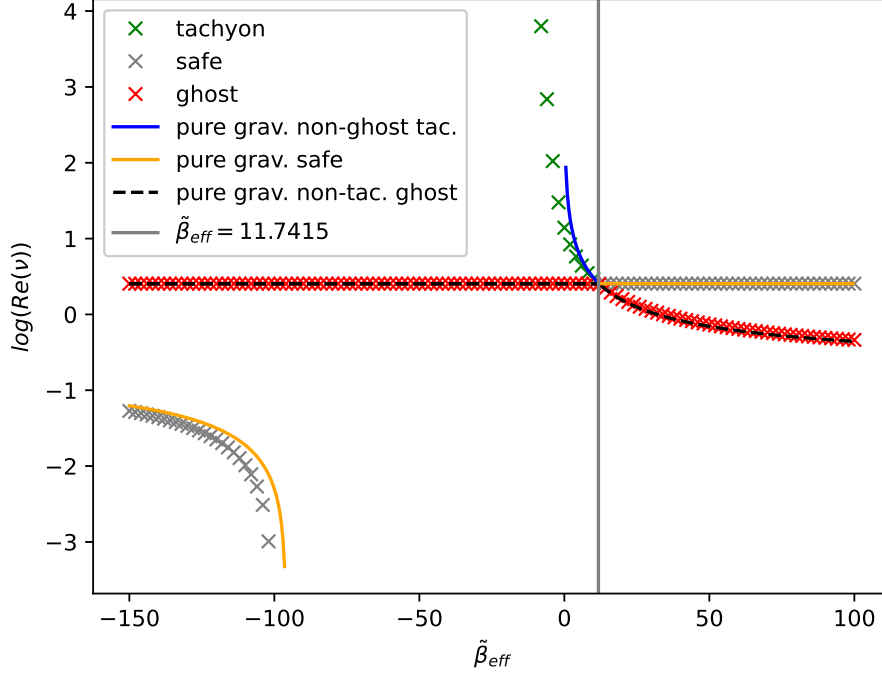


Figure 5: In this plot, we show the real part of the spin-2 poles in de Sitter, with the same parameters as in Figure 27. The real part also gives the inverse time scale (or strength) of the dS tachyonic instability (8.2), in units of the species cutoff, as a function of $\tilde{\beta}_{\text{eff}}$. Grey markers correspond to safe poles (one for large and negative $\tilde{\beta}_{\text{eff}}$ disappearing around ~ -100 , the other is massless for $\tilde{\beta}_{\text{eff}} > 11.7415$), while red and green markers correspond respectively to the non-ghostly tachyonic pole and the light ghost pole. For comparison, different curves show the case of pure gravity with $\beta = \tilde{\beta}_{\text{eff}}/\pi$ (6.6): the solid blue line is a non-ghostly tachyon, the solid yellow line is non-ghostly non-tachyonic, and the black dashed line is a non-tachyonic ghost. There is a gap at $-90 \lesssim \tilde{\beta}_{\text{eff}} < 0$ for pure gravity because the massive pole (6.6) is purely imaginary in this interval. In the presence of the CFT, the safe pole disappears into negative (i.e not allowed) values of $\text{Re}(\nu)$. For pure gravity curves, the horizontal axis is $\pi\beta$. The vertical grey line is the value of $\tilde{\beta}_{\text{eff}}$ corresponding to the transition from tachyonic to non-tachyonic (8.14), where the tachyon merges with the massless ghost at $\nu = 3/2$. This value is also displayed in snapshot (g) of Figure 27.

The modulus of the ghost mass agrees with the pure gravity massive mode for large values of $|\tilde{\beta}_{\text{eff}}|$. For generic values, both the ghost and the tachyon lie above the species cutoff. One can observe in this Figure that the massless pole is a ghost for $\tilde{\beta}_{\text{eff}} \lesssim 12$, whether the CFT is present or not. More precisely, the massless pole is a ghost for $\pi\beta < 12$ in pure gravity (6.4), whereas the actual value in the presence of the CFT is $\tilde{\beta}_{\text{eff}} \lesssim 11.7415$ as one can observe in snapshot (g) of Figure 27.

Qualitatively, the cases displayed in Figures 26 and 27 (which, we remind the reader, correspond to small GN^2H^2 and $O(1) GN^2H^2$ respectively) have a different behaviour as a function of $\tilde{\beta}_{\text{eff}}$: in the first case, a complex tachyonic ghost becomes non-tachyonic through the complex plane when $\tilde{\beta}_{\text{eff}}$ is increased; in the second case, a real tachyonic pole

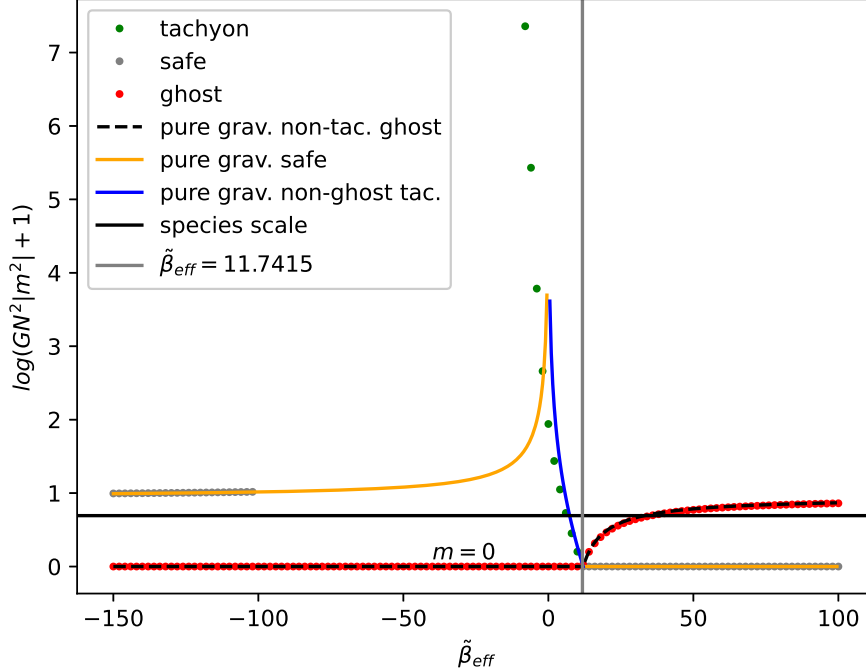


Figure 6: In this plot, obtained with the same parameters as in Figures 27 and 5, we show the complex modulus of the mass of the spin-2 tachyonic poles in de Sitter, defined in (5.26), in units of the species scale (1.7), as a function of $\tilde{\beta}_{\text{eff}}$. Grey markers correspond to safe poles (one for large and negative $\tilde{\beta}_{\text{eff}}$ disappearing around ~ -100 , the other is massless for $\tilde{\beta}_{\text{eff}} > 11.7415$), while red and green markers correspond respectively to the non-ghostly tachyonic pole and the light ghost pole. The species scale is shown by a horizontal solid black line. For comparison, different curves correspond to the pure gravity modes with $\beta = \tilde{\beta}_{\text{eff}}/\pi$: the blue curve is tachyonic, the black dashed curve is a non-tachyonic ghost, and the orange curve is safe. For pure gravity curves, the vertical axis is $\log(G^{\frac{1}{2}}|m|^2 + 1)$ while the horizontal axis is $\pi\beta$. The vertical grey line is the value of $\tilde{\beta}_{\text{eff}}$ corresponding to snapshot (g) of Figure 27), where the tachyonic pole becomes massless, and therefore stops being tachyonic.

becomes tachyon-stable on the real axis as $\tilde{\beta}_{\text{eff}}$ is increased. We chose to present only two different cases because they are paradigmatic of what happens in the whole parameter space. We span more values of GN^2H^2 and α in appendix M. As a result, any point choice of $(GN^2H^2, \tilde{\alpha})$ space should be similar to one of these two cases discussed above. The ArXiv webpage of this paper contains ancillary files, including animated gifs. Each snapshot of these gifs corresponds to a different value of $\tilde{\beta}_{\text{eff}}$ for fixed $(GN^2H^2, \tilde{\alpha})$.

In the next subsection, we present an analytic approximation which explains these two different behaviours.

Our findings indicate that once we stay below the species cutoff, qualitatively the behaviour is similar to the case without the CFT if we rescale the parameters of the effective gravity theory with a factor of N^2 . We also find that a richer set of phenomena can happen above the cutoff, but we cannot trust our description. In previous works, [58],

the analysis was done for situations that were in the general area of the cutoff or above.

8.2 Analytic results for tensor tachyonic modes in dS at large $|\nu|$

In this subsection, we provide approximate analytical results for the location of the tachyonic poles in the tensor propagator (5.39) on de Sitter. These analytics provide a better understanding of the qualitative picture presented in the previous subsection

We focus on the “non-trivial” poles, i.e. away from the massless graviton pole $\nu = 9/4$. Therefore, we look for the zeros of $Q_{\text{dS}}(\nu)$ defined in (5.37). There is no simple analytic expression to this function for an arbitrary location in the complex plane. However, it can be approximated by a logarithm when $|\nu|$ is large. This occurs in particular for small curvature, as it was the case in Figure 26: indeed, with $GN^2H^2 \ll 1$, and finite $\tilde{\alpha}$ and $\tilde{\beta}_{\text{eff}}$, solving $Q_{\text{dS}}(\nu) = 0$ requires cancelling the large value of $\frac{2\pi}{GN^2H^2}$ against a large value of $|\nu|$, as it is argued in [74].

With these considerations, in the rest of this subsection, we develop an analytic approximation for the poles in the limit of large $|\nu|$. In this limit, we can use the Stirling formula

$$\mathcal{H}(z) \underset{|z| \rightarrow \infty}{=} \log z + \gamma_E + \mathcal{O}(z^{-1}), \quad (8.3)$$

where γ_E is the Euler-Mascheroni constant. The large ν expansion of (5.37) is then given by

$$Q_{\text{dS}} = 1 - \frac{2\pi}{GN^2H^2} + 2\tilde{\alpha} - \frac{\nu^2}{2} \left[\tilde{\beta}_{\text{eff}} - \frac{1}{2} + \log(GN^2H^2) + 2\log \nu - 2\gamma_E + \mathcal{O}(|\nu|^{-1}) \right]. \quad (8.4)$$

We have $2\log(\nu) = \log(\nu^2)$, since we have chosen $\text{Re}(\nu) > 0$ in (5.29), insofar as the branch-cut of the log function in (8.3) is on the negative real axis. The equation of motion (5.36) then takes a similar form to the one of flat space (7.3),

$$X \log X = -a, \quad (8.5)$$

where now X and a depend on the curvature and are given by:

$$X \equiv \nu^2 GN^2 H^2 \exp \left\{ \tilde{\beta}_{\text{eff}} - \frac{1}{2} + 2\gamma_E \right\}, \quad (8.6)$$

$$a \equiv 2GN^2 H^2 \left[2 \left(\frac{\pi}{GN^2 H^2} - \tilde{\alpha} \right) - 1 \right] \exp \left\{ \tilde{\beta}_{\text{eff}} - \frac{1}{2} + 2\gamma_E \right\}. \quad (8.7)$$

We can observe that there are similar definitions for X and a in flat space-time (7.4). However, a can now be negative using specific combinations of $\tilde{\alpha}$ and the curvature.

Equations (8.5,8.6,8.7) hold for large $|\nu|$ and any curvature. In particular, they can be used to understand the flat space limit: indeed, by comparing the eigenvalue equations for de Sitter (5.26) to the one for Minkowski (5.6), we observe that the flat limit can be taken by defining

$$\nu^2 H^2 \underset{H^2 \rightarrow 0}{\rightarrow} k^2, \quad (8.8)$$

where the limit is taken by sending $|\nu| \rightarrow \infty$ so that k^2 is kept finite. In this limit, $\tilde{\alpha}$ becomes negligible and we find:

$$\mathcal{F}_{\text{dS}} \xrightarrow[H \rightarrow 0]{k^2 \rightarrow \nu^2 H^2} \mathcal{F}_{\text{flat}}. \quad (8.9)$$

which coincides with the result we have obtained by the direct flat space calculation, equation (7.3). We have therefore shown that the dS propagator matches continuously onto the flat space propagator when we take the curvature to zero.

The de Sitter tachyon-stability condition (5.28) also becomes the flat space condition (5.10) in this limit. Indeed, taking the flat space limit of de Sitter condition $|\text{Re}(\nu)| < 3/2$ we obtain

$$\text{Re}(k) \sim H|\text{Re}(\nu)| < \frac{3H}{2} \rightarrow 0, \quad (8.10)$$

i.e. the flat space tachyon-stability condition.

We now turn to arbitrary curvatures, but still, search for solutions satisfying $|\nu| \gg 1$. This allows us to use equation (8.5) to better understand the results we have found in the two typical examples in the last subsection. We keep GN^2H^2 and $\tilde{\alpha}$ finite, so X (8.6) and a (8.7) differ from their flat space analogs (7.4). In particular, a can be negative for finite curvature, unlike in flat space where $a > 0$.

When looking for solutions of (8.5), one can distinguish three cases:

- If $a < 0$, the unique solution X of (8.5) is real.
- If $0 \leq a \leq e^{-1}$, there are two real solutions, one degenerate solution if $a = e^{-1}$.
- If $e^{-1} < a$, there are two complex conjugate solutions.

The second and third items describe Figure 26. Snapshots (a) and (b) correspond to $0 \leq a \leq e^{-1}$. As $\tilde{\beta}_{\text{eff}}$ increases, a increases up to e^{-1} where the two solutions merge in snapshot (c). Using the definition of a in (8.7), one can obtain approximately the critical value at the merging:

$$\tilde{\beta}_{\text{eff}}^{\text{merge}} \equiv -\frac{1}{2} - 2\gamma_E - \log(2GN^2H^2) - \log\left[2\left(\frac{\pi}{GN^2H^2} - \tilde{\alpha}\right) - 1\right]. \quad (8.11)$$

Applying this formula to the parameters of Figure 26, we find $\tilde{\beta}_{\text{eff}}^{\text{merge}} = -4.18386$, which corresponds to snapshot (c). After the merging, the complex solution travels in the complex plane up to crossing the green stability line. The value of $\tilde{\beta}_{\text{eff}}$ chosen to plot snapshot (h) corresponds to equation (8.19) obtained in the small H approximation.

We now consider the case $a < 0$, which corresponds to a single real tachyonic solution. From equation (8.7), $a < 0$ is equivalent to

$$\frac{\pi}{GN^2H^2} < \tilde{\alpha} + \frac{1}{2}. \quad (8.12)$$

It is intriguing that the inequality (8.12) turns out to be the same as the condition for the scalar mode to be a ghost (4.13).

Equation (8.12) holds in every snapshot of Figure 27, in which $\tilde{\alpha}$ and GN^2H^2 are fixed. Therefore in all these snapshots, we have $a < 0$. Even if we are not in the large- $|\nu|$ regime, it is a remarkable fact the analysis above still gives an accurate qualitative description of the results: we have a single real tachyon which moves along the real axis towards the massless pole.

If the transition from tachyonic to non-tachyonic does indeed happen on the real axis, then it must be at $\nu = 3/2$. If this is the case, it is sufficient to evaluate $Q_{\text{ds}}(\nu)$ at $\nu = 3/2$ to obtain a stability condition for the other parameters as follows. Using $\mathcal{H}(1) = 1$ in (5.37), we obtain

$$Q_{\text{ds}}(3/2) = -\frac{1}{2} - \log(GN^2H^2) - 2 \left[\frac{\pi}{GN^2H^2} + \frac{\tilde{\beta}_{\text{eff}}}{2} - \tilde{\alpha} \right]. \quad (8.13)$$

The transition between stability and instability corresponds to $Q_{\text{ds}}(3/2) = 0$, in which case we obtain

$$\tilde{\beta}_{\text{eff}}^{\text{massless}} \equiv -\frac{1}{2} - \log(GN^2H^2) + 2 \left(\tilde{\alpha} - \frac{\pi}{GN^2H^2} \right). \quad (8.14)$$

If the parameters of the theory satisfy (8.14), then $\nu = 3/2$ is a double pole of the tensor two-point function. But if $\tilde{\beta}_{\text{eff}} > \tilde{\beta}_{\text{eff}}^{\text{massless}}$, then the theory is tachyon-stable. Evaluating (8.14) for the parameters taken in Figure 27 gives the value chosen to plot snapshot (c). It is clear from this snapshot that the solution which was unstable in snapshot (b) crosses the stability line. Therefore, the assumption made for (8.14) that the transition would happen on the real axis is verified numerically for this particular set of parameters.

In the $a < 0$ case, we were able to derive an exact formula for tachyonic stability as a function of $\tilde{\beta}_{\text{eff}}$ in (8.14). This was obtained assuming that the tachyonic solution would cross the point $\nu = 3/2$. However, in the case of $a > 0$, the tachyonic solution is complex and can cross the stability line with a generic imaginary part, as was shown in Figure 26.

If we make the further assumption that $a \gg 1$, it is possible to perform an additional approximation to find X . As argued also in [74] in the case $\alpha = 0$, a solution of equation (8.5) for large and positive a can be found using the ansatz

$$X \underset{a \rightarrow +\infty}{\sim} = -\frac{a}{\log(-a)}. \quad (8.15)$$

Injecting this ansatz in the original equation (8.5), we then find

$$X \log X = -a \left[1 - \frac{\log(\log(-a))}{\log(-a)} \right] \underset{a \rightarrow 0}{\sim} -a, \quad (8.16)$$

which is a “slow” convergence as $\frac{\log(\log(-a))}{\log(-a)} \rightarrow 0$. We then have an imaginary part in the solution X (8.15) since $\log(-a) = \pm i\pi + \log a$. The complex square root of the slowly converging solution (8.15) is then

$$\sqrt{X} = i \sqrt{\frac{a}{\log a}} \left[\pm 1 - \frac{i\pi}{2 \log a} \right] + \mathcal{O} \left(\frac{1}{\log^{3/2} a} \right). \quad (8.17)$$

The branch with a positive real part has been taken because the real part of ν is assumed to be positive in the bulk radial solution (5.33). Then, replacing a and X by their definitions (8.6,8.7), one gets the approximate solution for ν

$$\nu \approx \frac{2 \left(\frac{\pi}{GN^2 H^2} - \tilde{\alpha} - \frac{1}{2} \right)^{1/2}}{\left\{ \tilde{\beta}_{\text{eff}} - \frac{1}{2} + 2\gamma_E + \log \left[4GN^2 H^2 \left(\frac{\pi}{GN^2 H^2} - \tilde{\alpha} - \frac{1}{2} \right) \right] \right\}^{1/2}} \times \left[\pm i + \frac{\pi/2}{\tilde{\beta}_{\text{eff}} - \frac{1}{2} + 2\gamma_E + \log \left[4GN^2 H^2 \left(\frac{\pi}{GN^2 H^2} - \tilde{\alpha} - \frac{1}{2} \right) \right]} \right]. \quad (8.18)$$

For $\alpha = 0$, the solution (8.18) reduces to the results of [74] derived for small curvature. The stability condition (5.28) is then

$$\tilde{\beta}_{\text{eff}} \geq \tilde{\beta}_{\text{eff}}^c \equiv \frac{1}{2} - 2\gamma_E - \log \left[4GN^2 H^2 \left(\frac{\pi}{GN^2 H^2} - \tilde{\alpha} - \frac{1}{2} \right) \right] + \left[\frac{4\pi^2}{9} \left(\frac{\pi}{GN^2 H^2} - \tilde{\alpha} - \frac{1}{2} \right) \right]^{1/3}. \quad (8.19)$$

Applying this result to the case where $\alpha = 0$ and $GN^2 H^2 = 0.01$, we obtain that stability is reached for $\tilde{\beta}_{\text{eff}} \geq 7.94268$ which is chosen for snapshot (f) in Figure 26.

The approximation used to arrive at (8.18) cannot hold for large negative values of $\tilde{\beta}_{\text{eff}}$: in this case there are two real tachyonic solutions, which cannot be described by (8.18). This is due to the fact that the large a approximation, equivalent to (8.15), cannot not hold for large negative values $\tilde{\beta}_{\text{eff}}$ because a is proportional to $e^{\tilde{\beta}_{\text{eff}}}$.

8.3 Tachyonic and ghost-like instabilities for dS in parameter space

After having addressed the qualitative features of the spectrum in the previous sections, we now present a full numerical scan of parameter space, identify the stability and instability regions (concerning ghosts and tachyons) and determine the characteristic scale of the instability. We do this first for tachyonic instabilities, then we move on to investigate ghost instabilities.

Figure 7 shows the distinction between tachyon-stable and tachyon-unstable regions, as a function of the parameters $(GN^2 H^2, \tilde{\alpha}, \tilde{\beta}_{\text{eff}})$. In this figure, the critical value for $\tilde{\beta}_{\text{eff}}$ is given as a function of the curvature for several values of $\tilde{\alpha}$. Each curve corresponds to a different $\tilde{\alpha}$. For a given $\tilde{\alpha}$, the region below the curve is unstable because it corresponds to lower values of $\tilde{\beta}_{\text{eff}}$, which are tachyonic. The region above the curve is stable because it corresponds to higher values of $\tilde{\beta}_{\text{eff}}$, for which the tachyon has entered the stability region $|\text{Re}(\nu)| < 3/2$ exactly at the critical value.

On each curve of figure 7, there is a regime (which roughly corresponds to small curvatures, and corresponds to the left part of the figure) in which the critical value of $\tilde{\beta}_{\text{eff}}$ decreases with increasing curvature, regardless of the value of $\tilde{\alpha}$. For larger curvatures, one may observe a different regime: for large enough $\tilde{\alpha}$ we observe that $\tilde{\beta}_{\text{eff}}$ starts increasing with the curvature to then decrease again. This behaviour sets in approximatively at $\tilde{\alpha} \approx 0$. The larger $\tilde{\alpha}$ is, the higher the increase in the critical value of $\tilde{\beta}_{\text{eff}}$.

From the large- $|\nu|$ approximation, we expect that the small curvature regime (left part of the figure) contains a complex tachyon, whereas the eventual *bump* on the right part of

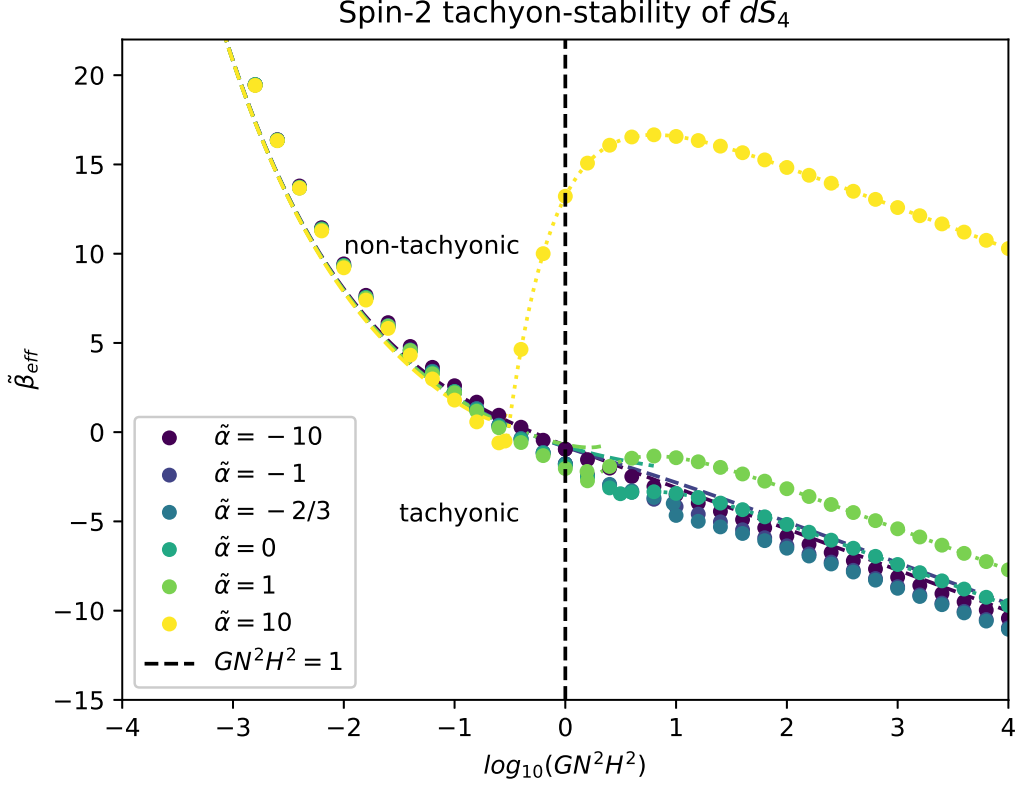


Figure 7: Spin-2 tachyonic instability of de Sitter space depending on $\tilde{\beta}_{\text{eff}}$ and GN^2H^2 , for different values of $\tilde{\alpha}$. Dotted lines with large dots, are the boundaries between the stable and unstable regions and have been computed numerically. Above each curve, we are in a non-tachyonic regime ($\text{Re}(\nu) \leq 3/2$), while the region below is tachyonic ($\text{Re}(\nu) > 3/2$). The dotted lines with small dots are given by the exact formula (8.14) assuming that there is only one tachyon and it is located on the real axis. There is one such line for each positive $\tilde{\alpha}$ but they are always very close to the exact boundary. The dashed lines are given by the large $|\nu|$ and large a approximation (8.19).

the figure should contain a single tachyonic pole on the real axis. The boundary between these two regions should correspond to the value of the curvature when $a = 0$, i.e. where (8.12) is an equality.

We have checked how well the analytic large- $|\nu|$ approximation matches the numerical results: in the region where $a > 0$ (left part of Figure 7), the analytic approximation (8.19) is represented by dashed lines. On the right, where $a < 0$, the approximation (8.14) is represented by dotted lines. The two analytic regimes are separated by a critical value of the curvature given by the value that saturates (8.12). For curvatures above this value, there is a single tachyonic pole located on the real axis. This critical curvature exists only for $\tilde{\alpha} > -1/2$. For $\tilde{\alpha} < -1/2$, the large- $|\nu|$ approximation (8.19) extends to all curvatures and leads to a monotonic behaviour of $\tilde{\beta}_{\text{eff}}^{\text{critical}}$ as a function of the curvature.

The analytical approximations do not exactly match the numerical results, especially the dashed lines when curvatures are not small. However, we can observe in Figure 7 that

large curvatures are very well described by the exact formula (8.14), where (8.12) holds. In the large- $|\nu|$ regime, a single tachyonic pole is located on the real axis, and we have assumed that it would stay on the real axis even for $\nu = 3/2$ while entering the stability zone. This hypothesis seems to be confirmed by the numerics because dotted lines (approximation) coincide with the large circles (numerics).

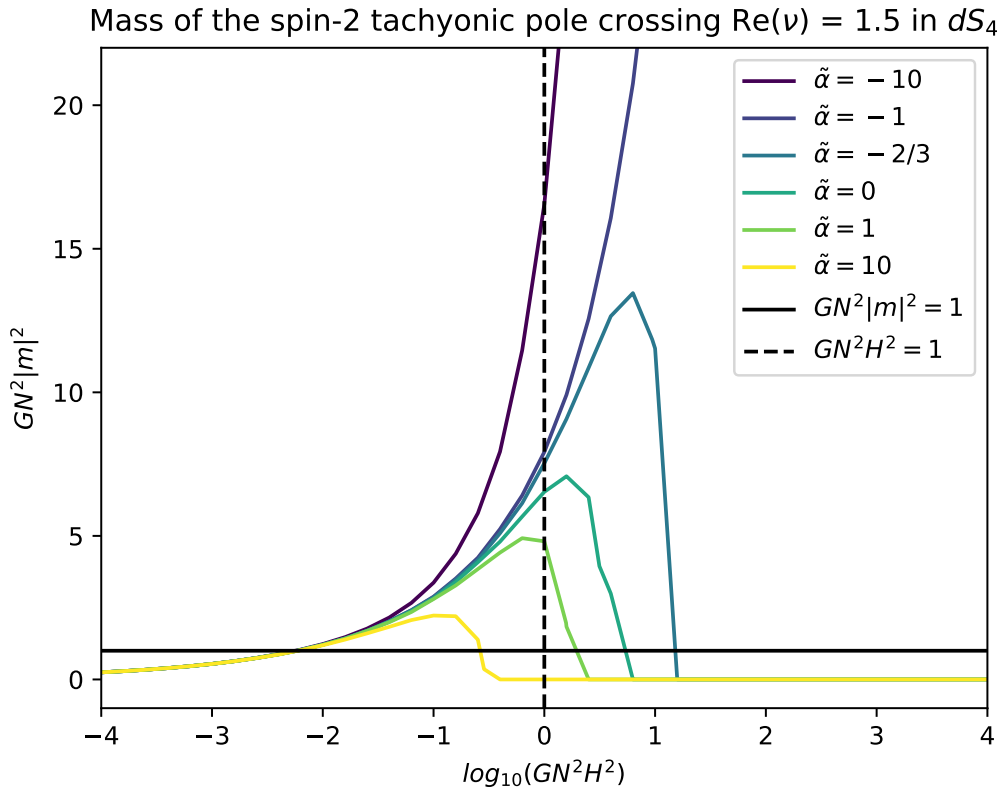


Figure 8: Mass of the spin-2 tachyonic instability of de Sitter space when it crosses the $\text{Re}(\nu) = 3/2$ line, for a given set of parameters $(\tilde{\alpha}, GN^2H^2)$ while varying $\tilde{\beta}_{\text{eff}}$. The mass is plotted in units of the species scale (1.7). Each coloured curve is a different choice of $\tilde{\alpha}$.

Figure 8 shows the mass of the spin-2 tachyonic instability of de Sitter for the value of $\tilde{\beta}_{\text{eff}}$ at which it stops being tachyonic ($\text{Re}(\nu) = 3/2$). The mass is plotted as a function of the curvature for different values of $\tilde{\alpha}$. The remaining parameter is then $\tilde{\beta}_{\text{eff}}$, which is then fixed by the $\text{Re}(\nu) = 3/2$ requirement. At this transition between tachyonic and non-tachyonic, we measure the mass numerically and report it on the figure. We observe in this figure that the mass is below the cutoff for small curvatures. The mass starts to move above the cutoff at curvatures around $GN^2H^2 \approx 10^{-2.22}$ for $\tilde{\alpha} = 10$ and $GN^2H^2 \approx 10^{-2.25}$ for $\tilde{\alpha} = -10$. The value of $\tilde{\alpha}$ does not play an important role in the regime of such small curvatures because we are close to the flat space case in which the spin-2 pole locations do not depend on $\tilde{\alpha}$. The tachyonic pole eventually goes back beyond the species cutoff for large curvatures if $\tilde{\alpha}$ is not too negative. For example, for $\tilde{\alpha} = -2/3$, the mass goes beyond

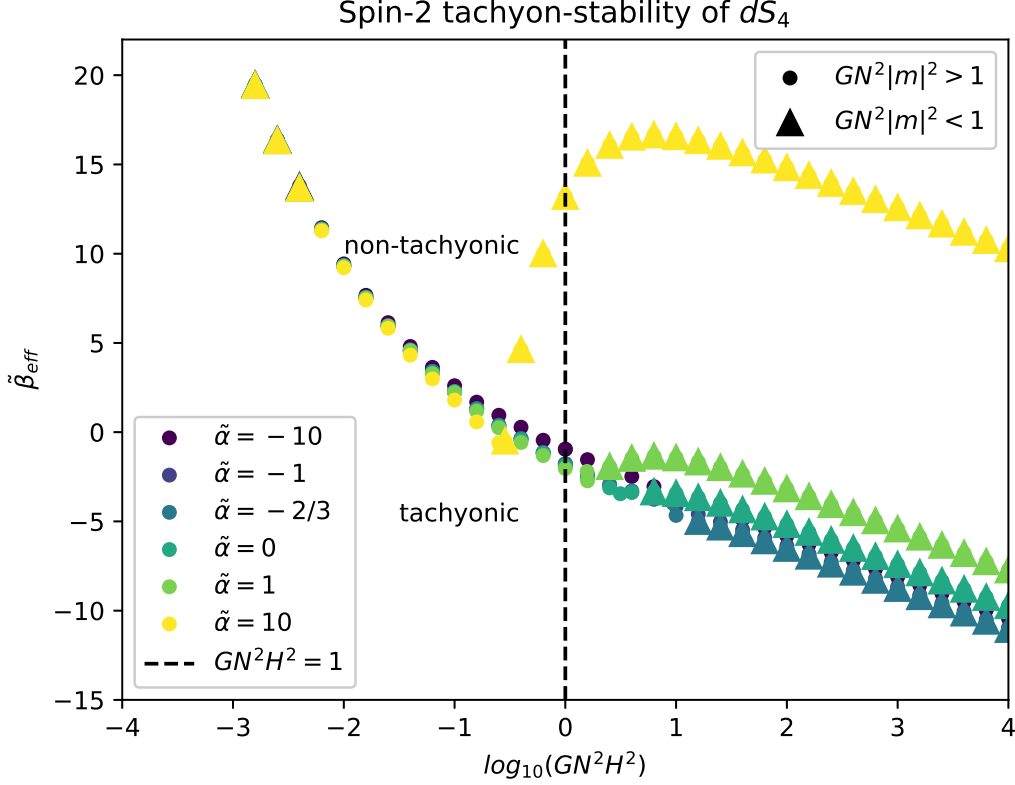


Figure 9: Spin-2 tachyonic instability of de Sitter space depending on $\tilde{\beta}_{\text{eff}}$ and the curvature H , for different values of $\tilde{\alpha}$. Markers are placed on the boundary $\text{Re}(\nu) = 3/2$ between the tachyonic and non-tachyonic regions which have been computed numerically. Each colour corresponds to a given value of $\tilde{\alpha}$. For each coloured curve, we are in a tachyonic regime ($\text{Re}(\nu) > 3/2$) below the markers, while the region above is non-tachyonic ($\text{Re}(\nu) \leq 3/2$).

the cutoff at $GN^2H^2 \approx 10^{1.2}$ which is itself above the species cutoff at $GN^2H^2 = 1$. It is then possible to identify the points of Figure 7 which are above the species scale. This additional information is shown in Figure 9, which is similar to Figure 7, except that triangles correspond to poles with mass below the species cutoff whereas large dots have a mass larger than the cutoff.

Figure 10 is a different representation of the critical value of $\tilde{\beta}_{\text{eff}}$ which separates the tachyon-stable from the tachyon-unstable regime: in this figure, the colour code corresponds to the critical value of $\tilde{\beta}_{\text{eff}}$ which separates between tachyon-stable and tachyon-unstable in the $(\tilde{\alpha}, GN^2H^2)$ parameter space. It also compares the value of $\tilde{\beta}_{\text{eff}}$ obtained numerically with the analytical approximations (8.14) and (8.19). Each row of this figure gives a different window for $(\tilde{\alpha}, GN^2H^2)$. The top row gives a more extensive view while the bottom row is a zoom on a space where the analytics are supposed to break down. The right panels correspond to the analytical approximations (8.19 - 8.14) with a larger number of pixels than the numerics given on the left panels.

The apparent discontinuity in the right panels comes from a junction between approx-

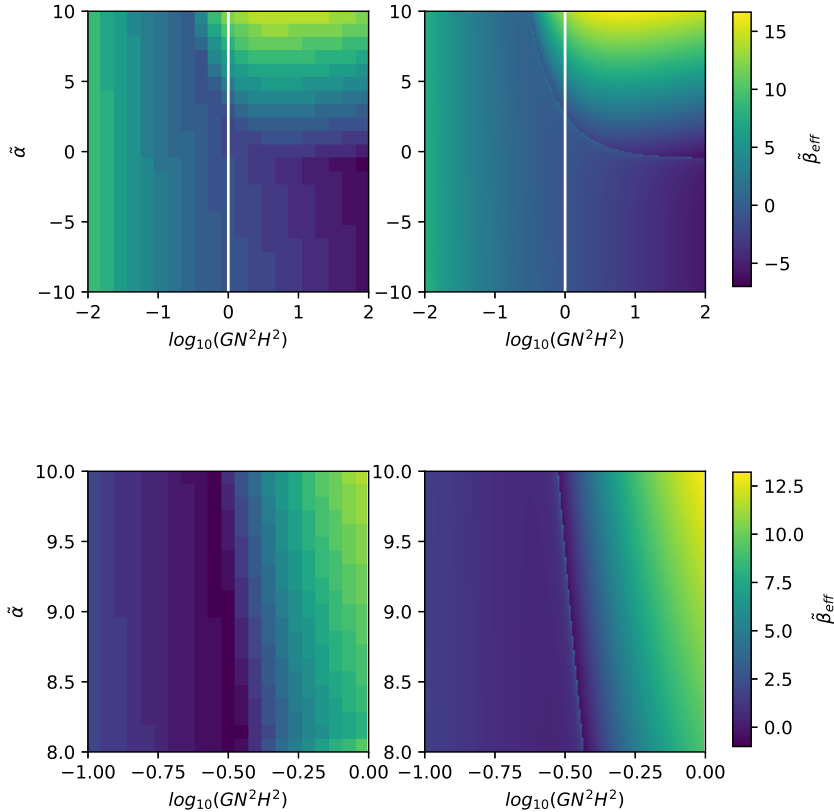


Figure 10: Values of $\tilde{\beta}_{\text{eff}}$ such that de Sitter space goes from tachyonic-unstable to tachyonic-stable for the spin-2 mode, plotted in the $(\tilde{\alpha}, GN^2H^2)$ plane. For each pixel, values of $\tilde{\beta}_{\text{eff}}$ lower than the given colour corresponds to instability, and higher values correspond to stability. The white vertical line on the top row panels is the separation between curvatures above and below the species cutoff (1.7). The right panels are obtained using large- $|\nu|$ analytical approximations, while the left panels are numerical results. As it was done for Figure 7, approximations are split into two regimes: if the inequality (8.12) holds, then (8.14) is used. Otherwise, (8.19) is used. The bottom panels are zoomed on a smaller parameter space, where the analytical approximation is supposed to break down around $a \approx 0$ (8.7), which corresponds to the contour of the area on the top right of each panel.

imation (8.14) for real-axis tachyon and (8.19) for complex tachyon. Around this junction, the large- $|\nu|$ approximation is not valid anymore. The discontinuity which is visible on both panels on the right is an artefact of the large- $|\nu|$ approximation and is absent from the numerics in the middle panels. Instead of a discontinuity, one can observe a valley of values for $\tilde{\beta}_{\text{eff}}$ which are lower than expected by the analytics. This behaviour could also be observed in Figure 7 at the minima of $\tilde{\beta}_{\text{eff}}$.

Figure 7 separates tachyonic from non-tachyonic regions, but it does not contain any information on the location of the poles, which encodes the characteristic scale of the tensor tachyonic instability. In what follows, we investigate this scale numerically.

The instabilities of the tensor sector are studied in Figure 11. The colour coding

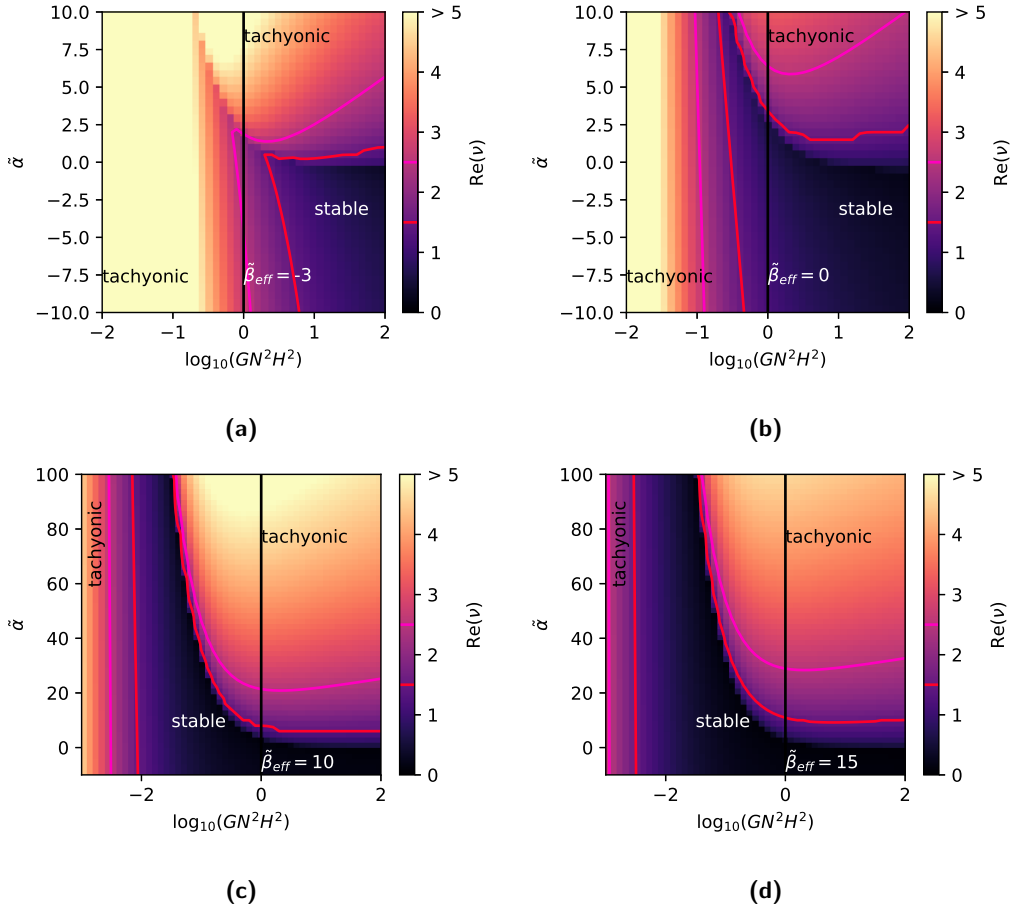


Figure 11: Regions and inverse time-scale of the tachyonic instability (defined in (8.2) for the spin-2 sector in the de Sitter case. The colour code of each of the figures above gives the value of the real part of ν at the zero of the inverse propagator (5.39) for a given value of $\tilde{\beta}_{\text{eff}}$. The black vertical line separates curvatures which are below the species cutoff defined in (1.7) from curvatures which are above. The unstable region (5.28) is delimited by the red lines where $\text{Re}(\nu) = 3/2$. The pink lines are placed at $\text{Re}(\nu) = 5/2$, where the inverse time scale of the tachyonic instability (8.2) has the value $\Gamma = H$. As $\tilde{\beta}_{\text{eff}}$ increases, the stability region becomes larger.

corresponds to the real part of ν for the tachyonic modes⁴¹. This is the quantity that controls the divergence rate of the mode, via equation (8.2). The red line $\text{Re}(\nu) = 3/2$ separates tachyon-unstable from tachyon-stable regions. The four different sub-figures of Figure 11 show, using a colour code, the size of $\text{Re}(\nu)$ as a function of two of the parameters ($\tilde{\alpha}$, GN^2H^2), for fixed values of $\tilde{\beta}_{\text{eff}}$. The four sub-figures correspond to different values of $\tilde{\beta}_{\text{eff}}$. We observe that there are two tachyonic regions, one for low enough values of $\log(GN^2H^2)$, the other for large values of both $\tilde{\alpha}$ and $\log(GN^2H^2)$. As $\tilde{\beta}_{\text{eff}}$ increases, these two regions move out in parameter space. In this figure, the word “stable” refers exclusively to the absence of tachyonic instabilities: we remind the reader that there are always ghost-like spin-2 poles at all points in parameter space. We shall come back to these

⁴¹It should be remembered that ν controls the mode mass in units of the dS Hubble scale.

modes at the end of this section.

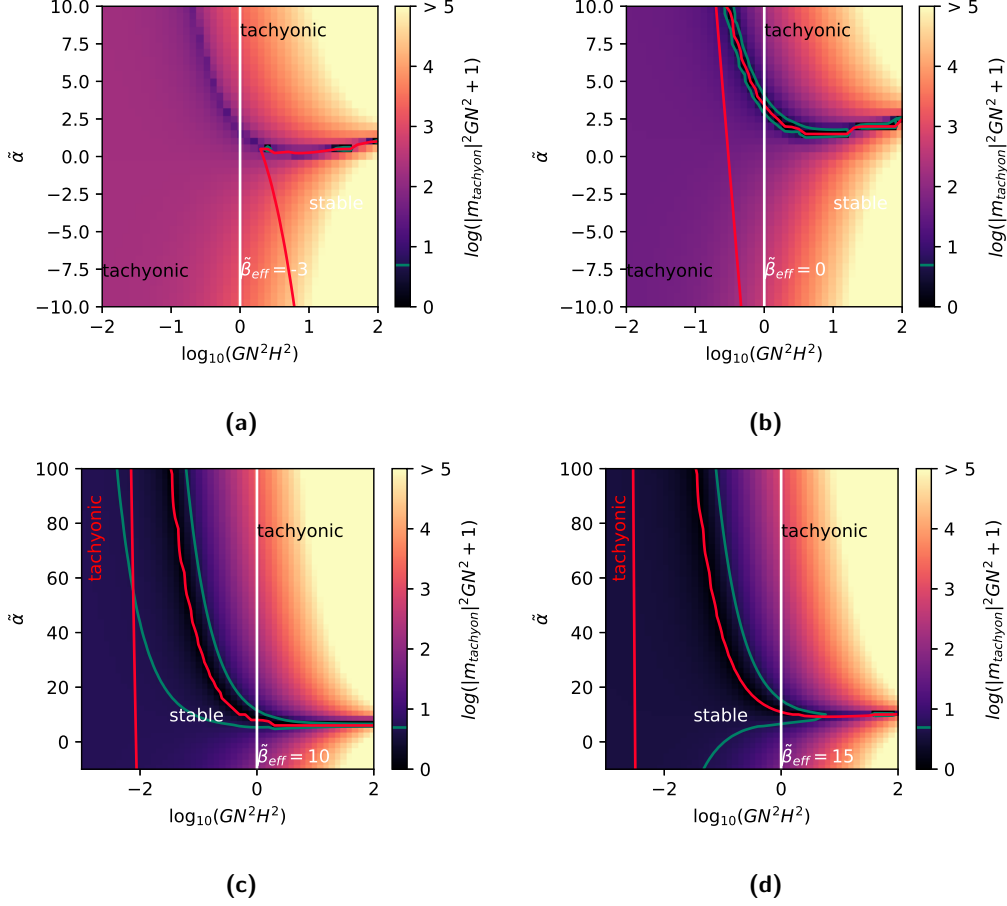


Figure 12: $|Mass|^2$ (5.26) of the de Sitter spin-2 lightest tachyonic pole in units of the species scale (1.7), plotted in the $(\tilde{\alpha}, GN^2 H^2)$ plane. The red line separates the tachyonic region from the non-tachyonic region obtained from Figure 11. The green curve corresponds to the species scale $GN^2 |m|^2 = 1$. The vertical white line separates curvatures that are below the species scale (on the left) from curvatures which are above (on the right). In the two first panels, the mass of the tachyonic pole is always larger than the species scale. The two bottom panels show that a larger $\tilde{\beta}_{\text{eff}}$ allows for some tachyonic poles under the species scale but only for small curvatures or large $\tilde{\alpha}$. In the last panel, the small curvature region is entirely below the species cutoff.

Figure 12 shows the mass squared (5.26) of the lightest spin-2 tachyonic pole in units of the species scale (1.7). The red curves obtained from the previous Figure 11 delimit the tachyonic regions in the plane $(\tilde{\alpha}, GN^2 H^2)$. Whereas the green curve corresponds to the species scale $GN^2 |m_2|^2 = 1$. The darker regions which are delimited by the green curve are then below the species cutoff. Each panel of Figure 12 corresponds to a different value of $\tilde{\beta}_{\text{eff}}$. Negative values, such as $\tilde{\beta}_{\text{eff}} = -3$ plotted in panel (a) contain a large tachyonic region, but the tachyon is always above the cutoff. When $\tilde{\beta}_{\text{eff}}$ is increased, the non-tachyonic region becomes larger. The small areas in panel (b) where the pole is below the cutoff are included in the non-tachyonic regions. Therefore, the tachyon is always above the cutoff in panel

(b) too. For larger values of $\tilde{\beta}_{\text{eff}}$, such as $\tilde{\beta}_{\text{eff}} = 10$ in panel (c), we finally observe some overlap between the tachyonic and light (below the cutoff) regions. It means that around $\tilde{\beta}_{\text{eff}} \approx 10$ and above, de Sitter can contain a tachyon which lies below the effective cutoff of the species scale. Increasing $\tilde{\beta}_{\text{eff}}$ even more, such as in panel (d), the light tachyonic regions increase in size, the small curvature tachyon is then always below the cutoff, whereas the larger curvatures necessitate a large $\tilde{\alpha}$ to get a light tachyon.

It seems from Figure 12, that around $\tilde{\beta}_{\text{eff}} \approx 10$ and above, the small curvature region goes below the cutoff. This can be understood from inserting equation (8.15) into $|m_2|^2 \approx GN^2 H^2 |\nu|^2 \leq 1$, which would correspond to the relation between $\tilde{\beta}_{\text{eff}}$, $\tilde{\alpha}$ and the curvature such that the complex pole (with $\text{Re}(\nu) = 3/2$) is below the cutoff. For small curvatures ($GN^2 H^2 \ll 1$), this relation is

$$\tilde{\beta}_{\text{eff}} \geq \tilde{\beta}_{\text{eff}}^{\text{species}} \equiv \sqrt{16\pi^2 - 1} - \log(4\pi) + \frac{1}{2} - 2\gamma_E \approx 9.34. \quad (8.20)$$

If the inequality (8.20) holds, the small curvature region lies below the species cutoff. This value agrees with panel (d) of Figure 12, where we observe that small curvatures are below the cutoff. However, in panel (c), $\tilde{\beta}_{\text{eff}} = 10 > 9.34$ so small curvatures should lie below the cutoff. However, we observe that this is not the case. The value obtained in (8.20) does not only rely on a small curvature approximation but also on the validity of the ansatz (8.15) for large a , which converges rather slowly with first corrections given in (8.16). In particular, for $\tilde{\beta}_{\text{eff}} = \tilde{\beta}_{\text{eff}}^{\text{species}} \approx 9.34$ and $GN^2 H^2 = 10^{-3}$, the $\log(\log(-a))/\log(-a)$ correction term in (8.16) is approximatively equal to 0.2. This error propagates into the value obtained for $\tilde{\beta}_{\text{eff}}^{\text{species}}$, which could explain why the left of the panel (b) disagrees with (8.20). Moreover, the correction term in (8.16), does not go to zero when $GN^2 H^2 \rightarrow 0$ but converges to a finite value around 0.2 for $\tilde{\beta}_{\text{eff}} = \tilde{\beta}_{\text{eff}}^{\text{species}}$. The only way to make this error vanish is the $\tilde{\beta}_{\text{eff}} \rightarrow +\infty$ limit.

Figure 13 shows the analysis of the instabilities in the scalar sector. Plotting this figure does not require a numerical approach, since the scalar propagator (4.11) is directly written as a pole for the Laplacian operator \square . Formulae (4.13) and (4.19) are used to plot the criterion for tachyonic and ghost-like instabilities respectively. In this case (unlike for the tensor) we can display both ghost-like and tachyonic instabilities on the same figure because there is only one pole in the scalar case (4.11). On the left subfigure, we plot the real part of ν as a function of the different parameters (in the scalar sector, the equation of motion does not depend on $\tilde{\beta}_{\text{eff}}$). Tachyonic regions are delimited by red lines and ghost-like regions by blue lines. On the right subfigure, we plot the effective mass of the scalar mode in units of the species scale $(GN^2)^{-1/2}$, see equation (1.7).

From figure 13 we see that the scalar ghost is below the species scale (1.7) for large enough values of $\tilde{\alpha}$. For reasonable values of $GN^2 H^2$ (below or comparable to the species scale), this ghost is also a tachyon. Therefore, we focus on tachyonic stability for the scalar mode in the following.

In Figure 14 we compare the “strength” of the tensor tachyonic instability with that of the scalar tachyonic instability. By strength, we mean the inverse time scale associated with the instability, defined by Γ in (8.2). The decay rate Γ of the scalar sector is given

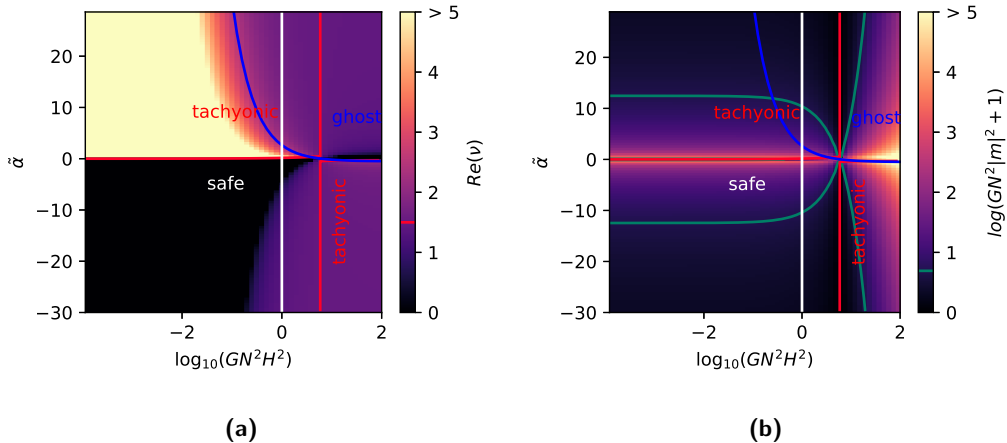


Figure 13: Regions of instabilities for the spin-0 sector in the de Sitter case. The colour code on the left panel indicates the real part of the solution ν of the scalar sector plotted in the $(\tilde{\alpha}, GN^2H^2)$ plane. Tachyonic regions (4.27) are delimited by red lines. They correspond to regions where $\text{Re}(\nu) > 3/2$. The blue line delimits the region given by (4.13) where the scalar solution becomes a ghost. A white vertical line separates curvatures which are above (on the right) and below (on the left) the species scale (1.7). The green curve corresponds to the species scale $GN^2|m|^2 = 1$. On the right panel, we compare the mass of the scalar solution with the cutoff of the theory, given by the species scale. For most of the ghost regions, the ghost is very massive compared to the cutoff. For $\alpha = 0$, the kinetic term of the scalar mode vanishes. The tachyon is also heavier than the species cutoff, except in the top left region for small curvatures and large $\tilde{\alpha}$.

in (4.28), while it is computed numerically for the tensor sector in Figure 11. For fixed $\tilde{\beta}_{\text{eff}}$, the regions in the (α, GN^2H^2) plane where the tensor instability is stronger than the scalar one are coloured in green; in blue regions, the scalar tachyon instability is stronger; in white regions, there are no tachyonic instabilities.

It is interesting to compare our results with those obtained by Vilenkin in [53] for the (original) Starobinsky model. In this work, the renormalized cosmological constant was chosen to vanish, i.e. $\Lambda = 0$ in our equation (2.57). This choice corresponds to the red vertical line in the four subfigures of Figure 14. In [53], the value of $\tilde{\beta}_{\text{eff}}$ was irrelevant as this work concerned only the scalar mode. Vilenkin found that the scalar mode was unstable for large negative $\tilde{\alpha}$. According to our results in Figure 14, in his case, the scalar instability was indeed the strongest instability for small values of $\tilde{\beta}_{\text{eff}}$. However, our results extend also to other regions. We observe that for small values of $\tilde{\beta}_{\text{eff}}$ and large and negative values of $\tilde{\alpha}$, for sufficiently small GN^2H^2 , the tensor tachyonic instability dominates over the scalar one. There are other regions in which the spin-2 instability is the strongest. Moreover, there are smaller regions (in white) which are tachyon-stable. These regions grow in size as $\tilde{\beta}_{\text{eff}}$ becomes large and positive, and shrink as $\tilde{\beta}_{\text{eff}}$ becomes large and negative.

As we have mentioned, in the regions denoted “stable” in Figure 11, all tensor modes are non-tachyonic. However, even in those regions, as we have seen in subsection 8.1, there is always one ghost pole⁴². Its residue can be positive or complex. This was already seen

⁴²Except for some fine-tuned values of the parameters for which two poles merge to form a double pole.

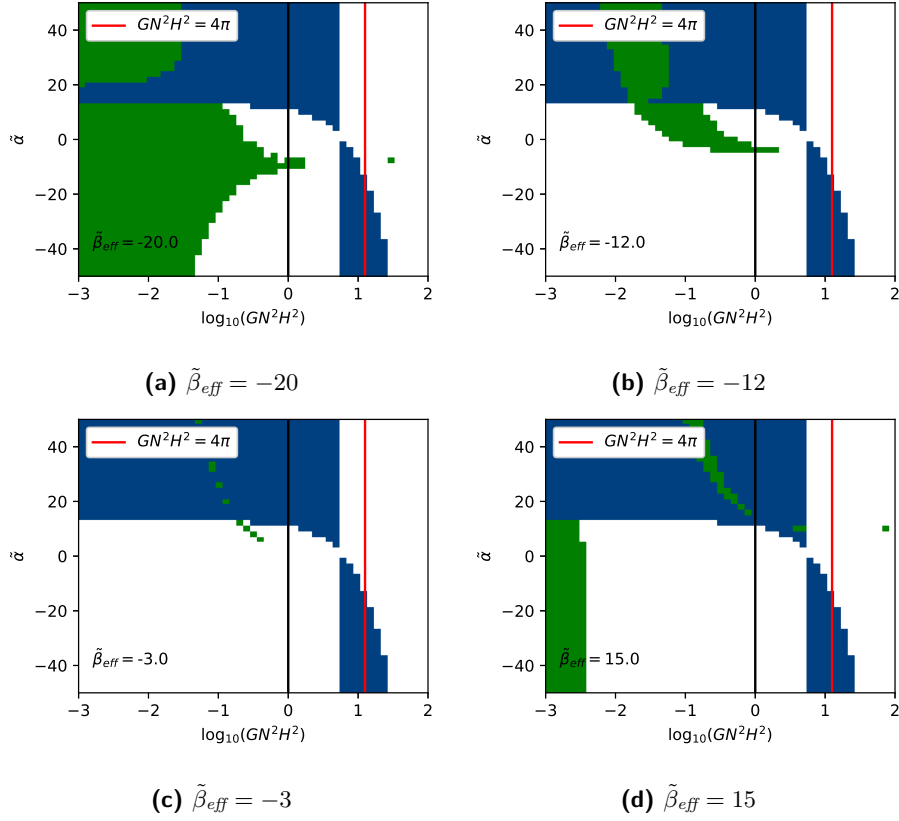


Figure 14: Regions of parameter space in de Sitter, for several values of $\tilde{\beta}_{\text{eff}}$, showing whether the strength of the tensor tachyonic instability is larger or smaller than the strength of the scalar tachyonic instability. In green regions, the tensor tachyon instability dominates. In blue regions, the scalar tachyon instability dominates. In white regions, there are no tachyonic instabilities (if there is one, its mass is above the cutoff). In this figure, we only consider tachyonic poles which are below the species cutoff. The vertical black line separates curvatures which are below (left) and above (right) the species cutoff. The red line in the plots corresponds to the value of the curvature chosen in [53], which can be obtained by setting the renormalized cosmological constant Λ to zero, as it was done in (2.57). At this fixed curvature, the scalar instability dominates over the tensorial instability for negative $\tilde{\alpha}$. The last panel shows the region which is tachyonic for large values of $\tilde{\beta}_{\text{eff}}$ and small curvatures (see (d) of Figure 12). Increasing $\tilde{\beta}_{\text{eff}}$ will make this region disappear from the selected window because it will move to even smaller curvatures.

in the two examples given by Figures 26 and 27.

One important question is whether the ghost pole is above or below the UV cutoff scale (1.7): if the ghost mass is below the cutoff, then it must be regarded as a true instability of the low energy effective theory. The results of this analysis are shown in Figure 15, in which the colour code represents the mass squared for the spin-2 ghost in units of the species cutoff (1.7). The green line separates the regions where the ghost mass is below the cutoff (darker colours) from the regions where it is above (lighter colours). In this figure, we observe that the ghost becomes lighter and lighter as $\tilde{\beta}_{\text{eff}}$ becomes large and positive, as well as when the parameter GN^2H^2 decreases. In conclusion, de Sitter space-time is

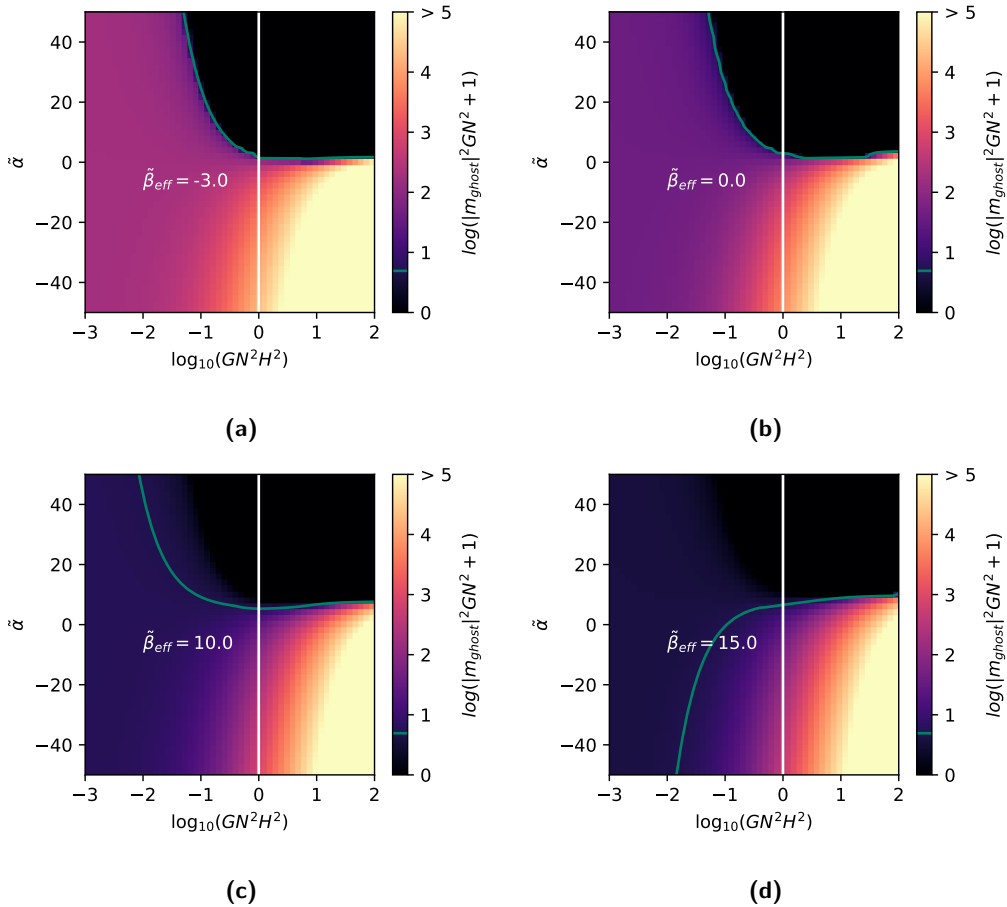


Figure 15: This figure indicates the modulus of the mass squared defined in (5.26), for the ghost pole of the spin-2 propagator (5.39) in units of the species cutoff defined in (1.7), in the de Sitter case. The parameter space is spanned by the dimensionless curvature on the horizontal axis and the R^2 parameter $\tilde{\alpha}$ on the vertical axis. The vertical white line separates curvatures that are above and below the species cutoff. The green line is the boundary of the region where the ghost mass is below the cutoff, which corresponds to darker areas.

generally ghost-unstable for large and positive $\tilde{\beta}_{\text{eff}}$, whereas generic values of $\tilde{\beta}_{\text{eff}}$ are ghost-unstable only in the top-right corner of Figure 15, corresponding to large curvatures and/or large $\tilde{\alpha}$.

9. Poles of the AdS spin-two propagator and stability

We now turn to the negative curvature case, and repeat the same analysis as in the previous for AdS. First, we study two paradigmatic regions of parameters. Then, we provide analytical approximations to understand these two examples. Finally, we study numerically the stability of the system of gravity plus holographic CFT in AdS.

A new feature we find in this case is the presence of an infinite tower of stable solutions which only exists in AdS-slicing. These solutions are found near the poles of the stress-tensor two-point function, which in AdS appear in an infinite discrete set.

9.1 Results for two typical sets of parameters

In this subsection, we focus on two examples (with small and large curvature, respectively), solve the spectral equation (5.52) for tensor modes numerically and follow the evolution of the solutions as we change the parameters. In the following, when it is not specified, it will be understood that we are using the single-boundary condition (5.46), which leads to the inverse propagator $\mathcal{F}_{(-)}$ given in (5.54).

Recall that in the negative curvature case, a tachyon corresponds to a pole on the imaginary axis, see section 5.3 and in particular equation (5.44).

The results of our first example are shown in Figure 39. In this case, we choose a small value of $GN^2\chi^2$ (i.e. the AdS curvature in species-scale units) and $\tilde{\alpha} = 0$. As we can observe from figure 39, large and negative values of $\tilde{\beta}_{\text{eff}}$ always display two tachyons lying on the imaginary axis, with opposite signs for their residues: snapshot (b) shows that the lightest tachyon is also a ghost whereas the heavy tachyon is not. These two tachyon-unstable solutions merge for a value of $\tilde{\beta}_{\text{eff}}$ close to -4.18 , snapshot (c).

For larger values of $\tilde{\beta}_{\text{eff}}$, there are no imaginary solutions and the theory is tachyon-stable. Following snapshots from (d) up to (g), a complex solution moves closer and closer to the real axis when $\tilde{\beta}_{\text{eff}}$ is increased. This solution merges with the lightest stable pole (close to $\nu = 3/2$) and forms a double pole in snapshot (h). If we continue to increase $\tilde{\beta}_{\text{eff}}$, two single poles appear. First, a pole stays close to the massless $\nu = 3/2$, with a negative residue. A second pole moves towards $\nu = 1/2$ with a positive residue. The cloud of stable poles denoted by green points on the real axis is an infinite series of poles lying close to every half-integer: these half-integers are not poles, but zeros of the propagator, corresponding to poles of the stress-tensor two-point function, for which the inverse propagator $\mathcal{F}_{(-)}$ defined in (5.54), diverges. These can be traced back to poles in the harmonic number \mathcal{H} appearing in $Q_{(-)}$ given in (5.53).

The mass of every pole in the snapshots of Figure 39 (except the infinite series of safe poles on the real axis) is plotted in Figure 16. By plotting the masses in units of the species scale, this figure allows us to see directly which pole is above or below the cutoff given by $GN^2|m|^2 = 1$. As a result, for generic values of $\tilde{\beta}_{\text{eff}}$, the tachyon, the ghost and the complex ghost are all above the cutoff. Whereas large values of $|\tilde{\beta}_{\text{eff}}|$ have a ghost-like pole lying below the cutoff, as is also the case for the pure gravity massive pole shown in dashed lines. This figure shows that the two tachyons (the ghost shown in red and the ghost-free in green) merge to form a pair of complex conjugate poles (non-tachyonic). This merging happens at masses that are much above the species cutoff.

Our second example is displayed in Figure 40. In this case, we take the AdS curvature to be of the order of the species scale, specifically $GN^2\chi^2 = \pi/4$. We observe a very different approach to stability as $\tilde{\beta}_{\text{eff}}$ is increased: we have a single tachyon on the imaginary axis, which we observe entering the region shown in snapshot (d), and moves from large imaginary values to small imaginary values until it reaches the origin $\nu = 0$ in snapshot (g). As we further increase $\tilde{\beta}_{\text{eff}}$, the mode becomes stable because the pole moves off the imaginary axes. The tachyon-safe solution converges to $\nu = 1/2$ when $\tilde{\beta}_{\text{eff}}$ is increased to high positive values.

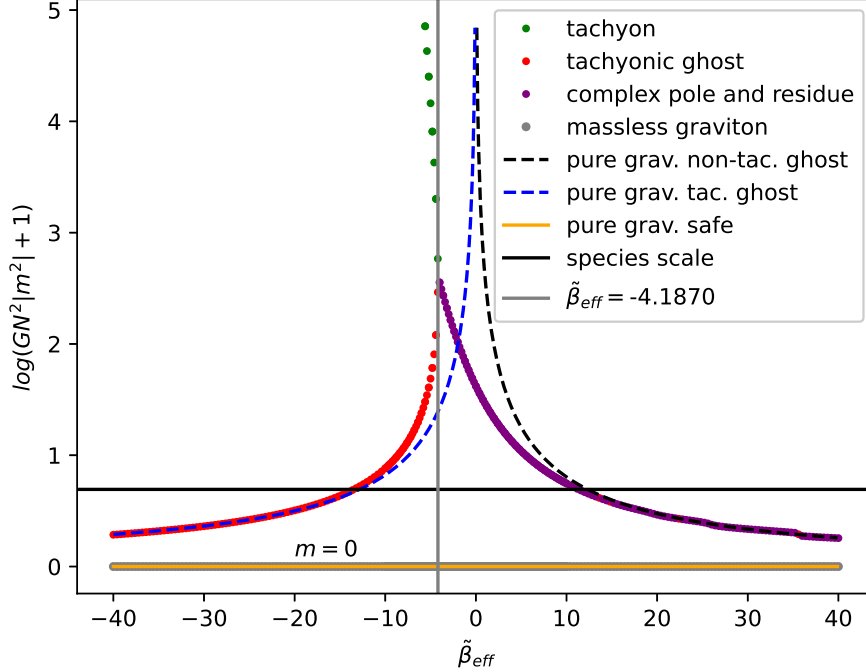


Figure 16: In this plot, obtained with the same parameters as in Figure 39, we show the modulus of the mass of the spin-2 tachyonic poles in AdS, defined in (5.42), in units of the species scale (1.7), as a function of $\tilde{\beta}_{\text{eff}}$. Red and green markers correspond respectively to the light ghost-like tachyon and the heavy non-ghostly tachyon. Purple markers correspond to the complex conjugate pair of poles, which also have a complex residue. The species scale is shown by a horizontal solid black line. Black and blue curves correspond to the pure gravity modes with $\beta = \tilde{\beta}_{\text{eff}}/\pi$: the blue line is tachyonic and the black line is non-tachyonic, both are non-ghostly. The vertical grey line is the value of $\tilde{\beta}_{\text{eff}}$ at which the two tachyonic poles merge and move off the imaginary axis as $\tilde{\beta}_{\text{eff}}$ is further increased. This merging is displayed in snapshot (c) of Figure 39.

It is important to remark that a pole with negative residue (corresponding to a ghost) is present for all values of $\tilde{\beta}_{\text{eff}}$. For large and negative $\tilde{\beta}_{\text{eff}}$, it is close to $\nu = 1/2$, whereas for large and positive values of $\tilde{\beta}_{\text{eff}}$, it approaches $\nu = 3/2$. This can be understood using equation (6.5) which is valid for asymptotically large values of $\tilde{\beta}_{\text{eff}}$ since it was derived for $N = 0$. One can observe that two poles are present in this formula. For large and negative $\tilde{\beta}_{\text{eff}}$, the massless $\nu = 3/2$ poles are healthy residue and the $\nu = 1/2$ is a ghost. This is verified in snapshot (a) where the lightest pole is a ghost, and the first pole after $\nu = 3/2$ is safe. For large and positive $\tilde{\beta}_{\text{eff}}$ the sign of their residue switch. This is observed in the last snapshot where the $\nu = 1/2$ pole is safe whereas the massless $\nu = 3/2$ is a ghost.

Figure 17 shows the mass of the poles that are found in Figure 40. The mass of the poles which are obtained in the presence of the CFT is shown in coloured dots, while the poles which were already present in pure gravity are shown using coloured curves. In this

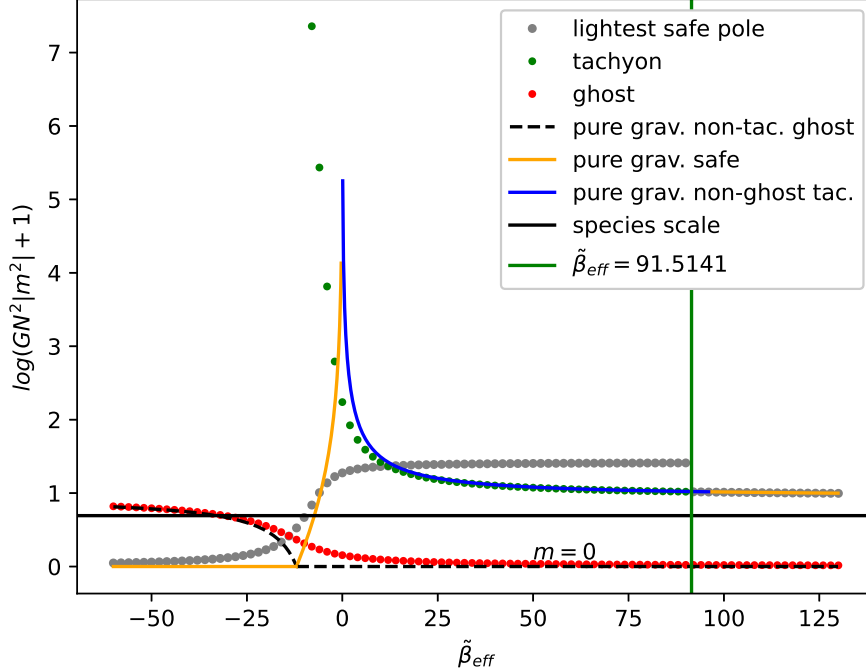


Figure 17: In this plot, obtained with the same parameters as in Figure 40, we show the modulus of the mass of the spin-2 tachyonic poles in AdS, defined in (5.42), in units of the species scale (1.7), as a function of $\tilde{\beta}_{\text{eff}}$. Grey markers show the mass of the lightest safe mode. Red and green markers correspond respectively to the light non-tachyonic ghost and the heavy non-ghostly tachyon. The species scale is shown by a horizontal solid black line. The black, blue and orange curves correspond to the pure gravity modes with $\beta = \tilde{\beta}_{\text{eff}}/\pi$: the blue line is tachyonic, the black dashed line is the non-tachyonic ghost, and the orange line is safe. For pure gravity curves, the vertical axis is $\log(G^{\frac{1}{2}}|m|^2 + 1)$ while the horizontal axis is $\pi\beta$. The vertical green line is the value of $\tilde{\beta}_{\text{eff}}$ at which the tachyonic pole forms a double zero at $\nu = 0$ and becomes real (non-ghostly) as $\tilde{\beta}_{\text{eff}}$ is further increased. This double zero is displayed in snapshot (g) of Figure 40, where the transition between tachyonic and non-tachyonic happens. For larger values of $\tilde{\beta}_{\text{eff}}$, the pole becomes safe. In pure gravity, the tachyonic pole becomes stable at $\pi\beta = 96$, which is slightly different from the value with the CFT given by the vertical green line, where the tachyonic pole stops being tachyonic, crosses the origin at $\nu = 0$ and becomes the lightest safe pole. Larger values of $\tilde{\beta}_{\text{eff}}$ coincide with pure gravity.

plot, we observe that all poles are above the species cutoff except a safe (non-tachyonic, non-ghost) pole for large and negative values of $\tilde{\beta}_{\text{eff}}$ (as in pure gravity) which is massless in the $\tilde{\beta}_{\text{eff}} \rightarrow -\infty$ limit. This pole becomes massive when $\tilde{\beta}_{\text{eff}}$ is increased, while the ghost (in red) moves below the species cutoff. For large and positive values of $\tilde{\beta}_{\text{eff}}$, only the ghost is below the cutoff. Its mass goes to zero in the $\tilde{\beta}_{\text{eff}} \rightarrow +\infty$ limit. This analysis holds in the pure gravity case. Indeed, the only regime where the CFT plays a role is for generic values of $\tilde{\beta}_{\text{eff}}$, where most of the poles have a mass higher than the species cutoff and must therefore be discarded from the EFT analysis.

Qualitatively, the two cases displayed in Figures 39 and 40 represent quite different

behaviours when $\tilde{\beta}_{\text{eff}}$ is varied. We have chosen to discuss only these two cases because they turn out to be paradigmatic of what happens in the whole parameter space. More cases are shown in appendix M, where each point in $(GN^2\chi^2, \alpha)$ space corresponds to a set of snapshots. Each example turns out to have the same behaviour as either one of the two cases already discussed. The ArXiv webpage of this paper contains ancillary files, including animated gifs. Each snapshot of these gifs corresponds to a different value of $\tilde{\beta}_{\text{eff}}$ for fixed $(GN^2\chi^2, \tilde{\alpha})$.

In the following subsection, we present an analytical argument which explains why these two cases are typical of what happens more generally, and how we can distinguish between these two types of behaviour.

9.2 Analytic results for tensor tachyonic modes in AdS in the large- $|\nu|$ regime

Tachyonic modes in AdS correspond to purely imaginary ν . In this section, we provide an analytical approximation which allows us to better understand the two examples given in the previous subsection. This approximation is the limit for large $|\nu|$, in which case the pole mass is much larger than the AdS curvature scale (but it may still lie below the species cut-off).

Interestingly, as was the case in dS, we shall observe that the approximation for large $|\nu|$ turns out to be still valid for poles with values of $|\nu|$ which may even be close to 1. We shall observe that the two cases studied in the previous subsection are paradigmatic: the whole parameter space may be separated into two regions, in which the behaviour of the poles is similar to the one shown in Figures 39 and 40, respectively.

In the large- $|\nu|$ regime, we can use Stirling's approximation (8.3) to replace the harmonic number \mathcal{H} with a simpler log function. The validity of the large- $|\nu|$ approximation will be checked afterwards, by comparing the analytical predictions with numerical evaluations of the inverse propagator.

Using Stirling formula (8.3), equation (5.52) becomes

$$Q_{(-)}(\nu) = 1 + 2 \left(\frac{\pi}{GN^2\chi^2} + \tilde{\alpha} \right) - \frac{\nu^2}{2} \left[\tilde{\beta}_{\text{eff}} - \frac{1}{2} + \log(GN^2\chi^2) + \log(\nu) + \log(-\nu) - 2\gamma_E + \mathcal{O}(|\nu|^{-1}) \right]. \quad (9.1)$$

One can already see the difference with the de Sitter case (8.4): the log is split in a sum which is symmetric in $\nu \leftrightarrow -\nu$. If we write $\nu = |\nu|e^{i\arg(\nu)}$, then

$$Q_{(-)}(\nu) = 1 + 2 \left(\frac{\pi}{GN^2\chi^2} + \tilde{\alpha} \right) - \frac{\nu^2}{2} \left[\tilde{\beta}_{\text{eff}} - \frac{1}{2} + \log(|\nu|^2 GN^2\chi^2) + 2i\arg(\nu) - i\pi\text{sign}(\arg(\nu)) - 2\gamma_E + \mathcal{O}(|\nu|^{-1}) \right]. \quad (9.2)$$

We now apply (9.2) it to tachyonic modes,

$$\nu = ix, \quad x \text{ real}. \quad (9.3)$$

The complex phases cancel in (9.2). Then, the equation of motion (5.52) can be written as

$$X \log X = -a, \quad (9.4)$$

where

$$X \equiv x^2 GN^2 \chi^2 \exp \left\{ \tilde{\beta}_{\text{eff}} - \frac{1}{2} + 2\gamma_E \right\}, \quad (9.5)$$

$$a \equiv 2GN^2 \chi^2 \left[2 \left(\frac{\pi}{GN^2 \chi^2} + \tilde{\alpha} \right) + 1 \right] \exp \left\{ \tilde{\beta}_{\text{eff}} - \frac{1}{2} + 2\gamma_E \right\}. \quad (9.6)$$

This is similar to the corresponding equations we found in the de Sitter case, (8.5), (8.6) and (8.7), up to a few sign flips.

The large x regime described by equations (9.4), (9.5) and (9.6) is valid both for the asymmetric condition in the bulk (5.46), and for the symmetric boundary condition (5.55). To see why this regime is independent of boundary conditions, we observe that the difference between $Q_{(-)}$ (5.53) for single-boundary condition (5.46) and Q_{sym} for the symmetric case (5.55) vanishes exponentially with x .

Similarly to the large $|\nu|$ regime for de Sitter space-time, to discuss equation (9.4) we distinguish three cases :

- If $0 < a < e^{-1}$ there are two tachyonic solutions (x real).
- If $a > e^{-1}$, no real solution for x , the theory is then tachyonic-stable. Therefore, large x solutions are always stable when $a > e^{-1}$. This is equivalent to

$$\tilde{\beta}_{\text{eff}} > \tilde{\beta}_{\text{eff}}^{\text{merge}} \equiv -\frac{1}{2} - 2\gamma_E - \log(2GN^2 \chi^2) - \log \left[2 \left(\frac{\pi}{GN^2 \chi^2} + \tilde{\alpha} \right) + 1 \right], \quad (9.7)$$

which is similar to (8.11) in de Sitter. However, the physics of the poles is different: in de Sitter, β_{merge} does not correspond to a transition from instability to stability, but rather to the merging of two real solutions which then move off the real axis. In AdS on the other hand, (9.7) indicates the critical value at which solutions leave the imaginary axis, and therefore it represents a stability condition, valid for large x and $a > 0$. This condition is valid in the example of Figure 39, where the transition between tachyonic and non-tachyonic behaviour occurs around the value of $\tilde{\beta}_{\text{eff}}$ chosen for the snapshot (c) for which $\tilde{\beta}_{\text{eff}} = \tilde{\beta}_{\text{eff}}^{\text{merge}}$ (9.7).

- If $a < 0$, there is a single tachyonic solution x , whose value decreases when a is increased. In terms of the parameters, the condition $a < 0$ is equivalent to

$$\frac{\pi}{GN^2 \chi^2} < -\tilde{\alpha} - \frac{1}{2}. \quad (9.8)$$

The condition (9.8) for having only one solution $\nu = ix$ is analogous to equation (8.12) in de Sitter, which in that case was the condition for having a single ν on the real axis. However, unlike in dS, in the AdS case, this equation also gives information about the number of tachyons. If (9.8) is verified, we have one tachyon, and if it is not, then we have either none or two tachyons depending on the value of $\tilde{\beta}_{\text{eff}}$ through inequality (9.7).

Interestingly the condition (9.8), like the analogous inequality for de Sitter (8.12), turns out to be the same as the condition (4.13) for the scalar to be a ghost⁴³.

⁴³We do not know whether there is a deep reason for this.

If we select the parameters such that (9.8) is verified, and if the tachyonic pole stays on the imaginary axis even for small values of x where the approximation above breaks down, then this pole should cross the origin $\nu^2 = 0$ (and becomes stable) as $\tilde{\beta}_{\text{eff}}$ is increased. This corresponds to the usual BF bound, which is respected for positive ν^2 . Increasing $\tilde{\beta}_{\text{eff}}$ increases a , such that the unique solution for x decreases. At some point, x eventually crosses the origin at $x = 0$ and the pole becomes non-tachyonic. Therefore, the tachyon-stability condition for negative a corresponds to

$$\tilde{\beta}_{\text{eff}} \geq \tilde{\beta}_{\text{eff}}^{\text{BF}} \equiv \frac{1}{2} - \log(GN^2\chi^2) - 2\mathcal{H}(-1/2) - 8 \left[1 + 2 \left(\frac{\pi}{GN^2\chi^2} + \tilde{\alpha} \right) \right], \quad (9.9)$$

where $\tilde{\beta}_{\text{eff}}^{\text{BF}}$ corresponds to the value for which we have $Q_{(-)}(0) = 0$. The stability condition (9.9) is different from (9.7) because it applies to the $a < 0$ case. In the large- x approximation, the tachyon stays on the imaginary axis as we vary a . If this statement continues to hold for small x down to $x = 0$ where this solution becomes non-tachyonic, then the formula (9.9) would give an exact stability condition. This is indeed what happens in the example of Figure 40: the formula (9.9) describes exactly the transition and gives an accurate condition for the onset of the tachyonic instability, as we chose $\tilde{\beta}_{\text{eff}} = \tilde{\beta}_{\text{eff}}^{\text{BF}}$ in snapshot (g) where the theory is at the transition from tachyon-unstable to tachyon-stable.

Large- $|\nu|$ solutions exist as long as a term in $Q_{(-)}(\nu)$ (5.53) (or $Q_{\text{sym}}(\nu)$) (5.60) is large and positive, which is the case for example when $\tilde{\beta}_{\text{eff}}$ is large and negative or when $GN^2\chi^2$ is small. In the small curvature regime (or in the large and negative $\tilde{\beta}_{\text{eff}}$ regime), the cancellation in the spectral equation can be done using the ν dependent terms $\mathcal{H}(-1/2 \pm \nu)$. This includes two types of solutions. First, large- $|\nu|$ type of solutions were studied in this subsection. Second, ν can be close to a pole of the harmonic number \mathcal{H} . All these poles are located on the real axis, for each half-integer. This second type of solution, which was not present in dS, will be studied in the next subsection. Before that, we first comment on the flat space limit of the AdS spin-2 propagator.

Flat space limit of the AdS spin-2 propagator In the limit of vanishing curvatures $GN^2\chi^2 \rightarrow 0$, the curvature-dependent term of the propagator (5.53 or 5.60 depending on IR conditions) diverges, as it was the case in de Sitter. Indeed, the term $\frac{\pi}{GN^2\chi^2}$ in $Q_{(-)}$ (5.53), must be cancelled by the harmonic numbers $\mathcal{H}(-1/2 \pm \nu)$. This can be done by taking $|\nu|$ large as it was done for de Sitter [74]. However, in AdS, the bulk normalizable modes are present in the inverse-propagator in the form of poles of the harmonic number $\mathcal{H}(-1/2 - \nu)$.

In the flat space limiting procedure, we exclude real-valued ν because they would go to non-tachyonic poles in flat space. To see why we first ask that the flat space limit should be taken such that the eigenvalues of both Laplacians (the AdS₄ Laplacian and the Minkowski Laplacian) match. This requires

$$\nu^2\chi^2 \underset{\chi \rightarrow 0}{\sim} -k^2. \quad (9.10)$$

We then directly observe that real-valued ν corresponds to $k^2 < 0$, which was excluded from the flat space propagator in (5.21). We can therefore ignore real-valued ν and therefore avoid the poles of the harmonic number located on the real axis.

Inserting the large- $|\nu|$ limit into the asymmetric 2-point function of AdS (5.52) or the symmetric one (5.59) leads in both cases to

$$\mathcal{F}_{(-)} \xrightarrow{\chi \rightarrow 0} \frac{N^2 k^2}{64\pi^2} \left\{ \frac{2\pi}{GN^2 k^2} + \frac{k^2}{2} \left[\tilde{\beta}_{\text{eff}} - \frac{1}{2} + \log(|\nu|^2 GN^2 \chi^2) + 2i\arg(\nu) - i\pi \text{sign}(\arg(\nu)) - 2\gamma_E \right] \right\}. \quad (9.11)$$

Comparing this with the flat space propagator (5.21), we find that

$$\mathcal{F}_{(-)}(\nu) \xrightarrow[\chi \rightarrow 0]{k^2 \rightarrow -\nu^2 \chi^2} \mathcal{F}_{\text{flat}}. \quad (9.12)$$

The terms involving the complex phase $\text{Arg}(\nu)$ in (9.11) coincide with the expression of the Minkowski propagator in this limit only if we require

$$\chi\nu \sim \text{sign}(\text{Im}(\nu))ik. \quad (9.13)$$

If ν is imaginary, we recover the purely tachyonic modes where k is real, and therefore $k^2 > 0$. On the other hand, when ν is real, this constraint is ill-defined because $\nu^2 > 0$ corresponds to $k^2 < 0$. In Minkowski space, we have defined the propagator away from the real axis which contains all the healthy propagating modes.

9.3 Infinite series of stable solutions

As one can observe in Figure 40, there is an infinite set of massive solutions on the real axis. It is also remarkable that these poles are not displayed in every snapshot, and this is due to the lack of numerical precision when these poles are too close to a half-integer. There is a pole for every blue circle near each half-integer. In Figure 39, these poles can also be seen (albeit less clearly) for some regions on the real axis. These poles are present for every half-integer but most of them are too close to a pole at half-integers to be resolved by the numerics.

Numerically, one finds that the solutions on the real axis are near each half-integer $\nu = n + 1/2$, where $\mathcal{H}(-\nu - 1/2)$ has poles. To understand this feature is then instructive to expand the harmonic-number function close to its poles:

$$\mathcal{H}(\epsilon - n) = -\frac{1}{\epsilon} + \mathcal{H}(n - 1) + \mathcal{O}(\epsilon). \quad (9.14)$$

Using this expression in equation (5.52), the result for $n > 1$ is:

$$\mathcal{F}_{(-)}(n + 1/2 + \epsilon) = \frac{N^2 \chi^4}{64\pi^2} [a_1 \epsilon^{-1} + a_0 + \mathcal{O}(\epsilon)], \quad (9.15)$$

where

$$a_1 = -\frac{1}{2}(n - 1)n(n + 1)(n + 2), \quad (9.16)$$

$$a_0 = a_1 \left\{ \frac{2n+1}{(n-1)(n+2)} - 2n(n+1) \left[2 \left(\frac{\pi}{GN^2\chi^2} + \tilde{\alpha} \right) + \frac{1}{2} - n \right] + \right. \\ \left. - \frac{1}{2} + \tilde{\beta}_{\text{eff}} + \log(GN^2\chi^2) + 2\mathcal{H}(n) \right\}. \quad (9.17)$$

In the vicinity of half integer $\nu = n + 1/2 + \epsilon$, with $\epsilon \ll 1$, solutions to the spectral equation (5.52) are then given approximately by choosing ϵ small but finite and approximately given by

$$\epsilon \simeq -\frac{a_1}{a_0}. \quad (9.18)$$

A zero of $\mathcal{F}_{(-)}(\nu)$ is then found at

$$\nu_0 \equiv n + \frac{1}{2} + \epsilon. \quad (9.19)$$

Neglecting $\mathcal{O}(\epsilon)$ terms in (9.15), it is then possible to conclude from (9.18) that there is always a solution near a half-integer value of ν as long as $a_1/a_0 \ll 1$. If a_1/a_0 turns out to be of order 1 or larger, then (9.18) cannot be trusted. Since we have a formula both for a_1 and a_0 in (9.17), we can check the value for ϵ for every n . The value of $\epsilon(n)$ is plotted by the green curve in the left panels of Figure 18. The green curves are continuous (not a discrete set of values) because n is replaced by $\text{Re}(\nu) - 1/2$ in this plot. It turns out that most of the $\epsilon(n)$ are small. There are some values of n however, for which $\epsilon(n)$ is large. These values of n which correspond to a large ϵ are centred around a particular value for which $\epsilon^{-1} \sim 0$, where we observe a sign flip of ϵ . This region of the real axis is displayed in Figure 18.

In Figure 18, we observe a small part of the real axis centred to the point where $\epsilon^{-1} \sim 0$. The green lines in this figure show the expected value of $\epsilon(n)$ (9.18) which can be compared to the size of the blue circles. The radius of these circles roughly corresponds to the distance between a half-integer and the closest pole of the propagator. The actual pole of the propagator found numerically, is the intersection between the blue circles and the real axis, where green dots are placed. The green line predicts well the size of the blue circles everywhere, except where it is above 1, as one could have expected. The place where ϵ is supposed to diverge according to (9.18) corresponds to the place in Figure 18 where the unique open blue curve crosses the real axis. The exact place where it crosses lies exactly at a half-integer, and this half-integer corresponds to a value of n for which $\epsilon(n)$ is maximum.

It turns out that the breakdown of the small ϵ expansion, roughly at $\epsilon^{-1} \sim 0$, corresponds to the middle of the cloud of solutions in Figure 39 where the open blue curve crosses the real axis and ϵ changes sign. This region of large values for ϵ is the same as in Figure 39 where the numerics can find these zeros. Large values of ϵ make these blue circles large enough to be resolved by the numerics.

This analysis shows that there is always a solution near a half-integer $\nu = n + 1/2$. The small ϵ expansion is valid for every n , except in an interval where these solutions are not close enough ($\epsilon \sim 1$) to a half-integer. In this region where the approximation cannot

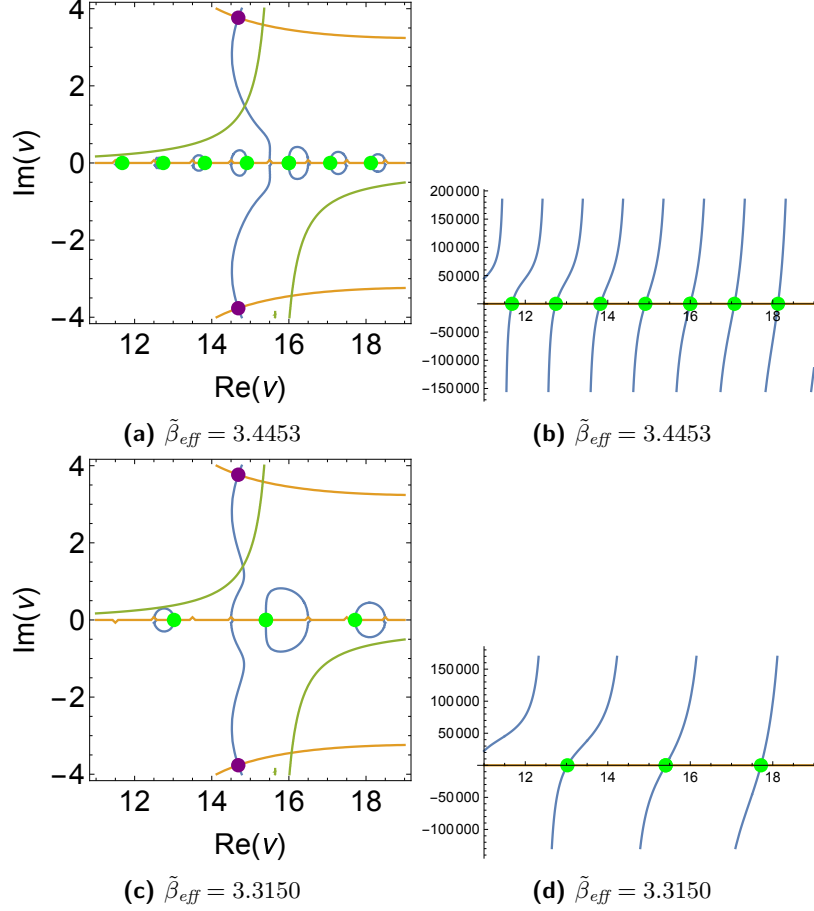


Figure 18: Zeros of the AdS spin-2 inverse correlators $\mathcal{F}_{(-)}$ and \mathcal{F}_{sym} , for a small region in the complex plane of ν (5.42), where the ϵ -approximation (9.14) is expected to break down. Parameters are chosen as $GN^2\chi^2 = 0.01$ and $\tilde{\alpha} = 0$. The left-hand side snapshots show zeros of the real part (blue) and zeros of the imaginary part (yellow) of $\mathcal{F}_{(-)}$ (top plot) and \mathcal{F}_{sym} (bottom plot). The green curve shows the value of $\epsilon(n)$ given by (9.18), it should give an estimate for the size of the blue circles. The approximation breaks down exactly at $n = 15$ since we have chosen $\tilde{\beta}_{\text{eff}}$ to make the circle of the radius diverge exactly there. This is done using (9.18) by solving $\epsilon^{-1} = 0$ for $n = 15$. The right-hand side shows the real part of $\mathcal{F}_{(-)}$ which has a positive slope everywhere it crosses the real axis. Each intersection with the real axis is then a ghost-free pole of the tensor propagator.

be trusted, the numerics in Figure 18 confirm the existence of such solutions even if ϵ is not small.

We shall now investigate whether solutions corresponding to (9.19) are ghost-like. For this purpose, we need to expand the inverse propagator $\mathcal{F}_{(-)}$ (5.54) close to a solution of the form (9.19), such that

$$\nu = n + 1/2 - \frac{a_1}{a_0} + \varepsilon, \quad (9.20)$$

where ε is a book-keeping parameter defined in order to expand $\mathcal{F}_{(-)}$ close to a given zero. When $\varepsilon = 0$, we sit exactly at the zero of the inverse propagator found perturbatively in

(9.15). The expansion of $\mathcal{F}_{(-)}$ near the zero at $\varepsilon = 0$ then reads

$$\mathcal{F}_{(-)}\left(n + \frac{1}{2} - \frac{a_1}{a_0} + \varepsilon\right) = \frac{N^2 \chi^4}{64\pi^2} \left[-\frac{a_0^2}{a_1} \varepsilon + \mathcal{O}(\varepsilon^2) \right]. \quad (9.21)$$

As a reminder of what was done in the dS case (5.63), the residue of the pole of $\mathcal{F}_{(-)}^{-1}$ near ν_0 in the ν^2 plane is given by

$$\text{res}[\mathcal{F}_{(-)}^{-1}](\nu_0^2) = \frac{\nu_0}{\mathcal{F}_{(-)}(\nu_0)} \frac{1}{\nu^2 - \nu_0^2}. \quad (9.22)$$

Therefore, applying this formula to (9.21), we find that the residue of a pole lying close to a half-integer is given by

$$\text{Res}[\mathcal{F}_{(-)}^{-1}([n + 1/2 - a_1/a_0]^2)] = -\frac{64\pi^2}{N^2 \chi^4} \frac{a_1}{a_0^2} \left(n + \frac{1}{2} - \frac{a_1}{a_0} \right). \quad (9.23)$$

Since $a_1 < 0$ the residue (9.23) is positive for the whole tower of massive particles close to half integers. They have the same sign as the massless graviton in AdS with pure gravity. The argument that the residue is positive near the real axis is verified numerically in Figure 18. This Figure shows some poles of the tensor propagators $\mathcal{F}_{(-)}$ and \mathcal{F}_{sym} on the real axis near the region where the ε expansion breaks down. This figure also confirms that ε changes sign where the open blue curve (not the circles) crosses the real axis. This crossing happens at the position of the half-integer for which we have $\varepsilon^{-1} \sim 0$.

For the symmetric boundary condition, the propagator \mathcal{F}_{sym} (5.59) can also be expanded in ε as in (9.18) but with an additional term on the right-hand-side coming from the $\frac{\pi}{\cos \pi \nu}$ piece in (5.59). Using

$$\frac{\pi}{\cos \pi \nu} = \frac{(-1)^n}{\varepsilon} + \mathcal{O}(\varepsilon), \quad (9.24)$$

we obtain new expressions for a_0 and a_1 defined in (9.15) for asymmetric boundary conditions. For symmetric boundary conditions, we define

$$\mathcal{F}_{\text{sym}}(n + 1/2 + \varepsilon) = \frac{N^2 \chi^4}{64\pi^2} [a_1^{\text{sym}} \varepsilon^{-1} + a_0^{\text{sym}} + \mathcal{O}(\varepsilon)]. \quad (9.25)$$

In the case of n odd,

$$a_1^{\text{sym}} = 0, \quad (9.26)$$

which does not allow for a solution near odd half integers. However, if n is even, then

$$a_1^{\text{sym}} = 2a_1, \quad (9.27)$$

which allows for a solution near an even half-integer, but where ε is approximatively twice as big as in the asymmetric case (9.18).

As a consequence, we do not find a linear solution near $n + \frac{1}{2}$ if n is odd for the symmetric boundary condition. This perturbative result is confirmed numerically in the bottom part of Figure 18, where only even integers present a blue circle, which is twice the size of the same circles in the asymmetric case (top panels of Figure 18).

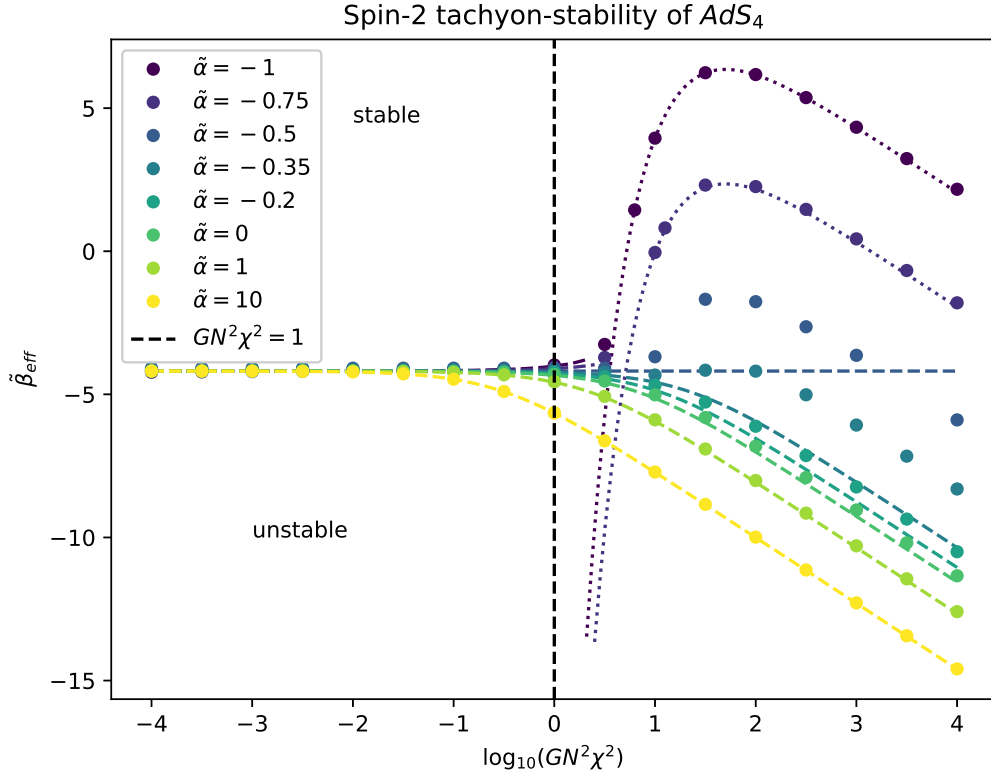


Figure 19: Tachyonic regions of the spin-2 AdS perturbations. Tachyonic regions correspond to the existence of a solution ν to the spectral equation (5.52) such that $\text{Re}(\nu) = 0$ (5.44). Several values of $\tilde{\alpha}$ are taken and stability is plotted in the space of $(\tilde{\beta}_{\text{eff}}, GN^2\chi^2)$. Dashed lines are the analytical predictions obtained from the large $|\nu|$ and large a approximation (9.7). Lines made of small squares are obtained assuming that the tachyonic pole stays on the imaginary axis and becomes stable at the origin (9.9). Large dots are numerical results.

9.4 Tachyons and ghosts in parameter space for the AdS case

We first discuss the tensor sector. The regions of parameter space where tachyonic tensor modes occur in AdS can be read-off from Figure 19, which was obtained by solving the spectral equation numerically. This figure is the negative-curvature analogue of Figure 7.

Figure 19 shows the value of $\tilde{\beta}_{\text{eff}}$ at which the tachyonic pole becomes non-tachyonic, for a given set of parameters $(GN^2\chi^2, \tilde{\alpha})$. When $\tilde{\beta}_{\text{eff}}$ is above the curve shown in this figure, the theory is tachyon-free. As we have seen in the two typical examples in Figures 39,40, the would-be tachyonic pole leaves the imaginary axis at a particular value of $\tilde{\beta}_{\text{eff}}$ and never goes back to the imaginary axis as $\tilde{\beta}_{\text{eff}}$ goes to $+\infty$. Therefore, the critical value of $\tilde{\beta}_{\text{eff}}$ shown in Figure 19 is the border in parameter space between tachyonic and non-tachyonic theories. The dashed coloured lines correspond to the large- $|\nu|$ analytical approximation obtained in section 9.2 for the case $a > 0$ (9.7), whereas the dotted lines correspond to the case $a < 0$ (9.9).

For large $\tilde{\alpha}$ the interpolating curves are monotonic in the curvature, and as $\tilde{\alpha}$ decreases

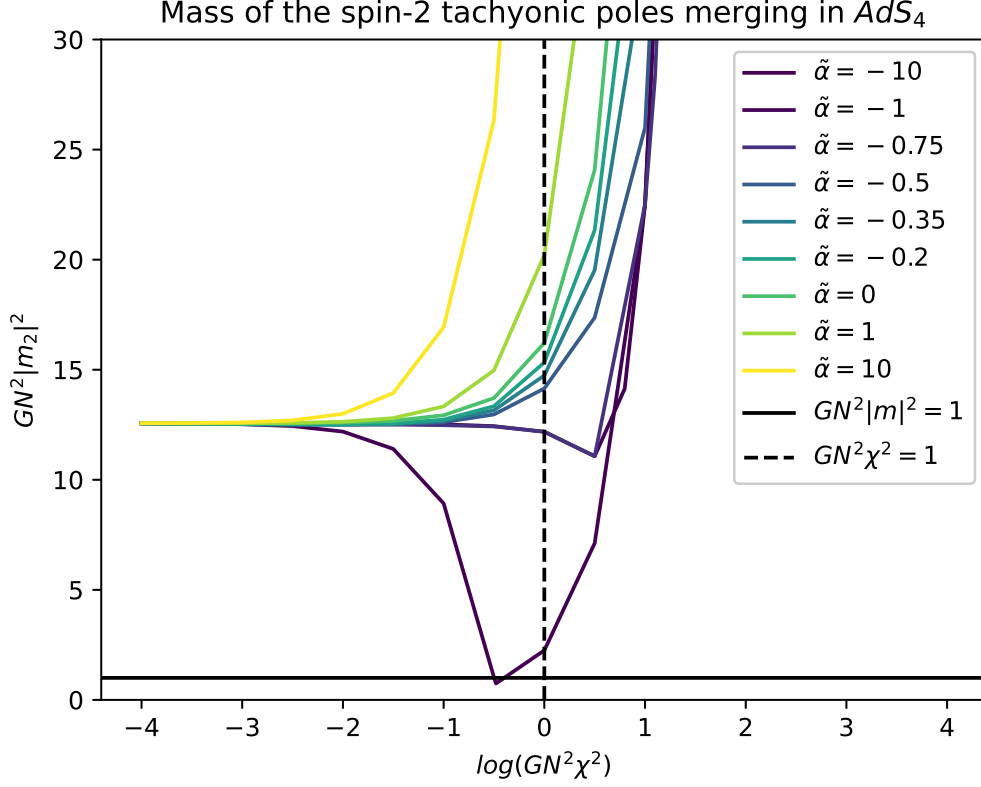


Figure 20: Mass of the spin-2 tachyonic pole of AdS space-time for the value of $\tilde{\beta}_{\text{eff}}$ given by Figure 19. This value of $\tilde{\beta}_{\text{eff}}$ corresponds to the merging of two tachyons on the imaginary axis $\text{Re}(\nu) = 0$, creating a complex pole, which is non-tachyonic ($\text{Re}(\nu) \neq 0$). The mass is plotted in units of the species scale (1.7). Each colored curve is a different choice of $\tilde{\alpha}$.

they start displaying a maximum. From the large- $|\nu|$ approximation we expect there to be a critical curvature, given by equation (9.8), above which a is negative. This is where we decide to start the dotted lines. In the $a < 0$ case, the large- $|\nu|$ approximation suggests that there is only one single tachyon on the imaginary axis. We then make the further hypothesis that the transition from tachyon-instability to tachyon-stability occurs at the origin $\nu = 0$, where the large- $|\nu|$ approximation cannot be valid. However, this hypothesis is verified numerically since the dotted lines agree perfectly with the numerics. An example of such transition was already shown in snapshot (g) of Figure 40.

Figure 20 shows the mass of the spin-2 tachyonic pole of AdS corresponding to the circles of Figure 19, at the value of $\tilde{\beta}_{\text{eff}}$ corresponding to the transition between tachyonic and non-tachyonic regimes. Therefore, the mass plotted in this figure corresponds to a tachyonic pole, lying on the imaginary axis, which is about to merge with another tachyon and leave the imaginary axis for larger values of $\tilde{\beta}_{\text{eff}}$. According to this figure, the transition between tachyonic and non-tachyonic regimes appears to happen always above the species scale, except for large and negative values of $\tilde{\alpha}$, for which the masses are below the species scale in a small interval of curvatures.

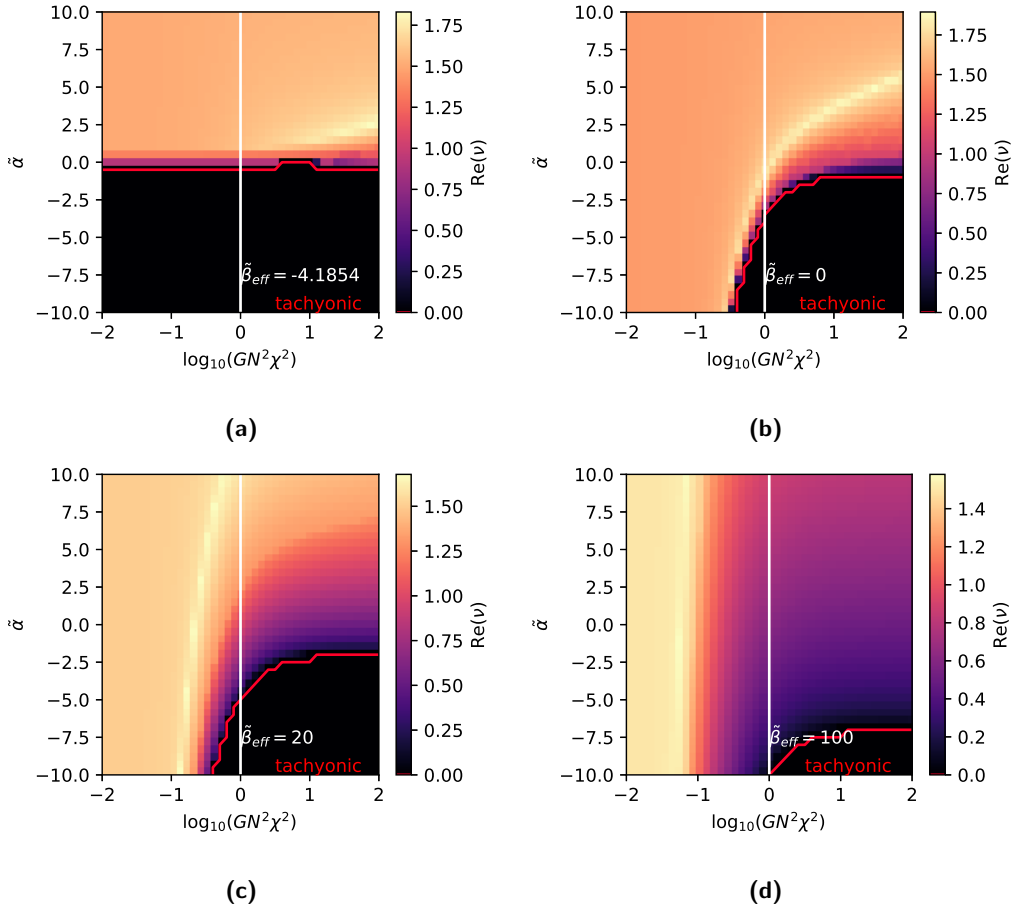


Figure 21: Regions of tachyon-stability of the spin-2 mode in the AdS case. The colour code of each of the subfigures above gives the minimum value of the real part of ν among all the spin-2 poles, at a fixed value of $\tilde{\beta}_{\text{eff}}$. Different panels correspond to different values of $\tilde{\beta}_{\text{eff}}$. The vertical white line separates curvatures that are above and below the species cutoff. The red line separates tachyonic regions with $\text{Re}(\nu) = 0$ as shown in appendix H, from the tachyon-safe regions with $\text{Re}(\nu) \neq 0$. The first panel takes the value corresponding to the zero-curvature limit of (9.7). Increasing $\tilde{\beta}_{\text{eff}}$ moves the tachyonic regions to lower values of $\tilde{\alpha}$ and larger values of $GN^2\chi^2$.

Figure 21 shows the occurrence of tachyon-instability in the tensor sector for a few fixed values of $\tilde{\beta}_{\text{eff}}$, with additional information shown about the value of the real part of the pole which is closest to the imaginary axis (recall that a tachyon corresponds to a purely imaginary ν .) In the first panel (a) the value of $\tilde{\beta}_{\text{eff}}$ corresponds to the critical value separating tachyon-stability and instability in the zero-curvature limit of equation (9.7). As $\tilde{\beta}_{\text{eff}}$ increases above this value (panels (b), (c) and (d)) the small curvature region becomes tachyon-stable as expected from equation (9.7), and the size of the tachyon-stable region increases.

The region marked “stable” in Figure 21 are such only concerning tachyonic instabilities: even in these regions there is always one ghost-like tensor mode. The mass of the ghost (in units of the species scale) is represented by the colour code in Figure 23. Lighter

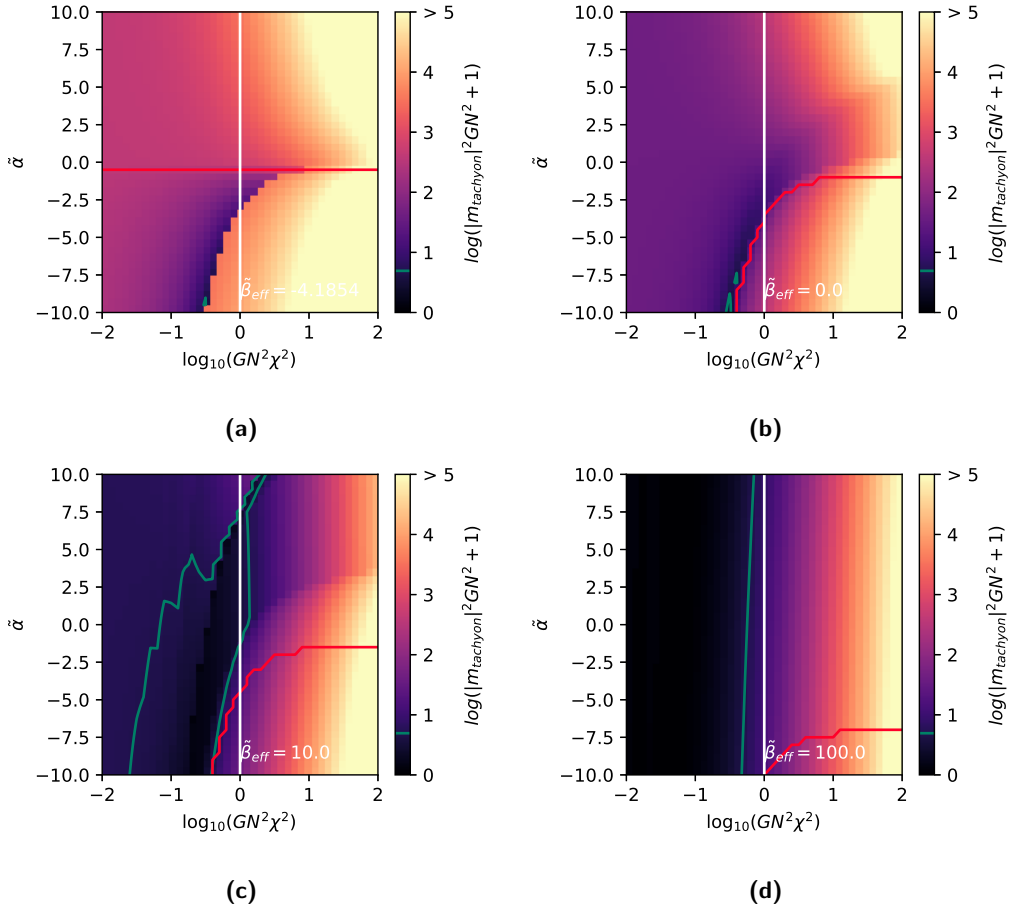


Figure 22: *The would-be tachyonic spin-2 mode in AdS. The colour code of each of the subfigures above represents the mass (5.42) of this pole in units of the species scale (1.7), at a fixed value of $\tilde{\beta}_{\text{eff}}$. The different panels correspond to different values of $\tilde{\beta}_{\text{eff}}$. The first panel takes the value for $\tilde{\beta}_{\text{eff}}$ corresponding to the zero-curvature limit of (9.7), for which asymptotically small curvatures are critical between tachyon-stable and tachyon-unstable. The tachyonic region on the bottom right corner of each panel is delimited by the red line. The cut-off at $GN^2|m|^2 = 1$ corresponds to the green line, which separates masses which are above the cutoff (bright colours) from masses which are below the cutoff (darker colours). The first panel presents a discontinuity in the bottom half (tachyonic region) because the bottom-right corner has only 1 heavy tachyonic pole (as in Fig. 17) while the bottom-left corner has a second tachyonic pole, which is lighter and ghost-like (as in Fig. 16).*

colours correspond to heavier ghosts. The green lines indicate the boundary of the region beyond which the ghost is heavier than the species cut-off, and therefore is outside of the regime of validity of effective field theory.

For small values of $\tilde{\beta}_{\text{eff}}$, the ghost mass is always above the species scale except in a small region for negative values of $\tilde{\alpha}$ (panels (a) and (b)). As $\tilde{\beta}_{\text{eff}}$ is increased to large and positive values, the ghost becomes lighter and lighter. Ghost masses that are below the species scale appear for small curvatures in the last two panels of Figure 23. Increasing $\tilde{\beta}_{\text{eff}}$ even more than 100 will not change the result since the ghost stabilizes at $\nu = 3/2$.

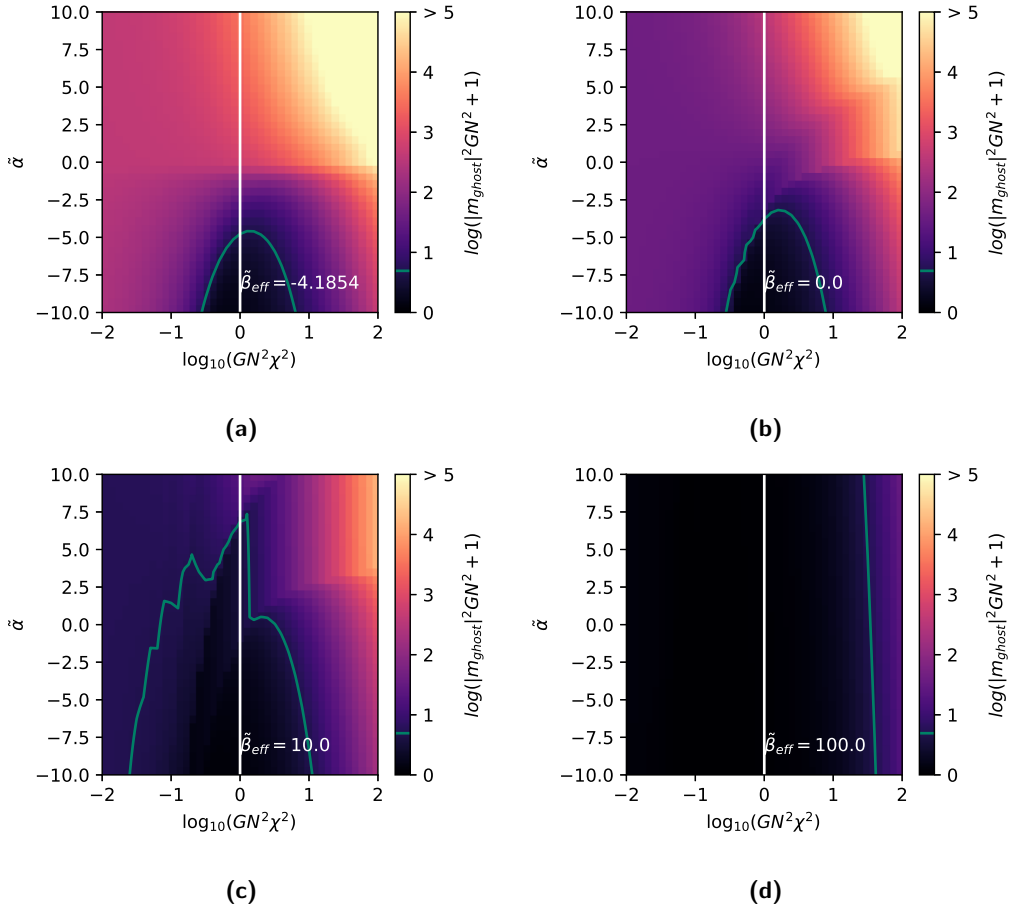


Figure 23: This figure displays the modulus of the mass of the ghost tensor pole in AdS, in units of the species scale (1.7). The colour coding shows the mass of the ghost in units of the species scale in a log scale. Each panel of this figure corresponds to one particular value of $\tilde{\beta}_{\text{eff}}$. The green line shows where the mass is equal to the species cutoff $GN^2|m|^2 = 1$. Darker colours are below the cutoff.

We now turn to the scalar sector which has a single excited mode given by the solution of equation (4.19). Therefore, the graphical representation of ghost-like and tachyon-like instabilities can be given in a single figure. Figure 24 shows the mass of the scalar solution (4.19) in units of the AdS_4 scale χ^{-1} (left panel) and in units of the species scale (right panel). In the scalar sector, only $\tilde{\alpha}$ and the curvature are relevant parameters since $\tilde{\beta}_{\text{eff}}$ does not enter the scalar spectral equation. The red lines separate tachyon-unstable from tachyon-stable regions and correspond to the points where equation (4.22) is saturated. The blue lines separate the regions in which the scalar mode is a ghost from those in which the scalar is healthy, as prescribed by equation (4.13).

Acknowledgements

We would like to thank D. Anninos, M. Kleban, D. Mateos, M. Montero, V. Niarchos, A. Porfyriadis, C. Rosen and I. Valenzuela. E. Kiritsis, F. Nitti and V. Nourry are supported

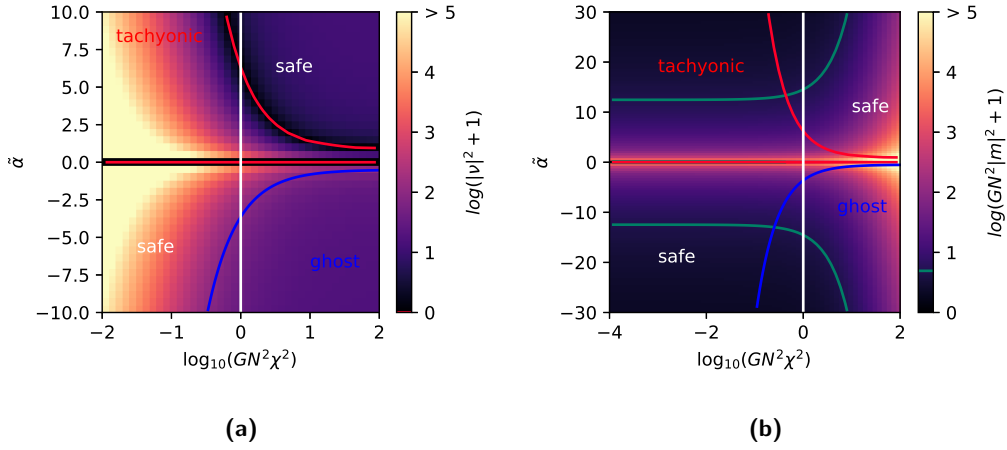


Figure 24: Regions of instabilities for the spin-0 sector in the anti-de Sitter case. The colour code on the left panel indicates $|\nu|^2$. It is plotted as a function of $\tilde{\alpha}$ and $GN^2\chi^2$. Tachyonic regions, where $\text{Re}(\nu) = 0$, are delimited by the red lines and the ghost region is delimited by the blue line using the inequality (4.13). The vertical white line separates the curvatures which are above (on the right) and below (on the left) the species cutoff (1.7). The green curve corresponds to the species scale $GN^2|m|^2 = 1$. On the right panel, we compare the mass of the scalar solution with the species scale (1.7). These diagrams do not depend on $\tilde{\beta}_{\text{eff}}$. On the left of the vertical white dashed line, the AdS scale is below the species cutoff.

in part by CNRS grant IEA 199430.

Appendices

A. Ghosts and tachyons in Effective Field Theory

It is well known that, when starting from a healthy UV theory, ghosts and/or tachyons can appear in effective field theories as an artefact of integrating out some degrees of freedom and performing the low-energy expansion. In these cases, the mass of the unstable mode is always of the order of, or above the cut-off (the mass of the states which were integrated out).

We give an example of this phenomenon in a simple model based on free scalar fields.

A.1 A simple model

Consider two massive scalars coupled to each other.

$$L = \frac{1}{2} [(\partial\varphi_1)^2 - m_1^2\varphi_1^2] + \frac{1}{2} [(\partial\varphi_2)^2 - m_2^2\varphi_2^2] + g\varphi_1\varphi_2 \quad (\text{A.1})$$

This action can be diagonalized by an orthogonal transformation

$$\varphi_1 = \cos\theta\varphi_+ + \sin\theta\varphi_- \quad , \quad \varphi_2 = -\sin\theta\varphi_+ + \cos\theta\varphi_- \quad (\text{A.2})$$

with

$$\tan(2\theta) = \frac{2g}{m_1^2 - m_2^2} \quad (\text{A.3})$$

and the action becomes

$$L = \frac{1}{2} [(\partial\varphi_+)^2 - m_+^2\varphi_+^2] + \frac{1}{2} [(\partial\varphi_-)^2 - m_-^2\varphi_-^2] \quad , \quad 2m_\pm^2 = m_1^2 + m_2^2 \pm \sqrt{(m_1^2 - m_2^2)^2 + 4g^2} \quad (\text{A.4})$$

When

$$g \leq m_1 m_2 \quad (\text{A.5})$$

the theory contains two non-interacting scalars with positive kinetic terms and with $m_\pm^2 \geq 0$. Of course if $m_2 > m_1$ φ_2 is unstable to decay (convert) to φ_1 , but φ_\pm are stable. This is a typical example that will cause oscillations like in the case of neutrinos. φ_\pm are the eigenstates of the Hamiltonian. So we have in terms of one-particle states, for example

$$|\varphi_1(p=0, t)\rangle = \cos\theta e^{im_+t}|\varphi_+\rangle + \sin\theta e^{im_-t}|\varphi_-\rangle \quad (\text{A.6})$$

A.2 EFT

We now assume $m_2 \gg m_1$ and we integrate out⁴⁴ φ_2 . The two equations of motion are

$$(\square + m_1^2)\varphi_1 = g\varphi_2 \quad , \quad (\square + m_2^2)\varphi_2 = g\varphi_1 \quad (\text{A.7})$$

We solve for φ_2

$$\varphi_2 = g(\square + m_2^2)^{-1}\varphi_1 \quad (\text{A.8})$$

⁴⁴We do this by solving the classical equation of motion, but since the theory is Gaussian this is the same as performing the path integral over φ_2 .

and substitute in the equation for φ_1

$$(\square + m_1^2)\varphi_1 = g^2(\square + m_2^2)^{-1}\varphi_1 \quad (\text{A.9})$$

which is obtained from the effective action

$$L_{\text{eff}} = -\frac{1}{2}\varphi_1 [(\square + m_1^2) - g^2(\square + m_2^2)^{-1}] \varphi_1 \quad (\text{A.10})$$

L_{eff} is completely equivalent to L and the effective propagator is

$$D_{L'}^{-1} = \frac{\square + m_2^2}{(\square + m_1^2)(\square + m_2^2) - g^2} = \frac{R_+}{\square + m_+^2} + \frac{R_-}{\square + m_-^2} = \langle \varphi_1 \varphi_1 \rangle \quad (\text{A.11})$$

with

$$R_{\pm} = \frac{\pm(m_1^2 - m_2^2) + \sqrt{(m_1^2 - m_2^2)^2 + 4g^2}}{2\sqrt{(m_1^2 - m_2^2)^2 + 4g^2}} \quad (\text{A.12})$$

Both residues are positive.

Similarly

$$\frac{R_-}{\square + m_+^2} + \frac{R_+}{\square + m_-^2} = \langle \varphi_2 \varphi_2 \rangle \quad (\text{A.13})$$

A.3 The IR expansion

We shall now evaluate the EFT by taking a low-energy approximation to our integrating-out procedure. We expand (A.8) in the IR

$$\varphi_2 = \frac{g}{m_2^2} \left(1 - \frac{\square}{m_2^2} + \frac{\square^2}{m_2^4} + \dots \right) \varphi_1 \quad (\text{A.14})$$

Substituting in (A.7) we obtain

$$(\square + m_1^2)\varphi_1 = \frac{g^2}{m_2^2} \left(1 - \frac{\square}{m_2^2} + \frac{\square^2}{m_2^4} + \dots \right) \varphi_1 \quad \Rightarrow \quad (\text{A.15})$$

$$\Rightarrow \left[m_1^2 - \frac{g^2}{m_2^2} + \left(1 + \frac{g^2}{m_2^4} \right) \square - \frac{g^2}{m_2^6} \square^2 + \mathcal{O}(\square^3) \right] \varphi_1 = 0 \quad (\text{A.16})$$

Stopping our expansion at that order, we can write the relevant action as

$$L_{IR} = -\frac{1}{2}\varphi_1 \left[m_1^2 - \frac{g^2}{m_2^2} + \left(1 + \frac{g^2}{m_2^4} \right) \square - \frac{g^2}{m_2^6} \square^2 \right] \varphi_1 \quad (\text{A.17})$$

with propagator

$$D_{IR}^{-1} = \frac{1}{m_1^2 - \frac{g^2}{m_2^2} + \left(1 + \frac{g^2}{m_2^4} \right) \square - \frac{g^2}{m_2^6} \square^2} = \frac{\tilde{R}_-}{\square + \tilde{m}_-^2} - \frac{\tilde{R}_+}{\square + \tilde{m}_+^2} \quad (\text{A.18})$$

with

$$\tilde{m}_{\pm}^2 = -\frac{m_2^2}{2g^2} \left[m_2^4 + g^2 \pm \sqrt{(m_2^4 + g^2)^2 + 4g^2(m_1^2 m_2^2 - g^2)} \right] \quad (\text{A.19})$$

$$\tilde{R}_\pm = \frac{m_2^4}{\sqrt{(m_2^4 + g^2)^2 + 4g^2(m_1^2 m_2^2 - g^2)}} \quad (\text{A.20})$$

Using $m_2 \gg m_1$ and (A.5) we can simplify the expressions above as

$$\sqrt{(m_2^4 + g^2)^2 + 4g^2(m_1^2 m_2^2 - g^2)} \simeq m_2^4 + g^2 + 2g^2 \frac{m_1^2}{m_2^2} \quad (\text{A.21})$$

$$\tilde{m}_-^2 \simeq m_1^2 \quad , \quad \tilde{m}_+^2 \simeq -\frac{m_2^6}{g^2} \quad , \quad \tilde{R}_\pm \simeq \mp 1 \quad (\text{A.22})$$

The pole associated \tilde{m}_- has the correct positive residue and the correct position corresponding to the slightly corrected light state φ_1 , The extra pole at \tilde{m}_+ is ghost-like and tachyonic with a mass scale

$$|m_+^2| = \frac{m_2^6}{g^2} \geq \frac{m_2^4}{m_1^2} \geq m_2^2 \quad (\text{A.23})$$

that is above the cutoff of the theory that is the mass of the heavier state.

This simple example shows that integrating out degrees of freedom in an IR expansion of the EFT may generically create ghosts and tachyons, even if the underlying UV theory is perfectly healthy. However, these ghosts/tachyons always have masses above the cutoff scale.

In conclusion, in the context of EFT, only unstable modes whose masses are parametrically smaller than the UV cut-off can be considered as giving rise to true instabilities of the theory. Conversely, one cannot reach any conclusion about the stability of the theory based on the presence of ghosts or tachyons whose mass is at or above the cut-off.

B. Renormalized action

In this appendix we briefly review the results of [82] in $d = 4$ for the computation of divergent terms of the bulk action (2.13) evaluated on-shell. These divergences are then cancelled by the bare gravity action defined in (2.14).

The Gibbons-Hawking term of S_{bulk} contains the extrinsic curvature which is defined by

$$K = G^{ab} \nabla_a n_b, \quad (\text{B.1})$$

where n^a is the unit vector normal to the boundary which points to the exterior. The induced metric and normal vector n^a on the $\rho = \epsilon$ boundary are given by

$$\gamma_{\omega\sigma}(\epsilon, x) = \frac{1}{\epsilon} g_{\omega\sigma}(\epsilon, x) \quad (\text{B.2})$$

$$n^a = \frac{\partial^a \rho}{\sqrt{G_{cd} \partial^c \rho \partial^d \rho}} \Big|_{\rho=\epsilon} = \frac{2\epsilon}{L} \delta^{\rho a} \quad (\text{B.3})$$

The bulk action (2.13) evaluated on-shell can then be written in terms of $g_{\alpha\beta}(\rho, x)$ as

$$S_{\text{bulk}} = \frac{1}{16\pi G_N L} \int d^d x \left[\int_\epsilon^{+\infty} d\rho \frac{d}{\rho^{\frac{d}{2}+1}} \sqrt{g} + \frac{1}{\rho^{\frac{d}{2}}} (-2d\sqrt{g} + 4\rho \partial_\rho \sqrt{g}) \Big|_{\rho=\epsilon} \right] \quad (\text{B.4})$$

This action can be written as a power series of ϵ by inserting the expansion of the metric (2.21) into (B.4). Furthermore, the first few terms of (2.21) are obtained in terms of $g_{\omega\sigma}^{(0)}$ by solving perturbatively the bulk Einstein field equation [82]

$$L^2 R_{ab}[G] + dG_{ab} = 0. \quad (\text{B.5})$$

The linear term is then given by

$$g_{\omega\sigma}^{(2)} = -\frac{L^2}{d-2} \left(R_{\omega\sigma} - \frac{R}{2(d-1)} g_{\omega\sigma}^{(0)} \right), \quad (\text{B.6})$$

where, in our notation $R_{\omega\sigma} \equiv R_{\omega\sigma}[g^{(0)}]$. However, only the trace and the divergence of $g^{(4)}$ are constrained by the near-boundary reconstruction of the bulk. We shall obtain $g^{(4)}$ and its perturbation starting from the AdS_5 bulk in section 5. The log-term \hat{g} is given by

$$\hat{g}_{\omega\sigma} = \frac{L^4}{16} \left\{ 2R_{\omega\kappa\sigma\lambda} R^{\kappa\lambda} - \frac{1}{3} \nabla_\omega \nabla_\sigma R + \nabla^2 R_{\omega\sigma} - \frac{2}{3} R R_{\omega\sigma} + \left(\frac{1}{6} R^2 - \frac{1}{6} \nabla^2 R - \frac{1}{2} R_{\kappa\lambda} R^{\kappa\lambda} \right) g_{\omega\sigma}^{(0)} \right\}, \quad (\text{B.7})$$

which is traceless. Inserting (2.21) into the bulk action (B.4) gives a power series in ϵ , given in $d = 4$ by

$$S_{\text{bulk}} = \frac{1}{16\pi G_N L} \int d^4x \sqrt{g^{(0)}} \left(\epsilon^{-2} a_{(0)} + \epsilon^{-1} a_{(2)} - \log \epsilon a_{(4)} \right) + \mathcal{O}(\epsilon^0), \quad (\text{B.8})$$

where

$$a_{(0)} = 2(1-d) = -6, \quad (\text{B.9})$$

$$a_{(2)} = \frac{(4-d)(d-1)}{d-2} \text{Tr} g^{(2)} = 0, \quad (\text{B.10})$$

$$a_{(4)} = \frac{1}{2} \left((\text{Tr}(g^{(2)}))^2 - \text{Tr}((g^{(2)})^2) \right) = -\frac{L^4}{8} \left(R^{\omega\sigma} R_{\omega\sigma} - \frac{1}{3} R^2 \right). \quad (\text{B.11})$$

The divergent piece of the bulk action

$$S_{\text{bulk}} = S_{\text{div}} + \mathcal{O}(\epsilon^0) \quad (\text{B.12})$$

is then given by

$$S_{\text{div}} = \frac{1}{16\pi G_N L} \int d^4x \sqrt{g^{(0)}} \left\{ -6\epsilon^{-2} + \frac{1}{8} \log \epsilon \left(R^{\omega\sigma} R_{\omega\sigma} - \frac{1}{3} R^2 \right) \right\}. \quad (\text{B.13})$$

Inverting perturbatively series for \sqrt{g} and $R_{\omega\sigma}[g]$ in powers of ϵ allows one to express $\sqrt{g^{(0)}}$ and $R_{\omega\sigma} = R_{\omega\sigma}[g^{(0)}]$ covariantly in a power series of curvature tensors of the induced metric $\gamma_{\omega\sigma}$. These useful formulae are given by

$$\sqrt{g^{(0)}} = \epsilon^2 \sqrt{\gamma} \left[1 - \frac{\epsilon}{2} \text{Tr} g_{(2)} + \frac{\epsilon^2}{8} (\text{Tr} g_{(2)}^2 + (\text{Tr} g_{(2)})^2) + \mathcal{O}(\epsilon^3) \right], \quad (\text{B.14})$$

$$R = \frac{1}{\epsilon} \left\{ R[\gamma] - \frac{L^2}{2} \left(R^{\omega\sigma}[\gamma] R_{\omega\sigma}[\gamma] - \frac{1}{6} R[\gamma]^2 \right) + \mathcal{O}(R[\gamma]^3) \right\}. \quad (\text{B.15})$$

Using these expansions into (B.13) allows us to obtain the covariant counterterms written in the main text (2.27).

C. Comparison with the Starobinsky model

In this appendix, we relate our analysis to the Starobinsky $R + R^2$ model of inflation which is one of the most favoured single-field inflationary models by CMB observations [56]. This model is obtained from the original Starobinsky model of anomaly-driven inflation without a cosmological constant [52, 53], by neglecting the non-local anomaly terms and keeping only the local R^2 term. This can be justified when the coefficient α of the R^2 term dominates. In our setup, this amounts to ignoring the CFT contribution (setting $N = 0$) as well as setting $\beta = 0$, and keeping only the αR^2 pure gravity term.

Dropping the non-local terms pushes the de Sitter solution to infinite curvature: in equation (2.57) with $\Lambda = 0$, the de Sitter solution is the non-trivial one with $\bar{R} = 48\pi/GN^2$, and in the limit $N \rightarrow 0$ the curvature diverges. However, by writing the model as a scalar-tensor theory and performing a Weyl transformation to the Einstein frame, one obtains a single-field inflationary model with a quasi-de Sitter solution with a finite Hubble parameter.

The action for the simplified R^2 Starobinsky model is

$$S = - \int d^d x \sqrt{-g} \left\{ \frac{R}{16\pi G} - \hat{\alpha} R^2 \right\}. \quad (\text{C.1})$$

Identifying this action to the R^2 action of our model (2.4) gives the relation between $\hat{\alpha}$ and α :

$$\hat{\alpha} = \frac{\alpha}{384\pi} \quad (\text{C.2})$$

The favoured observational value is

$$\alpha \approx -5.95 \times 10^{11}, \quad (\text{C.3})$$

obtained from the amplitude of the power spectrum of primordial curvature fluctuations [96].

As mentioned above, the model (C.1) corresponds to the $H \rightarrow \infty$ limit of our analysis. We can still compare our results with the full model (including the CFT) [53, 52] with the same value of α as the one favoured by data. In this case, the curvature is fixed to

$$GN^2 H^2 = 4\pi. \quad (\text{C.4})$$

The large R^2 term (2.4) makes the scalaron ψ light and tachyonic as we see below. Notice that this model, due to (C.4), falls outside of the regime of effective field theory.

Scalar sector in Starobinsky inflation We first discuss the scalar mode (scalon), which is the one that, in the pure $R + R^2$ model, can be identified with the inflaton and in the presence of the CFT makes de Sitter unstable.

Indeed, by inserting (C.4) into the condition (4.27), we conclude that $\alpha < 0$ is in the tachyonic regime. The characteristic decay rate Γ of the scalaron instability can be read off by substituting (C.4) into (4.28):

$$\Gamma = H \left[-\frac{3}{2} + \sqrt{\frac{9}{4} - \frac{1}{\tilde{\alpha}}} \right], \quad (\text{C.5})$$

where $\tilde{\alpha} = \frac{\pi\alpha}{N^2}$, which agrees with the value found in [53] close to the de Sitter solution. For a long-lived de Sitter, we need $|\tilde{\alpha}| \sim |\alpha|/N \gg 1$, which also implies $|\alpha| \gg 1$. This model then matches qualitatively the features of the pure $R + R^2$ model, with an unstable de Sitter replaced by a slowly-rolling FRW space-time.

Tensor sector in Starobinsky inflation As explained above, our more general setup can retrieve the $R+R^2$ model (C.1) by setting $N = \beta = 0$. In this case, the only propagating tensor mode is the massless graviton $\nu = 3/2$ as one can see from equation (6.4) applied to $\beta = 0$. Therefore, there is no ghost or tachyonic spin-2 mode in the Starobinsky model.

We now turn on $\beta \neq 0$ while keeping $|\tilde{\alpha}| \gg 1$. Now the tensor sector acquires an additional propagating mode. In such a regime, the R^2 term of the action dominates over the CFT. Therefore, the spin-2 propagator with the CFT (5.39) can be approximated by the pure (modified) gravity propagator (6.4). This propagator contains the usual massless pole and a massive one.

The massless pole is a ghost if

$$\frac{1}{2\pi} - 2\tilde{\alpha} + \tilde{\beta} < 0, \quad \Rightarrow \quad \text{massless ghost} \quad (\text{C.6})$$

otherwise, the massive pole is a ghost. The second case holds for large and negative $\tilde{\alpha}$ and generic values of $\tilde{\beta}$. In addition to ghost-like instabilities, the massive pole is a tachyon if

$$\frac{2}{\tilde{\beta}} \left(\tilde{\alpha} - \frac{1}{4} \right) < 1. \quad \Rightarrow \quad \text{tachyonic} \quad (\text{C.7})$$

Thus, large and negative $\tilde{\alpha}$ are associated with tachyonic spin-2 perturbations for positive and generic values of $\tilde{\beta}$.

However, the massive mode lies below the species scale when $|\tilde{\beta}| \gg |\tilde{\alpha}| \gg 1$. If β is positive, the spin-2 pole is tachyonic and ghost-like. If β is negative, the spin-2 pole is only ghost-like.

If we decide to take the CFT contribution into account, one must refer to Figure 14 instead of equation (C.7). This figure shows which sector (scalar or tensor) represents the strongest tachyonic instability. The vertical red line is for $\Lambda = 0$ as is the case in Starobinsky's model. This figure shows that negative $\tilde{\alpha}$ are associated with scalar tachyonic instability, which is convenient for an inflationary scenario. However, small curvatures can be associated with tensor tachyonic instabilities dominating the usual scalaron.

D. AdS slicing coordinates

In this appendix, we describe the AdS_{d+1} metric in AdS_d slice coordinates.

Lorentzian AdS_{d+1} is the hyperboloid

$$\eta_{AB} X^A X^B = -L^2. \quad (\text{D.1})$$

where $A, B = -1, \dots, d+1$ and $\eta_{AB} = \text{diag}(-1, -1, 1, \dots, 1)$. global AdS_{d+1} coordinates are obtained by choosing

$$X^{-1} = L \cos t \cosh \rho, \quad (\text{D.2a})$$

$$X^0 = -L \sin t \cosh \rho, \quad (\text{D.2b})$$

$$X^\mu = L \Omega^\mu \sinh \rho, \quad (\text{D.2c})$$

where $\mu = 1, \dots, d$ and

$$\delta_{\mu\nu} \Omega^\mu \Omega^\nu = 1 \quad (\text{D.3})$$

AdS slicing is obtained by choosing u as a radial coordinate crossing Lorentzian AdS_d slices. Global coordinates can be chosen to describe the d -dimensional slice. The AdS slicing coordinates are then given by

$$X^{-1} = L \cosh u \cos \tau \cosh r, \quad (\text{D.4a})$$

$$X^0 = -L \cosh u \sin \tau \cosh r, \quad (\text{D.4b})$$

$$X^i = L n^i \cosh u \sinh r, \quad (\text{D.4c})$$

$$X^d = L \sinh u, \quad (\text{D.4d})$$

where $i, j = 1, \dots, d-1$ and

$$\delta^{ij} n^i n^j = 1. \quad (\text{D.5})$$

Using this coordinate system, we can reach the infinity of the embedding space X^A either by taking $u \rightarrow \pm\infty$ or $r \rightarrow +\infty$. Therefore, the boundary of the hyperboloid has two pieces (both infinities for u) which are connected by the common boundary $r \rightarrow +\infty$ of the slice AdS_4 .

To obtain a map between these two coordinate systems, we first rewrite $(X^\mu)^2$ using both (D.2) and (D.4). It gives the relation

$$\sinh^2 \rho = \cosh^2 u \sinh^2 r + \sinh^2 u. \quad (\text{D.6})$$

This can be rewritten as

$$\sinh \rho = (\cosh^2 u \cosh^2 r - 1)^{\frac{1}{2}}. \quad (\text{D.7})$$

For all u and r we have $\cosh u \cosh r > 1$ (global AdS is ill-defined when $\rho = 0$), so we can use the formula $\sqrt{x^2 - 1} = \sinh(\text{Arccosh} x)$. Therefore we obtain

$$t = \tau \quad (\text{D.8a})$$

$$\cosh \rho = \cosh u \cosh r. \quad (\text{D.8b})$$

$$\Omega^d = \sinh u (\cosh^2 u \cosh^2 r - 1)^{-\frac{1}{2}} \quad (\text{D.8c})$$

$$\Omega^i = \cosh u \sinh r (\cosh^2 u \cosh^2 r - 1)^{-\frac{1}{2}} n^i \quad (\text{D.8d})$$

The inverse transformation can be obtained using

$$\cosh r = \frac{\cosh \rho}{\cosh u} \quad (\text{D.9})$$

and the expression for X^d in the two sets of coordinates which gives

$$\sinh u = \Omega^d \sinh \rho, \quad (\text{D.10})$$

$$\cosh u = \sqrt{1 + (\Omega^d \sinh \rho)^2}, \quad (\text{D.11})$$

so that we can replace each u and r into every equation in (D.4). The transformation from AdS slicing to global AdS is then

$$\tau = t \quad (\text{D.12a})$$

$$u = \text{Arcsinh} \left(\Omega^d \sinh \rho \right), \quad (\text{D.12b})$$

$$\cosh r = \cosh \rho \left(1 + (\Omega^d \sinh \rho)^2 \right)^{-\frac{1}{2}} \quad (\text{D.12c})$$

$$n^i = \Omega^i \left(1 - (\Omega^d)^2 \right)^{-\frac{1}{2}} \quad (\text{D.12d})$$

One can easily check that $\delta_{ij} n^i n^j = 1$ is still true using (D.3). Indeed,

$$\delta_{ij} n^i n^j = \frac{\delta_{ij} \Omega^i \Omega^j}{1 - (\Omega^d)^2} = \frac{\delta_{\mu\nu} \Omega^\mu \Omega^\nu - (\Omega^d)^2}{1 - (\Omega^d)^2} = 1. \quad (\text{D.13})$$

We can also choose a parametrisation of the $(d-1)$ -sphere Ω^μ and specifically pick Ω^d to be the polar axis (so that it is parametrized by only one angle $\theta \in [0, \pi]$):

$$\begin{aligned} \Omega^d &= \cos \theta, \\ \Omega^1 &= \sin \theta \cos \varphi_1, \\ &\vdots \\ \Omega^i &= \sin \theta \sin \varphi_1 \dots \sin \varphi_{i-1} \cos \varphi_i, \\ &\vdots \\ \Omega^{d-1} &= \sin \theta \sin \varphi_1 \dots \sin(\varphi_{d-2}). \end{aligned} \quad (\text{D.14})$$

where $\varphi_i \in [0, 2\pi[$. Now the change of coordinates from AdS slicing to global AdS is written as

$$\tau = t \quad (\text{D.15a})$$

$$u = \text{Arcsinh} (\cos \theta \sinh \rho), \quad (\text{D.15b})$$

$$\cosh r = \cosh \rho \left(1 + (\cos \theta \sinh \rho)^2 \right)^{-\frac{1}{2}} \quad (\text{D.15c})$$

$$n^i = \frac{\Omega^i}{\sin \theta} \quad (\text{D.15d})$$

The induced metric in AdS slicing is given by

$$ds^2 = L^2 \{ du^2 + (\cosh u)^2 ds_d^2 \} = G_{ab} dx^a dx^b, \quad (\text{D.16})$$

where ds_d^2 is the metric of unit AdS_d .

E. Schrodinger problem in the bulk

In this appendix, we write the bulk radial equation for the spin-2 perturbation (3.12) as a Schrodinger equation for each slicing (flat, de Sitter and anti-de Sitter). This procedure gives a physical interpretation for bulk solutions with different values of the slice momentum ν (in dS and AdS) and k (in Minkowski) which is identified to the energy of this Schrodinger problem.

Moreover, the Schrodinger problem provides a norm which we can use to check the normalizability of the solutions. In particular, we want to check the normalizability of solutions near the horizon $u = 0$ in de Sitter slicing coordinates.

The easiest way to write the bulk equation for the spin-2 modes (3.12) as a Schrodinger equation is to write the background metric (2.46)

$$ds_{d+1}^2 = L^2 du^2 + a^2 \bar{\zeta}_{\omega\sigma} dx^\omega dx^\sigma \quad (\text{E.1})$$

into conformal coordinates

$$= a^2 [\ell^2 dr^2 + \bar{\zeta}_{\omega\sigma} dx^\omega dx^\sigma], \quad (\text{E.2})$$

where ℓ is the radius of the slice metric $\bar{\zeta}_{\omega\sigma}$ which we write here in order to keep r dimensionless like u . To find such a coordinate r , we need to solve

$$\ell^2 dr^2 = L^2 a^{-2} du^2, \quad (\text{E.3})$$

where the conformal factors we consider are $a = L\chi \cosh u$ (2.50) in AdS slicing, $a = LH \sinh u$ (2.47) in dS slicing and $a = e^{-u}$ (2.48) in flat slicing. We just need to find the appropriate conformal coordinate r , compute $a(r)$ and transform the bulk equation of motion (3.11) into a Schrodinger equation in this new coordinate.

AdS slicing

For AdS slicing (2.50), $\ell = \chi^{-1}$, we find

$$\tan\left(\frac{r}{2}\right) = \tanh\left(\frac{u}{2}\right). \quad (\text{E.4})$$

The conformal boundary of AdS₅ located at $u \rightarrow \pm\infty$ corresponds to $r = \pm\pi$. From (E.4), we obtain

$$\begin{cases} \sinh u &= \tan r \\ \cosh u &= \frac{1}{\cos r}. \end{cases} \quad (\text{E.5})$$

Using (E.5), it is then possible to write equation (5.43) in terms of the conformal coordinate r . The equation is

$$\left\{ \partial_r^2 + (d-1) \tan r \partial_r + \nu^2 - \left(\frac{d-1}{2}\right)^2 \right\} F = 0. \quad (\text{E.6})$$

Defining the rescaled field Ψ as

$$\Psi = a^{\frac{d-1}{2}} F, \quad (\text{E.7})$$

the equation becomes a Schrodinger problem

$$\left\{ -\frac{d^2}{dr^2} + V(r) \right\} \Psi = E\Psi, \quad (\text{E.8})$$

where

$$V(r) \equiv \left(\frac{d-1}{2} \right) \left[1 + \left(\frac{d+1}{2} \right) \tan^2 r \right], \quad (\text{E.9})$$

$$E \equiv -\nu^2 + \left(\frac{d-1}{2} \right)^2 \quad (\text{E.10})$$

dS slicing

For dS slicing (2.48), $\ell = H^{-1}$ and the conformal coordinate r is a solution of (E.3), which for positive u is given by

$$e^r = \tanh\left(\frac{u}{2}\right). \quad (\text{E.11})$$

The limit $u \rightarrow +\infty$ which goes to the conformal boundary of AdS₅ then corresponds to taking $r \rightarrow +\infty$. The horizon at $u = 0$ then corresponds to $r = -\infty$.

The following steps are identical to the ones done in AdS-slicing. Instead of (E.5), we have the following relations

$$\begin{cases} \sinh u &= \frac{1}{\sinh r} \\ \cosh u &= -\coth r. \end{cases} \quad (\text{E.12})$$

The bulk radial equation of motion for spin-2 perturbations (5.27) is then written in terms of the conformal coordinate r as

$$\left\{ \partial_r^2 - (d-1) \coth r \partial_r - \nu^2 + \left(\frac{d-1}{2} \right)^2 \right\} F = 0. \quad (\text{E.13})$$

Using the same redefinition as in (E.7) with $a = LH \sinh u$, we find the Schrodinger equation (E.9,E.10) satisfied by $\Psi = a^{\frac{d-1}{2}} F$. The potential and energy are respectively given by

$$V(r) \equiv \left(\frac{d-1}{2} \right) \left[-1 + \left(\frac{d+1}{2} \right) \coth^2 r \right], \quad (\text{E.14})$$

$$E \equiv \nu^2 - \left(\frac{d-1}{2} \right)^2. \quad (\text{E.15})$$

The scalar product associated with this Schrodinger problem is defined as

$$\langle f, g \rangle = \int_{\mathbb{R}_*} dr f^*(r) g(r). \quad (\text{E.16})$$

The two linearly independent solutions obtained in (5.29) should be normalizable according to the norm associated with the scalar product (E.16). The asymptotic behaviour of the Schrodinger field near $u = 0$ for $d = 4$ is given by

$$\Psi(u) = (\sinh u)^{\frac{3}{2}} F(u) \underset{u \rightarrow 0}{\sim} u^{\pm\nu}. \quad (\text{E.17})$$

The normalizable condition near the horizon at $u = 0$ for the Schrodinger field Ψ for $d = 4$ is then

$$|\Psi|^2 = \langle \Psi(r, \nu), \Psi(r, \nu) \rangle = \int_{-\frac{\pi}{2}}^{\frac{\pi}{2}} dr |\Psi(r)|^2 \sim \int_0^{\frac{\pi}{2}} \frac{du}{u} u^{\pm\nu} < \infty. \quad (\text{E.18})$$

This integral converges on the horizon $u = 0$ if $\text{Re}(\nu) > 0$ for the “ C_- ” solution in (5.29), which has a negative sign exponent in (E.18). Conversely, it converges if $\text{Re}(\nu) < 0$ for the “ C_+ ” solution. In conclusion, the sign of $\text{Re}(\nu)$ determines which solution C_{\pm} is normalizable. In section 5.2, we decide to take a positive real part of ν and therefore need to choose $C_- = 0$ which is not normalizable because the norm (E.18) diverges near the horizon $u = 0$.

F. Flat space tachyonic time scale

In this appendix, we study the time dependence of a tachyonic perturbation using the formalism of Green functions. We show that a tachyonic pole of the Minkowski propagator is associated with a runaway in the retarded Green function of the perturbation.

Both the scalar (4.15) and the tensor (5.6) perturbations are decomposed into eigenmodes of the Minkowski Laplacian operator ∂^2 . Then, a single mode φ perturbation associated with the eigenvalue k^2 is a solution of the Klein-Gordon equation

$$(\partial^2 - m^2)\varphi(x) = 0, \quad (\text{F.1})$$

where x stands for the 4-dimensional coordinate vector $x \equiv (t, \mathbf{x})$. Equation (F.1) can be separated into 3 different cases. First, we study the case $m^2 > 0$, which corresponds to the usual Klein-Gordon equation for a positive mass squared. Second, we study the $m^2 < 0$ case. Finally, we study the case where m^2 is complex but away from the real axis. We shall observe that the retarded Green function contains a runaway in the two last cases, and obtain the characteristic time of this runaway.

The spectral equation for (F.1) is obtained by performing a Fourier transform over the four space-time coordinates:

$$\varphi(t, \mathbf{x}) = \int d^4x e^{-ik \cdot x} \tilde{f}(\omega, \mathbf{k}) = \int dt d^3\mathbf{x} e^{-ik \cdot x + i\omega t} \tilde{\varphi}(\omega, \mathbf{k}). \quad (\text{F.2})$$

The spectral equation is then

$$(\omega^2 - \mathbf{k}^2 - m^2)\tilde{\varphi} = 0 \quad (\text{F.3})$$

The most general solution of (F.3) is given by

$$\tilde{\varphi} = \alpha(\mathbf{k})\delta(\omega - E_k) + \beta(\mathbf{k})\delta(\omega + E_k), \quad (\text{F.4})$$

where we have defined E_k as one of the square roots of

$$E_k^2 \equiv \mathbf{k}^2 + m^2. \quad (\text{F.5})$$

We can choose arbitrarily one of the two square roots. Taking one or the other would simply exchange $\alpha(\mathbf{k})$ and $\beta(\mathbf{k})$ in the solution (F.4). We specify which square root is chosen for each following subsection (m^2 positive, negative or complex).

The Green function G associated to equation (F.1) is defined as

$$(\partial^2 - m^2)G(x) = \delta(x) \quad (\text{F.6})$$

The most general solution for G is then given by

$$G(x) = \varphi(x) + G_p(x), \quad (\text{F.7})$$

where $\delta(x)$ is a Dirac distribution centered at $x = 0$, φ is the homogeneous solution (F.4) and G_p is a particular solution. This particular solution can be obtained via the inverse 4-dimensional Fourier transform of (F.6). The result is

$$G_p(x) = \int \frac{d^3\mathbf{k}}{(2\pi)^3} e^{-i\mathbf{k}\cdot\mathbf{x}} \int \frac{d\omega}{2\pi} e^{i\omega t} \frac{1}{\omega^2 - E_k^2}. \quad (\text{F.8})$$

Positive mass squared

In that case, E_k is real, and we choose it to be the positive square root of (F.5). The integral over ω is evaluated using the residue theorem, and the contour can be chosen arbitrarily (one can choose either the retarded, advanced or the Feynman prescription). For example, the retarded prescription circles the two poles $E_k = \pm\omega$ for positive t . The result is then

$$G_p^R(t > 0, \mathbf{x}) = - \int \frac{d^3\mathbf{k}}{(2\pi)^3} e^{-i\mathbf{k}\cdot\mathbf{x}} \frac{\sin(E_k t)}{E_k}. \quad (\text{F.9})$$

This is the usual retarded Green function of the Klein-Gordon operator. Its time dependence appears only in a sine function and therefore does not contain a runaway. Another prescription would have given another combination of complex exponentials with positive and negative signs. Therefore, all the different prescriptions are safe. For example, the Feynman prescription would have given

$$G_p^F(x) = i \int \frac{d^3\mathbf{k}}{(2\pi)^3} e^{-i\mathbf{k}\cdot\mathbf{x}} \frac{e^{iE_k|t|}}{2E_k}. \quad (\text{F.10})$$

Negative mass squared $m^2 = -\mu^2$

In that case, it is necessary to separate the values of $|\mathbf{k}|$ into two distinct regimes.

- When $|\mathbf{k}| \geq \mu$, then E_k is real and we choose the positive square root of (F.5) as we did in the last subsection.
- When $|\mathbf{k}| < \mu$, then E_k is purely imaginary, and we choose the positive imaginary square root of (F.5).

We can then write the integral (F.8) as a sum of two integrals :

$$G_p(x) = \left[\int_{|\mathbf{k}| < \mu} \frac{d^3\mathbf{k}}{(2\pi)^3} + \int_{|\mathbf{k}| \geq \mu} \frac{d^3\mathbf{k}}{(2\pi)^3} \right] e^{-i\mathbf{k}\cdot\mathbf{x}} \int \frac{d\omega}{2\pi} e^{i\omega t} \frac{1}{\omega^2 - E_k^2} \quad (\text{F.11})$$

$$\equiv G_1(x) + G_2(x) \quad (\text{F.12})$$

The first term of $G_p(x)$, for which E_k is imaginary, is called G_1 . The second term, for which E_k is real, is called G_2 . The G_2 integral has poles on the real axis of ω . The prescription for the contour can be chosen similarly as in the previous case with positive mass squared. In particular, the retarded prescription gives (F.8) with a UV cutoff at $|\mathbf{k}| = \mu$. G_1 , however, has poles on the imaginary axis of ω . Therefore, the path along the real axis does not encounter any poles. As a consequence, the contour prescription is fixed. The residue theorem then gives

$$G_1(x) = i \int_{|\mathbf{k}| < \mu} \frac{d^3 \mathbf{k}}{(2\pi)^3} e^{-i\mathbf{k}\cdot\mathbf{x}} \frac{e^{iE_k|t|}}{2E_k}. \quad (\text{F.13})$$

In this case, we already observe the absence of a runaway, because $iE_k < 0$, so the integrand of (F.13) decreases exponentially with time. However, G_1 breaks the causality of G_p because it is not zero for negative times, and this cannot be cancelled by G_2 .

Following the same idea as in [97], we remark that an acausality can be traded with a runaway by changing the prescription of the Green function. To retrieve causality and build a retarded propagator, we now add the homogeneous solution φ (F.4) to G_p . First, we choose the Feynman prescription for G_2 (F.10), such that the integrand of G_2 coincides with the one of (F.13) at $|\mathbf{k}| = k$, where $E_k = 0$. The most general Green function (F.7) is then given by

$$\begin{aligned} G(x) &= \left[\int_{|\mathbf{k}| < \mu} \frac{d^3 \mathbf{k}}{(2\pi)^3} + \int_{|\mathbf{k}| \geq \mu} \frac{d^3 \mathbf{k}}{(2\pi)^3} \right] e^{-i\mathbf{k}\cdot\mathbf{x}} \left[i \frac{e^{iE_k|t|}}{2E_k} + \alpha(\mathbf{k}) e^{iE_k t} + \beta(\mathbf{k}) e^{-iE_k t} \right] \\ &= \int_{\mathbb{R}^3} \frac{d^3 \mathbf{k}}{(2\pi)^3} e^{-i\mathbf{k}\cdot\mathbf{x}} \left[i \frac{e^{iE_k|t|}}{2E_k} + \alpha(\mathbf{k}) e^{iE_k t} + \beta(\mathbf{k}) e^{-iE_k t} \right] \end{aligned} \quad (\text{F.14})$$

The retarded Green function corresponding to $G^{\text{R}}(t < 0) = 0$ is obtained by setting

$$\alpha(\mathbf{k}) = 0, \quad (\text{F.15a})$$

$$\beta(\mathbf{k}) = -\frac{i}{2E_k}. \quad (\text{F.15b})$$

The result for positive t is given by

$$G^{\text{R}}(t > 0, \mathbf{x}) = - \int_{\mathbb{R}^3} \frac{d^3 \mathbf{k}}{(2\pi)^3} e^{-i\mathbf{k}\cdot\mathbf{x}} \frac{\sin(E_k t)}{E_k}. \quad (\text{F.16})$$

Again, this integral can be written as a sum of two integrals as $G^{\text{R}} = G_1^{\text{R}} + G_2^{\text{R}}$, where G_2^{R} is the same as (F.9) with a UV cutoff at $|\mathbf{k}| = k$, and G_1^{R} is different because $E_k = i\sqrt{\mu^2 - k^2}$ is purely imaginary. More explicitly,

$$G_1^{\text{R}}(t > 0, \mathbf{x}) = - \int_{|\mathbf{k}| < \mu} \frac{d^3 \mathbf{k}}{(2\pi)^3} e^{-i\mathbf{k}\cdot\mathbf{x}} \frac{\sin(E_k t)}{E_k}. \quad (\text{F.17})$$

Since the integrand only depends on the modulus of \mathbf{k} , we define $k = |\mathbf{k}|$ and $r \equiv |\mathbf{x}|$ as new variables for our integral which is now written as

$$G_1^{\text{R}}(t > 0, r) = -\frac{1}{4\pi^2} \int_0^\mu dk k^2 \frac{\sin sr}{sr} \frac{\sinh(t\sqrt{\mu^2 - k^2})}{\sqrt{k^2 - s^2}}. \quad (\text{F.18})$$

For $r = 0$, we have

$$\begin{aligned} G_1^{\text{R}}(t > 0, r = 0) &= -\frac{1}{4\pi^2} \int_0^\mu dk k^2 \frac{\sinh(t\sqrt{\mu^2 - k^2})}{\sqrt{\mu^2 - k^2}} \\ &= -\frac{1}{4\pi^2} \int_0^\mu dE_k \sqrt{E_k^2 - k^2} \sinh(E_k t) \end{aligned} \quad (\text{F.19})$$

For small times, it is easy to expand the \sinh in (F.19) and integrate over E_k . The result is

$$G_1^{\text{R}}(t \sim 0^+, r = 0) = -\frac{\mu^2}{16\pi} t + \mathcal{O}(t^2) \quad (\text{F.20})$$

The large-time asymptotic behaviour of (F.19) is obtained by remarking that the integral is proportional to the Struve function denoted $L_1(\mu t)$. As a result,

$$G_1^{\text{R}}(t > 0, r = 0) = -\frac{1}{8\pi} \frac{\mu}{t} L_1(\mu t). \quad (\text{F.21})$$

This function behaves as the modified Bessel K_1 for large arguments. Therefore, we have

$$G_1^{\text{R}}(t > 0, r = 0) \underset{\mu t \rightarrow +\infty}{\propto} \frac{e^{\mu t}}{(\mu t)^{3/2}} \quad (\text{F.22})$$

This diverges exponentially with time, where μ is the inverse time scale.

Complex m^2

In this subsection, we assume m^2 is complex, and we write its real and imaginary parts as

$$m^2 = a + ib \quad (\text{F.23})$$

First, we relate E_k (F.5) to the real and imaginary parts of m^2 . We define the real and imaginary parts of E_k as A and B respectively. We find that

$$A = \pm \frac{1}{2} \left(\tilde{a} + \sqrt{\tilde{a}^2 + b^2} \right), \quad (\text{F.24})$$

$$B = \frac{b}{2A}, \quad (\text{F.25})$$

where

$$\tilde{a} \equiv a + \mathbf{k}^2. \quad (\text{F.26})$$

As in the previous cases, we choose arbitrarily one of the two square roots for E_k . We pick the sign in (F.24) such that $B > 0$. This is always possible since the case $b = 0$ was already studied in the previous two subsections. Therefore, the sign to pick in (F.24) should be the same sign as b such that we have $B > 0$.

The two poles $\pm E_k$ of G_p (F.8) are now located on the complex plane, away from the real axis. Therefore, the contour prescription is fixed, as in the negative mass squared case. We then obtain the particular solution

$$G_p(x) = i \int_{\mathbb{R}^3} \frac{d^3 \mathbf{k}}{(2\pi)^3} e^{-i\mathbf{k}\cdot\mathbf{x}} \frac{e^{iE_k|t|}}{2E_k}. \quad (\text{F.27})$$

This does not contain a runaway since $\text{Im}(E_k) > 0$. However, the retarded Green function is obtained the same way as in (F.14), by adding the homogenous solution to G_p . By fixing α and β to the same values as in (F.15), we obtain the retarded Green function

$$G^{\text{R}}(t > 0, \mathbf{x}) = - \int_{\mathbb{R}^3} \frac{d^3 \mathbf{k}}{(2\pi)^3} e^{-i\mathbf{k}\cdot\mathbf{x}} \frac{\sin(E_k t)}{E_k}, \quad (\text{F.28})$$

and $G^{\text{R}}(t \leq 0) = 0$. This retarded Green function now contains a runaway, coming from the imaginary part of E_k . We would need to perform the integral over \mathbf{k} to obtain the exact time dependence of this runaway. However, we can observe directly that the strongest runaway for large times will come from the largest imaginary part of E_k , B , which was chosen to be positive. In order to maximize B (F.25) for a fixed a and b , the only possibility is to minimize \tilde{a} , and therefore take $\mathbf{k}^2 = 0$. Therefore, the strongest runaway comes from the homogeneous mode $\mathbf{k} = \mathbf{0}$. In this case, $E_k^2 = m^2$. $\sin(E_k t)$ diverges exponentially with time, and the inverse time scale is given by

$$B = \frac{|b|}{a + \sqrt{a^2 + b^2}}. \quad (\text{F.29})$$

Figure 1 shows the inverse time scale of the runaway corresponding to the worst possible mode $\mathbf{k} = \mathbf{0}$, as a function of the parameters of the theory in flat space. The inverse time scale corresponds to the real part of k . Indeed, for $\mathbf{k}^2 = 0$, we have

$$E_k = \pm m. \quad (\text{F.30})$$

If k is the square root of k^2 with the positive real part, then we have to take the $+$ branch of (F.30) and it follows that

$$B = \text{Im}(m). \quad (\text{F.31})$$

In the main text, we are searching for poles of the propagator for the Laplacian eigenvalue defined by (5.6), where $k^2 \equiv -m^2$. Therefore, the strength of a tachyonic pole where $k^2 > 0$ is then given by

$$B = \text{Re}(k). \quad (\text{F.32})$$

G. Tachyonic tensor eigenmodes in de Sitter

In this appendix, we determine which tensor perturbations are tachyonic. Since these perturbations are decomposed into eigenmodes of the covariant de Sitter Laplacian, we study the tachyon nature of the spin-two perturbation for a single eigenvalue $\nu \in \mathbb{C}$ defined in (5.26). We then obtain a criterion on the value of ν .

The perturbed expanding Poincaré coordinates of d -dimensional de Sitter are given by

$$ds_{dS}^2 = g_{\omega\sigma}^{(0)} dx^\omega dx^\sigma = \left[(H\tau)^{-2} \eta_{\omega\sigma} + \delta\zeta_{\omega\sigma}^b \right] dx^\alpha dx^\beta. \quad (\text{G.1})$$

The equation of motion for metric perturbations follows from the linearization of the Einstein equation (2.6). One can substitute the cosmological constant using the background equation (2.57). The Einstein equation is then a sum of linear curvature terms,

quadratic curvature terms and matter content in the stress tensor. The Lichnerowicz operator $L[\delta\zeta^b]_{\omega\sigma}$ is defined by the variation of the linear curvature terms with respect to $\delta\zeta^b_{\omega\sigma}$ by

$$L[\delta\zeta^b]_{\omega\sigma} = \delta \left(R_{\omega\sigma} - \frac{1}{2} R g_{\omega\sigma}^{(0)} - H^2 \frac{d(d-1)}{2} g_{\omega\sigma}^{(0)} \right). \quad (\text{G.2})$$

If we restrict to the transverse traceless perturbations $h_{\omega\sigma}^{(0)}$ (4.4), then it takes the very simple form

$$L[h^{(0)}]_{\omega\sigma} = \left(H^2 - \frac{1}{2} \nabla^2 \right) h_{\omega\sigma}, \quad (\text{G.3})$$

where we recognize the last term of (5.24). The eigenvalue problem (5.26) for $h_{(0)\alpha\beta}$ is then just written in terms of the Lichnerowicz operator as

$$-2H^{-2} L[h^{(0)}]_{\omega\sigma} = - \left(\nu^2 - \frac{(d-1)^2}{4} \right) h_{\omega\sigma}^{(0)}. \quad (\text{G.4})$$

In order to write this equation as a set of scalar equations acting on each component of $h_{\omega\sigma}^{(0)}$, we define the new metric perturbation $\gamma_{\omega\sigma} = (H\tau)^2 h_{\omega\sigma}^{(0)}$ such that the metric (G.1) is now written

$$ds_{dS}^2 = (H\tau)^{-2} (\eta_{\omega\sigma} + \gamma_{\omega\sigma}) dx^\omega dx^\sigma. \quad (\text{G.5})$$

We now define a differential operator acting on the new metric perturbation $\gamma_{\alpha\beta}$ as

$$D[\gamma]_{\omega\sigma} \equiv -2\tau^2 L \left[\frac{\gamma}{\tau^2} \right]_{\omega\sigma} \quad (\text{G.6})$$

Equation (G.4) is then written as

$$D[\gamma]_{\omega\sigma} = - \left(\nu^2 - \frac{(d-1)^2}{4} \right) \gamma_{\omega\sigma}. \quad (\text{G.7})$$

We now try to write an explicit formula for $D[\gamma]$ in terms of γ . A direct computation using Poincaré coordinates (G.1) gives

$$D[\gamma]_{\omega\sigma} = H^{-2} \square \gamma_{\omega\sigma} - 2d\gamma_{0(\omega} \delta_{\sigma)}^0 + 4\tau \partial_{(\omega} \gamma_{\sigma)0} + 2\eta_{\omega\sigma} \gamma_{00}, \quad (\text{G.8})$$

where \square is the de Sitter Laplacian acting on scalars. Derivatives with respect to τ are now labelled with the index 0. The expression (G.8) shows us that different components of γ_{00} are coupled to each other in equation (G.7). The strategy is now to further decompose (G.7) into 3 equations; a scalar equation for γ_{00} , a vector equation for γ_{0i} and a tensor equation for γ_{ij} ⁴⁵. This splitting is done by using

$$D[\gamma]_{00} = \{ H^{-2} \square - 2(d+1) + 4\tau \partial_0 \} \gamma_{00}, \quad (\text{G.9a})$$

$$D[\gamma]_{0i} = \{ H^{-2} \square - d + 2\tau \partial_0 \} \gamma_{0i} + 2\tau \partial_i \gamma_{00}, \quad (\text{G.9b})$$

$$D[\gamma]_{ij} = H^{-2} \square \gamma_{ij} + 4\tau \partial_{(i} \gamma_{j)0} + 2\delta_{ij} \gamma_{00}. \quad (\text{G.9c})$$

⁴⁵Index i and j will refer to the spatial coordinates of the d -dimensional metric.

These three equations are still coupled because γ_{00} contributes to $D[\gamma]_{0i}$, and $\gamma_{0\alpha}$ contributes to $D[\gamma]_{ij}$. Furthermore, these components are also related to each other through the transverse-traceless property of $h_{\omega\sigma}$. Indeed, the tracelessness condition (3.8) gives

$$\eta^{\omega\sigma}\gamma_{\omega\sigma} = 0, \quad (\text{G.10})$$

and transversality conditions (3.9) give

$$\gamma_{0\omega} + \frac{\tau}{d}\partial^\sigma\gamma_{\sigma\omega} = 0. \quad (\text{G.11})$$

After taking these constraints into account, $\gamma_{\omega\sigma}$ only propagates 5 degrees of freedom. We now solve equations (G.9). To do that, we first give the scalar Laplacian of the de Sitter background (G.1) as

$$H^{-2}\square = \tau^2(-\partial_0^2 + \partial_i^2) + \tau(d-2)\partial_0. \quad (\text{G.12})$$

The first step is to diagonalize the $(d-1)$ -dimensional euclidean Laplacian $\delta^{ij}\partial_i\partial_j = \partial_i^2$ using a Fourier transform⁴⁶. In Fourier space, the scalar de Sitter Laplacian acting on a Fourier mode $\tilde{\gamma}_{\omega\sigma}$ is given by⁴⁷

$$H^{-2}\square = -\tau^2(\partial_0^2 + \mathbf{k}^2) + (d-2)\tau\partial_0, \quad (\text{G.13})$$

where the momentum squared is defined as

$$\mathbf{k}^2 \equiv \delta_{ij}k^ik^j. \quad (\text{G.14})$$

Scalar equation

The only equation in (G.9) which involves only one component of the perturbation $\gamma_{\alpha\beta}$ is the scalar equation (G.9a). The solution to the eigen-problem (G.7) is then any linear combination of the solutions $\tilde{\gamma}_{00}^\pm$ written as

$$\tilde{\gamma}_{00}^\pm = (k\tau)^{\frac{3+d}{2}}J_{\pm\nu}(k\tau) \underset{\tau \rightarrow 0}{\sim} (k\tau)^{\frac{3+d}{2} \pm \nu}, \quad (\text{G.15})$$

where λ_\pm are integration constants, they do not depend on τ . We also defined $k = \sqrt{\mathbf{k}^2}$. Since we are only interested in the eventual divergence of $\tilde{\gamma}_{00}$ for large time ($H\tau = e^{-2Ht} \rightarrow 0$), then (G.15) shows that this scalar quantity is unstable if

$$|\text{Re}(\nu)| > \frac{3+d}{2}. \quad (\text{G.16})$$

The exact solution (G.15) for $\tilde{\gamma}_{00}$ can then be used to find an exact solution for $\tilde{\gamma}_{0i}$ (G.9b).

⁴⁶The convention of the Fourier transform is chosen to be $\gamma_{\omega\sigma} = \int \frac{dk^i}{(2\pi)^{d-1}} e^{-ik^i y^i} \tilde{\gamma}_{\omega\sigma}$

⁴⁷a slight abuse of notation allows us to write the scalar Laplacian in momentum space the same way as we write it in real space.

Vector equation

Instead of solving (G.9b), which is an inhomogeneous equation for γ_{0i} coupled to γ_{00} , we can use the transversality constraint (G.11). We split γ_{0i} into a transverse and a longitudinal component. In Fourier space (of the 3-dimensional spatial coordinates)

$$\tilde{\gamma}_{0i} = b_i + k_i b, \quad (\text{G.17})$$

such that

$$k_i b_i = 0, \quad (\text{G.18})$$

then transversality (G.11) fixes the longitudinal part in terms of γ_{00} which we already solved. It gives

$$i k^2 b = \left(-\partial_0 + \frac{d}{\tau} \right) \tilde{\gamma}_{00}. \quad (\text{G.19})$$

We already know the solution (G.15) for $\tilde{\gamma}_{00}$. Therefore, b is given by a linear combination of the two independent solutions b^\pm given by

$$i k b^\pm = (k\tau)^{\frac{1+d}{2}} \left[\frac{d-3}{2} - (k\tau) \frac{d}{d(k\tau)} \right] J_{\pm\nu}(k\tau), \quad (\text{G.20})$$

which for large time evaluates to

$$i k b^\pm \underset{\tau \rightarrow 0}{\sim} \left(\frac{d-3}{2} - \nu \right) (k\tau)^{\frac{1+d}{2} \pm \nu}. \quad (\text{G.21})$$

The transverse part of (G.9b) in Fourier space is obtained by applying the transverse projection operator given by

$$b_i = \left(\delta_{ij} - \frac{k_i k_j}{k^2} \right) \tilde{\gamma}_{0j}. \quad (\text{G.22})$$

This projection is applied to the "0i" component of equation (G.7) to obtain

$$\left\{ H^{-2} \square + \nu^2 - \frac{(d-1)^2}{4} - d + 2\tau \partial_0 \right\} \tilde{b}_i = 0. \quad (\text{G.23})$$

Again, this equation is solved using Bessel functions as any linear combination of the two independent solutions b_i^\pm given by

$$b_i^\pm = (k\tau)^{\frac{1+d}{2}} J_{\pm\nu}(k\tau). \quad (\text{G.24})$$

To conclude on the vector perturbation, both longitudinal and transverse parts of γ_{0i} are unstable if

$$|\text{Re}(\nu)| > \frac{d+1}{2}. \quad (\text{G.25})$$

By comparing with the result from the scalar component, the scalar instability criterion (G.16) is stronger than the vector result (G.25). A scalar instability implies a vector instability.

Tensor equation

As we did for the vector perturbation, we decompose $\tilde{\gamma}_{ij}$ into

$$\tilde{\gamma}_{ij} = \theta_{ij} + k_i k_j \varphi + 2k_{(i} \mathcal{V}_{j)} + \delta_{ij} \Psi, \quad (\text{G.26})$$

such that

$$\delta^{ij} \theta_{ij} = k_i \mathcal{V}_i = 0 \quad (\text{G.27})$$

and

$$k_i \theta_{ij} = 0. \quad (\text{G.28})$$

Every quantity defined in (G.26) can be expressed as a projection of $\tilde{\gamma}_{ij}$, where the projector is a function of k_i , as it was the case for the vector transverse projection in (G.22). We now search for a solution for each quantity in (G.26).

First, the tracelessness constraint (G.10) written in terms of the decomposition (G.26) is

$$\gamma_{00} = (d-1)\Psi + k^2 \varphi. \quad (\text{G.29})$$

The spatial components of the transversality constraint (G.12) are given by

$$k_i \left[\left(\frac{d}{\tau} - \partial_0 \right) b - i\Psi - ik^2 \varphi \right] + \left(\partial_0 - \frac{d}{\tau} \right) b_i - \partial_j^2 \mathcal{V}_i = 0. \quad (\text{G.30})$$

The longitudinal part of equation (G.30) is

$$\left[\left(\frac{d}{\tau} - \partial_0 \right) b - i(\Psi + k^2 \varphi) \right] = 0, \quad (\text{G.31})$$

and the transverse part is obtained using the same projection as in (G.22):

$$-ik^2 \tilde{\mathcal{V}}_i + \left(\frac{d}{\tau} - \partial_0 \right) b_i = 0. \quad (\text{G.32})$$

The three constraints in momentum space (G.29, G.31, G.32) are solved algebraically for φ , Ψ and \mathcal{V}_i in terms of the known solutions γ_{00} , b and b_i . The result is

$$\Psi = \frac{1}{d-2} \left[\tilde{\gamma}_{00} + i \left(\frac{d}{\tau} - \partial_0 \right) \tilde{b} \right], \quad (\text{G.33a})$$

$$k^2 \tilde{\varphi} = -\frac{1}{d-2} \left[\tilde{\gamma}_{00} + i(d-1) \left(\frac{d}{\tau} - \partial_0 \right) \tilde{b} \right], \quad (\text{G.33b})$$

$$-k^2 \tilde{\mathcal{V}}_i = \left(\partial_0 - \frac{d}{\tau} \right) \tilde{b}_i. \quad (\text{G.33c})$$

From the solutions for $\tilde{\gamma}_{00}$ (G.15), for b (G.21) and b_i (G.24), one can observe that each of these three perturbations scales for large time as $\sim \tau^{\frac{d-1}{2} \pm \nu}$. We now solve the transverse-traceless part of the eigenproblem (G.7) which is simply given by

$$\left\{ \square + \nu^2 - \left(\frac{d-1}{2} \right)^2 \right\} \theta_{ij} = 0 \quad (\text{G.34})$$

Therefore, the solution to the spatial tensor part of (G.7) (which is also a Bessel equation) is

$$\tilde{\theta}_{ij} = \lambda_{ij}^{\pm}(k^i)(k\tau)^{\frac{d-1}{2}} J_{\pm}(k\tau). \quad (\text{G.35})$$

We therefore find that the instability conditions on θ_{ij} , φ , Ψ and \mathcal{V}_i all read

$$|\text{Re}(\nu)| > \frac{d-1}{2}, \quad (\text{G.36})$$

which is weaker than the vector criterion (G.25). Therefore, the existence of an instability relies only on the tensor component γ_{ij} . The criterion (G.36) was also derived in [74] but using a different decomposition which made all 5 degrees of freedom equally unstable.

H. Tachyonic tensor eigenmodes in anti de Sitter

In this appendix, we derive a criterion on the eigenvalue ν which determines if a given mode is tachyonic or not. All the steps done in the previous appendix G can be adapted to AdS in Poincaré coordinates by changing the metric (G.5) to

$$ds_{AdS}^2 = (\chi z)^{-2}(dz^2 - dt^2 + d\mathbf{x}^2) + h_{\alpha\beta} dx^{\alpha} dx^{\beta}, \quad (\text{H.1})$$

$$= [(\chi z)^{-2}\eta_{\omega\sigma} + h_{\omega\sigma}] dx^{\omega} dx^{\sigma}. \quad (\text{H.2})$$

where \mathbf{x} is a (d-2)-dimensional vector, and we define $\eta_{\omega\sigma} = \text{diag}(+1, -1, +1, \dots, +1)$. Greek indices ω, σ are for the full set of d -dimensional coordinates. We also use the index "0" for the time coordinate t , and roman letters such as i, j for (t, \mathbf{x}) . As we did for de Sitter slicing, the eigenproblem (5.42) is studied using the rescaled perturbation

$$\gamma_{\omega\sigma} = (\chi z)^2 h_{\omega\sigma}. \quad (\text{H.3})$$

Similarly to de Sitter (G.7), we define a differential operator from the left-hand side of the eigenproblem (5.42). It is written as

$$\bar{D}[\gamma]_{\omega\sigma} \equiv z^2(\chi^{-2}\nabla^2 + 2)(\gamma_{\omega\sigma}z^{-2}), \quad (\text{H.4})$$

And the eigen-problem (5.42) is then written as

$$\bar{D}[\gamma]_{\omega\sigma} = \left[\nu^2 - \left(\frac{d-1}{2} \right)^2 \right] \gamma_{\omega\sigma}. \quad (\text{H.5})$$

Doing the same computation which resulted in (G.8), we obtain

$$\bar{D}[\gamma]_{\omega\sigma} = \square\gamma_{\omega\sigma} + 2d\delta_{(\omega}^z\gamma_{\sigma)z} - 4z\partial_{(\omega}\gamma_{\sigma)z} + 2\eta_{\omega\sigma}\gamma_{zz}. \quad (\text{H.6})$$

We are now going to solve this equation in momentum space as we did for de Sitter because it allows us to solve ordinary differential equations. The scalar AdS Laplacian appearing in (H.6) in Poincaré coordinates is given by

$$\chi^{-2}\square = z^2(\partial_z^2 - \partial_t^2 + \partial_{\mathbf{x}}^2) - (d-2)z\partial_z \quad (\text{H.7})$$

In de Sitter, we diagonalized the $(d-1)$ -dimensional Laplacian ∂_i^2 using Fourier modes. However, in AdS, the Laplacian we want to diagonalize is the $(d-1)$ -dimensional Minkowski space Laplacian as

$$(-\partial_0^2 + \partial_{\mathbf{x}}^2)\gamma_{\omega\sigma} = [-(k^0)^2 + \mathbf{k}^2]\gamma_{\omega\sigma} \equiv -k^2\gamma_{\omega\sigma}. \quad (\text{H.8})$$

which can contain complex eigenvalues k^2 if the Laplacian is not self-adjoint. In particular, if we assume self-adjointness of the spatial part $\partial_{\mathbf{x}}^2$ but allow for solutions which diverge with time, the imaginary part of k^2 will be contained in $(k^0)^2$. A frequency squared $(k^0)^2$ has two square roots k^0 . Its imaginary part is then responsible for an exponentially growing solution of (H.8) corresponding to one of the two square roots k^0 . Using (H.8), the scalar Laplacian of AdS in Poincaré coordinates is given by

$$\chi^{-2}\square = z^2(\partial_z^2 - k^2) - (d-2)z\partial_z. \quad (\text{H.9})$$

We then decompose $\gamma_{\omega\sigma}$ into as we did for de Sitter. We had seen that it was enough to solve the eigenproblem (5.42) for 3 quantities γ_{00} , b_i and θ_{ij} defined in (G.17) for the transverse vector and (G.26) for the tensorial decomposition. All the other quantities (namely b , φ , Ψ and \mathcal{V}) are constrained by the transverse-traceless properties of $h_{\omega\sigma}$ (3.8,3.9), so they cannot represent new instabilities. In Poincaré AdS (H.2), the constraints read

$$\eta^{\omega\sigma}\gamma_{\omega\sigma} = 0, \quad (\text{H.10})$$

$$\frac{\tau}{d}\partial^\sigma\gamma_{\omega\sigma} = \gamma_{0\omega}. \quad (\text{H.11})$$

It is therefore enough to study three equations obtained from (H.5). They are given by:

- the zz component of (H.5)

$$\left\{ \chi^{-2}\square - \nu^2 + \left(\frac{d-1}{2}\right)^2 + 2(d+1) - 4z\partial_z \right\} \gamma_{zz} = 0, \quad (\text{H.12a})$$

- the transverse part of the $0i$ component of (H.5)

$$\left\{ \chi^{-2}\square - \nu^2 + \left(\frac{d-1}{2}\right)^2 + d - 2z\partial_z \right\} b_i = 0, \quad (\text{H.12b})$$

- and the transverse-traceless part of the ij component of (H.5)

$$\left\{ \chi^{-2}\square - \nu^2 + \left(\frac{d-1}{2}\right)^2 \right\} \theta_{ij} = 0. \quad (\text{H.12c})$$

Since all these equations are solved by (modified) Bessel functions, we can bring them to the same form. We define the spin $s = 0, 1$ or 2 perturbation \mathcal{Z}_s being either equal to $\tilde{\gamma}_{00}$ for $s = 0$, b_i for $s = 1$ or θ_{ij} for $s = 2$. A rescaled function ψ_s is also defined as

$$\psi_s(w, k^i) = e^{-n_s w} \mathcal{Z}_s(w, k^i), \quad (\text{H.13})$$

with the radial coordinate $w \equiv \log z$. A direct computation using (H.9) into equations (H.12) shows that each ψ_s satisfies the same Schrodinger equation

$$\left[-\frac{d^2}{dw^2} + k^2 e^{2w} \right] \psi_s = -\nu^2 \psi_s \quad (\text{H.14})$$

if

$$n_s = \frac{d+3}{2} - s. \quad (\text{H.15})$$

The most general solution of (H.14) is

$$\psi_s = \lambda_s^\pm I_{\pm\nu}(ke^w), \quad (\text{H.16})$$

where k is the square root of k^2 with positive real part. We now study its solutions depending on the sign of $\text{Re}(k)$.

- If $\text{Re}(k) = 0$, this corresponds to timelike $k^2 < 0$ modes which possess real frequencies k^0 . These modes do not diverge with time and are timelike. They are therefore stable. The solution (H.16) is then evaluated at an imaginary argument, which gives Bessel functions (not modified)

$$\psi_s = \lambda_s^\pm J_{\pm\nu}(|k|e^w). \quad (\text{H.17})$$

The timelike solution which is regular at $z \rightarrow 0$ is given by one of these two Bessel functions depending on the sign of the real part of ν . In conclusion, timelike solutions allow any eigenvalue $\nu \in \mathbb{C}$.

- We now turn to complex k^2 , with $|\text{Arg}(k^2)| < \pi$ which are necessarily unstable. For example, $k^2 > 0$ corresponds to a tachyonic mode. Since k^2 contains two square roots, we take the k with a positive real part. The linear combination of (H.16) solutions which is regular at the horizon $z \rightarrow +\infty$ is the Bessel K_ν :

$$\psi_s = \lambda_s K_\nu(ke^w) \xrightarrow{z \rightarrow +\infty} \sqrt{\frac{\pi}{2kz}} \exp\{-ke^w\}. \quad (\text{H.18})$$

As one could already observe from (H.1), the radial coordinate of AdS is not time but z . Furthermore, the eigenproblem (5.42) defines a momentum ν which is dual to z in AdS. In dS, the value of ν was fixing the characteristic time of the instability. In AdS, however, the boundary does not correspond to infinite time. In order to address stability in AdS, we turn to a viewpoint similar to the BF bound analysis [93]. The stability condition is following: For a given $\nu \in \mathbb{C}$, AdS is unstable if there exist a regular solution ψ_s with $\text{Re}(k) \neq 0$.

To address the stability of a given ν , we then need to look if there is a ψ_s solution (H.18) which is regular at $w \rightarrow -\infty$, since (H.18) is already exponentially decreasing at $w \rightarrow +\infty$.

- If $\text{Re}(\nu) > 0$, the leading behavior is then

$$K_\nu(ke^w) \underset{w \rightarrow -\infty}{\sim} \frac{\pi}{2 \sin(\pi\nu)} \frac{2^\nu k^{-\nu} e^{-w\nu}}{\Gamma(1-\nu)} \rightarrow \infty. \quad (\text{H.19})$$

- If $\text{Re}(\nu) < 0$

$$K_\nu(ke^w) \underset{w \rightarrow -\infty}{\sim} \frac{\pi}{2 \sin(\pi\nu)} \frac{2^{-\nu} k^\nu e^{w\nu}}{\Gamma(1+\nu)} \rightarrow \infty. \quad (\text{H.20})$$

- If $\text{Re}(\nu) = 0$, or $\nu = i\mu$ for $\mu \in \mathbb{R}$, the solution is a combination of plane waves:

$$\psi_s(ke^w) \underset{w \rightarrow -\infty}{\rightarrow} \frac{1}{2i\mu} \left[\left(\frac{k}{2}\right)^{-i\mu} \Gamma(1+i\mu) e^{-i\mu w} - \left(\frac{k}{2}\right)^{i\mu} \Gamma(1-i\mu) e^{i\mu w} \right]. \quad (\text{H.21})$$

We therefore find plane-wave normalizable $\psi_s(w)$ for imaginary ν and spacelike ($k^2 > 0$) modes. We conclude that $\nu = i\mu$ allows for a regular solution with non-zero $\text{Re}(k)$. These modes are unstable eigenvalues of the operator $\bar{D}[\gamma]$ defined for AdS slicing in (H.4).

To conclude, the only possibility for a spacelike $k^2 > 0$ mode to be regular both at the AdS boundary $w \rightarrow -\infty$ and the horizon $w \rightarrow +\infty$ is to have $\text{Re}(\nu) = 0$. It agrees with the usual BF bound $\nu^2 < 0$ [93] in the limit where ν^2 is real. Indeed, the usual BF bound analysis was done for real mass squared, which is the eigenvalue of the scalar Laplacian. By looking at the equation for θ_{ij} (H.12c), we can observe that the mass squared is identified to $\nu^2 - \frac{(d-1)^2}{4}$.

I. Asymptotic behaviour of Legendre functions

This appendix is devoted to the asymptotic behaviour of associated Legendre functions of argument $x \in]-1, 1[$, which enter into the solution of tensor modes in the bulk with AdS₃ slicing. This appendix allows us to relate boundary conditions (see 5.3.1 and 5.3.2) to the value of constants of integrations λ_1, λ_2 in (5.45).

In the AdS-slicing case (5.3), the bulk equation of motion for tensor perturbations (5.40) can be written as a Legendre function for the holographic coordinate u (5.43). Its solutions are given by the linear combination

$$F(u, \nu) = (\cosh u)^{-2} \left(\lambda_1 P_{\nu-1/2}^2(\tanh u) + \lambda_2 Q_{\nu-1/2}^2(\tanh u) \right). \quad (\text{I.1})$$

In the single-boundary case 5.3.1, it is easy to fix the integration constants of (I.1) because Legendre functions are defined as hypergeometric series in $\tanh u$ and $\lambda_1 (\cosh u)^{-2} P_{\nu-1/2}^2(\tanh u)$ is the only solution which vanishes at $u \rightarrow +\infty$. Therefore, imposing $F(u, \nu) \rightarrow 0$ at $u \rightarrow +\infty$ sets $\lambda_2 = 0$ and one can obtain the expansion of the remaining solution using the usual expression for associated Legendre functions in terms of hypergeometric series :

$$P_\nu^\mu(x) = \frac{1}{\Gamma(1-\mu)} \left(\frac{1+x}{1-x}\right)^{\frac{\mu}{2}} {}_2F_1\left(-\nu, \nu+1; 1-\mu; \frac{1-x}{2}\right), x \in [-1, 1]. \quad (\text{I.2})$$

The formula (I.2) is applied to (I.1) for

$$x = \tanh u. \quad (\text{I.3})$$

The formula (I.2) is convenient for an expansion close to $x \rightarrow 1$ using the definition of the hypergeometric series (from now we use the short notation $F = {}_2F_1$)

$$F(a, b; c; x) = \sum_{n=0}^{+\infty} \frac{(a)_n (b)_n}{(c)_n} \frac{x^n}{n!}, \quad (\text{I.4})$$

where

$$(a)_n \equiv a(a+1)\dots(a+n-1). \quad (\text{I.5})$$

Using (I.2) into (I.2) gives

$$(1-x^2)P_{\nu-1/2}^2(x) = 2 \left(\frac{1-x}{2} \right)^2 \left(\nu^2 - \frac{9}{4} \right) \left(\nu^2 - \frac{1}{4} \right) + \mathcal{O}((1-x)^3). \quad (\text{I.6})$$

Therefore, the only contribution to $F(x=1)$ comes from $Q_{\nu-1/2}^2$, which is fixed to zero by the boundary condition (5.46). However, for other boundary conditions, we may need to expand (I.1) close to $x = -1$. The hypergeometric transformation adapted to the limit $\mu \rightarrow 2$. This transformation is given on page 49 of [94], or (15.3.12) of [Abramowitz and Stegun - Hypergeometric functions](#). We reproduce it here for consistency :

$$\begin{aligned} F(a, b; a+b-\mu; y) &= \frac{\Gamma(\mu)\Gamma(a+b-\mu)}{\Gamma(a)\Gamma(b)} \sum_{n=0}^{m-1} \frac{(a-\mu)_n (b-\mu)_n}{n!(1-\mu)_n} (1-y)^{n-m} \\ &\quad - \frac{(-1)^\mu \Gamma(a+b-\mu)}{\Gamma(a-\mu)\Gamma(b-\mu)} \sum_{n=0}^{+\infty} \frac{(a)_n (b)_n}{n!(n+\mu)!} (1-y)^n [\log(1-y) \\ &\quad - \psi(n+1) - \psi(n+\mu+1) + \psi(a+n) + \psi(b+n)], \end{aligned} \quad (\text{I.7})$$

valid for $|1-y| < 1$ and $|\text{Arg}(1-y)| < \pi$. This is the case because we take

$$y = \frac{1-x}{2}, \quad (\text{I.8})$$

Therefore, the small parameter of our expansion at $u \rightarrow -\infty$ is going to be

$$1-y = \frac{1+x}{2} \in]0, 1[. \quad (\text{I.9})$$

Applying (I.7) to

$$a = \frac{1}{2} - \nu, \quad (\text{I.10})$$

$$b = \nu + \frac{1}{2}, \quad (\text{I.11})$$

we obtain

$$\begin{aligned} (1-x^2)P_{\nu-1/2}^2(x) &= -4 \frac{\cos(\pi\nu)}{\pi} \left\{ 1 + \left(\nu^2 - \frac{9}{4} \right) \left(\frac{1+x}{2} \right) - \right. \\ &\quad \left. \frac{1}{2} \left(\frac{1+x}{2} \right)^2 \left(\nu^2 - \frac{9}{4} \right) \left(\nu^2 - \frac{1}{4} \right) \right\} \end{aligned}$$

$$\times \left[\log \left(\frac{1+x}{2} \right) - \frac{3}{2} + \mathcal{H} \left(\nu - \frac{1}{2} \right) + \mathcal{H} \left(-\nu - \frac{1}{2} \right) \right] \Big\} + \mathcal{O}((1+x)^3) \quad (\text{I.12})$$

We now compute the expansions of $Q_{\nu-1/2}^\mu(x)$ near the two boundaries. The first one can be obtained using the formula from page 170 of [94]

$$P_\nu^\mu(-x) = \cos(\pi(\nu + \mu))P_\nu^\mu(x) - \frac{2}{\pi} \sin(\pi(\nu + \mu))Q_\nu^\mu(x), \quad (\text{I.13})$$

valid for $0 < x < 1$. Isolate $Q_\nu^\mu(x)$ and take $\mu = 2$:

$$Q_{\nu-1/2}^2(x) = -\frac{\pi}{2 \cos(\pi\nu)} \left[\sin(\pi\nu)P_{\nu-1/2}^2(x) - P_{\nu-1/2}^2(-x) \right]. \quad (\text{I.14})$$

The expansion in powers of $(1-x)$ for the second term is simply given by (I.12) evaluated at $-x$. The first term is (I.6). The result is

$$(1-x^2)Q_{\nu-1/2}^2(x) = -2 \left\{ 1 + \left(\nu^2 - \frac{9}{4} \right) \left(\frac{1-x}{2} \right) - \frac{1}{2} \left(\frac{1-x}{2} \right)^2 \left(\nu^2 - \frac{9}{4} \right) \left(\nu^2 - \frac{1}{4} \right) \right. \\ \left. \times \left[\pi \tan(\pi\nu) + \log \left(\frac{1-x}{2} \right) - \frac{3}{2} + \mathcal{H} \left(\nu - \frac{1}{2} \right) + \mathcal{H} \left(-\nu - \frac{1}{2} \right) \right] \right\} + \mathcal{O}((1-x)^3). \quad (\text{I.15})$$

The last expansion we need is $Q_{\nu-1/2}^2(x)$ close to $x = -1$. This can be obtained using another formula from page 170 of [94]:

$$Q_\nu^\mu(-x) = -\cos(\pi(\nu + \mu))Q_\nu^\mu(x) - \frac{\pi}{2} \sin(\pi(\nu + \mu))P_\nu^\mu(x) \quad (\text{I.16})$$

valid for $0 < x < 1$. Therefore, for $-1 < x < 0$, we can use

$$Q_\nu^\mu(x) = -\cos(\pi(\nu + \mu))Q_\nu^\mu(-x) - \frac{\pi}{2} \sin(\pi(\nu + \mu))P_\nu^\mu(-x) \quad (\text{I.17})$$

where the first term expansion is given by (I.15) evaluated at $-x$ and the second term is given by (I.6) evaluated at $-x$ too. The result is given by

$$(1-x^2)Q_{\nu-1/2}^2(x) = 2 \sin(\pi\nu) \left\{ 1 + \left(\nu^2 - \frac{9}{4} \right) \left(\frac{1+x}{2} \right) - \frac{1}{2} \left(\frac{1+x}{2} \right)^2 \left(\nu^2 - \frac{9}{4} \right) \left(\nu^2 - \frac{1}{4} \right) \right. \\ \left. \left[\pi \tan(\pi\nu) - \pi \cot(\pi\nu) + \log \left(\frac{1+x}{2} \right) - \frac{3}{2} + \mathcal{H} \left(\nu - \frac{1}{2} \right) + \mathcal{H} \left(-\nu - \frac{1}{2} \right) \right] \right\} + \mathcal{O}((1+x)^3). \quad (\text{I.18})$$

Finally, the two different expansions for $F(x)$ are given by

$$F(x) \underset{x \rightarrow 1}{=} 2\lambda_1 \left(\frac{1-x}{2} \right)^2 \left(\nu^2 - \frac{9}{4} \right) \left(\nu^2 - \frac{1}{4} \right) \\ + 2\lambda_2 \left\{ 1 + \left(\nu^2 - \frac{9}{4} \right) \left(\frac{1-x}{2} \right) - \frac{1}{2} \left(\frac{1-x}{2} \right)^2 \left(\nu^2 - \frac{9}{4} \right) \left(\nu^2 - \frac{1}{4} \right) \right.$$

$$\times \left[\pi \tan(\pi\nu) + \log\left(\frac{1-x}{2}\right) - \frac{3}{2} + \mathcal{H}\left(\nu - \frac{1}{2}\right) + \mathcal{H}\left(-\nu - \frac{1}{2}\right) \right] + \mathcal{O}((1-x)^3) \quad (\text{I.19})$$

$$\begin{aligned} F(x) \underset{x \rightarrow -1}{=} & \left(\frac{4\lambda_1 \cos \pi\nu}{\pi} - 2\lambda_2 \sin \pi\nu \right) \left\{ 1 + \left(\nu^2 - \frac{9}{4} \right) \left(\frac{1+x}{2} \right) - \right. \\ & \left. \frac{1}{2} \left(\frac{1+x}{2} \right)^2 \left(\nu^2 - \frac{9}{4} \right) \left(\nu^2 - \frac{1}{4} \right) \left[\log\left(\frac{1+x}{2}\right) - \frac{3}{2} + \mathcal{H}\left(\nu - \frac{1}{2}\right) + \mathcal{H}\left(-\nu - \frac{1}{2}\right) \right] \right\} \\ & + \frac{\pi\lambda_2}{\cos \pi\nu} \left(\frac{1+x}{2} \right)^2 \left(\nu^2 - \frac{9}{4} \right) \left(\nu^2 - \frac{1}{4} \right) + \mathcal{O}((1-x)^3) \end{aligned} \quad (\text{I.20})$$

The limits of $F(x)$ on both direction are

$$F(u) \longrightarrow \begin{cases} 2\lambda_2 & \text{when } u \longrightarrow +\infty \\ \frac{4\lambda_1}{\pi} \cos(\pi\nu) - 2\lambda_2 \sin(\pi\nu) & \text{when } u \longrightarrow -\infty \end{cases} \quad (\text{I.21})$$

In order to read out the vacuum expectation value term $h^{(4)}$ from the Fefferman-Graham expansion (3.13), we first take the coordinate transformation (I.3) to obtain

$$\frac{1 \pm x}{2} = e^{\pm 2u} (1 - e^{\pm 2u}) + \mathcal{O}(e^{\pm 4u}). \quad (\text{I.22})$$

And the Fefferman-Graham coordinate ρ^\pm is related to u by

$$e^{\mp 2u} = \left(\frac{L\chi}{2} \right)^2 \rho^\pm. \quad (\text{I.23})$$

In terms of u , the expansions of F near each boundary is then given by

$$\begin{aligned} F(u) \underset{u \rightarrow +\infty}{=} & 2\lambda_1 e^{-4u} \left(\nu^2 - \frac{1}{4} \right) \left(\nu^2 - \frac{9}{4} \right) + \\ & 2\lambda_2 \left\{ 1 + \left(\nu^2 - \frac{9}{4} \right) e^{-2u} - e^{-4u} \left(\nu^2 - \frac{9}{4} \right) \left[1 + \right. \right. \\ & \left. \left. \frac{1}{2} \left(\nu^2 - \frac{1}{4} \right) \left(\pi \tan(\pi\nu) - 2u - \frac{3}{2} + \mathcal{H}\left(\nu - \frac{1}{2}\right) + \mathcal{H}\left(-\nu - \frac{1}{2}\right) \right) \right] \right\} \end{aligned} \quad (\text{I.24})$$

$$\begin{aligned} F(u) \underset{u \rightarrow -\infty}{=} & \left(\frac{4\lambda_1}{\pi} \cos(\pi\nu) - 2\lambda_2 \sin(\pi\nu) \right) \left\{ 1 + \left(\nu^2 - \frac{9}{4} \right) e^{2u} - \right. \\ & \left. e^{4u} \left(\nu^2 - \frac{9}{4} \right) \left[1 + \frac{1}{2} \left(\nu^2 - \frac{1}{4} \right) \left(2u - \frac{3}{2} + \mathcal{H}\left(\nu - \frac{1}{2}\right) + \mathcal{H}\left(-\nu - \frac{1}{2}\right) \right) \right] \right\} + \\ & \lambda_2 \pi \cos(\pi\nu) e^{4u} \left(\nu^2 - \frac{1}{4} \right) \left(\nu^2 - \frac{9}{4} \right) \end{aligned} \quad (\text{I.25})$$

Replacing in (I.24, I.25) the integration constants λ_1 and λ_2 by boundary conditions (5.46) gives the result (5.49). In the case of symmetric boundary conditions (5.55), the bulk radial solution is given by

$$\begin{aligned} F_{\text{sym}}(u) \underset{u \rightarrow \pm\infty}{=} & 1 + e^{\mp 2u} \left(\nu^2 - \frac{9}{4} \right) - e^{\mp 4u} \left(\nu^2 - \frac{9}{4} \right) \left[1 + \right. \\ & \left. \frac{1}{2} \left(\nu^2 - \frac{1}{4} \right) \left(\mp 2u - \frac{\pi}{\cos(\pi\nu)} - \frac{3}{2} + \mathcal{H}\left(\nu - \frac{1}{2}\right) + \mathcal{H}\left(-\nu - \frac{1}{2}\right) \right) \right]. \end{aligned} \quad (\text{I.26})$$

From this solution, one can then identify equations (5.41) with (3.13) to obtain all the terms in (5.51).

J. Quadratic action for tensor modes

In this appendix, we obtain the quadratic terms of the boundary action (2.1) for tensor perturbations. The scalar case is subtle and we discuss it separately in the next appendix.

We start from the action (2.38):

$$S[g^{(0)}] = S_{\text{CFT}}[g^{(0)}] - \frac{1}{16\pi G} \int \sqrt{g^{(0)}} \left\{ R - 2\Lambda + \frac{\alpha G}{24} R^2 + 4\beta G \left(R^{\omega\sigma} R_{\omega\sigma} - \frac{1}{3} R^2 \right) \right\} \quad (\text{J.1})$$

Doing an expansion in the metric with respect to a spin-2 TT perturbation $h_{\omega\sigma}^{(0)}$ as

$$g_{\omega\sigma}^{(0)} = \bar{\zeta}_{\omega\sigma} + \epsilon h_{\omega\sigma}^{(0)}, \quad (\text{J.2})$$

where ϵ is a book-keeping parameter. A Taylor expansion of the action (J.1) in ϵ is written as

$$S[g_{(0)}] = S[\bar{\zeta}] + \epsilon S^{(1)}[\bar{\zeta}] + \frac{\epsilon^2}{2} S^{(2)}[\bar{\zeta}] + \mathcal{O}(\epsilon^3). \quad (\text{J.3})$$

The linear order $S^{(1)}$ is already given by the generalized Einstein tensor computed in (4.6). This has to be evaluated on the background metric $\bar{\zeta}_{\omega\sigma}$, and the general metric perturbation is specialized to the TT mode $h^{(0)}$, so $\delta g^{(0)\omega\sigma} = h^{(0)\omega\sigma}$. We recall here the definition (4.5) of the generalized Einstein tensor:

$$S^{(1)}[g_{(0)}] = -\frac{1}{16\pi G} \int \sqrt{g_{(0)}} h^{(0)\omega\sigma} E_{\omega\sigma}[g^{(0)}]. \quad (\text{J.4})$$

Taking the second derivative of the action (J.1) is equivalent to taking the first derivative of $E_{\omega\sigma}[g^{(0)}]$ with respect to ϵ . We give some useful linearization formulae in the following. First, we rewrite the generalized Einstein tensor where we replace Λ by its expression (2.57) which comes from the trace of the background Einstein equation (4.6). The result is

$$E_{\omega\sigma} = \tilde{G}_{\omega\sigma} + 8\pi G \left({}^{(\alpha)}H_{\omega\sigma} + {}^{(\beta)}H_{\omega\sigma} - \langle T_{\omega\sigma} \rangle^T \right), \quad (\text{J.5})$$

where

$$\tilde{G}_{\omega\sigma} \equiv R_{\omega\sigma} - \frac{1}{2} R g_{\omega\sigma}^{(0)} + \frac{R}{4} g_{\omega\sigma}^{(0)}, \quad (\text{J.6})$$

and

$$\langle T_{\omega\sigma} \rangle^T \equiv \langle T_{\omega\sigma} \rangle - \frac{1}{4} \bar{\zeta}_{\omega\sigma} \langle T^\kappa{}_\kappa \rangle. \quad (\text{J.7})$$

The linearization of each term in (J.5) is given by

$$\delta_h \tilde{G}_{\omega\sigma} = \left(-\frac{\nabla^2}{2} + \frac{R}{12} \right) h_{\omega\sigma}^{(0)}, \quad (\text{J.8})$$

$$\delta_h {}^{(\alpha)}H_{\omega\sigma} = \frac{\alpha}{8\pi} \frac{R}{12} \left(\frac{\nabla^2}{2} - \frac{R}{12} \right) h_{\omega\sigma}^{(0)}, \quad (\text{J.9})$$

$$\delta_h {}^{(\beta)}H_{\omega\sigma} = \frac{\beta}{32\pi} \left(\frac{1}{2} \square^2 h_{\omega\sigma} - \frac{R}{4} \square h_{\omega\sigma} + \frac{R^2}{36} h_{\omega\sigma} \right) = -\frac{\beta}{2\pi} \frac{\hat{h}_{\omega\sigma}}{L^4}, \quad (\text{J.10})$$

where $\hat{h}_{\alpha\beta}$ is defined in (3.13). And the linearization of the CFT stress tensor depends on the background choice (flat, dS or AdS). Since $\delta_h \langle T_{\omega\sigma} \rangle$ is only given for a single Laplacian mode, we first need to specify the background geometry and then decompose the action (J.1) into a complete basis of Laplacian eigenvalues.

Therefore, the quadratic part of the action is

$$S^{(2)}[\bar{\zeta}] = -\frac{1}{16\pi G} \int d^4x \sqrt{\bar{\zeta}} h^{(0)\omega\sigma} \left\{ \left(-\frac{\nabla^2}{2} + \frac{R}{12} \right) \left(1 - \frac{\alpha GR}{12} \right) h_{\omega\sigma}^{(0)} - 4G\beta \frac{\hat{h}_{\omega\sigma}}{L^4} - 8\pi G \langle T_{\omega\sigma} \rangle^T \right\}. \quad (\text{J.11})$$

Replacing the stress tensor by its expression in terms of the expansion $h^{(n)}$, we obtain

$$S^{(2)}[\bar{\zeta}] = \frac{N^2}{2\pi^2} \int d^4x \sqrt{\bar{\zeta}} h^{(0)\omega\sigma} \left\{ h_{\omega\sigma}^{(4)} + \left(\tilde{\beta}_{\text{eff}} + 1 - 2 \log(\mu L) \right) \hat{h}_{\omega\sigma} + \frac{RL^4}{24} \left(\nabla^2 - \frac{R}{6} \right) \left(\frac{3\pi}{GN^2 R} - \frac{\pi\alpha}{4N^2} - \frac{1}{4} \right) h_{\omega\sigma}^{(0)} \right\}. \quad (\text{J.12})$$

Flat space quadratic action The quadratic action given in (J.11) is applied to zero curvature. It gives

$$S^{(2)}[\eta] = -\frac{1}{16\pi G} \int d^4x h^{(0)\omega\sigma} \left\{ -\frac{\nabla^2}{2} h_{\omega\sigma}^{(0)} - \frac{4G\beta}{L^4} \hat{h}_{\omega\sigma} - 8\pi G \delta_h \langle T_{\omega\sigma} \rangle^T \right\} \quad (\text{J.13})$$

Since the last term is only known in momentum space (5.16), we first apply a usual Fourier transform to the metric perturbation

$$h_{\omega\sigma}^{(0)} = \int \frac{d^4k}{(2\pi)^4} e^{-ik \cdot x} \tilde{h}_{\omega\sigma}^{(0)}, \quad (\text{J.14})$$

in order to write the quadratic action (J.13) as

$$S^{(2)}[\eta] = -\frac{1}{16\pi G} \int \frac{d^4k}{(2\pi)^4} \tilde{h}^{(0)\omega\sigma}(-k) \left\{ \frac{k^2}{2} \tilde{h}_{\omega\sigma}^{(0)}(k) - \frac{4G\beta}{L^4} \hat{h}_{\omega\sigma}(k) - 8\pi G \delta_h \langle \tilde{T}_{\omega\sigma} \rangle^T(k) \right\} \quad (\text{J.15})$$

Using (5.16) and the fact that the trace anomaly is zero on a flat background, we obtain the result

$$S^{(2)}[\eta] = \int \frac{d^4k}{(2\pi)^4} \tilde{h}^{(0)\omega\sigma}(-k) \tilde{h}_{\omega\sigma}^{(0)}(k) \mathcal{F}_{\text{flat}}(k), \quad (\text{J.16})$$

where

$$\mathcal{F}_{\text{flat}}(k) \equiv \frac{N^2}{64\pi^2} k^2 \left\{ -\frac{2\pi}{GN^2} + \frac{k^2}{2} \left[\frac{1}{2} - 2\gamma_E - \log(GN^2 k^2) - \tilde{\beta}_{\text{eff}} \right] \right\} \quad (\text{J.17})$$

If we add a source to the action (J.16) as

$$S^{(2)}[J_{\omega\sigma}] \equiv \int \frac{d^4k}{(2\pi)^4} \tilde{h}^{(0)\omega\sigma}(-k) \left\{ \tilde{h}_{\omega\sigma}^{(0)}(k) \mathcal{F}_{\text{flat}}(k) - \tilde{J}_{\omega\sigma}(k) \right\}, \quad (\text{J.18})$$

then the classical solution which cancels the functional derivative of the quadratic action (J.18) with respect to $h^{(0)\omega\sigma}$ can be written as

$$h_{\omega\sigma}^{(0)}(x) = \int d^4z J_{\omega\sigma}(z) G(x-z), \quad (\text{J.19})$$

where

$$G(x) \equiv \int \frac{d^4 k}{(2\pi)^4} \frac{e^{-ik \cdot x}}{\mathcal{F}_{\text{flat}}(k)}. \quad (\text{J.20})$$

Curved space-time quadratic action The spin-2 perturbation is decomposed into a basis of tensor (transverse-traceless) eigenmodes $\theta_{\omega\sigma}(x)$ as

$$h_{\omega\sigma}^{(0)}(x) = \int d\nu \theta_{\omega\sigma}(\nu, x) \tilde{h}(\nu), \quad (\text{J.21})$$

where

$$(\nabla^2 - \frac{\bar{R}}{6})\theta_{\omega\sigma} = -\frac{\bar{R}}{12} \left(\nu^2 - \frac{9}{4} \right) \theta_{\omega\sigma}, \quad (\text{J.22})$$

where eigenvectors $\theta_{\omega\sigma}$ of different eigenvalues are orthogonal, and normalized such that

$$\int d^4 x \sqrt{\bar{\zeta}} \theta^{\omega\sigma}(\nu, x) \theta_{\omega\sigma}(\mu, x) = \delta(\mu - \nu). \quad (\text{J.23})$$

This orthogonality relation allows us to write

$$\int d^4 x \sqrt{\bar{\zeta}} \theta^{\omega\sigma}(\nu, x) h_{\omega\sigma}^{(0)}(x) = \int d\mu \delta(\mu - \nu) \tilde{h}(\mu) = \tilde{h}(\nu). \quad (\text{J.24})$$

which tells that \tilde{h} is the scalar product between the eigenvector and $h_{(0)\alpha\beta}$. In momentum space (J.21), $h^{(4)}$ can be written explicitly in terms of $h^{(0)}$ if we specialize to a specific boundary geometry.

- For AdS with single-sided boundary conditions, we use (5.51b) to replace $h^{(4)}$ and write the action (J.12) only in terms of $h^{(0)}$. Using the orthogonality (J.23), we obtain

$$S^{(2)}[\bar{\zeta}] = \int d\nu \tilde{h}(\nu)^2 \mathcal{F}_{(-)}(\nu), \quad (\text{J.25})$$

where

$$\mathcal{F}_{(-)} \equiv \frac{N^2 \chi^4}{64\pi^2} \left(\nu^2 - \frac{9}{4} \right) Q_{(-)}(\nu) \quad (\text{J.26})$$

and

$$Q_{(-)}(\nu) = 1 + \frac{2\pi}{N^2} \left(\frac{1}{G\chi^2} + \alpha \right) - \frac{1}{2}(\nu^2 - 1/4) \left[\tilde{\beta}_{\text{eff}} + \log(GN^2\chi^2) - \frac{1}{2} + \mathcal{H}\left(-\frac{1}{2} - \nu\right) + \mathcal{H}\left(-\frac{1}{2} + \nu\right) \right]. \quad (\text{J.27})$$

- For de Sitter, we replace $h^{(4)}$ using (5.35b) into (J.12). The result is

$$\mathcal{F}_{\text{dS}}(\nu) = \frac{N^2 H^4}{64\pi^2} \left(\nu^2 - \frac{9}{4} \right) Q_{\text{dS}}(\nu), \quad \text{Re}(\nu) > 0. \quad (\text{J.28})$$

where

$$Q_{\text{dS}}(\nu) \equiv 1 - \frac{2\pi}{GN^2 H^2} + 2\tilde{\alpha} - \frac{1}{2} \left(\nu^2 - \frac{1}{4} \right) \left[\log(GN^2 H^2) - \frac{1}{2} + 2\mathcal{H}(\nu - 1/2) + \tilde{\beta}_{\text{eff}} \right], \quad \text{Re}(\nu) > 0, \quad (\text{J.29})$$

K. Dynamics of scalar modes

As we have shown in section 4, the trace of the linearized Einstein equation results in (4.10), which is of fourth order in derivatives and therefore propagates two scalar modes. However, that equation is not the whole story because ψ also gets constrained from off-diagonal components of Einstein equation (2.6). To obtain the full set of equations, we need to know how $g_{\omega\sigma}^{(4)}$ depends on ψ to linear order.

Since ψ does not propagate in the bulk, one way to proceed is to perform a diffeomorphism in the bulk as shown in [98, 82]. This will give the full set of equations of motion for ψ . In order to obtain constraints on the variation of $g_{\omega\sigma}^{(4)}$ under a conformal transformation ψ , we solve order by order in the Fefferman-Graham expansion, a particular class of bulk diffeomorphisms which evaluate at ψ on the boundary $\rho = \epsilon$. In [98], such a diffeomorphism is defined as

$$\begin{cases} \tilde{\rho} = \rho e^{-\psi(x)} \approx \rho(1 - \psi(x)), \\ \tilde{x}^\sigma = x^\sigma + a^\sigma. \end{cases} \quad (\text{K.1})$$

Under $\rho \rightarrow \tilde{\rho}$ and $x^\sigma \rightarrow \tilde{x}^\sigma$, the slice metric transforms as

$$g_{\omega\sigma}(x, \rho) \rightarrow g_{\omega\sigma}(x, \rho) + \psi_{\omega\sigma}(x, \rho), \quad (\text{K.2})$$

where $\psi_{\omega\sigma}(x, \rho)$ is given by

$$\psi_{\omega\sigma} = \psi(1 - \rho\partial_\rho)g_{\omega\sigma} + 2\nabla_{(\omega}^g a_{\sigma)}. \quad (\text{K.3})$$

The covariant derivative ∇^g is the one compatible with $g_{\omega\sigma}(x, \rho)$. The bulk diffeomorphism $\psi_{\omega\sigma}(x, \rho)$ admits the Fefferman-Graham expansion

$$\psi_{\omega\sigma}(x, \rho) = \psi g_{\omega\sigma}^{(0)} + \rho\psi_{\omega\sigma}^{(2)} + \rho^2\psi_{\omega\sigma}^{(4)} + \rho^2 \log \rho \hat{\psi}_{\omega\sigma} + \mathcal{O}(\rho^3), \quad (\text{K.4})$$

where we have already used the leading order $\mathcal{O}(\rho^0)$ of (K.3), which gives $\psi g_{\omega\sigma}^{(0)}$. One can already observe that ψ in (K.1) is indeed the same scalar variation as in (4.4) because requiring that (K.1) preserves the tensorial structure of the Fefferman-Graham metric (such that cross-terms $dx^\omega d\rho$ vanish), one can relate the near-boundary expansion of a^σ with the one of $g_{\omega\sigma}$ [98]. The two first terms are enough in our case, they read

$$a^\sigma(x, \rho) = \rho \frac{L^2}{4} \partial^\sigma \psi(x) - \rho^2 \frac{L^2}{8} g^{(2)\omega\sigma} \partial_\omega \psi(x) + \mathcal{O}(\rho^3), \quad (\text{K.5})$$

where indices are now raised and lowered using the boundary metric $g_{\omega\sigma}^{(0)}$. Inserting (K.5) into (K.3) then leads to the result

$$\psi_{\omega\sigma} = \psi g_{\omega\sigma}^{(0)} \quad (\text{K.6})$$

$$\psi_{\omega\sigma}^{(2)} = \frac{L^2}{2} \nabla_\omega \partial_\sigma \psi \quad (\text{K.7})$$

$$\psi_{\omega\sigma}^{(4)} = -\psi(g_{\omega\sigma}^{(4)} + \hat{g}_{\omega\sigma}) + \frac{L^2}{4} \left[\partial^\kappa \psi \nabla_\kappa g_{\omega\sigma}^{(2)} - \nabla_{(\omega} \left\{ g_{\sigma)\kappa}^{(2)} \partial^\kappa \psi \right\} + 2g_{\kappa(\omega}^{(2)} \nabla_{\sigma)} \partial^\kappa \psi \right] \quad (\text{K.8})$$

$$\hat{\psi}_{\omega\sigma} = -\psi \hat{g}_{\omega\sigma} \quad (\text{K.9})$$

One can check the above formulae for $g_{\omega\sigma}^{(0)}$, $g_{\omega\sigma}^{(2)}$ and $\hat{g}_{\omega\sigma}$ starting with the solutions (B.6) and (B.7) and linearize them with ψ . However, the variation (K.8) can only be obtained from the bulk diffeomorphism (K.5). Substituting all of these variation formulae into the CFT stress-tensor we obtain that it transforms under (K.1) as

$$\begin{aligned} \langle T_{\omega\sigma} \rangle [(1+\psi)g^{(0)}] - \langle T_{\omega\sigma} \rangle [g^{(0)}] &= -\psi \langle T_{\omega\sigma} \rangle - \frac{N^2}{4\pi^2 L^4} \left\{ 2\psi \hat{g}_{\omega\sigma} - \frac{L^2}{2} \left[\partial^\kappa \psi \nabla_\kappa g_{\omega\sigma}^{(2)} - \nabla_{(\omega} \left\{ g_{\sigma)\kappa}^{(2)} \partial^\kappa \psi \right\} \right. \right. \\ &+ 2g_{\kappa(\omega}^{(2)} \nabla_{\sigma)} \partial^\kappa \psi \left. \left. \right] + 2(g^{(2)}\psi^{(2)})_{\omega\sigma} - \frac{1}{2}g_{\omega\sigma}^{(0)} \text{Tr} \left[g^{(2)}\psi^{(2)} \right] + \frac{1}{2}g_{\omega\sigma}^{(0)} \text{Tr} \left[g^{(2)} \right] \text{Tr} \left[\psi^{(2)} \right] \right. \\ &\left. \left. - \frac{1}{2} \left(\psi_{\omega\sigma}^{(2)} \text{Tr} \left[g^{(2)} \right] + g_{\omega\sigma}^{(2)} \text{Tr} \left[\psi^{(2)} \right] \right) \right\}. \quad (\text{K.10}) \end{aligned}$$

We now restrict to a variation around (A)dS background with constant \bar{R} . The background values of $g_{\omega\sigma}^{(2)}$ and $g_{\omega\sigma}^{(4)}$ are then given by table (2.53). The stress-tensor variation (K.10) then evaluates to the much simpler expression given by

$$\langle T_{\omega\sigma} \rangle [(1+\psi)\bar{\zeta}] - \langle T_{\omega\sigma} \rangle [\bar{\zeta}] = -\psi \langle T_{\omega\sigma} \rangle - \frac{N^2 \bar{R}}{192\pi^2} (\nabla_\omega \partial_\sigma - \bar{\zeta}_{\omega\sigma} \square) \psi, \quad (\text{K.11})$$

where now, all geometrical quantities such as \bar{R} and ∇_ω are built with the background metric $\bar{\zeta}_{\omega\sigma}$. The first term corresponds to the classical scaling law for the stress tensor under a Weyl transformation. However, the second term of (K.11) brings a correction coming from the conformal anomaly of the quantum vacuum expectation value $\langle T_{\omega\sigma} \rangle$. We now have all the ingredients to linearize the Einstein equation (2.6) under a conformal transformation ψ . One can use the conformal variation of the Ricci tensor

$$R_{\omega\sigma} [(1+\psi)\bar{\zeta}] - R_{\omega\sigma} [\bar{\zeta}] = -\frac{1}{2} (\bar{\zeta}_{\omega\sigma} \square + 2\nabla_\omega \partial_\sigma) \psi. \quad (\text{K.12})$$

Using (K.11) and linearizing all other terms with (K.12), we obtain the following equation

$$\begin{aligned} &\left\{ \bar{\zeta}_{\omega\sigma} \square - \nabla_\omega \partial_\sigma + \Lambda \bar{\zeta}_{\omega\sigma} + \frac{G\alpha}{4} \left[\left(\frac{\bar{R}}{4} + \square \right) \bar{\zeta}_{\omega\sigma} - \nabla_\omega \partial_\sigma \right] \square \right. \\ &\left. - \frac{GN^2 \bar{R}}{24\pi} \left[\frac{\bar{R}}{8} \bar{\zeta}_{\omega\sigma} + (\bar{\zeta}_{\omega\sigma} \square - \nabla_\omega \partial_\sigma) \right] \right\} \psi = 0. \quad (\text{K.13}) \end{aligned}$$

Inserting the value of Λ (2.57) allows us to write (K.13) in a simple, factorized form given by

$$\left\{ \left(\square + \frac{\bar{R}}{4} \right) \bar{\zeta}_{\omega\sigma} - \nabla_\omega \partial_\sigma \right\} \left[1 + \frac{G\alpha}{4} \square - \frac{GN^2 \bar{R}}{24\pi} \right] \psi = 0. \quad (\text{K.14})$$

Taking the trace of (K.14) gives back equation (4.10). The factor in curly braces is responsible for the solution we are now trying to discard.

The squared brackets in (K.14) are absorbed into an auxiliary field Ψ defined by

$$\Psi \equiv \left[1 + \frac{G\alpha}{4} \square - \frac{GN^2 \bar{R}}{24\pi} \right] \psi. \quad (\text{K.15})$$

As we show in the next subsection, Ψ is non-propagating and it can be consistently set to zero in the absence of sources. This does not occur in the case of conformal matter considered here. As a consequence, the equation of motion for the physical ψ is

$$\left[1 + \frac{G\alpha}{4}\square - \frac{GN^2\bar{R}}{24\pi}\right]\psi = 0 \quad (\text{K.16})$$

K.1 Constrained scalar mode

This subsection is devoted to showing that the only propagating mode for ψ is the solution to the equation $\Psi = 0$ as it is defined in (K.15). First, we observe that imposing flat space ($R = 0$) in (K.14) reduces to the case studied in [8]. More precisely, our equation (K.14) for $R = 0$ is their equation (8) for $K_2 = \frac{\alpha}{192\pi}$. We are going to follow their arguments and generalize them to space-time with non-zero curvature.

In flat space, equation (K.14) reduces to

$$(\square\eta_{\omega\sigma} - \partial_\omega\partial_\sigma)\Psi = 0, \quad (\text{K.17})$$

where

$$\Psi = \psi + \frac{G\alpha}{4}\square\psi. \quad (\text{K.18})$$

If there is an additional matter content with stress-tensor $\theta_{\omega\sigma}$, then (K.17) becomes:

$$(\square\eta_{\omega\sigma} - \partial_\omega\partial_\sigma)\Psi = 8\pi G\delta_\psi\theta_{\omega\sigma}, \quad (\text{K.19})$$

where δ_ψ means the linearization operator with respect to the conformal scalar ψ , as in the left-hand-side of (K.11). The scalar Ψ does not propagate because it is constrained by the “00” and “0*i*” components of Einstein’s equation as we now show. The “00” component of this equation is given by

$$-\delta^{ij}\partial_i\partial_j\Psi = 8\pi G\delta_\Psi\theta_{00}. \quad (\text{K.20})$$

Thus, Ψ solves a static equation, similar to an electric potential in classical E&M. If we demand that Ψ vanishes as $|\vec{x}| \rightarrow \infty$, then Ψ is completely fixed by equation (K.20).

To see even more explicitly that Ψ is non-propagating, it is enough to look at the solutions in the absence of sources: from the $i \neq j$ and $0i$ components of (K.17) we obtain:

$$\partial_i\partial_j\Psi = 0, \quad \partial_0\partial_i\Psi = 0 \quad (\text{K.21})$$

which implies that Ψ is the sum of separate linear functions of the spatial coordinates with time-independent coefficients, plus an arbitrary function of time only. Demanding that Ψ vanishes at spatial infinity forces us to set all the coefficients to zero, showing that $\Psi = 0$ is the only physical solution.

In de Sitter, Ψ defined in (K.15) is solution to the equation (K.14) rewritten as

$$\left\{ \left(\square + \frac{\bar{R}}{4} \right) \zeta_{\omega\sigma} - \nabla_{\omega} \partial_{\sigma} \right\} \Psi = 0. \quad (\text{K.22})$$

As in the flat space-time case, we show that Ψ solves a *static* equation and can be consistently set to zero. If there was an additional matter content with a stress-tensor $\theta_{\mu\nu}$, the linearized Einstein equation for ψ would read

$$\left\{ \left(\square + \frac{\bar{R}}{4} \right) \zeta_{\omega\sigma} - \nabla_{\omega} \partial_{\sigma} \right\} \Psi = 8\pi G \delta_{\psi} \theta_{\omega\sigma}. \quad (\text{K.23})$$

The “00” component of this equation written in Poincaré coordinates is given by

$$\left\{ -\partial_i^2 - 3(\tau^{-1} \partial_0 + \tau^{-2}) \right\} \Psi = 8\pi G \delta_{\psi} \theta_{00}. \quad (\text{K.24})$$

We see that the second order time derivative is absent and we are left with a non-propagating equation. We now set the source to zero on the right hand side. In this case, the two terms of the previous equation must separately vanish, as one can see using the $\omega = 0, \sigma = i$ components of (K.22):

$$(\partial_0 + \tau^{-1}) \partial_i \Psi = 0, \quad (\text{K.25})$$

The most general solution is

$$\Psi = f(\tau) + \tau^{-1} A(x_i). \quad (\text{K.26})$$

Inserting the above expression in (K.24) (with the right hand side set to zero) gives the two equations

$$-\nabla^2 A = 0, \quad (\partial_0 + \tau^{-1}) f = 0. \quad (\text{K.27})$$

The equation for f is solved by $f = \text{const}/\tau$, so that we can include this as a constant term in A and just write Ψ as

$$\Psi = \frac{A(x_i)}{\tau}, \quad \nabla^2 A = 0. \quad (\text{K.28})$$

Finally, inserting this result in the $\omega = i, \sigma = j$ component of (K.22), we obtain

$$\partial_i \partial_j A = 0, \quad (\text{K.29})$$

which is solved by $A = a + b^i x_i$. Therefore, the most general solution of (K.22) is

$$\Psi = \tau^{-1} (a + b^i x_i). \quad (\text{K.30})$$

Demanding that field configurations vanish at spatial infinity, we arrive at the same conclusion as in flat space, that Ψ is constraint to vanish.

By a similar computation as in dS, where τ^2 is replaced by $-z^2$, the conclusion that Ψ is constrained to vanish for AdS.

L. Comparison with previous results for a dS boundary

In this appendix, we map our parameters $(\tilde{\alpha}, \tilde{\beta}_{\text{eff}}, GN^2R)$ and compare some of our results to previous papers which have used a similar setup.

The first study of de Sitter stability with a non-perturbative CFT obtained holographically was done in [58]. This paper corresponds to the particular case where the (renormalized) cosmological constant is zero. So the only contribution to the background curvature comes from the CFT. We also compare our results to the more recent paper [74], which also studies the stability of de Sitter with a holographic CFT. In their study, the R^2 coefficient α is set to zero.

In our paper, stability conditions rely on the poles of the propagator of metric perturbations and on the residue of these poles. The variable of these propagators is the eigenvalue ν^2 of the laplacian operator. Thus, we must compare our definition of ν (and k for flat space) to the ones of previous papers. First, the definition of [74] for ν is the same as ours (5.26). In addition, the radial part of the bulk equation of motion (5.27) coincides with eq. (49) of [74]. Since one must choose the sign of $\text{Re}(\nu)$ (see discussion below (5.29)), their solution corresponds to taking $\text{Re}(\nu) < 0$, which is equivalent to $C_+ = 0$ in our case. As discussed already in the paper, negative real parts of ν are obtained by taking $\nu \rightarrow -\nu$ in (5.37).

To compare with the second paper [58], we relate ν to their eigenvalue labeled by p as

$$H^{-2}\nabla^2 h_{\omega\sigma}^{(0)} = (2 - p(p + 3))h_{\omega\sigma}^{(0)}. \quad (\text{L.1})$$

Comparing this equation with (5.26) leads to

$$p = \pm\nu - \frac{3}{2}. \quad (\text{L.2})$$

Similarly with the choice of $\text{Re}(\nu)$ positive or negative, the normalizability of the bulk solution depends on the choice of p in (L.2). In [58], they choose $\text{Re}(p) > -3/2$. Therefore, one needs to use the replacement $p = -\nu - 3/2$ to retrieve the results of [74] which has negative real parts for ν and $p = \nu - 3/2$ to compare with our results for which ν has positive real parts.

We now compare the spin-2 equation of motions in these different papers. In [74], the equation of motion is given by

$$\left(\nu^2 - \frac{9}{4}\right) Q_C(\nu) = 0, \quad (\text{L.3})$$

where

$$Q_C(\nu) \equiv 256 + \frac{8GN^2H^2}{\pi - GN^2H^2} \left\{ 16 + (1 - 4\nu^2) \left[3 - 4\mathcal{H} \left(-\frac{1}{2} - \nu \right) + 4 \log \left(\frac{2E}{H} \right) \right] \right\}, \quad (\text{L.4})$$

where E must be related to our parameter β . On the other hand, the inverse propagator $F(p)$ in eq. (3.82) of [58] is given by

$$F_H(p, \beta) = \Psi(p) + \frac{4\pi R^2}{GN^2} (p^2 + 3p + 6) + 2\beta_H p(p + 1)(p + 2)(p + 3) - 4\alpha_H p(p + 3), \quad (\text{L.5})$$

$$\begin{aligned} \Psi(p) = & p(p+1)(p+2)(p+3)[\psi(p/2+5/2) + \psi(p/2+2) - \psi(2) - \psi(1)] \\ & + p^4 + 2p^3 - 5p^2 - 10p - 6, \end{aligned} \quad (\text{L.6})$$

where α_H and β_H must be related to the parameters α and β from our setup (2.4), (2.5). Using (L.2), we obtain an algebraic relation between $Q_C(\nu)$ and $F(p)$ given by

$$F_H(p) = \frac{\pi - GN^2H^2}{64GN^2H^2} Q_C(\nu), \quad (\text{L.7})$$

if the parameters of [58] and [74] are related by

$$\alpha_H = 0, \quad (\text{L.8})$$

$$GN^2H^2 = 4\pi, \quad (\text{L.9})$$

$$\log\left(\frac{H}{E}\right) = \beta_H + \frac{3}{4}. \quad (\text{L.10})$$

First, (L.8) is due to the absence of a R^2 term in the boundary action of [74]. This additional term is proportional to α_H in [58]. Second, (L.9) is explained by the absence of a cosmological constant in the Einstein-Hilbert action of [58], which fixes the dimensionless curvature GN^2H^2 to 4π since the CFT is the only contribution to the background curvature. This is equivalent to setting $\Lambda = 0$ in (2.57), leading to (L.9). Before, we compare our results with these two previous papers. In our case, the curvature is not fixed (as in [74]), and the coefficient of the R^2 term is also arbitrary (as in [58]).

We now compare our inverse propagator $\mathcal{F}_{\text{as}}(\nu)$ (5.39) with $F_H(p)$ (L.7), which obey the algebraic relation

$$-2\mathcal{F}_{\text{as}}(\nu) = F_H(p), \quad (\text{L.11})$$

valid under the following conditions

$$\tilde{\alpha} = \alpha_H, \quad (\text{L.12})$$

$$GN^2H^2 = 4\pi, \quad (\text{L.13})$$

$$\tilde{\beta}_{\text{eff}} = \frac{1}{2} + 2\beta_H - \log(16\pi). \quad (\text{L.14})$$

Our results agree with [58] if we set the curvature as in (L.13). Their analysis is similar to the one done in the discussion of Figure 27, which corresponds to the special case where the massless spin-2 pole is a ghost. Our results also agree with [74] for $\alpha = 0$. For instance, their final result is the obtention of (8.19) for $\alpha = 0$, which tells the value of β from which the spin-2 sector is non-tachyonic. However, they do not discuss the presence of ghosts and whether their tachyon is above or below the species cutoff.

M. Snapshots for the spin-2 propagator

In this appendix, we provide snapshots for the poles of the tensor propagator in the $\nu \in \mathbb{C}$ plane, for a wide range of parameters $(\tilde{\alpha}, \tilde{\beta}_{\text{eff}}, GN^2R)$.

M.1 Minkowski

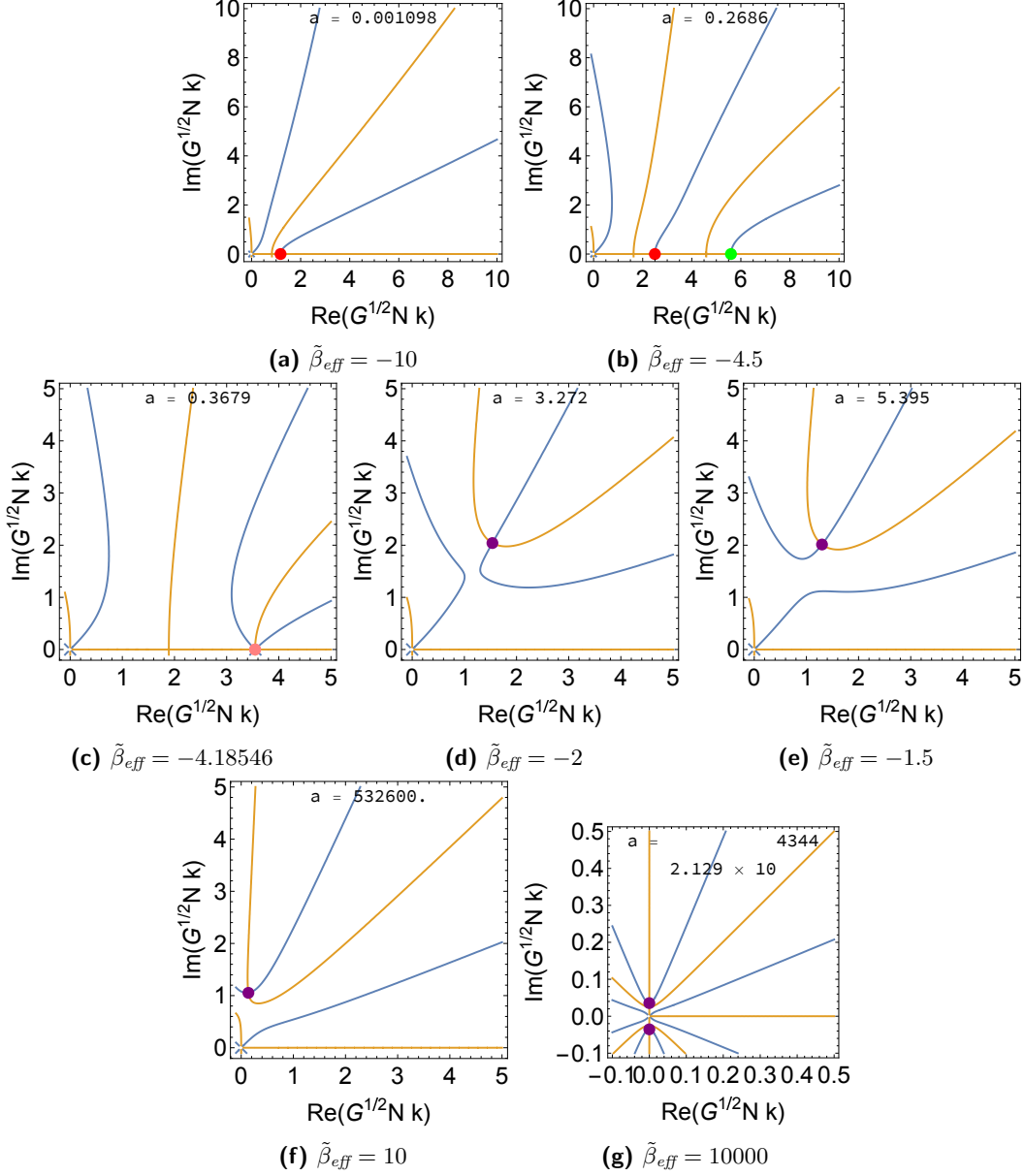


Figure 25: These snapshots show the poles of the spin-2 propagator in Minkowski space-time, for selected values of the parameter $\tilde{\beta}_{\text{eff}}$. The poles correspond to zeros of the real (blue curve) and imaginary (orange curve) parts of $\mathcal{F}_{\text{flat}}(k)$ (5.21) and are denoted by coloured dots. A green dot indicates a negative residue (ghost-free), while a red dot corresponds to a positive residue (ghost). A purple dot is for complex residue (also a ghost). As $\tilde{\beta}_{\text{eff}}$ is increased going from upper left to lower right, two tachyons located on the real axis for negative merge in snapshot (c) to form a second order pole. The merging happens at $\tilde{\beta}_{\text{eff}} = \tilde{\beta}_{\text{eff}}^{\text{merge}}$ (7.8). For $\tilde{\beta}_{\text{eff}} > \tilde{\beta}_{\text{eff}}^{\text{merge}}$ there is a complex conjugate pair, which moves to the origin for large and positive $\tilde{\beta}_{\text{eff}}$.

M.2 de Sitter

In the main text, we have given two examples of parameters $(\tilde{\alpha}, GN^2H^2)$ for which we find numerically the poles of the tensor propagator in de Sitter space-time in Figure 26 (small

curvature, zero $\tilde{\alpha}$) and in Figure 27 (generic curvature, negative $\tilde{\alpha}$). These two examples give different behaviours when $\tilde{\beta}_{\text{eff}}$ is varied. One could question if these two examples are paradigmatic or if another choice of $(\tilde{\alpha}, GN^2H^2)$ would lead to different results. In the following table, we give the links to snapshots for 9 different regimes.

$\tilde{\alpha} \backslash GN^2H^2$	$\ll 1$	$\sim \pi$	$\gg 1$
$-\tilde{\alpha} \gg 1$	Fig. 28	Fig. 29	Fig. 30
$ \tilde{\alpha} \leq 1$	Fig. 26	Fig. 35, Fig. 36	Fig. 37, Fig. 38
$\tilde{\alpha} \gg 1$	Fig. 34, Fig. 33	Fig. 32	Fig. 31

a (8.7) is either **positive** if “Fig” is written in green, or **negative** if it is written in red. **Blue boxes** correspond to regimes where the sign of a must be determined by the inequality (8.12) :

$$a < 0 \iff \frac{\pi}{GN^2H^2} < \tilde{\alpha} + \frac{1}{2} \quad (\text{M.1})$$

The conclusion is that a given point in the $(\tilde{\alpha}, GN^2H^2)$ plane corresponds either to the behaviour of

- **Type A:** Figure 26, where two tachyons merge on the real axis and form a pair of complex conjugate poles when $\tilde{\beta}_{\text{eff}}$ is increased.
- **Type B:** Figure 27, where all the poles are real valued ν^2 for any value of $\tilde{\beta}_{\text{eff}}$ (no complex pole).

In general, for a given point in the $(\tilde{\alpha}, GN^2H^2)$ plane, a positive a is type A and a negative a is type B as predicted by the large- $|\nu|$ approximation (8.5). However, this is not necessarily true for large GN^2H^2 and a close to zero, where the large- $|\nu|$ analysis breaks down.

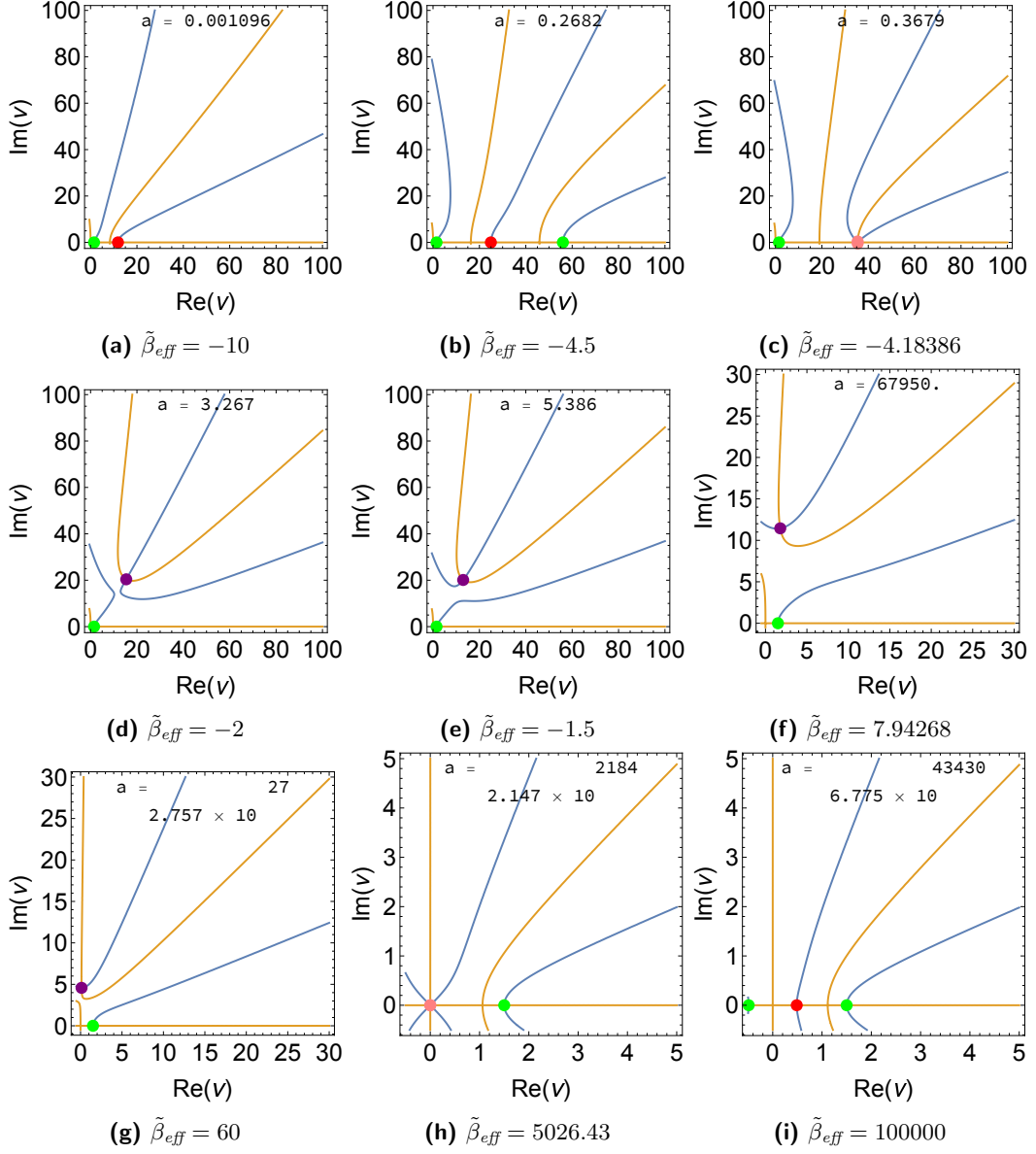


Figure 26: Zeros of the real (blue curve) and imaginary (orange curve) parts of the de Sitter tensor propagator $\mathcal{F}_{\text{dS}}(\nu)$ (5.36) for different values of $\tilde{\beta}_{\text{eff}}$, and $\alpha = 0$, $GN^2H^2 = 0.01$. Solutions are therefore given by the intersection of blue and orange lines. Small values of $\tilde{\beta}_{\text{eff}}$, have two tachyons on the real axis. They merge in snapshot (c) where $\tilde{\beta}_{\text{eff}}$ is given by (8.11). This merging forms a double zero because the first derivative of \mathcal{F}_{dS} vanishes. The instability crosses the green stability line $\text{Re}(\nu) = 3/2$ at another critical value of $\tilde{\beta}_{\text{eff}}$ (8.19).

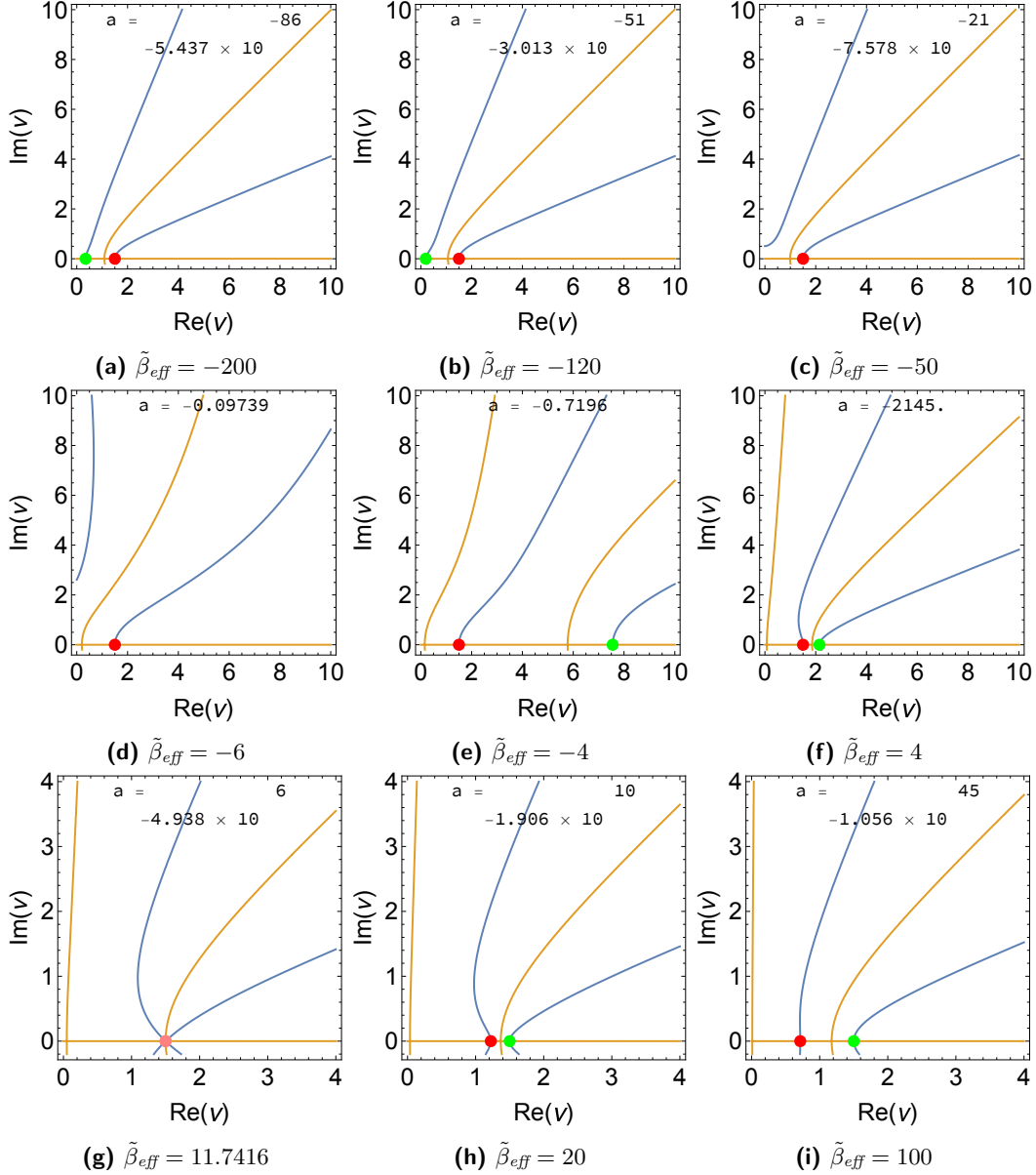


Figure 27: Zeros of the real (blue curve) and imaginary (orange curve) parts of the inverse spin-2 propagator of de Sitter $\mathcal{F}_{dS}^{-1}(\nu)$ (5.36) for different values of $\tilde{\beta}_{eff}$, with fixed $\tilde{\alpha} = 10$ and $GN^2H^2 = \pi/4$. Solutions are therefore given by the intersection of blue and orange lines. The tachyon, which was outside the window, arrives from snapshot (e) and merges at the critical value (8.14) in snapshot (g). Increasing $\tilde{\beta}_{eff}$ to large and positive values makes the ghost pole converge at $\nu = 1/2$.

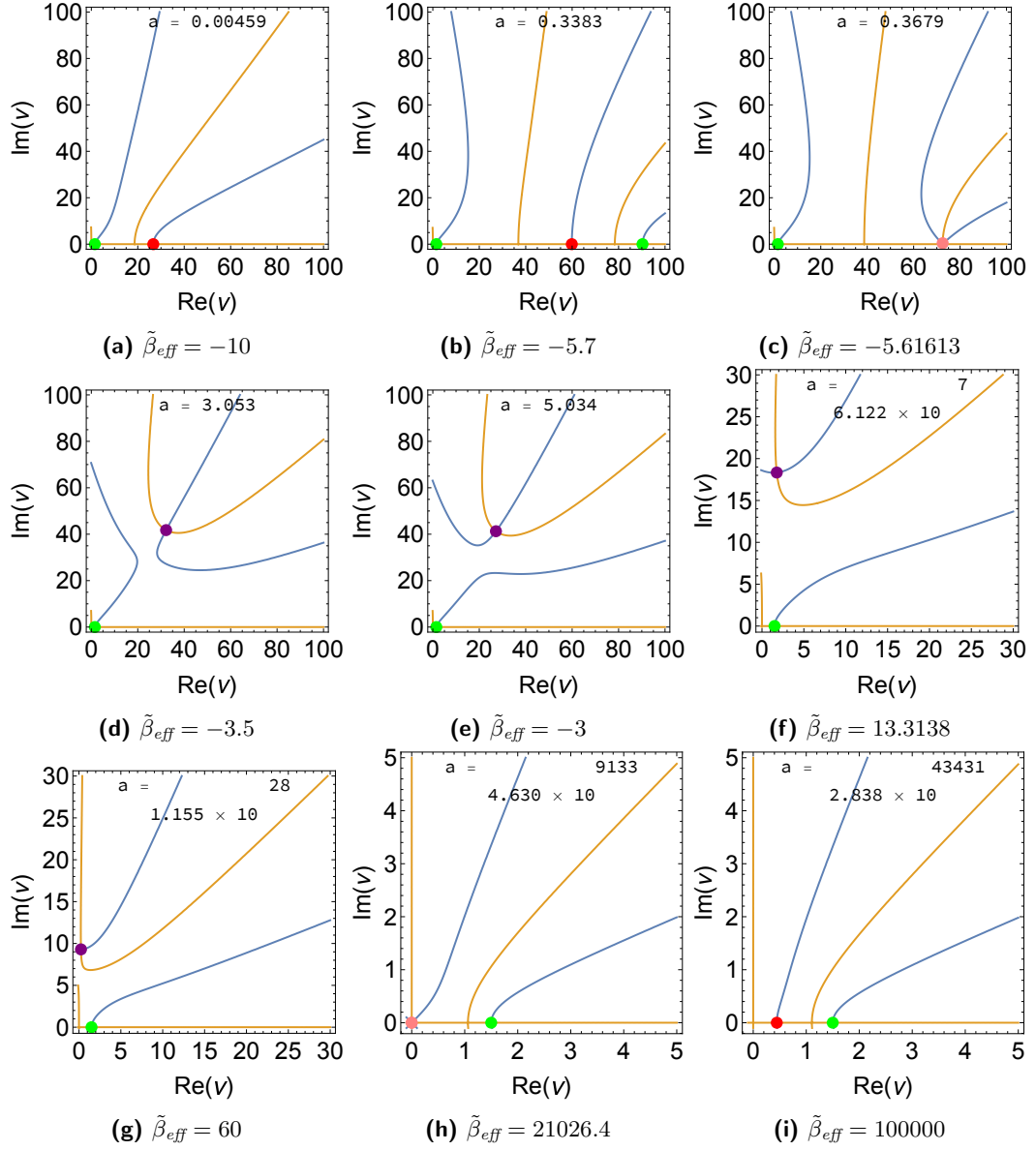


Figure 28: *de Sitter*, $\tilde{\alpha} = -1000$, $GN^2H^2 = 0.01$.

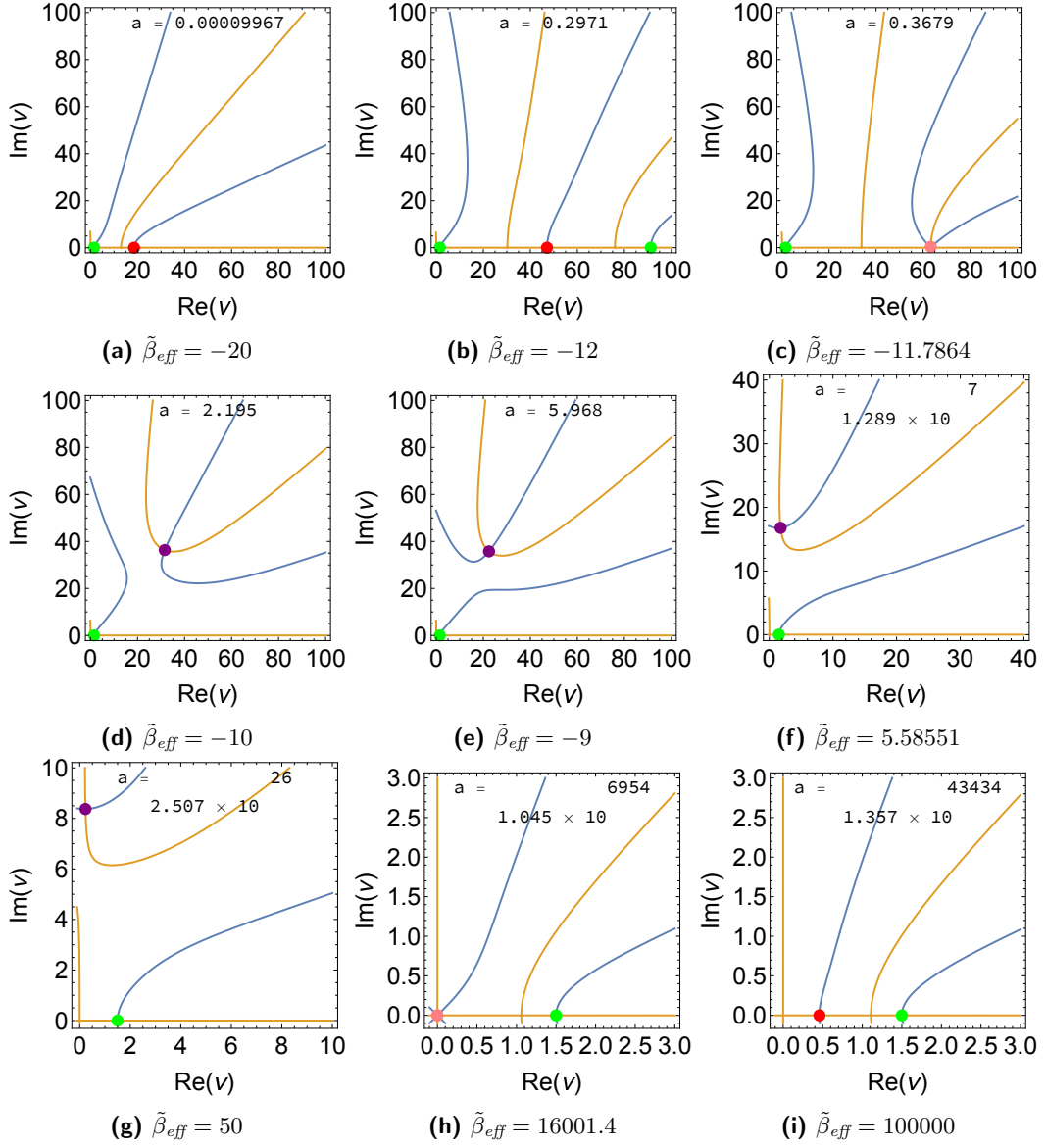


Figure 29: dS , $\tilde{\alpha} = -1000$, $GN^2H^2 = 2\pi$.

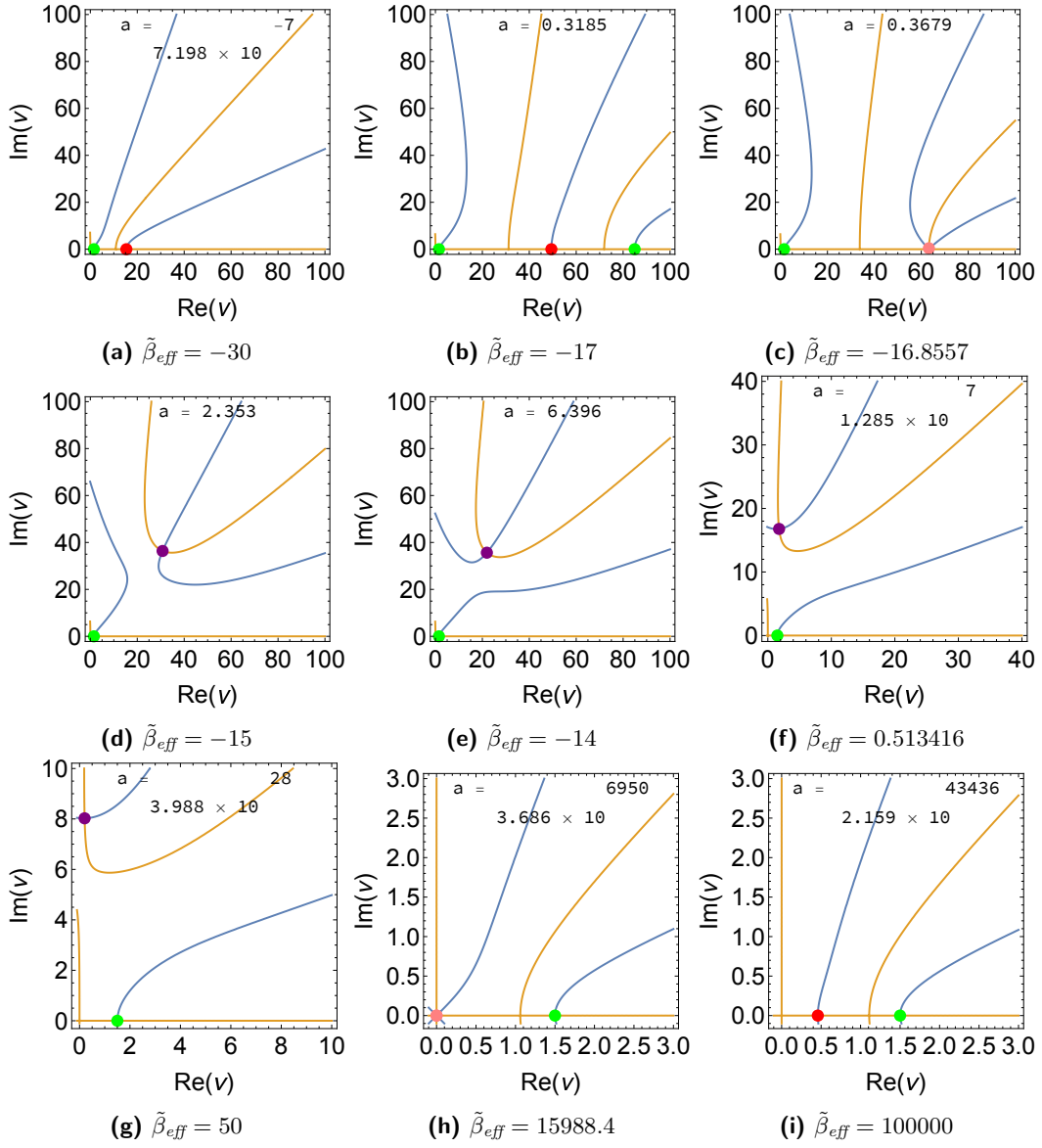


Figure 30: dS , $\tilde{\alpha} = -1000$, $GN^2H^2 = 1000$.

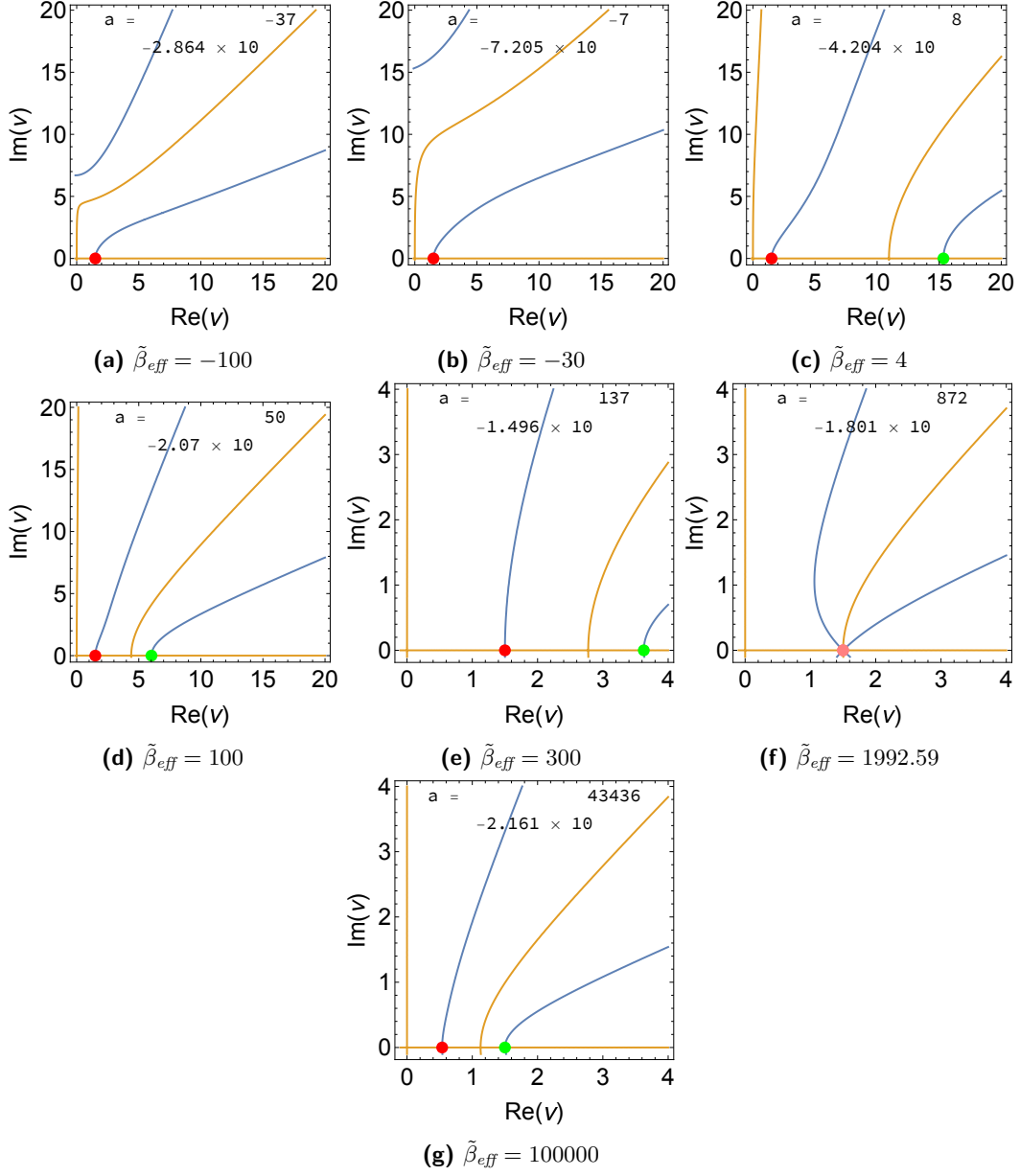


Figure 31: dS , $\tilde{\alpha} = 1000$, $GN^2H^2 = 1000$.

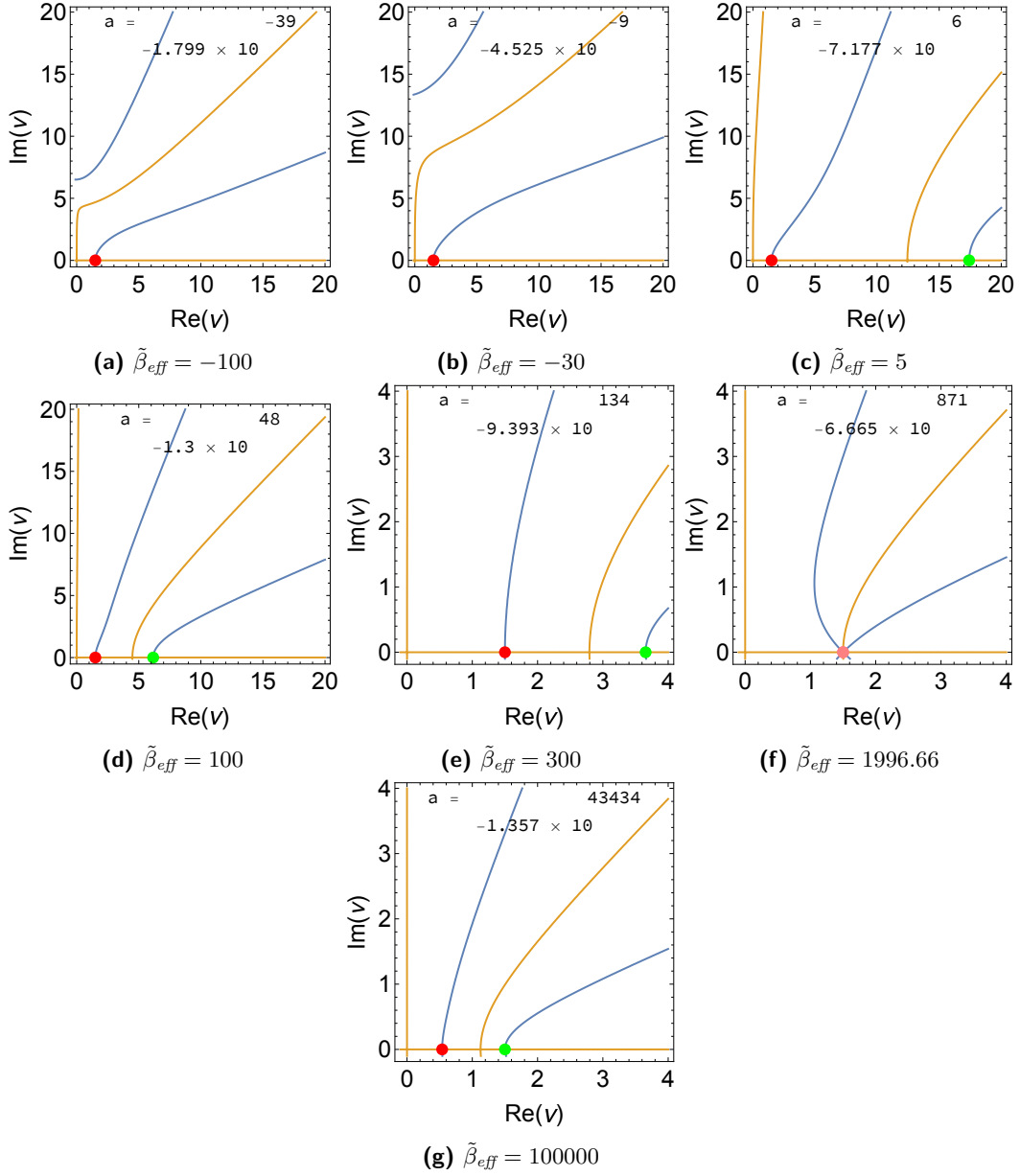


Figure 32: dS , $\tilde{\alpha} = 1000$, $GN^2H^2 = 2\pi$.

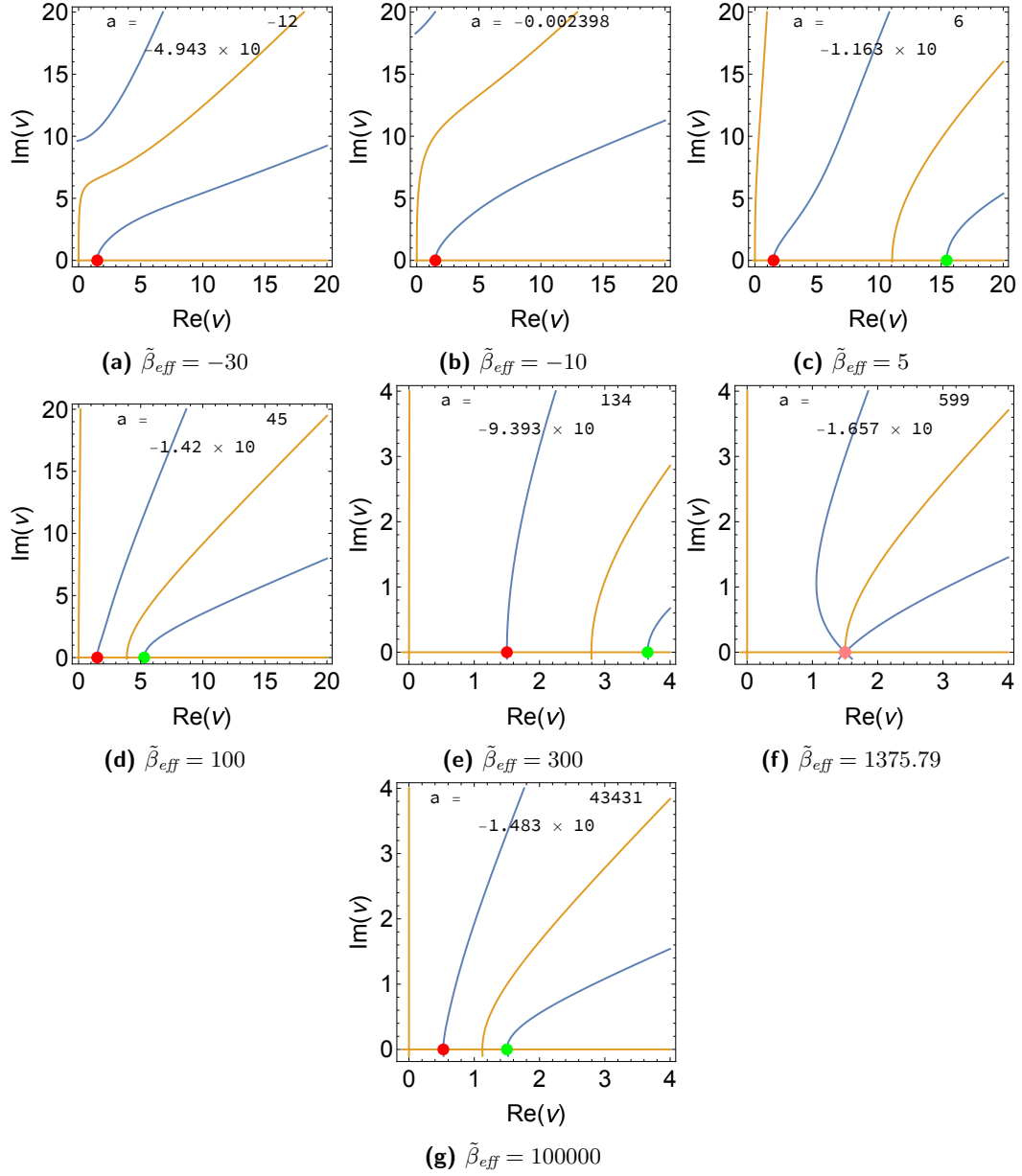


Figure 33: dS , $\tilde{\alpha} = 1000$, $GN^2H^2 = 0.01$.

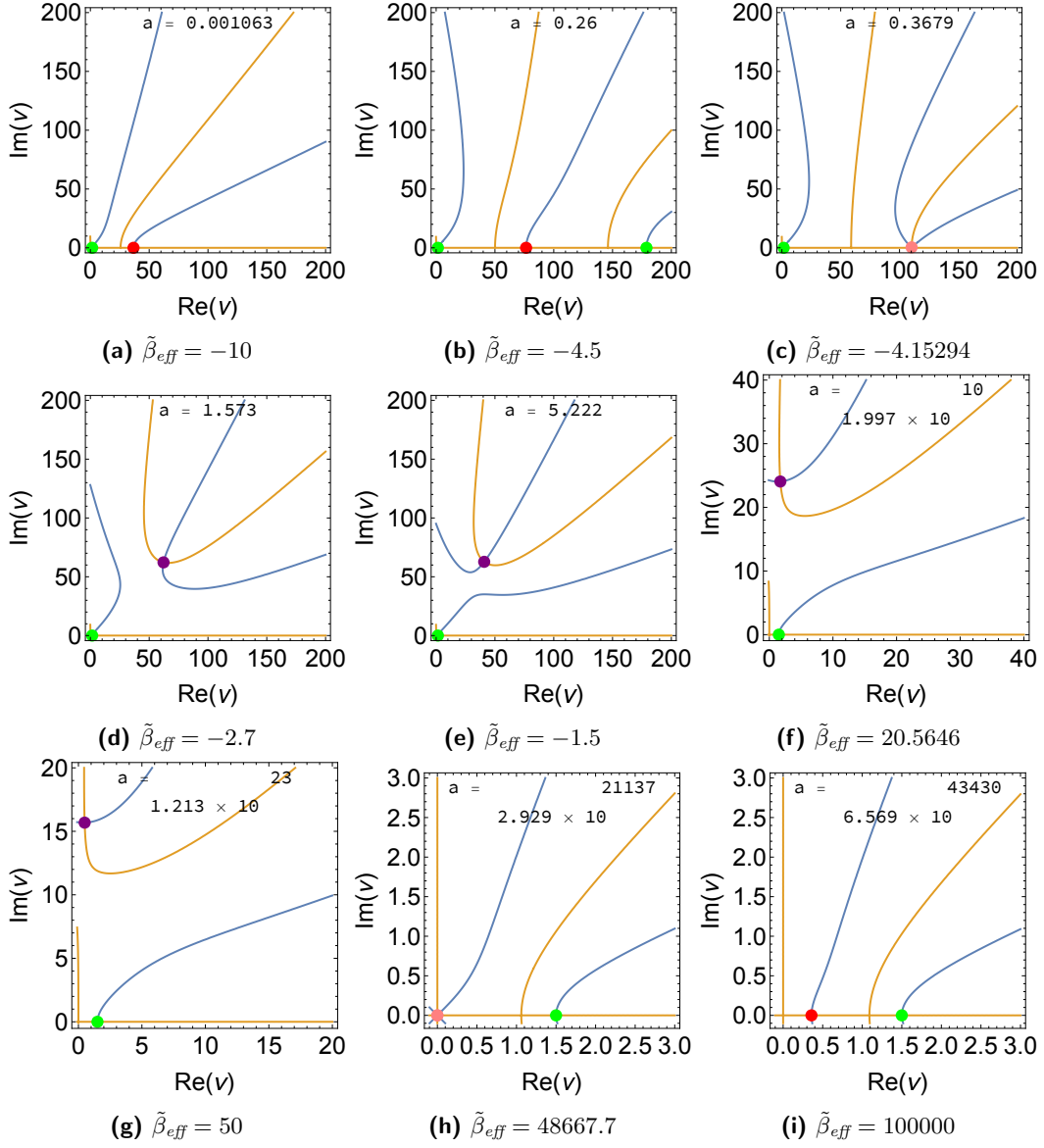


Figure 34: dS , $\tilde{\alpha} = 100$, $GN^2H^2 = 0.001$.

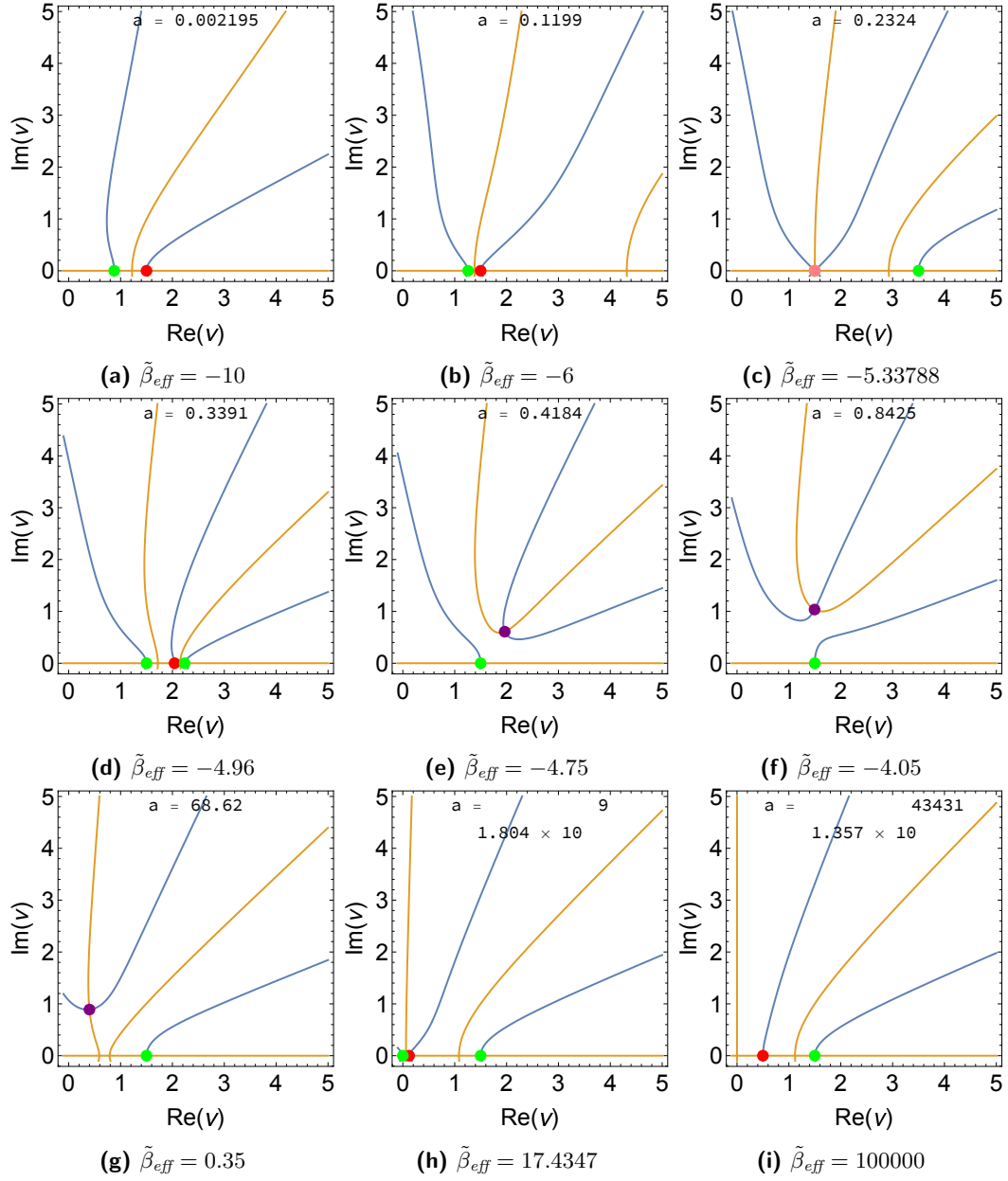


Figure 35: dS , $\tilde{\alpha} = -1$, $GN^2H^2 = 2\pi$.

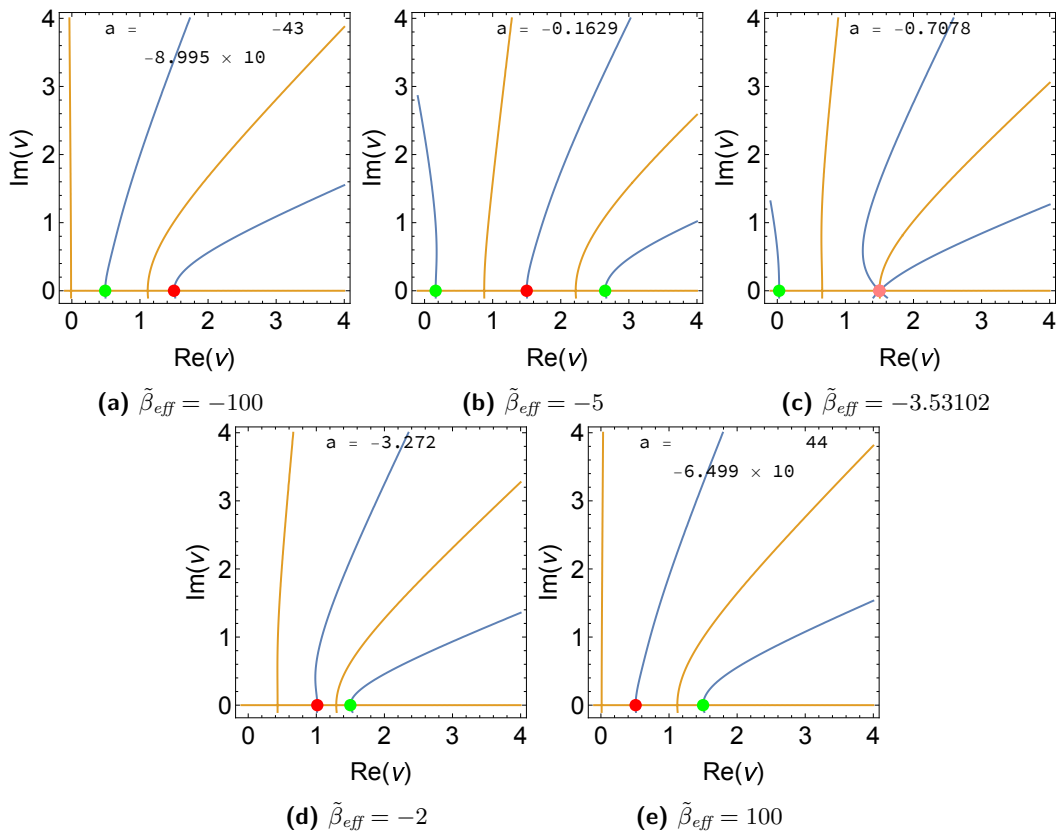


Figure 36: $\alpha = 0, GN^2H^2 = 4\pi$.

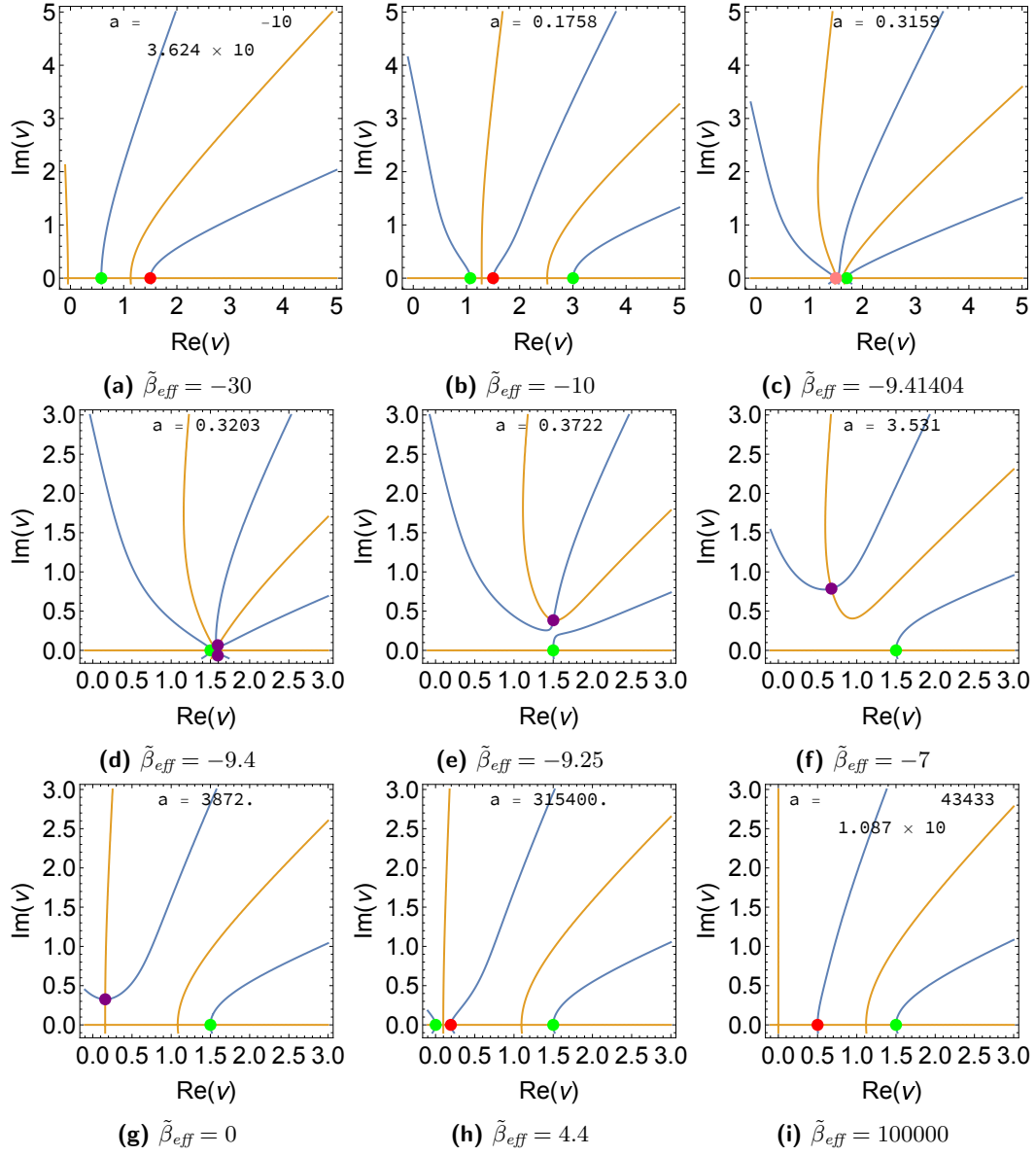


Figure 37: dS , $\tilde{\alpha} = -1$, $GN^2H^2 = 1000$.

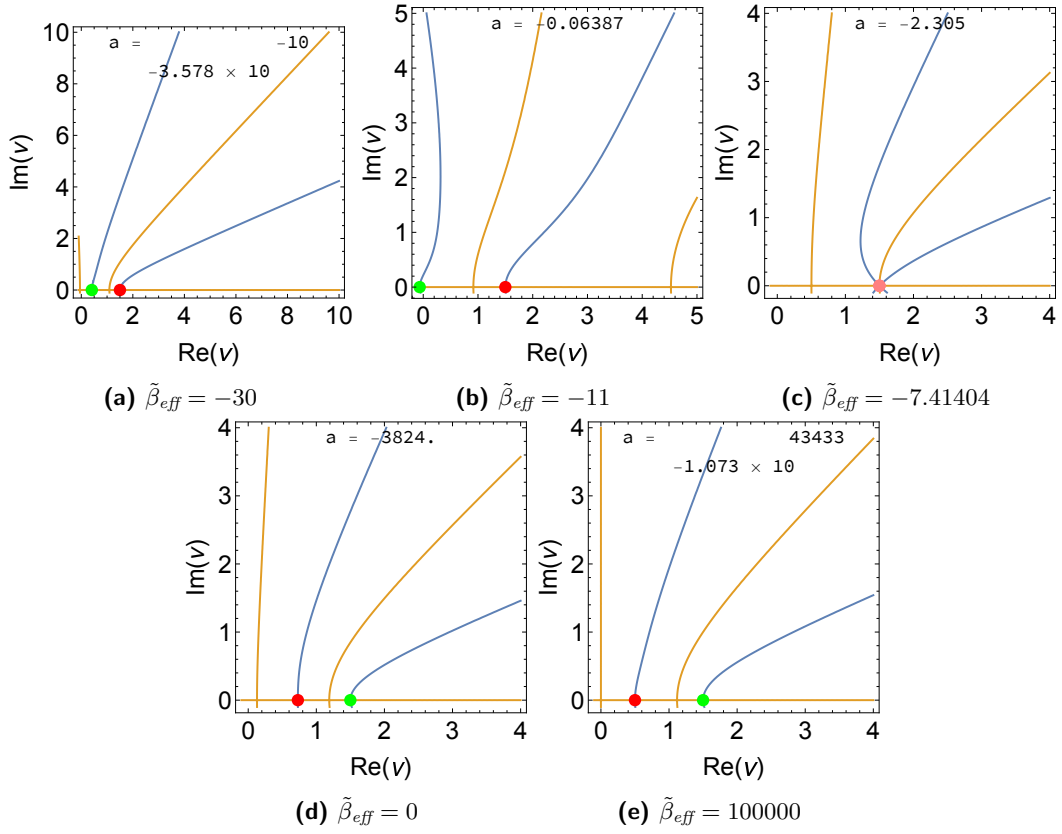


Figure 38: dS , $\tilde{\alpha} = 0$, $GN^2H^2 = 1000$.

M.3 Anti-de Sitter

As we did for dS in the previous subsection, we provide snapshots for some examples of parameters $(\tilde{\alpha}, GN^2H^2)$ while varying $\tilde{\beta}_{\text{eff}}$. They are summarized in the following table.

$\tilde{\alpha} \backslash GN^2\chi^2$	$\ll 1$	$\sim \pi$	$\gg 1$
$-\tilde{\alpha} \gg 1$	Fig. 47, Fig. 46	Fig. 45	Fig. 44
$ \tilde{\alpha} \leq 2$	Fig. 39	Fig. 48, Fig. 49	Fig. 50, Fig. 51
$\tilde{\alpha} \gg 1$	Fig. 41	Fig. 42	Fig. 44

a (9.6) is either **positive** if “Fig” is written in green, or **negative** if it is written in red. **Blue boxes** correspond to regimes where the sign of a must be determined by the inequality (9.8) :

$$a < 0 \iff \frac{\pi}{GN^2\chi^2} < -\left(\tilde{\alpha} + \frac{1}{2}\right) \quad (\text{M.2})$$

The conclusion is that a given point in the $(\tilde{\alpha}, GN^2\chi^2)$ plane corresponds either to the behaviour of

- **Type A:** Figure 39, where two tachyons merge on the imaginary axis and form a pair of complex conjugate poles when $\tilde{\beta}_{\text{eff}}$ is increased.
- **Type B:** Figure 40, where all the poles are real valued ν^2 for any value of $\tilde{\beta}_{\text{eff}}$ (no complex pole).

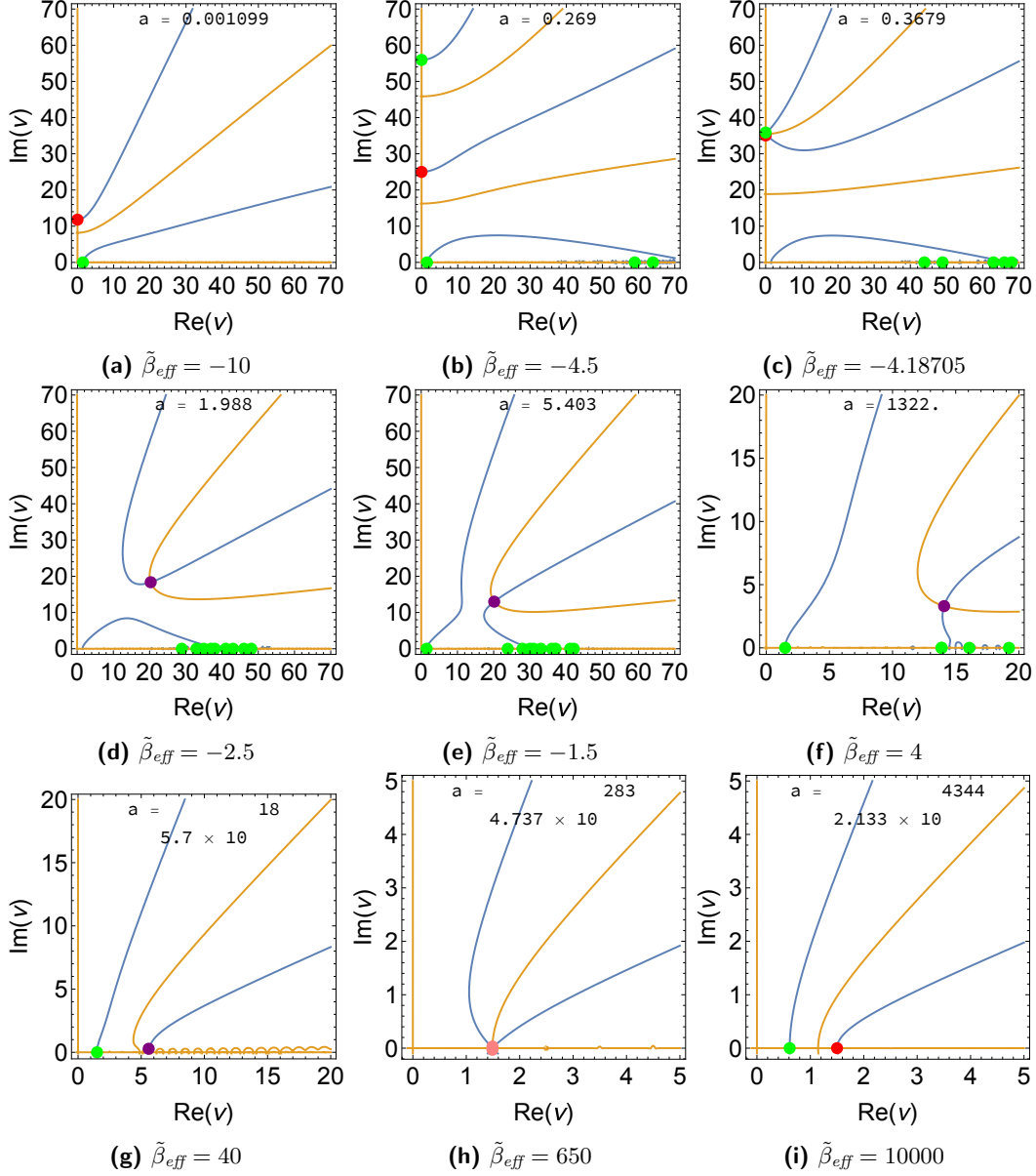


Figure 39: Zeros of the real (blue curve) and imaginary (orange curve) parts of the AdS spin-2 inverse correlator $\mathcal{F}_{(-)}^{-1}(\nu)$ (5.52) for $\alpha = 0$, $GN^2\chi^2 = 0.01$. Each panel is obtained for a different value of $\tilde{\beta}_{eff}$. The colour of a pole represents the sign of its residue. Green is for positive, red for negative and purple for complex residue. Two tachyons on the imaginary axis merge around the value of $\tilde{\beta}_{eff}$ given in equation (9.7), shown in snapshot (c). This merging is a second-order pole because \mathcal{F}'_{dS} vanishes. The two complex conjugate poles move to the complex plane as $\tilde{\beta}_{eff}$ is increased. Two poles in (g) merge in snapshot (h), where they form a massless second-order pole. Higher values of $\tilde{\beta}_{eff}$ (i) have a massless ghost and a $\nu = 1/2$ stable pole.

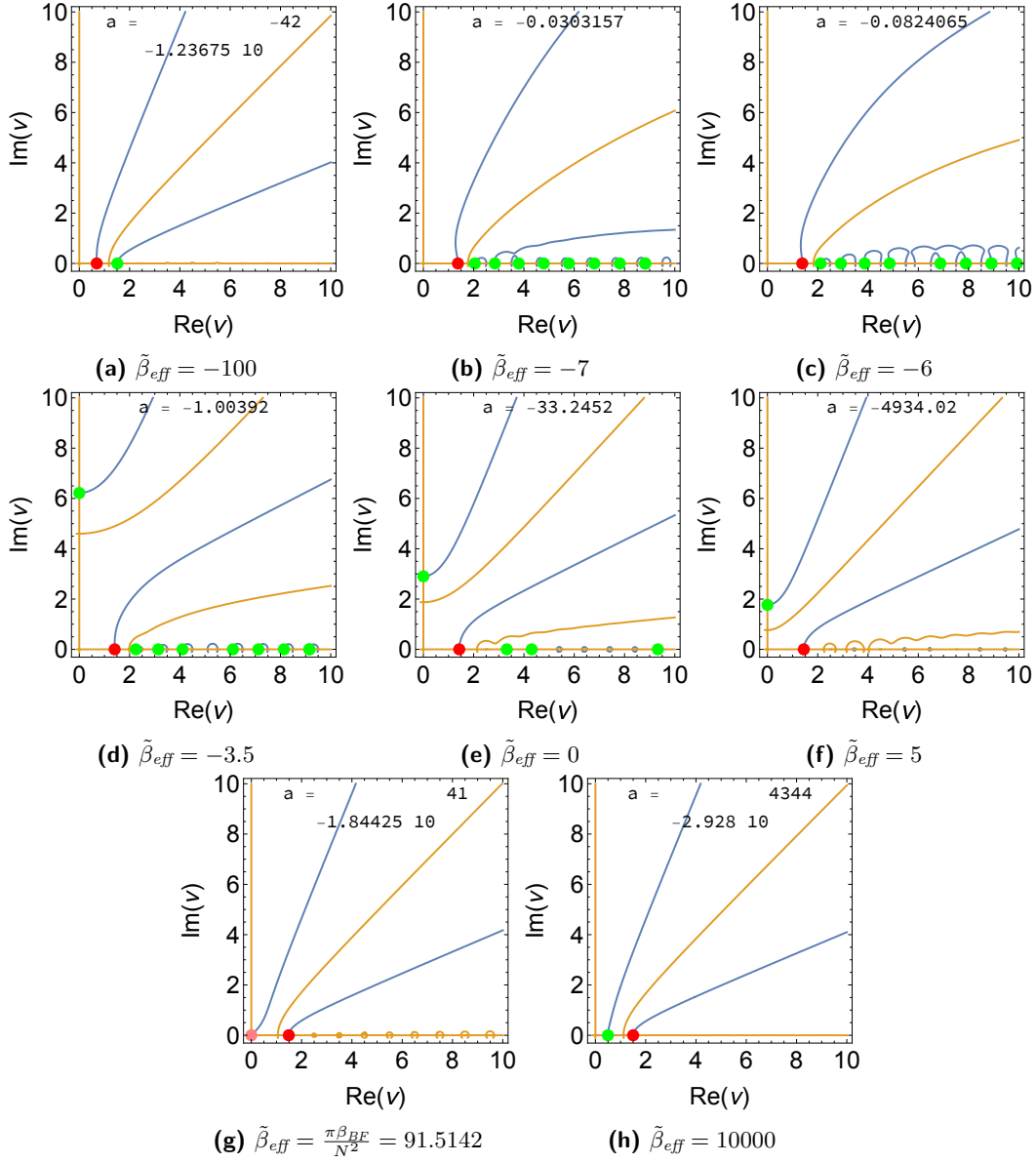


Figure 40: Zeros of the real (blue curve) and imaginary (orange curve) parts of the AdS spin-2 inverse correlator $\mathcal{F}_{(-)}^{-1}(\nu)$ (5.36) for different values of $\tilde{\beta}_{\text{eff}}$, with fixed $\alpha = -10$ and $GN^2\chi^2 = \pi/4$. The colour of a pole represents the sign of its residue. Green is for positive, red for negative and purple for complex residue. From negative values of $\tilde{\beta}_{\text{eff}}$, up to some critical value in snapshot (g), there is one tachyon which cannot be seen in snapshot (a) because it is outside the window and moves towards the origin. Snapshot (g) shows the transition from tachyonic instability to tachyonic stability, where the origin is a double pole.

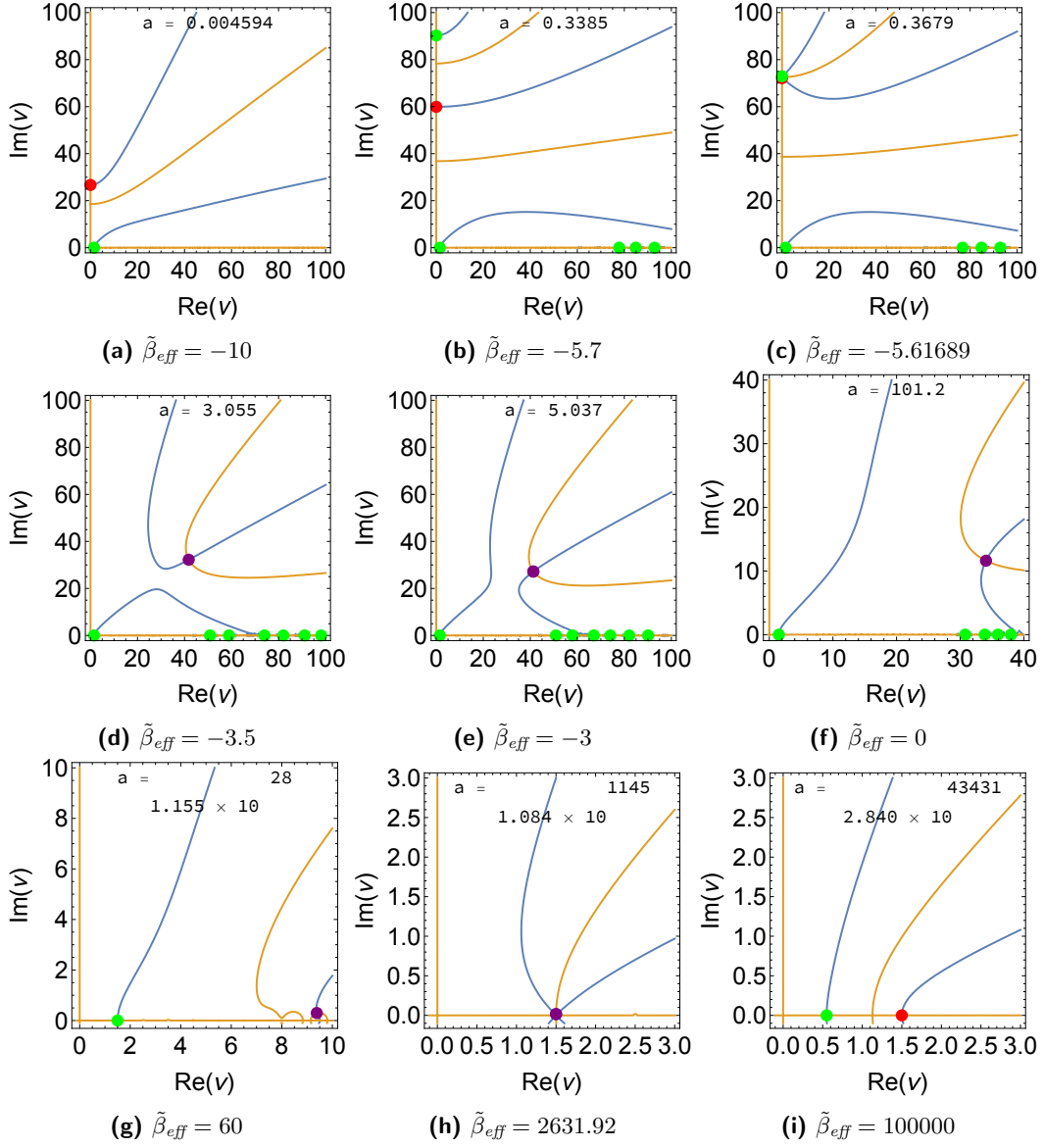


Figure 41: AdS , $\tilde{\alpha} = 1000$, $GN^2\chi^2 = 0.01$.

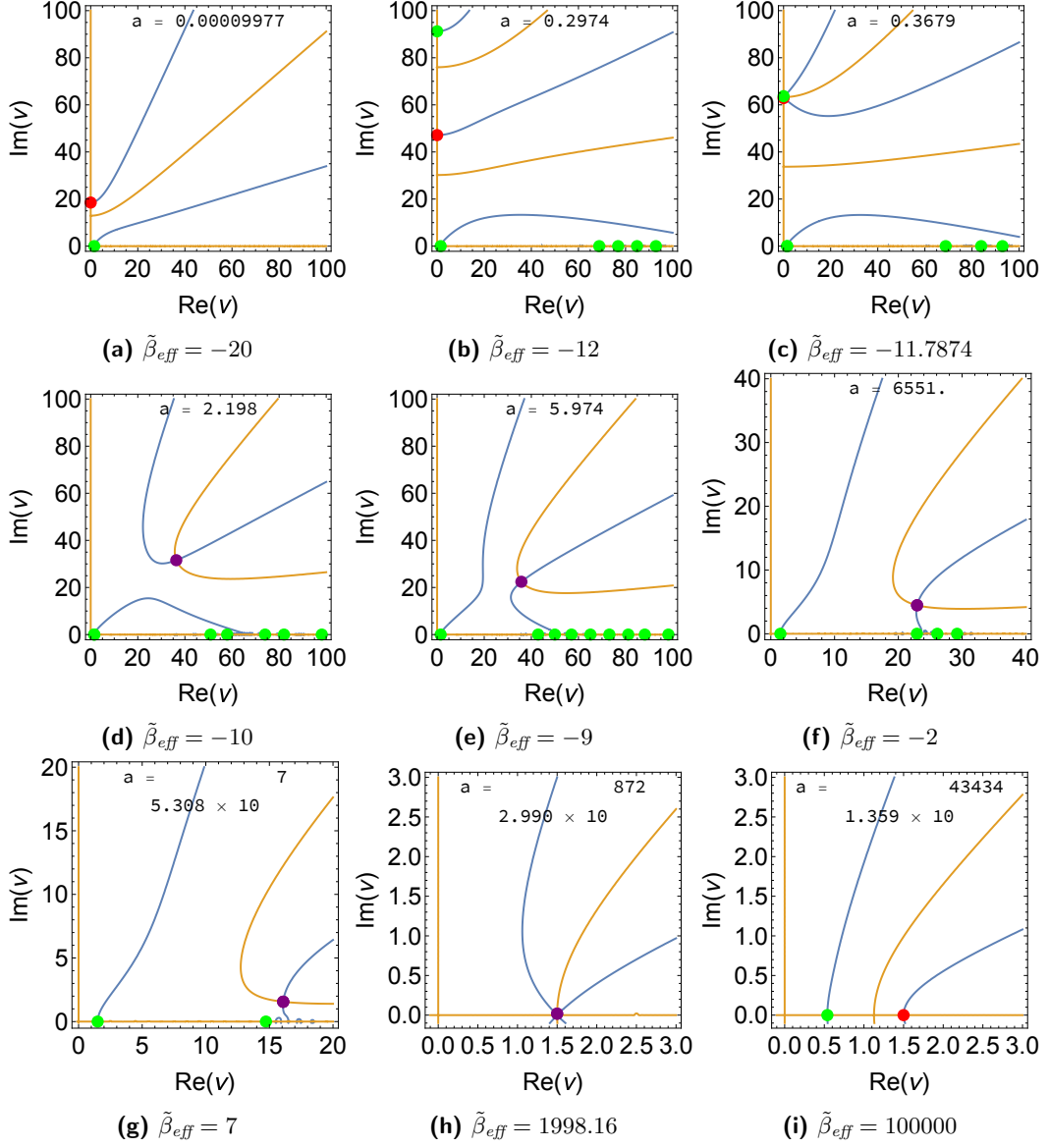


Figure 42: AdS , $\tilde{\alpha} = 1000$, $GN^2\chi^2 = 2\pi$.

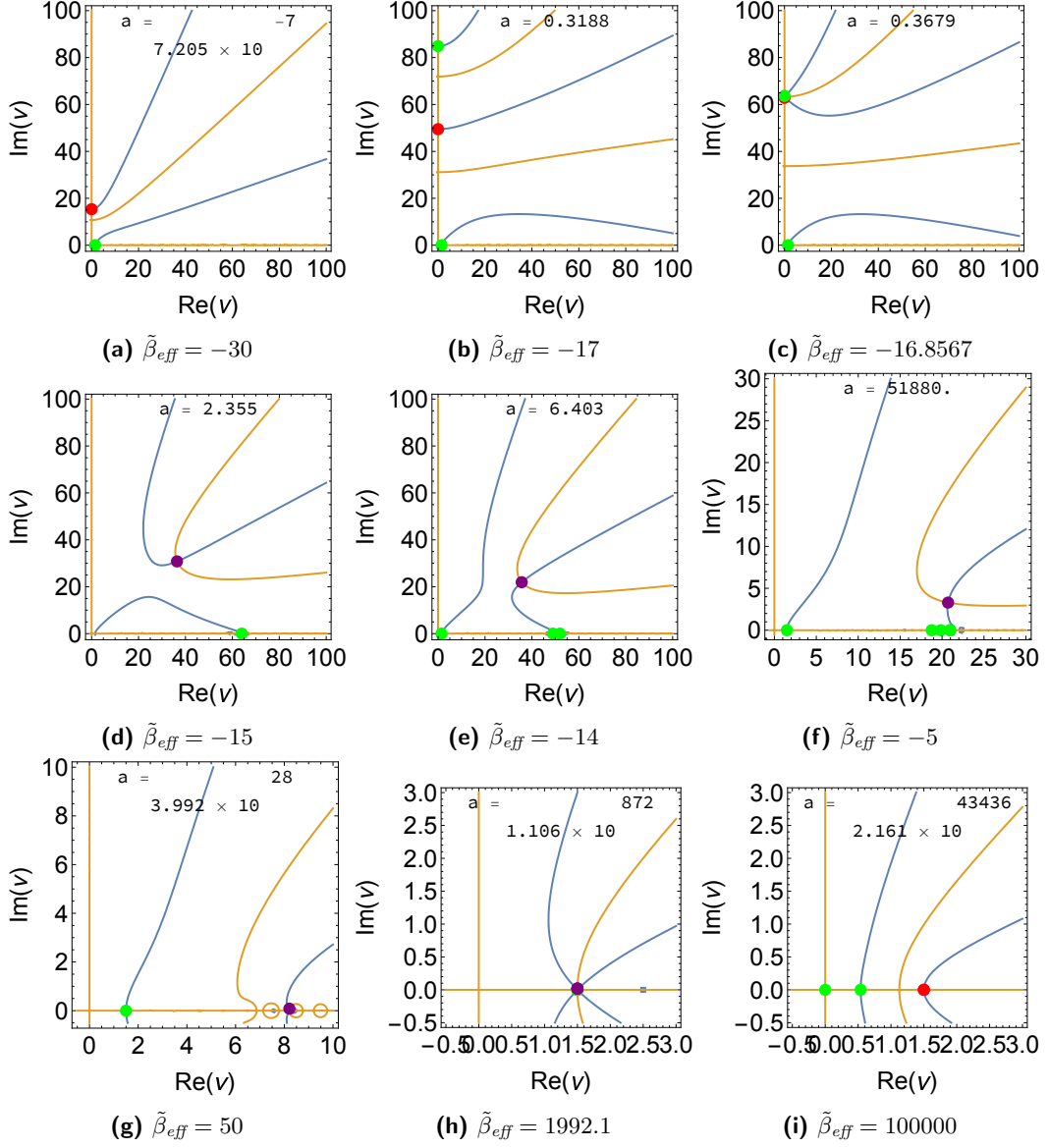


Figure 43: AdS , $\tilde{\alpha} = 1000$, $GN^2\chi^2 = 1000$.

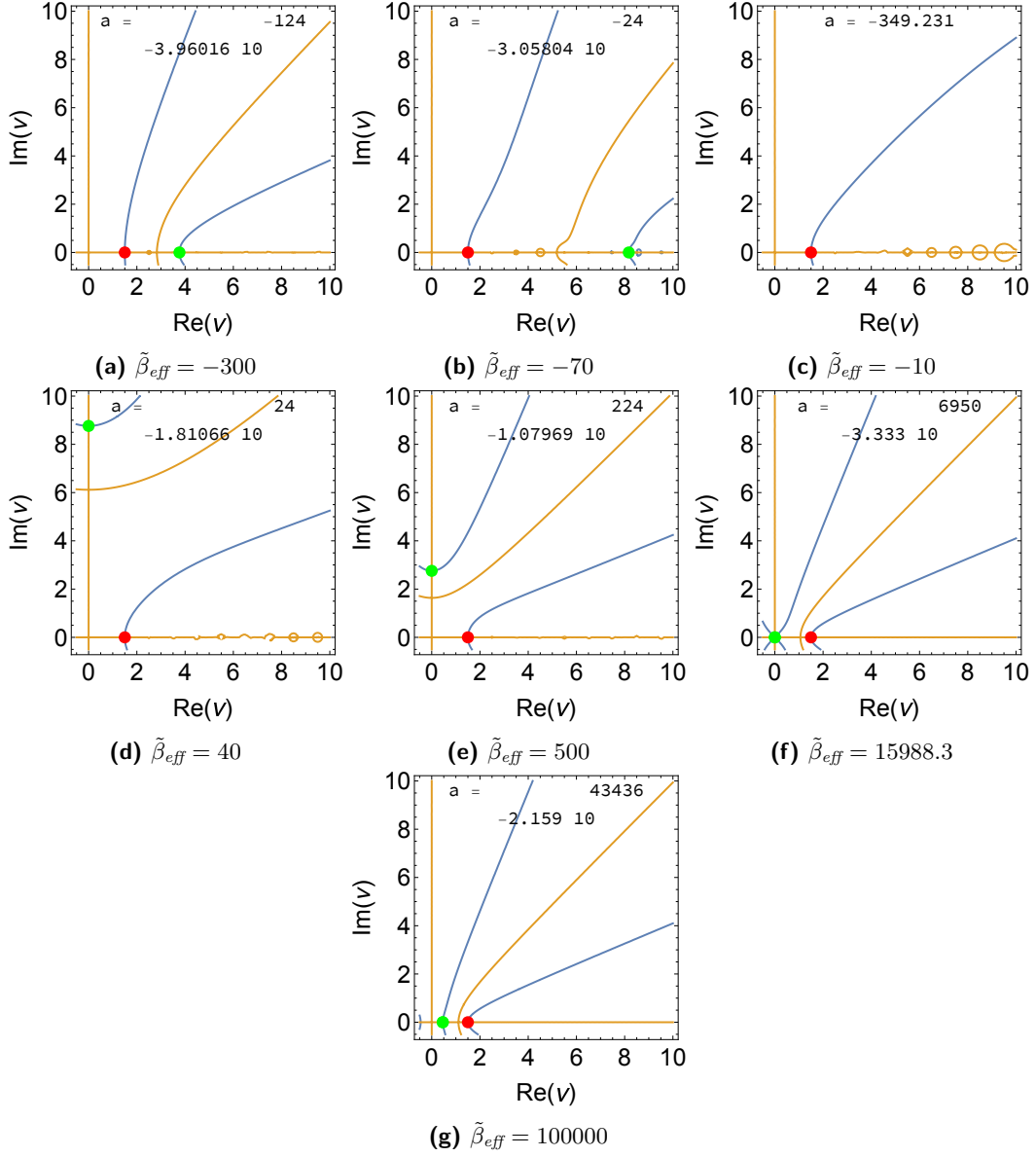


Figure 44: AdS , $\tilde{\alpha} = -1000$, $GN^2\chi^2 = 1000$.

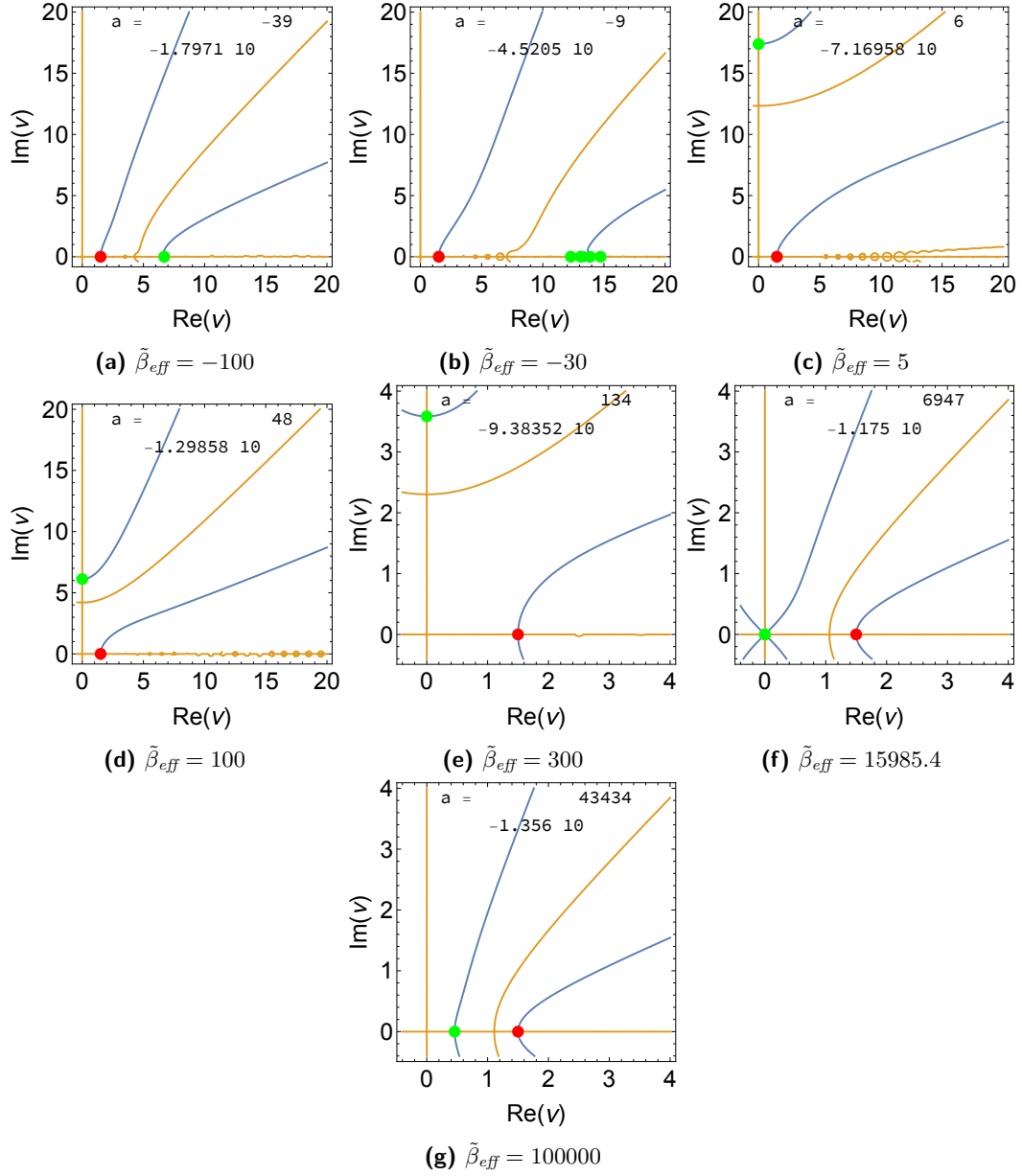


Figure 45: *AdS*, $\tilde{\alpha} = -1000$, $GN^2\chi^2 = 2\pi$.

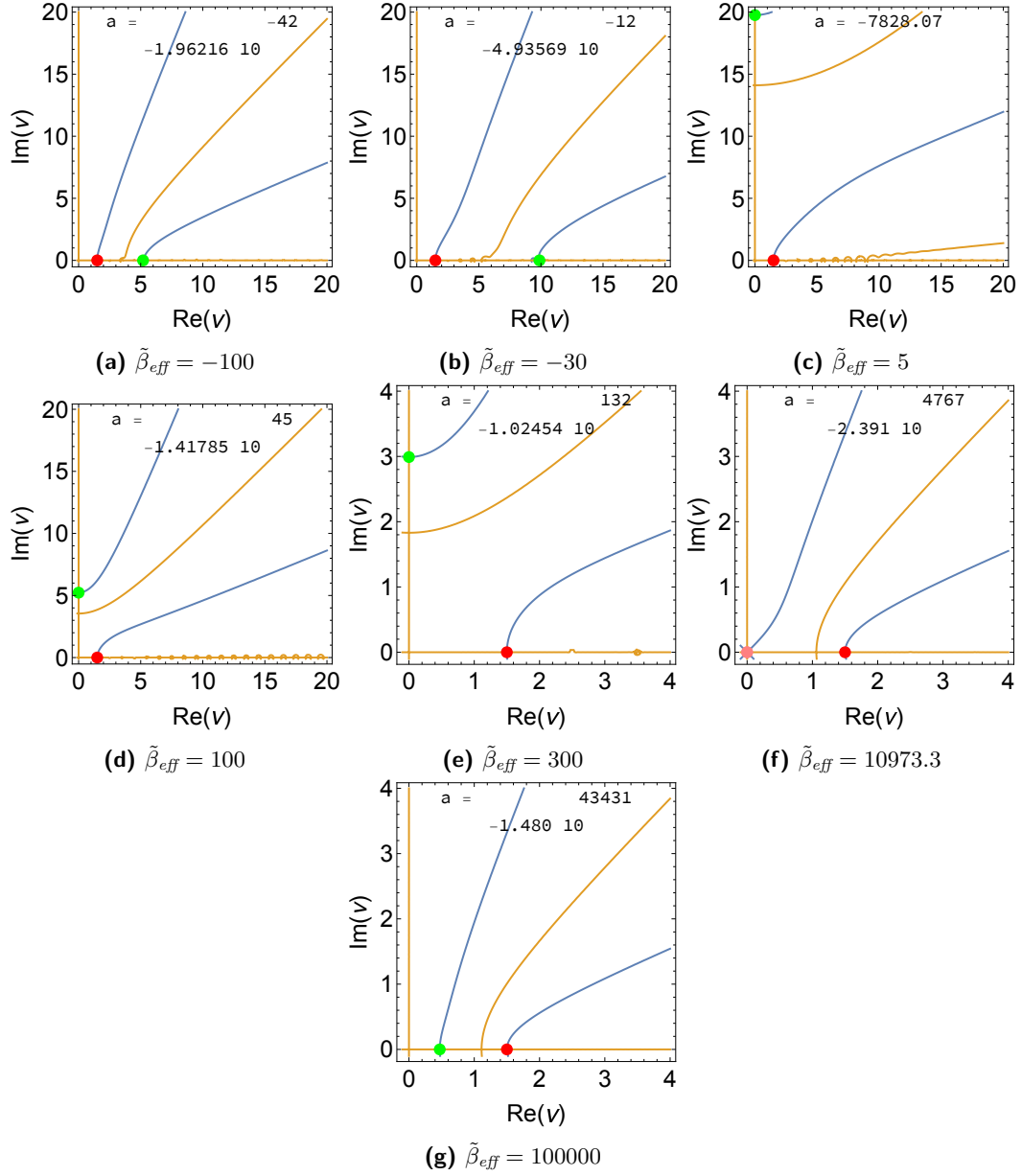


Figure 46: AdS , $\tilde{\alpha} = -1000$, $GN^2\chi^2 = 0.01$.

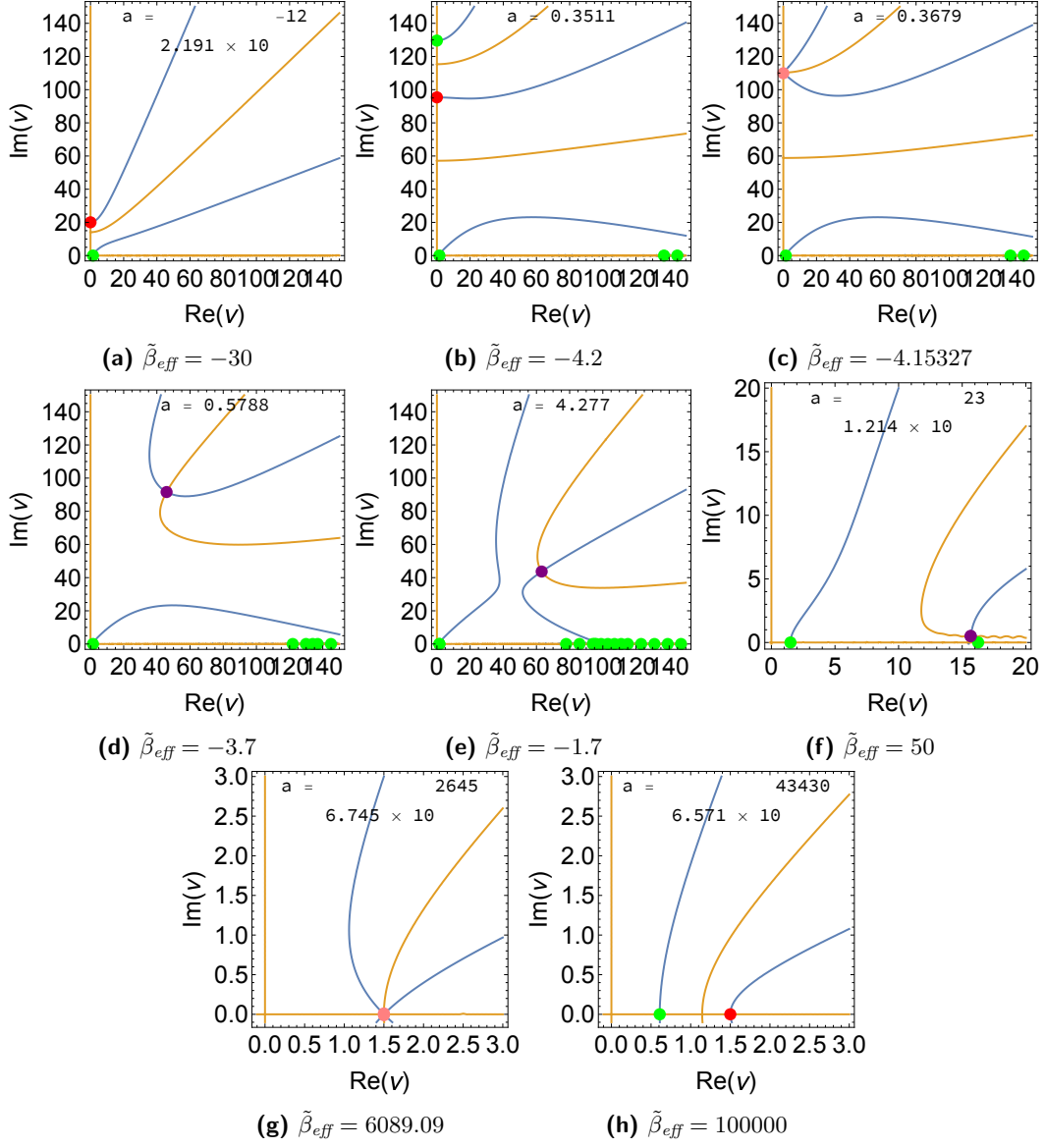


Figure 47: AdS, $\tilde{\alpha} = -100$, $GN^2\chi^2 = 0.001$.

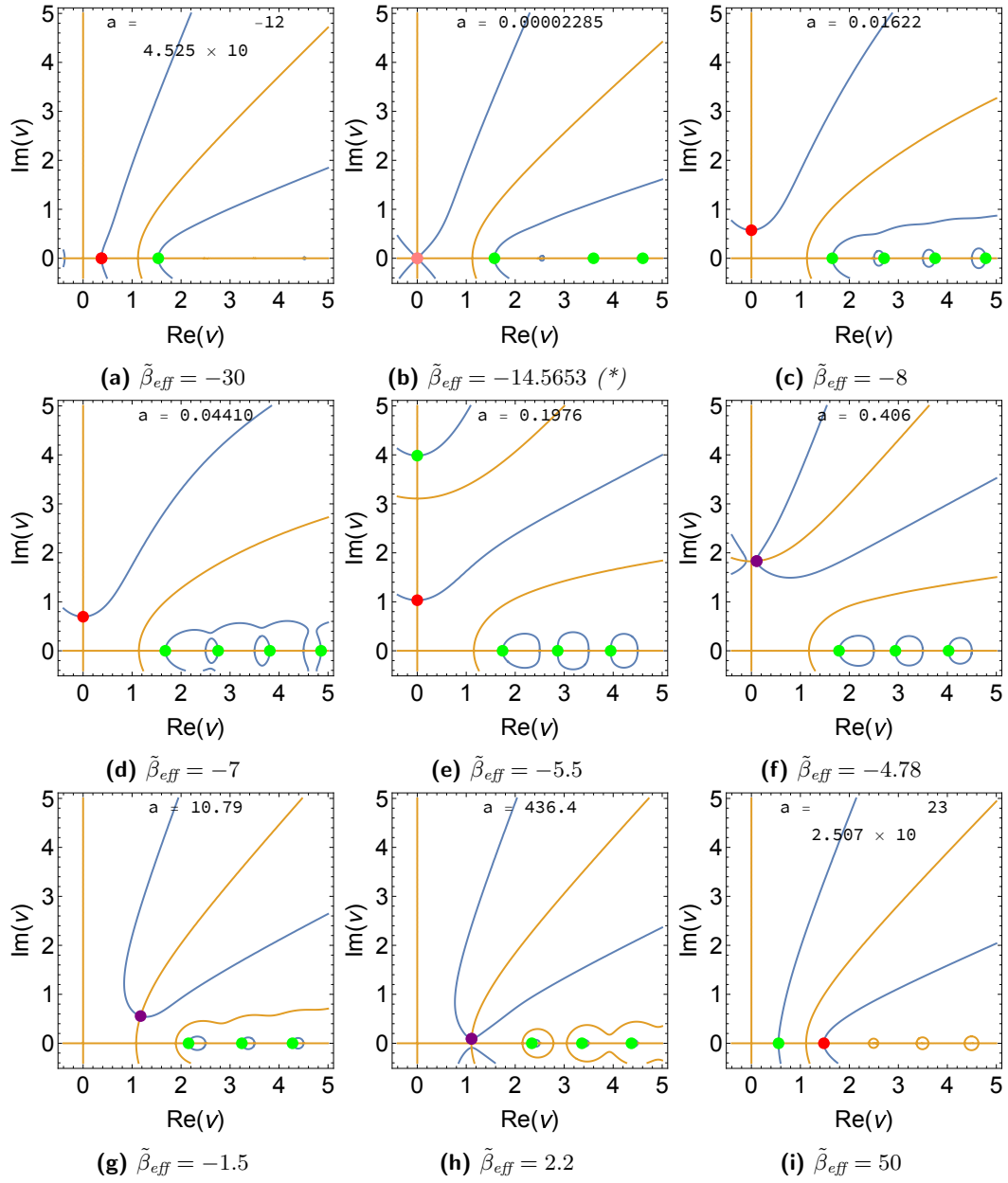


Figure 48: AdS , $\tilde{\alpha} = 0$, $GN^2\chi^2 = 2\pi$.

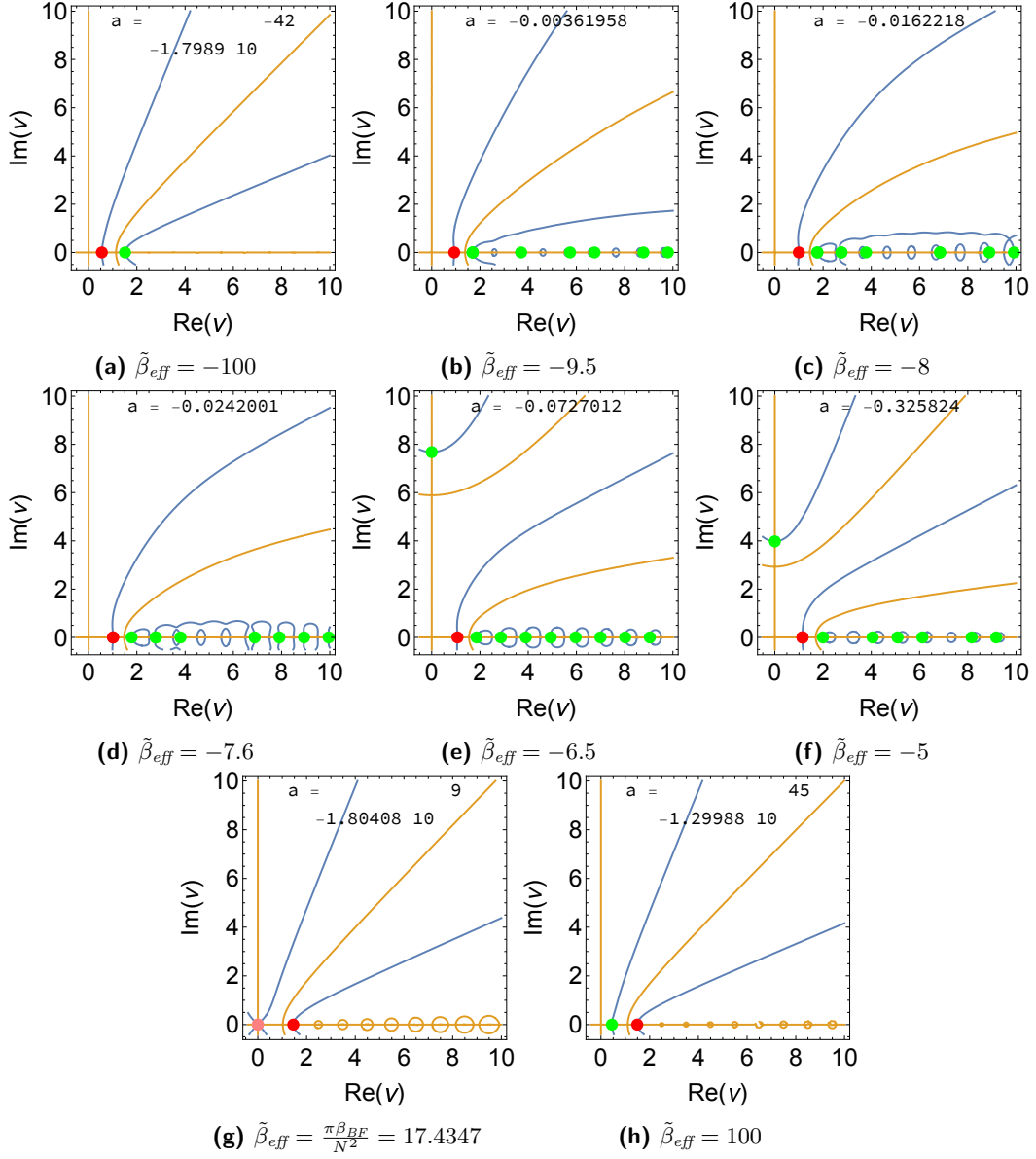


Figure 49: $\alpha = -2$, $GN^2\chi^2 = 2\pi$.

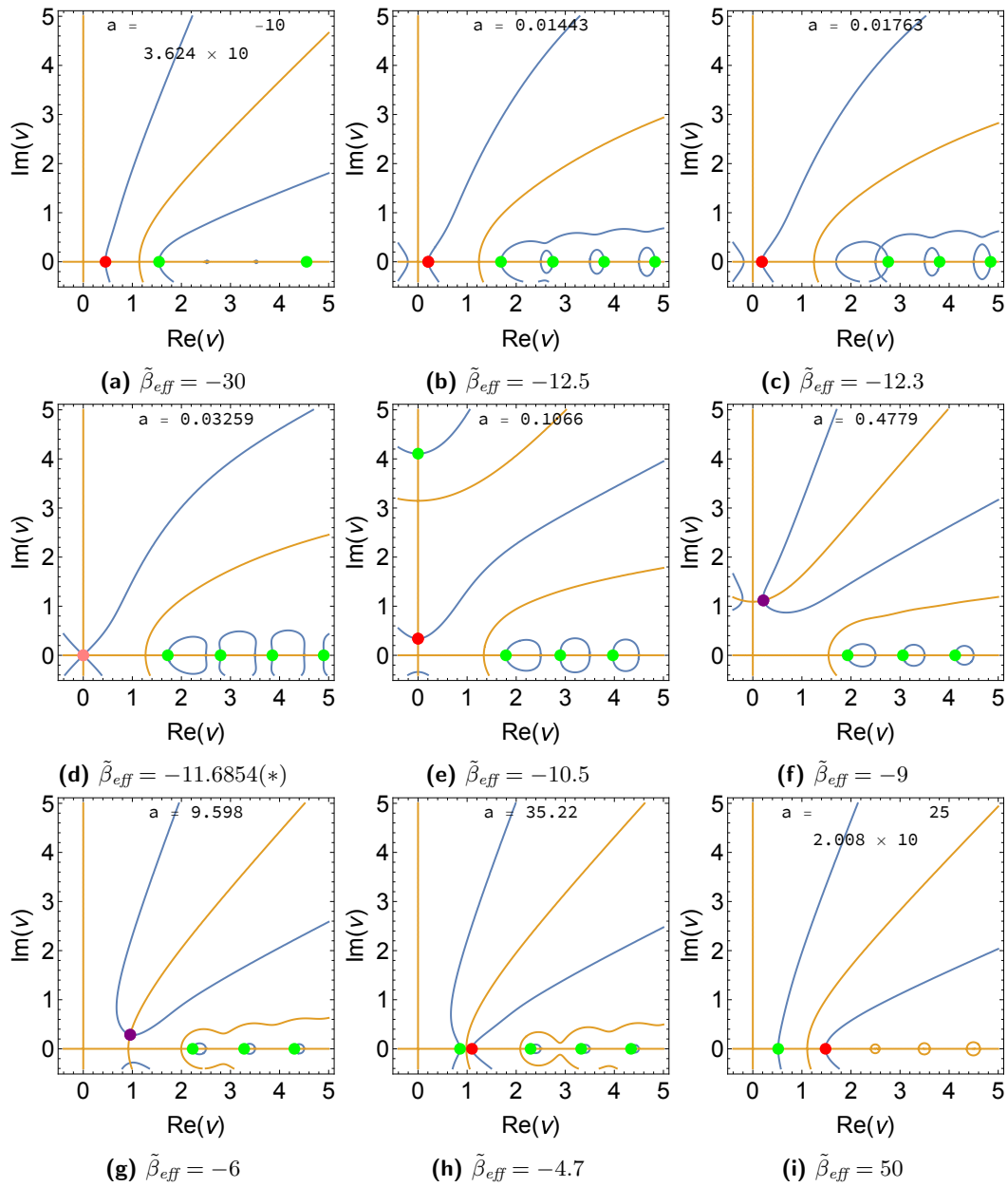


Figure 50: AdS , $\tilde{\alpha} = 0$, $GN^2\chi^2 = 1000$.

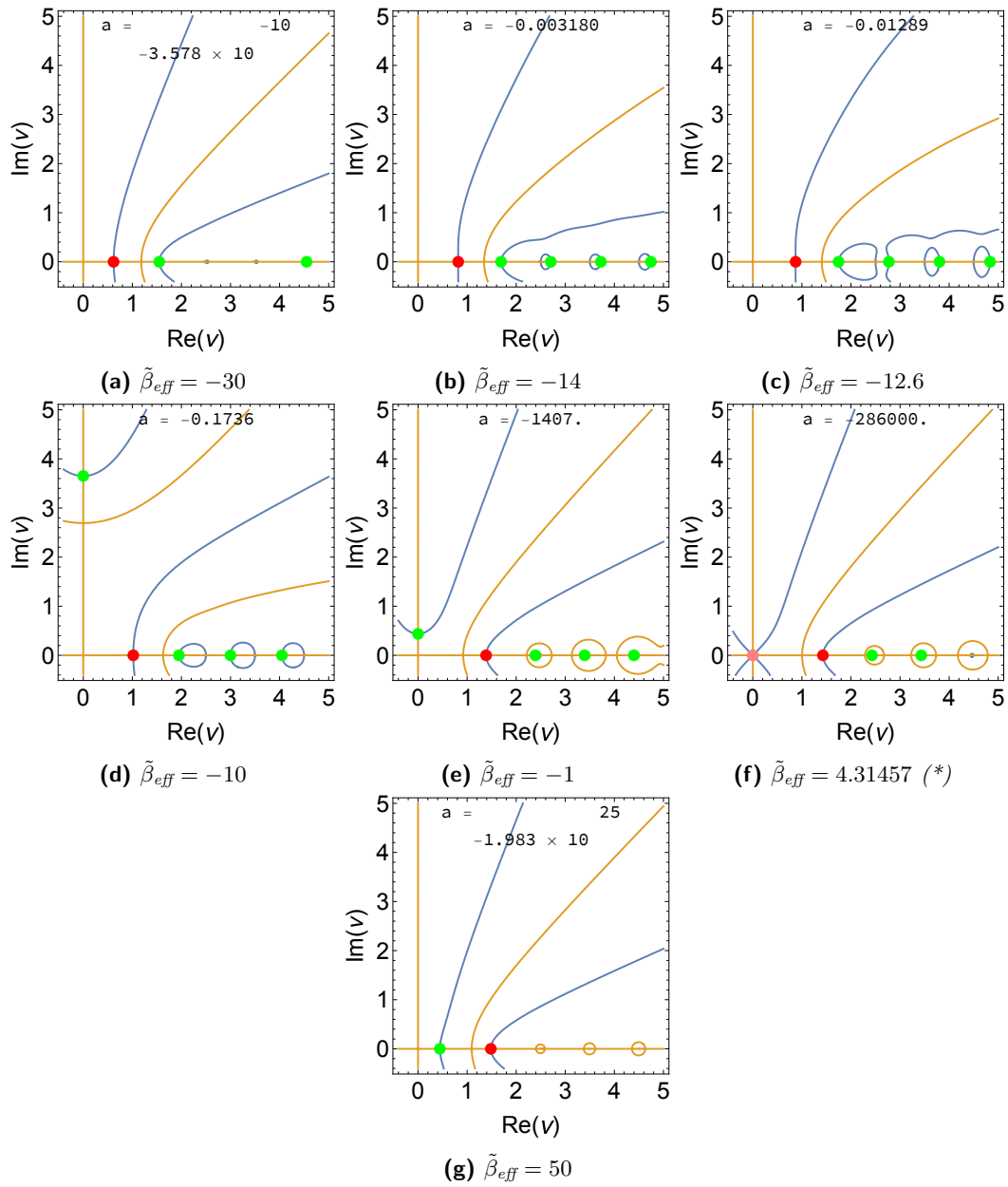


Figure 51: AdS , $\tilde{\alpha} = -1$, $GN^2\chi^2 = 1000$.

References

- [1] N. D. Birrell and P.C.W Davis, ” *Quantum Fields in Curved Space*”, Cambridge Univ. Press, Cambridge, UK, 1982.
- [2] P. Bizon and A. Rostworowski, “*On weakly turbulent instability of anti-de Sitter space,*” *Phys. Rev. Lett.* **107** (2011), 031102; [ArXiv:1104.3702/gr-qc].
- [3] H. Friedrich, “*On the existence of n -geodesically complete or future complete solutions of einstein’s field equations with smooth asymptotic structure*” *Comm. Math. Phys.* 107 (1986) no. 4, 587-609.
- [4] H. Friedrich, “*Existence and structure of past asymptotically simple solutions of einstein’s field equations with positive cosmological constant,*” *Journal of Geometry and Physics* 3 (1986) no. 1, 101-117.
- [5] M. T. Anderson, “*Existence and stability of even dimensional asymptotically de Sitter spaces,*” *Annales Henri Poincaré* 6 (2005) 801-820; [ArXiv:gr-qc/0408072].
- [6] D. Christodoulou and S. Klainerman, “*The Global nonlinear stability of the Minkowski space,*” *Séminaire Goulaouic-Schwartz* (1989-1990), Exposé no. 13, 29 p.
- [7] H. Lindblad and I. Rodnianski, “*The Global stability of the Minkowski space-time in harmonic gauge,*”; [ArXiv:math/0411109].
- [8] G. T. Horowitz and R. M. Wald, “*Dynamics of Einstein’s Equation Modified by a Higher Order Derivative Term*”, *Phys. Rev.* D17 (1978) 414-416.
- [9] G. T. Horowitz, “*Semiclassical Gravity and Weak Field Limit*” *Phys. Rev.* D21 (1980) 1445-1461.
- [10] J. B. Hartle and G. T. Horowitz, “*Ground State Expectation Value of the Metric in the $1/N$ or Semiclassical Approximation to Quantum Gravity,*” *Phys. Rev.* D24 (1981) 257-274.
- [11] W. M. Suen, “*Minkowski Space-time Is Unstable in Semiclassical Gravity,*” *Phys. Rev. Lett.* 62 (1989) 2217-2220.
- [12] W.-M. Suen, “*The Stability of the Semiclassical Einstein Equation*” , *Phys. Rev.* D40 (1989) 315.
- [13] R. D. Jordan, “*Stability of Flat Space-time in Quantum Gravity,*” *Phys. Rev.* D36 (1987) 3593-3603.
- [14] S. Randjbar-Daemi, “*Stability of the Minkowski Vacuum in the Renormalized Semiclassical Theory of Gravity,*” *J. Phys.* A14 (1981) L229.
- [15] P. R. Anderson, C. Molina-Paris and E. Mottola, “*Linear response, validity of semiclassical gravity, and the stability of flat space,*” *Phys. Rev. D* **67** (2003), 024026 [ArXiv:gr-qc/0209075].
- [16] H. Matsui, “*Instability of De Sitter Space-time induced by Quantum Conformal Anomaly,*”, *JCAP* 1901 (2019) no. 01, 003; [ArXiv:1806.10339][hep-th].
- [17] H. Matsui and N. Watamura, “*Quantum Space-time Instability and Breakdown of Semiclassical Gravity,*” *Phys. Rev. D* **101** (2020) no.2, 025014; [ArXiv:1910.02186][gr-qc].
- [18] H. Matsui, “*Space-time Instability and the Problems with Low Energy Quantum Gravity,*” *Gen. Rel. Grav.* **54** (2022) no.10, 123; [ArXiv:1901.08785] [hep-th].

- [19] I. Antoniadis, J. Iliopoulos and T. N. Tomaras, “*Quantum Instability of De Sitter Space*,” *Phys. Rev. Lett.* **56** (1986) 1319;
E. G. Floratos, J. Iliopoulos and T. N. Tomaras, “*Tree Level Scattering Amplitudes in De Sitter Space Diverge*,” *Phys. Lett. B* **197** (1987) 373.
- [20] I. Antoniadis and E. Mottola, “*Graviton Fluctuations in De Sitter Space*,” *J. Math. Phys.* **32** (1991) 1037.
- [21] N. C. Tsamis and R. P. Woodard, “*The Structure of perturbative quantum gravity on a De Sitter background*,” *Commun. Math. Phys.* **162** (1994), 217-248.
- [22] M. Sasaki, H. Suzuki, K. Yamamoto and J. Yokoyama, “*Superexpansive divergence: Breakdown of perturbative quantum field theory in space-time with accelerated expansion*,” *Class. Quant. Grav.* **10** (1993) L55;
“*Probability distribution functional for equal time correlation functions in curved space*,” *Int. J. Mod. Phys. A* **9** (1994) 221.
- [23] N. C. Tsamis and R. P. Woodard, “*The Physical basis for infrared divergences in inflationary quantum gravity*,” *Class. Quant. Grav.* **11** (1994) 2969.
- [24] A. A. Starobinsky, “*Stochastic De Sitter (inflationary) Stage In The Early Universe*,” *Lect. Notes Phys.* **246** (1986) 107;
A. A. Starobinsky and J. Yokoyama, “*Equilibrium state of a selfinteracting scalar field in the De Sitter background*,” *Phys. Rev. D* **50** (1994) 6357 [ArXiv:astro-ph/9407016].
- [25] N. C. Tsamis and R. P. Woodard, “*Stochastic quantum gravitational inflation*,” *Nucl. Phys. B* **724** (2005) 295, [ArXiv:gr-qc/0505115].
- [26] V. Gorbenko and L. Senatore, “ $\lambda\phi^4$ in dS ,” [ArXiv:1911.00022][hep-th].
- [27] D. Marolf and I. A. Morrison, “*The IR stability of de Sitter QFT: results at all orders*,” *Phys. Rev. D* **84** (2011) 044040, [ArXiv:1010.5327][gr-qc].
- [28] S. Hollands, “*Correlators, Feynman diagrams, and quantum no-hair in deSitter space-time*,” *Commun. Math. Phys.* **319** (2013) 1, [ArXiv:1010.5367][gr-qc].
- [29] V. F. Mukhanov, L. R. W. Abramo and R. H. Brandenberger, “*On the Back reaction problem for gravitational perturbations*,” *Phys. Rev. Lett.* **78** (1997) 1624, [ArXiv:gr-qc/9609026];
“*The Energy-momentum tensor for cosmological perturbations*,” *Phys. Rev. D* **56** (1997) 3248, [ArXiv:gr-qc/9704037].
- [30] L. R. W. Abramo and R. P. Woodard, “*One loop back reaction on chaotic inflation*,” *Phys. Rev. D* **60** (1999) 044010, [ArXiv:astro-ph/9811430].
- [31] B. Losic and W. G. Unruh, “*Long-wavelength metric backreactions in slow-roll inflation*,” *Phys. Rev. D* **72** (2005) 123510, [ArXiv:gr-qc/0510078];
“*Cosmological Perturbation Theory in Slow-Roll Space-times*,” *Phys. Rev. Lett.* **101** (2008) 111101, [ArXiv:0804.4296][gr-qc].
- [32] P. Mazur and E. Mottola, “*Spontaneous Breaking of De Sitter Symmetry by Radiative Effects*,” *Nucl. Phys. B* **278** (1986) 694.
- [33] B. Allen, “*Vacuum States in de Sitter Space*,” *Phys. Rev. D* **32** (1985) 3136;
B. Allen and A. Folacci, “*The Massless Minimally Coupled Scalar Field in De Sitter Space*,” *Phys. Rev. D* **35** (1987) 3771.

- [34] S. Hollands, “*Massless interacting quantum fields in deSitter space-time*,” *Annales Henri Poincare* **13** (2012) 1039, [ArXiv:1105.1996][gr-qc].
- [35] E. Mottola, “*Particle Creation in de Sitter Space*,” *Phys. Rev. D* **31** (1985) 754;
E. Mottola, “*Thermodynamic Instability Of De Sitter Space*,” *Phys. Rev. D* **33** (1986) 1616.
- [36] N. C. Tsamis and R. P. Woodard, “*Quantum gravity slows inflation*,” *Nucl. Phys. B* **474** (1996) 235, [ArXiv:hep-ph/9602315];
“*The Quantum gravitational back reaction on inflation*,” *Annals Phys.* **253** (1997) 1, [ArXiv:hep-ph/9602316].
- [37] V. K. Onemli and R. P. Woodard, “*Quantum effects can render $w < -1$ on cosmological scales*,” *Phys. Rev. D* **70** (2004) 107301, [ArXiv:gr-qc/0406098].
- [38] A. M. Polyakov, “*Infrared instability of the de Sitter space*,” [ArXiv:1209.4135][hep-th].
- [39] P. R. Anderson and E. Mottola, “*Instability of global de Sitter space to particle creation*,” *Phys. Rev. D* **89** (2014), 104038 [ArXiv:1310.0030].
- [40] P. R. Anderson and E. Mottola, “*Quantum vacuum instability of “eternal” de Sitter space*,” *Phys. Rev. D* **89** (2014), 104039 [ArXiv:1310.1963].
- [41] P. R. Anderson, E. Mottola and D. H. Sanders, “*Decay of the de Sitter Vacuum*,” *Phys. Rev. D* **97** (2018) no.6, 065016 [ArXiv:1712.04522].
- [42] P. R. Anderson, C. Molina-Paris and E. Mottola, “*Cosmological Horizon Modes and Linear Response in de Sitter Space-time*,” *Phys. Rev. D* **80** (2009), 084005 [ArXiv:0907.0823].
- [43] G. Dvali, “*On S-Matrix Exclusion of de Sitter and Naturalness*,” [ArXiv:2105.08411] [hep-th].
- [44] S. P. Miao, N. C. Tsamis and R. P. Woodard, “*Invariant Measure of the One Loop Quantum Gravitational Back-Reaction on Inflation*,” *Phys. Rev. D* **95** (2004) 125008, [ArXiv:1702.05694][gr-qc].
- [45] S. Weinberg, “*Quantum contributions to cosmological correlations*,” *Phys. Rev. D* **72** (2005) 043514, [ArXiv:hep-th/0506236];
“*Quantum contributions to cosmological correlations. II. Can these corrections become large?*,” *Phys. Rev. D* **74** (2006) 023508 [ArXiv:hep-th/0605244].
- [46] K. Chaicherdsakul, “*Quantum Cosmological Correlations in an Inflating Universe: Can fermion and gauge fields loops give a scale free spectrum?*,” *Phys. Rev. D* **75** (2007) 063522 [ArXiv:hep-th/0611352].
- [47] A. Riotto and M. S. Sloth, “*On Resumming Inflationary Perturbations beyond One-loop*,” *JCAP* **0804** (2008) 030, [ArXiv:0801.1845][hep-ph].
- [48] L. Senatore and M. Zaldarriaga, “*On Loops in Inflation*,” *JHEP* **1012** (2010) 008, [ArXiv:0912.2734][hep-th];
“*On Loops in Inflation II: IR Effects in Single Clock Inflation*,” *JHEP* **1301** (2013) 109, [ArXiv:1203.6354][hep-th];
“*The constancy of ζ in single-clock Inflation at all loops*,” *JHEP* **1309** (2013) 148 [ArXiv:1210.6048][hep-th];
G. L. Pimentel, L. Senatore and M. Zaldarriaga, “*On Loops in Inflation III: Time Independence of zeta in Single Clock Inflation*,” *JHEP* **1207** (2012) 166, [ArXiv:1203.6651][hep-th].

- [49] D. Seery, “*Infrared effects in inflationary correlation functions,*” *Class. Quant. Grav.* **27** (2010) 124005, [ArXiv:1005.1649][astro-ph.CO].
- [50] U. H. Danielsson and T. Van Riet, “*What if string theory has no de Sitter vacua?,*” *Int. J. Mod. Phys. D* **27** (2018) no.12, 1830007, [ArXiv:1804.01120][hep-th].
- [51] G. Obied, H. Ooguri, L. Spodyneiko and C. Vafa, “*De Sitter Space and the Swampland,*” [ArXiv:1806.08362][hep-th].
- [52] A. A. Starobinsky, “*A New Type of Isotropic Cosmological Models Without Singularity,*” *Phys. Lett. B* **91** (1980) 99, *Adv. Ser. Astrophys. Cosmol.* **3** (1987) 130.
- [53] A. Vilenkin, “*Classical and Quantum Cosmology of the Starobinsky Inflationary Model,*” *Phys. Rev. D* **32** (1985) 2511.
- [54] E. Kiritsis, “*Holography and brane-bulk energy exchange,*” *JCAP* **0510** (2005) 014, [ArXiv:hep-th/0504219].
- [55] M. J. Duff, “*Twenty years of the Weyl anomaly,*” *Class. Quant. Grav.* **11** (1994) 1387 [ArXiv:hep-th/9308075].
- [56] Y. Akrami *et al.* [Planck], “*Planck 2018 results. X. Constraints on inflation,*” *Astron. Astrophys.* **641** (2020), A10 [ArXiv:1807.06211][astro-ph.CO].
- [57] S. W. Hawking, T. Hertog and H. S. Reall, “*Brane new world,*” *Phys. Rev. D* **62** (2000), 043501; [ArXiv:hep-th/0003052].
- [58] S. W. Hawking, T. Hertog and H. S. Reall, “*Trace Anomaly Driven Inflation,*” *Phys. Rev. D* **63** (2001) 083504, [ArXiv:hep-th/0010232].
- [59] B. Freivogel, V. E. Hubeny, A. Maloney, R. C. Myers, M. Rangamani and S. Shenker, “*Inflation in AdS/CFT,*” *JHEP* **03** (2006), 007; [ArXiv:hep-th/0510046].
- [60] P. S. Apostolopoulos, G. Siopsis and N. Tetradis, “*Cosmology from an AdS Schwarzschild black hole via holography,*” *Phys. Rev. Lett.* **102**, 151301 (2009) [ArXiv:0809.3505][hep-th].
- [61] N. Tetradis, “*The Temperature and entropy of CFT on time-dependent backgrounds,*” *JHEP* **03**, 040 (2010) [ArXiv:0905.2763][hep-th].
- [62] D. Marolf, M. Rangamani and M. Van Raamsdonk, “*Holographic models of de Sitter QFTs,*” *Class. Quant. Grav.* **28** (2011), 105015; [ArXiv:1007.3996][hep-th]
- [63] N. Lamprou, S. Nonis and N. Tetradis, “*The BTZ black hole with a time-dependent boundary,*” *Class. Quant. Grav.* **29**, 025002 (2012) [ArXiv:1106.1533][gr-qc].
- [64] J. Maldacena and G. L. Pimentel, “*Entanglement entropy in de Sitter space,*” *JHEP* **02** (2013), 038; [ArXiv:1210.7244] [hep-th].
- [65] W. Fischler, S. Kundu and J. F. Pedraza, “*Entanglement and out-of-equilibrium dynamics in holographic models of de Sitter QFTs,*” *JHEP* **07** (2014), 021; [ArXiv:1311.5519] [hep-th].
- [66] W. Fischler, P. H. Nguyen, J. F. Pedraza and W. Tangarife, “*Fluctuation and dissipation in de Sitter space,*” *HEP* **08** (2014), 028; [ArXiv:1404.0347] [hep-th].
- [67] W. Fischler, P. H. Nguyen, J. F. Pedraza and W. Tangarife, “*Holographic Schwinger effect in de Sitter space,*” *Phys. Rev. D* **91** (2015) no.8, 086015 [ArXiv:1411.1787] [hep-th].
- [68] K. Nguyen, “*De Sitter-invariant States from Holography,*” *Class. Quant. Grav.* **35** no.22, 225006; [ArXiv:1710.04675] [hep-th].

- [69] A. Buchel and A. Karapetyan, “*de Sitter Vacua of Strongly Interacting QFT*,” *JHEP* **03** (2017), 114 [ArXiv:1702.01320] [hep-th].
- [70] J. K. Ghosh, E. Kiritsis, F. Nitti and L. T. Witkowski, “*De Sitter and Anti-de Sitter branes in self-tuning models*,” *JHEP* **11** (2018), 128; [ArXiv:1807.09794] [hep-th].
- [71] J. K. Ghosh, E. Kiritsis, F. Nitti and L. T. Witkowski, “*Holographic RG flows on curved manifolds and the F-theorem*,” *JHEP* **1902** (2019) 055, [ArXiv:1810.12318][hep-th].
- [72] J. K. Ghosh, E. Kiritsis, F. Nitti and L. T. Witkowski, “*Back-reaction in massless de Sitter QFTs: holography, gravitational DBI action and f(R) gravity*,” *JCAP* **07**, 040 (2020) [ArXiv:2003.09435][hep-th].
- [73] J. M. Penín, K. Skenderis and B. Withers, “*Massive holographic QFTs in de Sitter*,” *SciPost Phys.* **12** (2022), 182 [ArXiv:2112.14639][hep-th].
- [74] P. M. Chesler and A. Loeb, “*Holographic duality and mode stability of de Sitter space in semiclassical gravity*,” *JCAP* **11** (2020), 010 [ArXiv:2003.05501][hep-th].
- [75] G. Dvali, “*Black Holes and Large N Species Solution to the Hierarchy Problem*,” *Fortsch. Phys.* **58** (2010), 528-536; [ArXiv:0706.2050] [hep-th].
- [76] L. Castellani and P. Van Nieuwenhuizen, “QUADRATIC AND QUARTIC ONE LOOP DIVERGENCES IN GAUGE THEORIES AND THEIR CANCELLATION IN SUPERGRAVITY,” *Nucl. Phys. B* **213** (1983), 305-326.
- [77] E. Kiritsis and C. Kounnas, “Infrared regularization of superstring theory and the one loop calculation of coupling constants,” *Nucl. Phys. B* **442** (1995), 472-493 [ArXiv:hep-th/9501020].
- [78] E. Kiritsis, C. Kounnas, P. M. Petropoulos and J. Rizos, “On the heterotic effective action at one loop gauge couplings and the gravitational sector,” [ArXiv:hep-th/9605011].
- [79] E. Kiritsis, C. Kounnas, P. M. Petropoulos and J. Rizos, “String threshold corrections in models with spontaneously broken supersymmetry,” *Nucl. Phys. B* **540** (1999), 87-148; [ArXiv:hep-th/9807067].
- [80] E. Kiritsis, N. Tetradis and T. N. Tomaras, “Induced brane gravity: Realizations and limitations,” *JHEP* **08** (2001), 012; [ArXiv:hep-th/0106050].
- [81] I. Antoniadis, R. Minasian and P. Vanhove, “Noncompact Calabi-Yau manifolds and localized gravity,” *Nucl. Phys. B* **648** (2003), 69-93; [ArXiv:hep-th/0209030].
- [82] S. de Haro, K. Skenderis and S. Solodukhin, “*Holographic Reconstruction of Space-time and Renormalization in the AdS/CFT Correspondence*,” *Commun. Math. Phys.* **217** (2001) 595. [ArXiv:hep-th/0002230].
- [83] A. B. Clark, D. Z. Freedman, A. Karch and M. Schnabl, “*Dual of the Janus solution: An interface conformal field theory*,” *Phys. Rev. D* **71** (2005), 066003 [ArXiv:hep-th/0407073].
- [84] A. Ghodsi, J. K. Ghosh, E. Kiritsis, F. Nitti and V. Noury, “*Holographic QFTs on AdS_d, wormholes and holographic interfaces*,” *JHEP* **01** (2023), 121 [ArXiv:2209.12094][hep-th].
- [85] K. Stelle, “*Classical gravity with higher derivatives*,” *Gen. Relat. Grav.* **9**, 353-371 (1978).
- [86] B. Zwiebach, “*Curvature Squared Terms and String Theories*,” *Phys. Lett. B* **156** (1985), 315-317.

- [87] M. Brigante, H. Liu, R. C. Myers, S. Shenker and S. Yaida, “*The Viscosity Bound and Causality Violation*,” *Phys. Rev. Lett.* **100** (2008), 191601; [ArXiv:0802.3318] [hep-th].
- [88] M. Baggioli, B. Goutéraux, E. Kiritsis and W. J. Li, “*Higher derivative corrections to incoherent metallic transport in holography*,” *JHEP* **03** (2017), 170; [ArXiv:1612.05500] [hep-th].
- [89] K. Koyama and J. Soda, “*Strongly coupled CFT in FRW universe from AdS / CFT correspondence*,” *JHEP* **05** (2001), 027 [ArXiv:hep-th/0101164].
- [90] C. Fefferman, C. R. Graham, “*Conformal invariants*,” *Élie Cartan et les mathématiques d’aujourd’hui (Astérisque 1985)* 95.
- [91] J. K. Ghosh, E. Kiritsis, F. Nitti and L. T. Witkowski, “*Revisiting Coleman-de Luccia transitions in the AdS regime using holography*,” *JHEP* **09** (2021), 065 [ArXiv:2102.11881][hep-th].
- [92] L. Alvarez-Gaume, A. Kehagias, C. Kounnas, D. Lüst and A. Riotto, “*Aspects of Quadratic Gravity*,” *Fortsch. Phys.* **64** (2016) no.2-3, 176-189 [ArXiv:1505.07657/[hep-th]].
- [93] P. Breitenlohner and D. Z. Freedman, “*Positive Energy in anti-De Sitter Backgrounds and Gauged Extended Supergravity*,” *Phys. Lett. B* **115** (1982), 197-201
- [94] W. Magnus, F. Oberhettinger, R. P. Soni, “*Formulas and Theorems for the Special Functions of Mathematical Physics*,” Springer (1966).
- [95] A. A. Tseytlin, “*Comments on 4-derivative scalar theory in 4 dimensions*,” [ArXiv:2212.10599] [hep-th].
- [96] T. Faulkner, M. Tegmark, E. F. Bunn and Y. Mao, “*Constraining $f(R)$ Gravity as a Scalar Tensor Theory*,” *Phys. Rev. D* **76** (2007), 063505 [ArXiv:astro-ph/0612569].
- [97] S. Coleman, “*Acausality, in*” *Theory and Phenomenology in Particle Physics*, Ed. A. Zichichi (1970).
- [98] C. Imbimbo, A. Schwimmer, S. Theisen and S. Yankielowicz, “*Diffeomorphisms and holographic anomalies*,” *Class. Quant. Grav.* **17** (2000), 1129-1138 [ArXiv:hep-th/9910267].
- [99] E. Mottola, “*Scalar Gravitational Waves in the Effective Theory of Gravity*,” *JHEP* **07** (2017), 043; [erratum: *JHEP* **09** (2017), 107] [ArXiv:1606.09220] [gr-qc].
- [100] A. Lopez-Ortega, “*Electromagnetic quasinormal modes of D-dimensional black holes*,” *Gen. Rel. Grav.* **38** (2006), 1747-1770 doi:10.1007/s10714-006-0358-2 [ArXiv:gr-qc/0605034].